Dissertation
submitted to the
Combined Faculties of the Natural Sciences and Mathematics
of the Ruperto-Carola-University of Heidelberg. Germany
for the degree of
Doctor of Natural Sciences

Put forward by
Florian Thomas Köhler

born in: Bonn

Oral examination: 22nd of July 2015

Bound-Electron g-Factor Measurements for the Determination of the Electron Mass and Isotope Shifts in Highly Charged Ions

First referee: Priv. Doz. Dr. Wolfgang Quint

Second referee: Prof. Dr. Selim Jochim

Abstract - In the context of this thesis the electron mass has been determined in atomic mass units with a relative uncertainty of $2.8 \cdot 10^{-11}$, which represents a 13-fold improvement of the 2010 CODATA value. The underlying measurement principle combines a high-precision measurement of the Larmor-to-cyclotron frequency ratio on a single hydrogenlike carbon ion $^{12}C^{5+}$ with a very accurate g-factor calculation. Furthermore, this thesis contains the first isotope shift measurement of bound-electron g-factors of highly charged ions. Here, the g-factors of the valence electrons of the lithiumlike calcium isotopes $^{40}Ca^{17+}$ and $^{48}Ca^{17+}$ have been measured with relative uncertainties of a few 10^{-10}, constituting a so-far unrivaled level of precision for lithiumlike ions. These calcium isotopes provide a unique system across the entire nuclear chart to test the pure relativistic nuclear recoil effect. The corresponding and successfully tested theoretical prediction is based on bound-state quantum electrodynamics but goes beyond the standard formalism, the so-called Furry picture, where the nucleus is considered as a classical source of the Coulomb field. The three Larmor-to-cyclotron frequency ratios of $^{12}C^{5+}$, $^{40}Ca^{17+}$ and $^{48}Ca^{17+}$ have been determined in sequence in a non-destructive manner on single trapped ions stored in a triple Penning trap setup. The cyclotron frequency is measured by a dedicated phase-sensitive detection technique while simultaneously probing the Larmor frequency. The spin-state of the bound valence electron is determined by the continuous Stern-Gerlach effect. In the very last part of this thesis, a new design of a highly compensated cylindrical Penning trap has been developed, which will be used in next generation's high-precision Penning trap experiments.

Zusammenfassung - Im Rahmen dieser Doktorarbeit wurde die Elektronenmasse in atomaren Masseneinheiten mit einer relativen Unsicherheit von $2.8 \cdot 10^{-11}$ bestimmt. Dieser Wert ist 13 mal genauer als der Wert der CODATA 2010. Im zugrundeliegenden Messprinzip wird eine sehr präzise Bestimmung des Frequenzverhältnisses der Larmor- und Zyklotronfrequenz eines einzelnen wasserstoffähnlichen Kohlenstoffions $^{12}C^{5+}$ mit einer sehr genauen Rechnung des zugehörigen g-Faktors kombiniert. Des Weiteren beinhaltet diese Arbeit die erstmalige Messung einer Isotopieverschiebung in g-Faktoren hoch geladener Ionen. Hierbei wurden die g-Faktoren der lithiumähnlichen Kalziumisotope $^{40}Ca^{17+}$ und $^{48}Ca^{17+}$ mit relativen Genauigkeiten von wenigen 10^{-10} gemessen. Dieses Präzisionsniveau wurde bei lithiumähnlichen Ionen zum ersten Mal erreicht. Unter Berücksichtigung der gesamten Nuklidkarte bieten diese Kalziumisotope ein einmaliges System, um den rein relativistischen Kernrückstoßeffekt zu untersuchen. Die hierbei erfolgreich getestete theoretische Vorhersage basiert auf der Quantenelektrodynamik gebundener Zustände, die über den üblichen Formalismus, den sogenannten Furry-Ansatz, in dem der Atomkern als klassische Quelle eines Coulomb-Feldes genähert wird, hinausgeht. Die drei Larmor- zur Zyklotronfrequenz Verhältnisse von $^{12}C^{5+}$, $^{40}Ca^{17+}$ und $^{48}Ca^{17+}$ wurden nacheinander auf zerstörungsfreie Weise an einzelnen gespeicherten Ionen in einem dreifachen Penningfallensystem gemessen. Die Zyklotronfrequenz wurde hierbei jeweils mit einer geeigneten phasenempfindlichen Messmethode bestimmt, während gleichzeitig die Larmorfrequenz abgetastet wurde. Der Spinzustand des gebundenen Valenzelektrons wurde mit Hilfe des kontinuierlichen Stern-Gerlach Effekts festgestellt. Im letzten Teil dieser Arbeit wurde ein neues Design einer hochgradig kompensierten zylindrischen Penning-Falle entwickelt, die in zukünftigen Penning-Fallen Experimenten verwendet werden soll.

Contents

List of Figures

List of Tables

CHAPTER 1

Introduction

1.1 Quantum Electrodynamics and the Standard Model of Particle Physics

Today, the most fundamental models to describe the physical structure and dynamics of nature are based on quantum field theories. The collection of three quantum field theories: (1) quantum electrodynamics (QED), describing the electromagnetic interaction, (2) quantum flavordynamics (QFD), describing the weak interaction and (3) quantum chromodynamics (QCD), describing the strong interaction, are called the *Standard Model* (SM) of particle physics. The elementary assumption of local gauge invariance of these quantum field theories stimulated the development of the so-called Higgs mechanism in the 1960s, which explains the generation of all particle masses via spontaneous symmetry breaking [1, 2, 3]. This additional cornerstone of the SM has been verified recently in 2012 by the discovery of the predicted Higgs boson [4].

Aside from the tremendous predictive capabilities of the SM, which are partly highlighted in chapter 2, there are several limitations of this model to describe all fundamental processes in nature, e.g.: (1) So far it has not been possible to add gravity to the SM by the formulation of a proper quantum field theory. (2) Several observations of dark matter [5] and dark energy [6] cannot be explained within the SM. (3) The existence of neutrino masses, indicated by the experimentally observed neutrino oscillations [7, 8], are not yet included in the SM. (4) A seemingly unnatural fine-tuning of the bare mass of the Higgs boson and its radiative corrections is required to model the large difference between the fundamental couplings, e.g. the weak force and gravity, which is called the hierarchy problem [9]. (5) Moreover, many physicists consider it to be inelegant, that the SM relies on 19 input parameters[1], which up to now cannot be predicted.

The incompleteness of the SM requires further experiments, which on the one hand look for new physics at so far unreached energy scales, e.g. via the large-scale LHC experiments [10, 11], but on the other hand also probe the SM at the lower energy scale under various

1 The 19 input parameters of the SM include the particle masses for the electron, muon, tau and the six quarks, the three CKM mixing angles, the CKM cp-violating phase, the gauge coupling constants of the electric, the weak and the strong force, the QCD vacuum angle, the Higgs vacuum expectation value and the Higgs mass.

conditions to highest precision. In this thesis I focus on the mother of all quantum field theories, quantum electrodynamics (QED), which has been formulated by Richard Feynman, Julian Schwinger, Sin-Itiro Tomonaga and colleagues in the 1940s [12]. Here, the interaction between electrically charged particles is realized via photon exchange. Right from beginning the central driving force in the development of QED has been the predicted and measured electron g-factor, which will be introduced in detail in chapter 2. In this thesis the work on high-precision measurements of bound-electron g-factors is continued, which nowadays probes QED in the strongest electric fields on the highest level of precision and moreover provides a unique access to high-precision measurements of fundamental constants, e.g. the electron mass.

1.2 Content and Structure of the Thesis

When I arrived in Mainz in autumn 2011, I came upon an experimental apparatus for the measurement of bound-electron g-factors of highly charged ions, which was in an excellent shape, thanks to the great work of my preceding Ph.D colleagues: Birgit Schabinger, Sven Sturm and Anke Wagner (nowadays: Anke Kracke). In the beginning of 2011 Sven Sturm had performed the most stringent test of bound-state quantum electrodynamics, by measuring the g-factor of hydrogenlike $^{28}Si^{13+}$[13]. In 2011/2012 Anke Kracke continued the work by measuring the g-factor of lithiumlike $^{28}Si^{11+}$and thus performing the most stringent test of relativistic many-electron calculations in a magnetic field [14].
This thesis proceeds the experimental agenda of bound-electron g-factor measurements with highly charged ions. It covers three individual physical tasks:

- The electron's atomic mass has been determined with so far unrivaled precision. The relative uncertainty of $\delta m_e/m_e = 2.8 \cdot 10^{-11}$ surpasses the current literature value by a factor of 13.
- The first measurement of the isotope shift in atomic g-factors has been performed with highly charged ions, by measuring the bound-electron g-factor difference of lithiumlike $^{40}Ca^{17+}$ and $^{48}Ca^{17+}$. The corresponding calculations require bound-state QED theory beyond the external field approximation of the nucleus, providing a unique access to QED beyond the well-established Furry picture.
- Furthermore, a completely revised Penning trap design has been calculated. The layout comprises seven cylindrical electrodes, which provide an extremely harmonic trapping potential. The seven-electrode Penning trap represents a central building block of an experimental upgrade, planned in the near future, which will enable a high-precision measurement of the atomic mass of the proton.

Due to the variety of these topics, the thesis is structured as follows: In chapter 2 I will briefly introduce the theoretical framework of the bound-electron g-factors and summarize the status of these perturbative calculations. Moreover, the general measurement principle of the bound-electron g-factors will be explained. In the last two sections of chapter 2 the measurements of the electron mass and the isotope shift will be motivated. In chapter 3 the state-of-the-art trapping concept and all relevant high-precision frequency measurement techniques will be discussed in detail. In chapter 4 the experimental setup will be introduced.

Here, a special focus is set on the exisiting stabilization systems and beyond that on calculations of future radial compensation coils. In the following preparatory measurement procedures will be outlined. Furthermore, the automated measurement process will be explained step-by-step. The last section of chapter 4 contains a comprehensive line-shape study of the essential resonance for the g-factor determination, the so-called Γ-resonance. In the following two chapters the two major measurement results will be presented, firstly the determination of the electron mass, see chapter 5, and secondly the isotope shift measurement in the bound-electron g-factors of two lithiumlike calcium ions, $^{40}Ca^{17+}$and $^{48}Ca^{17+}$, see chapter 6. In the last chapter 7 I will present a new Penning trap design based on seven cylindrical electrodes. This Penning trap design will be used in the near future in a new generation of high-precision ion trap experiments, which will be briefly summarized in the last section of chapter 7.

CHAPTER 2

The g-Factor - Exploring Atomic Structure and Fundamental Constants

Slightly more than 100 years ago Ernest Rutherford in 1911 and Niels Bohr in 1913 made the first fundamental steps to explain the atomic structure of nature [15, 16]. Since then, enormous efforts have been undertaken, such that the SM nowadays is able to predict properties of elementary particles up to the thirteens digit[1] [17, 18, 19]. In the following chapter I will illuminate the present understanding of the fundamental electromagnetic dynamics in atomic structure. The main focus will be set on the present workhorse of the underlying theory, the so-called bound-state quantum electrodynamics (BS-QED): the bound-electron g-factor.
In section 2.1 the g-factor will be introduced and defined, followed by a summary of the most stringent test of QED in weak fields in section 2.2, the g-factor calculations and measurements of the free electron. In section 2.3 investigations of the bound-electron g-factor are motivated. Here, I will also report on the enormous progress of the theoretical calculations of the bound-electron g-factors and briefly summarize its various physical contributions. In section 2.4 the fundamental measurement principle of the bound-electron g-factor is introduced and an overview on the last measurements is given in section 2.5. The last two sections cover the specific theoretical backgrounds of the two physical topics of the present thesis: (1) The electron mass (section 2.6) and (2) the g-factor isotope shift in the lithiumlike calcium ions $^{40}Ca^{17+}$ and $^{48}Ca^{17+}$ (section 2.7).

2.1 The g-Factor

In 1922, Otto Stern and Walther Gerlach performed their famous Stern-Gerlach experiment by sending a beam of silver atoms through an inhomogeneous magnetic field, observing a discrete splitting of the beam into two beams [20]. Not until 1925 Samuel A. Goudsmit and George E. Uhlenbeck interpreted the phenomena in the nowadays well-established model, proposing an intrinsic quantized property of the electron, the so-called spin $\vec{s}$, which generates an intrinsic magnetic moment $\vec{\mu}_s$ [21]. In an external magnetic field $\vec{B} = B \cdot \vec{e}_z$[2] the electron-spin has two discrete quantum states with the eigenvalues $s_z = m_s\hbar = \pm\frac{1}{2}\hbar$,

1 Relative uncertainties of the g-factor of the free electron: $(\delta g/g)_{\text{theo}} = 0.8 \cdot 10^{-12}$ and $(\delta g/g)_{\text{exp}} = 0.3 \cdot 10^{-12}$, see also section 2.2.

2 In the following a homogeneous magnetic field will always point in z-direction.

where $\hbar = h/(2\pi)$ is the reduced Planck constant. The proportionality constant between the intrinsic magnetic moment and the spin in terms of the Bohr magneton μ_B is the g-factor:

$$\vec{\mu}_s = -g\mu_\mathrm{B}\frac{\vec{s}}{\hbar}, \tag{2.1}$$

where $\mu_\mathrm{B} \equiv \frac{|e|\hbar}{2m_e}$, e is the elementary electric charge and m_e the mass of the electron. The g-factor thus defines the strength of the interaction between the magnetic field and the spin of the electron, where the magnetic potential is given by $U_\mathrm{magn} = -\vec{\mu}\cdot\vec{B}$. Assuming the spin as a classical angular momentum ($\vec{s} = \vec{r}\times\vec{p}$) and a classical magnetic moment ($\vec{\mu} = I\cdot A\cdot\vec{n}_A$) the g-factor would have a value of $g = 1$. Already in 1922 Alfred Landé proposed a phenomenological electron g-factor of $g = 2$ (also called Landé g-factor) to interpret the observed anomalous Zeeman effect, not yet knowing about the electron spin [22]. In 1928 finally Paul Dirac formulated his famous equation, combining quantum mechanics with special relativity. This theory unification entailed the electron as a spin-1/2 particle. As a direct consequence, the electron g-factor was $g = 2$. Almost 20 years later, in 1947, small deviations from Dirac's theory have been observed in different experiments: (1) in the energy levels of the hydrogen atom, nowadays called Lamb shift [23], and (2) in the electron g-factor [24, 25, 26, 27]. Still in the same year Julian Schwinger managed to explain the deviation in the g-factor by considering the virtual coupling of the fields, more precisely the emission and subsequent absorbtion of photons. In that context, he performed first-order perturbation calculations within the especially developed framework of quantum electrodynamics (QED) [28]: $g = 2\left(1+\frac{\alpha}{2\pi}\right)$, where $\alpha \equiv \frac{1}{4\pi\varepsilon_0}\frac{e^2}{\hbar c} \approx 1/137$ is the fine structure constant, which defines the coupling strength of QED. Furthermore, ε_0 is the electric constant (vacuum permittivity) and c is the speed of light in vacuum. This successful model flags the dawn of quantum electrodynamics, the mother of all quantum field theories.

2.2 The g-Factor of the Free Electron

Since 1947 the electron g-factor is the key quantity for the most stringent test of QED and in that way of the SM. At present the anomalous magnetic momentum of the electron (g-factor anomaly): $a_e \equiv (g-2)/2$ is calculated in a series expansion in terms of (α/π) up to the fifth order:

$$a_e = C_2(\alpha/\pi) + C_4(\alpha/\pi)^2 + C_6(\alpha/\pi)^3 + C_8(\alpha/\pi)^4 + C_{10}(\alpha/\pi)^5 + \ldots\ . \tag{2.2}$$

The Schwinger correction (vertex correction), which is a first-order correction ($C_2 = 1/2$), is represented in fig. 2.1(a) as a one-loop Feynman diagram. The coefficients C_4 and C_6 have been also calculated analytically, whereas C_8 (891 Feynman diagrams) and C_{10} (12672 Feynman diagrams) have been numerically evaluated [17]. At the level of $C_{10}(\alpha/\pi)^5 = 6.2\cdot10^{-13}$ also contributions from hadronic vacuum-polarizations, $a_\mathrm{hadronic} = 1.68(2)\cdot10^{-12}$, become relevant. The most recent determination of the free electron g-factor has been performed in 2008 in the group of Gerald Gabrielse by David Hanneke [18]. Measuring directly the magnetic momentum anomaly of a single electron in a Penning trap, they

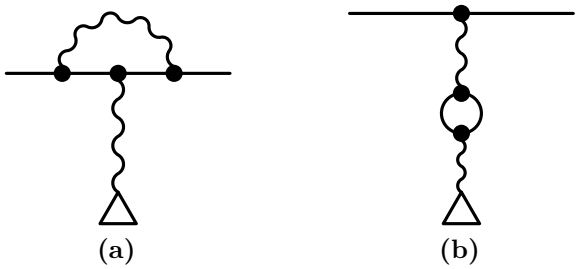

Figure 2.1: Feynman diagrams of the first-order QED corrections (one-loop corrections) of the free electron g-factor. The electron is symbolized as a straight line, the photons as curved lines and the magnetic field as a triangle. Like in all the following Feynman diagrams, the time arrow points to the right. In (a) the Schwinger term (self-energy) is shown. In (b) the vacuum-polarization term is illustrated.

determined the g-factor with a relative precision of $2.8 \cdot 10^{-13}$. In combination with the predicted series expansion in eq. (2.2) the fine structure constant $\alpha^{-1} = 137.035\,999\,173\,(35)$ has been derived with a relative uncertainty of $2.5 \cdot 10^{-10}$.
A competing alternative approach for the determination of the fine structure constant is given by the combination of the Rydberg constant R_∞, the ratio of the Planck constant over the mass of a rubidium atom M_{Rb} and the mass ratio M_{Rb}/m_e:

$$\alpha^2_{\mathrm{recoil}} = \frac{2R_\infty h}{c m_e} = \frac{2R_\infty}{c}\frac{M_{\mathrm{Rb}}}{m_e}\frac{h}{M_{\mathrm{Rb}}}. \tag{2.3}$$

At the moment the dominant uncertainty is caused by the determination of the ratio h/M_{Rb}, which has been quantified in the group of Francois Biraben in 2011 [19]. Here, the recoil velocity of a single rubidium atom $v_{\mathrm{recoil}} = \frac{\hbar k}{M_{\mathrm{Rb}}}$ is measured, when it absorbs a photon of momentum $\hbar k$. This approach determines the fine structure constant $\alpha^{-1}_{\mathrm{recoil}} = 137.035\,999\,037\,(91)$ with a relative uncertainty of $6.6 \cdot 10^{-10}$. The comparison of this value with the one obtained independently from the g-factor of the free electron represents the most stringent test of QED.

2.3 The g-Factor of the Bound Electron

In contrast to the g-factor of the free electron, where the electron is exposed to only small electromagnetic trapping fields, at our experiment we are interested to test QED under extreme conditions, by measuring g-factors in presence of strong electric fields. The strongest electric field which are accessible on the laboratory scale is the binding field of a heavy, highly charged nucleus[1]. In fig. 2.2 the relativistic prediction of the mean electric

1 Even stronger fields can be reached by muonic ions or even more exotic atomic systems. However, the measurement time is strongly limited by their short lifetimes.

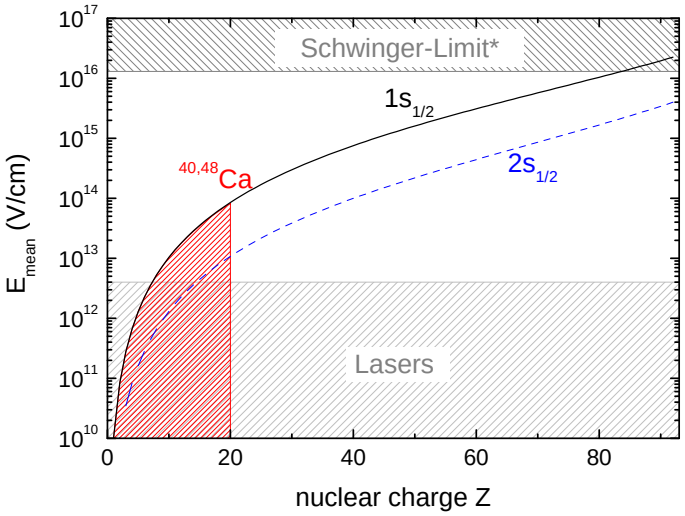

Figure 2.2: Illustration of the mean electric field in highly charged ions as a function of the nuclear charge Z. The red-hatched area marks the field strength we have experimental access to. The lower gray-hatched illustrates the electric field-strength accessible by the brightest laser sources and the upper gray-hatched area designates the Schwinger limit (for a homogeneous electric field), where the vacuum gets unstable. The black (blue) line represents the mean electric field strength, which acts on a single $1s_{1/2}$ ($2s_{1/2}$) - electron.

fields of $1s_{1/2}$ and $2s_{1/2}$ electrons are plotted versus the nuclear charge[1]. Already in the low Z region ($Z \gtrsim 8$) the bound-electron perceives a larger electric field strength than by the brightest laser sources, which reach intensities of about $2 \cdot 10^{22}$ W/cm^2 [30]. The field strengths in heavy hydrogenlike ions approach the Schwinger limit, where the vacuum gets unstable, since the external electric field accelerates apart the virtual electron-positron pairs. In a homogeneous electric field spontaneous electron-positron pair creation has been predicted for: $E_S = \frac{m_e^2 c^3}{e\hbar} = 1.3 \cdot 10^{16}$ V/cm [31, 32, 33]. At the surface ($r_{\mathrm{surf}} = \sqrt{5/3} r_{\mathrm{rms}}$) of a uranium nucleus ($Z = 92$) the electric field is $E(r_{\mathrm{surf}} = 7.6\,\mathrm{fm}) = 2.3 \cdot 10^{19}$ V/cm [34].

1 Here, the relativistic expectation value of $1/r^2$ has been used from [29]. For nuclear charges larger than 30, such a relativistic calculation is essential, e.g. for uranium ($Z = 92$) the mean electric field derived by the non-relativistic Schrödinger equation is a factor of 2.8 smaller than the relativistic calculation. The mean electric field of a $1s_{1/2}$ electron is:

$$E_{\mathrm{mean}}(1s_{1/2}) = \frac{Ze}{4\pi\varepsilon_0} \langle 1/r^2 \rangle = \frac{Ze}{4\pi\varepsilon_0} \frac{2(Z\alpha)^2 (m_e c/\hbar)^2 (2\sqrt{1-(Z\alpha)^2}+1)}{\sqrt{1-(Z\alpha)^2}(3-4(Z\alpha)^2)}. \tag{2.4}$$

Perturbative BS-QED - Series Expansions in (α/π), $(Z\alpha)$ and $(1/Z)$

The fundamental approach of QED calculations in atomic systems, referred to as bound-state quantum electrodynamics (BS-QED), has been developed in the 1950s. Treating e.g. a hydrogenlike ion which contains a nucleus and an electron as a complete two-body problem, at least two QED series-expansions have to be considered:

- Firstly, the radiative corrections, regarding the interaction between the electron and the external magnetic field, require a series-expansion in orders of (α/π), similar to the expansion for the free electron, see eq. (2.2).
- Secondly, radiative corrections also occur in the interaction between the electron and the nucleus, which require an additional expansion in orders of $(Z\alpha)$. Studying heavy highly charged ions, the convergence of this series-expansion deteriorates. For example for hydrogenlike helium $(Z = 2)$ the series-expansion converges quickly in powers of $(2 \cdot \alpha) \approx 0.01$, whereas for hydrogenlike lead $(Z = 82)$ the series-expansion converges much slower in powers of $(82 \cdot \alpha) \approx 0.60$.
- Beyond that, in many-electron systems the interactions between the bound-electrons require a third series-expansion in orders of $(1/Z)$, where the nth order corresponds to Feynman diagrams with n photons, which are exchanged between the bound-electrons[1].

To circumvent a series-expansion in $(Z\alpha)$, which is especially problematic for heavy highly charged nuclei, already in 1951 Wendell H. Furry reduced the two-body problem, where the electron (one body) interacts with the nucleus (other body), to an effective one-body problem of the electron, treating the nucleus classically as an time-independent static external potential $V(\vec{r})$ [35], e.g. as a Coulomb potential: $V_{\mathrm{nucl}}(r) = (Ze)/(4\pi\varepsilon_0 r)$. He added this potential to the Dirac equation of the single electron wave function $\psi(\vec{r},t)$:

$$\left(i\,\hbar\,\partial_t + i\,\hbar\,c\,\vec{\alpha}\cdot\vec{\nabla} - \beta\,m\,c^2 - e\,V_{\mathrm{nucl}}(\vec{r})\right)\psi(\vec{r},t) = 0, \tag{2.5}$$

where $\beta \equiv \begin{pmatrix} I_2 & 0 \\ 0 & -I_2 \end{pmatrix}$, $I_2 \equiv \begin{pmatrix} 1 & 0 \\ 0 & 1 \end{pmatrix}$, $\vec{\alpha} \equiv \begin{pmatrix} 0 & \sigma_{1,2,3} \\ \sigma_{1,2,3} & 0 \end{pmatrix}$ and $\sigma_{1,2,3}$ are the Pauli matrices. As a consequence of this approach, also referred to as the *Furry picture*, the interaction with the nuclear potential is already included in the propagator of the electron. In Feynman diagrams this approach is symbolized by a double line for the electron propagator. Limitations of this picture, which e.g. presumes an infinitely heavy nucleus, will be discussed in section 2.3.3.
In this thesis, we will focus on bound-electron g-factors in two different electron-configurations:

1 The following explanation roughly outlines the $1/Z$ parameter of the perturbative expansion of the interelectronic interaction: In general, the parameter of the perturbative expansion is given by the matrix-element of the perturbation operator over the typical energy difference. The matrix-element of the Coulomb repulsion scales with $\alpha/ < r_{12} >$, where $< r_{12} >$ (distance between two electrons) scales inversely with $(\alpha Z)^{-1}$. The energy difference typically scales with $(\alpha Z)^2$.

(1) in the already mentioned hydrogenlike configuration and (2) in the lithiumlike configuration, which has two core electrons on the 1s-level and one valence electron on the 2s-level. Various physical effects contribute to the g-factors of the respective valence electron:

$$g(\text{H-like}) = g_{\text{Dirac}}^{\text{H-like}} + \Delta g_{\text{QED}}^{\text{H-like}} + \Delta g_{\text{nucl}}^{\text{H-like}}, \tag{2.6}$$

$$g(\text{Li-like}) = g_{\text{Dirac}}^{\text{Li-like}} + \Delta g_{\text{QED}}^{\text{Li-like}} + \Delta g_{\text{nucl}}^{\text{Li-like}} + \Delta g_{\text{int}} + \Delta g_{\text{sQED}}, \tag{2.7}$$

where $g_{\text{Dirac}}^{\text{H-like, Li-like}}$ is the Dirac value for the particular valence electron, $\Delta g_{\text{QED}}^{\text{H-like, Li-like}}$ are the corresponding radiative corrections of the valence electron and $\Delta g_{\text{nucl}}^{\text{H-like, Li-like}}$ contain nuclear corrections. In lithiumlike systems the interactions between the three electrons are included in the interelectronic interaction corrections Δg_{int} and the corresponding radiative corrections, the so-called screened QED corrections, Δg_{sQED}. In fig. 2.3 the relative g-factor contributions for (a) hydrogenlike ions and (b) lithiumlike ions are listed in dependence on low and medium atomic numbers Z, which are accessible at our experimental apparatus. In the following these corrections are briefly introduced and the present status of the BS-QED calculations is summarized.

2.3.1 g_{Dirac} - Dirac Values of the Bound-Electron g-Factor

As seen in fig. 2.3(a), for atomic numbers larger than eight the dominant contribution of the bound-electron g-factor in a hydrogenlike ion is a relativistic correction. This contribution has been calculated already in 1928 by Gregory Breit [38]. Focusing on the zeroth-order approximation of BS-QED for a hydrogenlike ion, by solving its Dirac equation (eq. (2.5)) in the presence of a magnetic field, he derived the following analytical expression:

$$g_{\text{Dirac}}^{\text{H-like}} = 2 + \Delta_{\text{Breit}}^{\text{H-like}} = \frac{2}{3}\left[1 + 2\sqrt{1-(Z\alpha)^2}\right] = 2 - \frac{2}{3}(Z\alpha)^2 - \frac{1}{6}(Z\alpha)^4 + \dots . \tag{2.8}$$

A detailed derivation of this expression from the Dirac equation by means of the minimal coupling is given for example in chapter four of the textbook "Fundamental Physics in Particle Traps" [39]. Due to the leading-order scaling of $(Z\alpha)^2$ the Breit correction reduces the g-factor of hydrogenlike helium ($Z = 2$) by only 71 ppm (parts per million) and by 13% for hydrogenlike lead ($Z = 82$).
In lithiumlike systems this effect amounts to:

$$g_{\text{Dirac}}^{\text{Li-like}} = 2 + \Delta_{\text{Breit}}^{\text{Li-like}} = \frac{2}{3}\left[1 + \sqrt{2 + 2\sqrt{1-(Z\alpha)^2}}\right] = 2 - \frac{1}{6}(Z\alpha)^2 - \frac{5}{96}(Z\alpha)^4 + \dots , \tag{2.9}$$

see also fig. 2.3(b).

2.3.2 Δg_{QED} - Radiative Corrections

The recapitulation of the radiative corrections in hydrogenlike systems, which occur in the dynamics between the bound electron and the external magnetic field, is structured in terms of their (α/π) series-expansion. In lithiumlike systems very similar contributions occur in the zeroth order in $(1/Z)$, where photon exchange between the electrons does not occur.

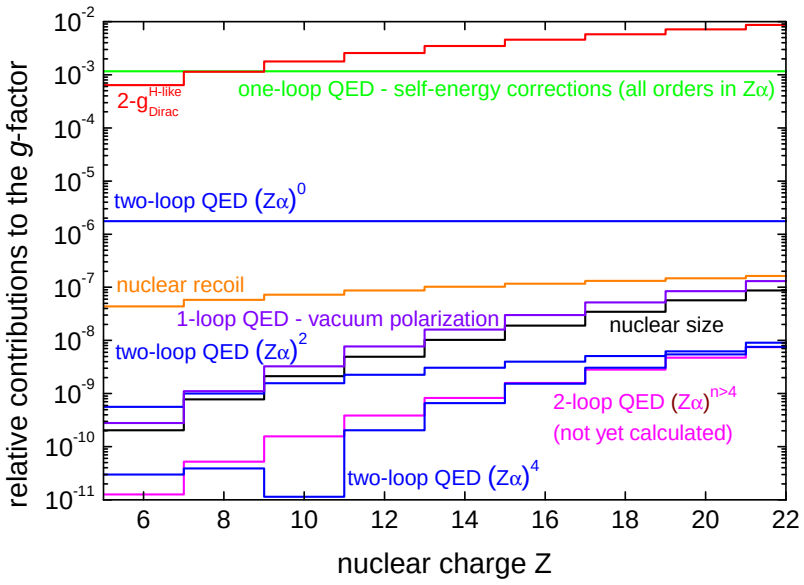

(a)

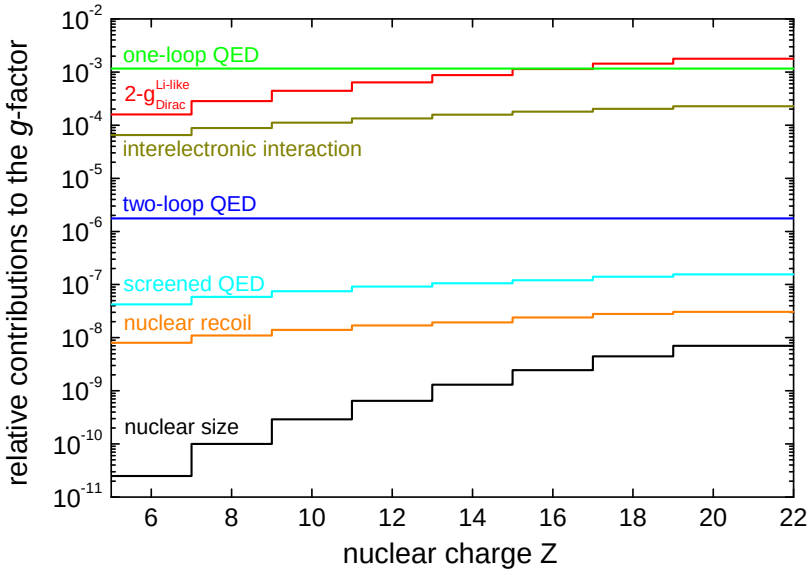

(b)

Figure 2.3: Relative contributions to the bound-electron g-factor (a) for hydrogenlike ions [36] and (b) for lithiumlike ions [37]: Relativistic Breit correction (red), 1-loop QED without vacuum-polarization (bright green), 1-loop QED only vacuum-polarization (violet), 2-loop QED up to the fourth order in $(Z\alpha)$ (blue), 2-loop QED not yet calculated (magenta), nuclear recoil (orange), nuclear size (black), interelectronic interaction (green) and screened QED (turquoises). Only ions with an even atomic number are plotted, since we focus on spinless nuclei.

One-loop BS-QED Corrections of the Order $(\alpha/\pi)^1$

In fig. 2.4 all six Feynman diagrams of the first-order in (α/π) are presented for hydrogenlike systems. In 1997 the three self-energy diagrams (a-c) have been solved for the first time within the Furry picture in all orders in $(Z\alpha)$ [40]. In 2004 these calculations have been improved and extended also to lithiumlike systems in all orders of $(Z\alpha)$ [41]. Besides self-energy corrections, also the vacuum-polarization corrections have been evaluated [42], which are at least four orders of magnitudes smaller in the nowadays accessible low and medium Z region.

Two-loop BS-QED Corrections of the Order $(\alpha/\pi)^2$

Already the two-loop BS-QED corrections contain 50 Feynman diagrams, see fig. 2.5. At present solutions for these second and higher-order corrections in (α/π) are not available in all orders in $(Z\alpha)$. Expanding the two-loop corrections in orders of $(Z\alpha)$, contributions of the order $(\alpha/\pi)^2(Z\alpha)^4$ have been derived in 2005 for all ns states (hydrogenlike, lithiumlike, sodiumlike ...) [43]. Nowadays uncalculated terms of $(Z\alpha)^5$ or higher-order in the two-loop QED expansion dominate the theoretical uncertainty of bound-electron g-factors in hydrogenlike systems.

2.3.3 Δg_{nucl} - Nuclear Corrections

Until now, the nucleus has been treated as a point charge, fixed in space, which is added as an external Coulomb potential to the Dirac equation, see eq. (2.5). The following nuclear properties require corrections of the bound-electron g-factor .

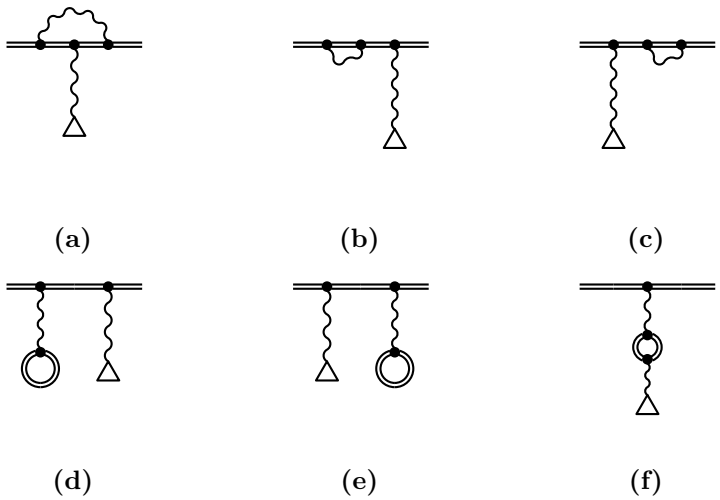

Figure 2.4: One-loop BS-QED radiative corrections for hydrogenlike ions. (a-c) represent the self-energy diagrams; (d-f) the vacuum-polarization diagrams, which contain the electric-loops in (d) and (e) and the magnetic-loop in (f). The double line symbolizes the electron propagator, calculated in the Furry picture.

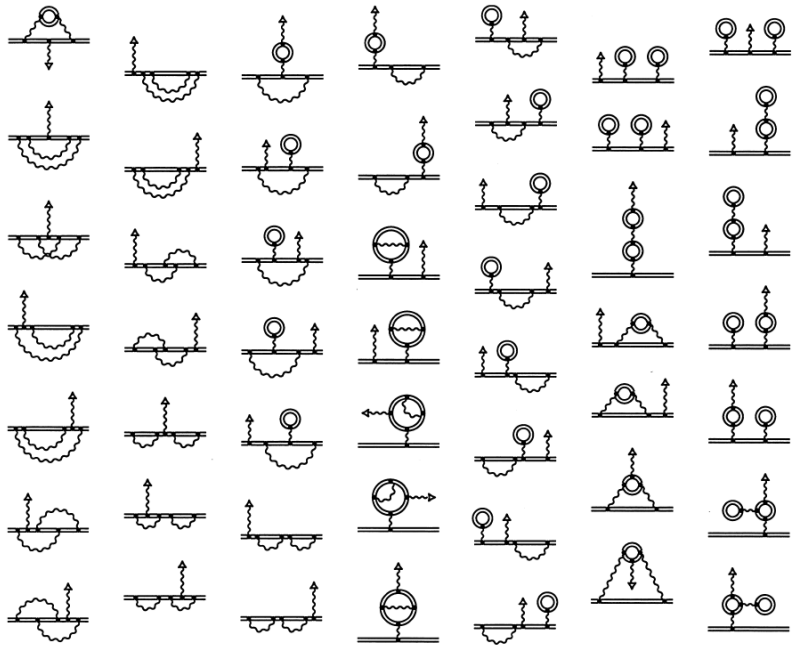

Figure 2.5: Two-loop BS-QED corrections for hydrogenlike ions. [T. Beier, [34]]

Nuclear Magnetic Moment

A nuclear magnetic moment leads to an additional splitting of the bound-electron energy levels. This so-called hyperfine structure also modifies the bound-electron g-factor [34]. Since the nuclear magnetic moment is caused by the spins of the constituents of the nucleons, i.e. the spins of the quarks and gluons, which combine to complicated structures via complex interactions, it cannot be rigorously calculated, but has to be measured. Furthermore it is not sufficient to describe the nuclear magnetic moment by a point-like dipole, but by a smeared-out nuclear magnetization, referred to as the *Bohr-Weisskopf* effect [44]. Avoiding these contributions, in this thesis we focus solely on spinless nuclei with even number of protons and neutrons.

Δg_{ns} - Nuclear Size and Δg_{nd} - Nuclear Deformation

The size of the nucleus is considered by modifications of the nuclear potential in the Dirac equation, see eq. (2.5). The modeled nuclear potential in principal relies on the root-mean-square charge radius, $r_{\mathrm{nucl}}^{\mathrm{rms}} = \sqrt{< r^2 >}$, which has to be measured in experiments. In 2002 the corresponding relativistic g-factor correction has been derived analytically for ns and $np_{1/2}$ electron states, which reside in our experimentally accessible nuclear charge range ($Z = 1 - 20$), [45]. In the non-relativistic limit this g-factor contribution scales with $\Delta g_{\mathrm{ns}} = \frac{8}{3n^3}(Z\alpha)^4 m_e^2 < r^2 >$. Due to the Z^4-scaling the knowledge of the nuclear charge distribution sets the limit of g-factor calculations for heavy highly charged ions. The determination of $r_{\mathrm{nucl}}^{\mathrm{rms}}$ via the measurement of a bound-electron g-factor has been

demonstrated by the measurement of the g-factor of hydrogenlike silicon [46].
In a recent study [47] the leading relativistic nuclear quadrupole and hexadecapole deformation corrections have been derived analytically. For heavy highly charged ions, e.g hydrogenlike uranium, the relative nuclear deformation contribution to the g-factor is about 10^{-6}. In the low and medium Z systems, studied in this thesis, the nuclear shape correction is not relevant at the current level of precision ($\Delta g_{\mathrm{nd}}(^{12}\mathrm{C}) = -7.9(5.3) \cdot 10^{-16}$ and $\Delta g_{\mathrm{nd}}(^{28}\mathrm{Si}) = -2.85(52) \cdot 10^{-13}$).

Δg_{rec} - Nuclear Mass / Recoil

So far the nucleus has been treated as a static point-charge (or charge distribution), fixed in space. This time-independent approximation, which would be exact for infinitely heavy ions, enabled the tremendous simplification of BS-QED, by reducing the two-body problem to an effective one-body problem for the bound electron. The motion of the nucleus itself (recoil motion) due to the finite nuclear mass requires BS-QED calculations beyond the Furry picture. In 2001 this effect has been calculated as a correction of the bound-electron g-factor to first-order in m_e/M and to all orders in $Z\alpha$ [48]. To zeroth order in $(1/Z)$, this formula describes also the recoil correction for electrons in ns states. In the lowest relativistic order the nuclear recoil correction scales as follows: $\Delta g_{\mathrm{rec}} = -\frac{m_e}{m_{ion}} \frac{(\alpha Z)^2}{n^2}$. This thesis includes a dedicated measurement of the recoil contribution by measuring the g-factor difference of $^{40}\mathrm{Ca}^{17+}$ and $^{48}\mathrm{Ca}^{17+}$, see section 2.7 and chapter 6 for more details.

Δg_{np} - Nuclear Polarization

Intrinsic nuclear dynamics enable virtual electromagnetic excitations, by the exchange of two photons between the nucleus and the bound electron. This so-called nuclear polarization correction is evaluated in a $(1/Z)$ series expansion. The lowest-order Feynman diagram is shown in fig. 2.6(a). Similar to the nuclear size corrections, the nuclear polarization correction is limited to the phenomenological description of the nucleon-nucleon interaction and in that way can set an ultimate accuracy limit of QED tests in heavy highly charged ions. The effect has been calculated for the bound-electron g-factor in 2002 [49] and has been improved in a recent paper [50], evaluating the zeroth and first-orders in $(1/Z)$ in heavy highly charged ions, e.g. $\Delta g_{\mathrm{np}}(^{208}\mathrm{Pb}^{81+}) = -1.977 \cdot 10^{-7}$. As the nuclear shape corrections, for the ions, studied in this thesis, the nuclear polarization correction is not relevant at the current level of precision.

2.3.4 Many-Electron Corrections

Focusing on the g-factor of a 2s electron in a lithiumlike electron configuration, which has got two core electrons (1s) and one valence electron (2s), one has to consider the interactions between these electrons. We distinguish between two different g-factor contributions.

Δg_{int} - Interelectronic Interaction Corrections for Lithiumlike Ions

The interelectronic interaction contribution contains all Feynman diagrams with photon exchanges between the electrons, like for example diagrams (b-d) in fig. 2.6, excluding diagrams with additional self-energy or vacuum-polarization loops. In an unusual way this correction requires also the analysis of the negative-energy Dirac states, which contribute to the interelectronic interaction correction of the g-factor with the same order of magnitude

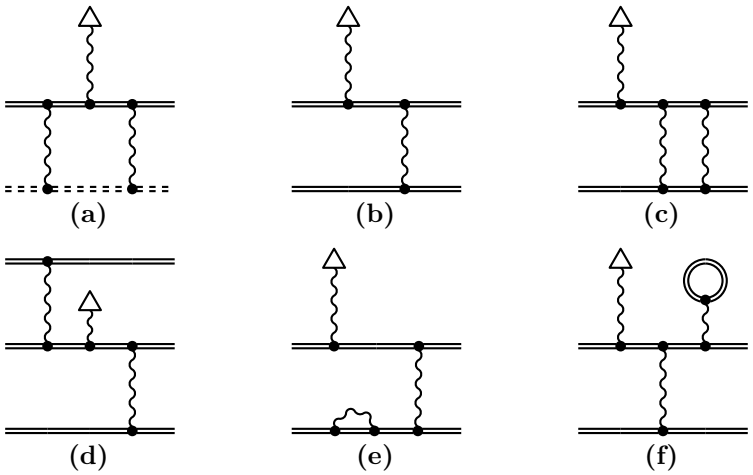

Figure 2.6: BS-QED diagrams of some particular physical effects: (a) Nuclear polarization (The nucleus is presented as a double dashed line.), (b) Interelectronic interaction (one photon exchange with one core electron), (c) Interelectronic interaction (two photon exchange with one core electron), (d) Interelectronic interaction (one photon exchanges with two core-electrons), (e) Screened QED (self-energy), (f) Screened QED (vacuum-polarization). These diagrams just highlight one diagram of the particular physical effect and not the complete set of diagrams of the corresponding order.

as the positive-energy states. In 2002 the one-photon exchange diagrams (first-order in $1/Z$) have been evaluated to all orders in $(Z\alpha)$ within a rigorous QED approach [51]. A recent paper from 2014 presents an extension of these rigorous QED calculations to the two-photon exchange diagrams (second order in $1/Z$) [52]. At present the interelectronic interaction contribution to the bound-electron g-factor dominates the theoretical uncertainty of lithiumlike g-factors in the low- and medium-Z region ($Z < 30$).

Δg_{sQED} - Screened QED Corrections for Lithiumlike Ions

The screened QED corrections include all Feynman diagrams with photon exchanges between the electrons, which contain additionally self-energy or vacuum-polarization loops. As an illustration, diagrams (e) and (f) in fig. 2.6 show some leading-order screened QED corrections. Since the convergence of the screened QED contributions differs for various atomic numbers, at present three different approaches are used: (1) For lower Z the convergence in a rigorous QED approach becomes worse, so that perturbation theory only in leading-order in $(Z\alpha)$ is applied. (2) In the medium-Z region an effective screening potential is introduced in the QED calculations to all orders in $(Z\alpha)$. (3) For heavy highly charged ions a rigorous QED approach is used [52].

2.4 Measurement Principle of the Bound-Electron g-Factor

In a homogeneous magnetic field $\vec{B} = B\vec{e_z}$ the Zeeman effect describes the shift of the bound-electron energy levels in dependence on the specific total angular momentum J and

the corresponding projection m_J parallel to the magnetic field:

$$\Delta E_{\mathrm{Z}}(J,m_J,B) = g_J\, m_J\, \mu_B\, B. \tag{2.10}$$

In this context the ns states energetically split into two states, the spin-up $|\uparrow>$ and spin-down $|\downarrow>$ states. The corresponding energy difference, the so-called Zeeman (level) splitting, amounts to:

$$\Delta E_{\mathrm{Z.\text{-}Splitting}} = \Delta E_{\mathrm{Z}}(|\uparrow>) - \Delta E_{\mathrm{Z}}(|\downarrow>) = h\frac{g}{4\pi}\frac{e}{m_e}B = h\cdot\nu_L, \tag{2.11}$$

where ν_L is the Larmor frequency, also called the spin precession frequency. For the determination of the magnetic field, the cyclotron frequency ν_c of the ion is measured:

$$v_c = \frac{1}{2\pi}\frac{q_{ion}}{m_{ion}}B. \tag{2.12}$$

The combination of eq. (2.11) and eq. (2.12) provides an experimental access to the bound-electron g-factor :

$$g = 2\frac{m_e}{m_{ion}}\frac{q_{ion}}{e}\frac{v_L}{v_c} = 2\frac{m_e}{m_{ion}}\frac{q_{ion}}{e}\Gamma, \tag{2.13}$$

which depends on the electron / ion mass-ratio, electron mass over ion mass, the charge ratio, which is a simple ratio of integers, and the Larmor- to cyclotron frequency ratio $\Gamma \equiv \frac{\nu_L}{\nu_c}$.

Higher-Order Zeeman Shifts

Multiple interactions between the bound electron and the external magnetic field, as for example illustrated in fig. 2.7, lead to higher-order Zeeman shifts, which are non-linear in the

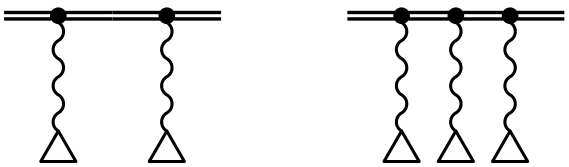

Figure 2.7: Leading-order diagrams of the 2nd and 3rd order Zeeman shifts.

magnetic field. Studying this effect, the Zeeman shift can be evaluated in a series-expansion:

$$\Delta E(J,m_J,B) = \Delta E^{(1)}(J,m_J,B) + \Delta E^{(2)}(J,m_J,B) + \Delta E^{(3)}(J,m_J,B) + ... \tag{2.14}$$

where: $\Delta E^{(i)}(J,m_J,B) = g_J^{(i)}\cdot m_J\cdot(\mu_B B)^i/(m_e c^2)^{i-1}$ and $i \in \mathbb{N}$, see also fig. 2.8. In the case of $J = 1/2$, the first-order coefficient $g_J^{(1)}$ is related to the theoretically predicted bound-electron g-factor described above: $g = g_{1/2}^{(1)}$. The higher-order shifts can be calculated, see [53]. Considering the symmetry relation: $g_J^{(2)}\cdot(m_J) = g_J^{(2)}\cdot(-m_J)$, the quadratic

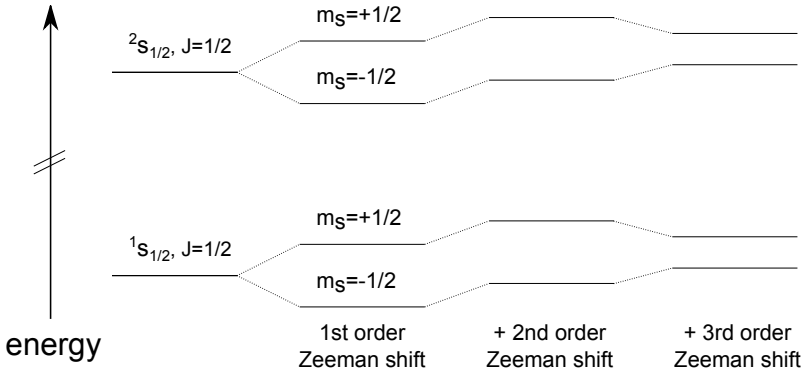

Figure 2.8: Level scheme of the higher-order Zeeman shifts for the $1s_{1/2}$ and $2s_{1/2}$ states. In the case of $^{12}C^{5+}$ and $^{40}Ca^{17+}$ the 2^{nd} order Zeeman effect shifts all the Zeeman sublevels in equal measure up, so that the Zeeman splitting is not influenced and the 3rd order Zeeman effect slightly diminishes the Zeeman splitting. The way of representing the shifts is exaggerated.

correction does not alternate the Zeeman splitting for $J = 1/2$ levels, so that for example hydrogenlike and lithiumlike ions are not effected. Nevertheless the third order Zeeman shift, where $g_J^{(3)} \cdot (m_J) = -g_J^{(3)} \cdot (-m_J)$, is the leading-order correction of the Zeeman splitting in hydrogenlike and lithiumlike ions. For $^{40}Ca^{17+}$ and $^{12}C^{5+}$ these higher-order Zeeman splittings are much smaller than the relative experimental uncertainty of a few $1 \cdot 10^{-11}$, see table 2.1.

Table 2.1: 2^{nd} and 3^{rd} Zeeman shifts for hydrogenlike carbon $^{12}C^{5+}$ and lithiumlike calcium $^{40}Ca^{17+}$ in a magnetic field of 3.76 T [54].

ion	$\lvert\Delta E^{(2)}/\Delta E^{(1)}\rvert$	$\lvert\Delta E^{(3)}/\Delta E^{(1)}\rvert$
$^{12}C^{5+}$	$2.2 \cdot 10^{-7}$	$2.6 \cdot 10^{-16}$
$^{40}Ca^{17+}$	$3.2 \cdot 10^{-7}$	$3.8 \cdot 10^{-16}$

2.5 Status of the Bound-Electron g-Factor Measurements

In parallel to the great improvements of the theoretical predictions of the bound-electron g-factor in the last 15 years, a tremendous progress has been made on the experimental determination of the bound-electron g-factor. One major breakthrough has been achieved in 2000, when, in the group of Günter Werth, Nikolaus Hermanspahn, Harmut Häffner and colleagues managed to trap a single hydrogenlike carbon ion in a Penning trap setup and measured the g-factor with the newly developed double-trap technique $(\delta g/g)_{\mathrm{exp}} = 2.5 \cdot 10^{-9}$ [55]. The theoretical uncertainty of that time was of the same order of magnitude $(\delta g/g)_{\mathrm{theo}} = 3.5 \cdot 10^{-9}$ [1]. In 2003 José Verdú and colleagues, also from the group of Günter Werth, published the g-factor of hydrogenlike oxygen $(\delta g/g)_{\mathrm{exp}} = 2.3 \cdot 10^{-9}$ [56]. The corresponding theoretical prediction at that time had a relative uncertainty of $(\delta g/g)_{\mathrm{theo}} = 3.0 \cdot 10^{-10}$. Seven years later Sven Sturm and colleagues had developed a

1 In this paragraph I quote the theoretical g-factors, which have been published together with the measurements at that time. Most calculations improved in the last years.

number of experimental improvements, e.g. an improved trap design, a significantly enlarged spatial separation of the two Penning traps, to improve the magnetic homogeneity [57], completely newly developed cryogenic detection systems to reduce the ion's temperatures, feedback techniques, pressure and room temperature stabilizations and beside that a new phase-sensitive detection technique, PnA [58], which will be also explained in this thesis in section 3.4.2. In 2011 Sven Sturm and colleagues published the g-factor of hydrogenlike silicon,$^{28}Si^{13+}((\delta g/g)_{\mathrm{exp}} = 5.0 \cdot 10^{-10}$ and $(\delta g/g)_{\mathrm{theo}} = 8.5 \cdot 10^{-10})$, which at present represents the most stringent test of BS-QED [46]. All QED contributions have been tested with a relative uncertainty of $8 \cdot 10^{-7}$; without the $(Z\alpha)^0$ contributions, the relative uncertainty is still $3 \cdot 10^{-4}$. Two years later Anke Kracke and colleagues measured the g-factor of lithiumlike silicon, $^{28}Si^{11+}((\delta g/g)_{\mathrm{exp}} = 1.1 \cdot 10^{-9}$ and $(\delta g/g)_{\mathrm{theo}} = 2.5 \cdot 10^{-8})$, which represents the most stringent test of many-electron BS-QED calculations [59]. To date, all the calculated bound-electron g-factors have been in good agreement with the correponding measurements.

Next Steps - Bound-Electron g-Factor Measurements Presented in this Thesis

In this thesis I will present an improved g-factor value of hydrogenlike carbon. From the result a new value for the electron's atomic mass has been derived, which reduces the uncertainty of the current literature value of the atomic mass of the electron m_e by a factor of 13. Furthermore, I will present high-precision g-factor measurements of the lithiumlike calcium isotopes $^{40}Ca^{17+}$ and $^{48}Ca^{17+}$. Their g-factor difference represents a unique test of BS-QED beyond the Furry picture.
In the last two sections of this chapter I will highlight firstly the status of electron mass measurements (section 2.6) and secondly the status of isotope shift measurements (section 2.7).

2.6 The Electron and its Atomic Mass

In 1897 Joseph J. Thomson and colleagues discovered the electron as a unique particle in cathode ray experiments [60]. In his Nobel lecture in 1906 he denominated the electron mass with a relative precision of the order of 6% ("... the mass of the corpuscle is only about 1/1700 of that of the hydrogen atom.") [61]. Nowadays, the electron is regarded as a massive, electrically charged, point-like, elementary spin-1/2 particle. A possible substructure would be smaller than $2 \cdot 10^{-20}$ m [62]. The Kobayashi–Maskawa phase in the quark sector of the SM can induce an electric dipole moment (EDM) of $d_e < 1 \cdot 10^{-38}\ e \cdot \mathrm{cm}$ via higher-order quark loops [63]. Larger electron EDMs are predicted in several SM extensions. At the moment, the upper limitations of the sought-after electron EDM amounts to $8.7 \cdot 10^{-29}\ e \cdot \mathrm{cm}$ at a 90% confidence level [64]. As the lightest electrically charged lepton of the SM, the electron is a stable particle. This outstanding property assigns the electron a prominent role in nature. Its intrinsic characteristics, especially its mass, which is one of the 19 fundamental input parameters of the SM, profoundly determines the atomic structure of our universe.

2.6.1 Benefits of an Improved Electron Mass

Theses days at least two fields of high-precision physics benefit from an improved electron mass:

- **The determination of the fine structure constant:**
  Introduced already in section 2.2, the most stringent test of QED, which is based on the theoretical prediction and the measurement of the anomalous magnetic moment of the free electron, requires an experimentally determined value for the fine structure constant α. At present, the most precise value relies on four fundamental constants, see eq. (2.3): (1) the Rydberg constant ($\delta R_\infty/R_\infty = 5.0 \cdot 10^{-12}$) [65], (2) the rubidium mass ($\delta M_{\mathrm{Rb}}/M_{\mathrm{Rb}} = 1.2 \cdot 10^{-10}$) [66], (3) the ratio Planck constant over rubidium mass ($\delta(h/M_{\mathrm{Rb}})/(h/M_{\mathrm{Rb}}) = 1.2 \cdot 10^{-9}$) [19] and (4) last but not least the mass of the electron.
  Further progress on this impressive QED test is motivated in particular by the $2.5-3.6\sigma$ discrepancy between the theoretically predicted and the measured anomalous magnetic moment of the muon $\delta a_\mu/a_\mu(\mathrm{exp}) = 5.4 \cdot 10^{-7}$ [67, 68]. Since the radiative loop contributions from hypothetical heavier new particles with masses $m_{\text{new phys}}$ scale with $m^2_{(\mu,e)}/m^2_{\text{new phys}}$, the muon has a 40000 times enhanced sensitivity to "new physics" compared to the about 200 times lighter electron. A confirmation of such a discrepancy also in the anomalous magnetic moment of the free electron requires amongst others a value of the fine structure constant with a relative uncertainty of about $4 \cdot 10^{-11}$. With the new value of the electron mass, reported in this thesis, we approach such requests.
- **Tests of QED in strong electric fields:**
  Mentioned in section 2.5, nowadays the most stringent tests of BS-QED are based on high-precision measurements of the bound-electron g-factor of hydrogenlike ions. Here, the measurement principle strongly depends on the electron mass, see eq. (2.13). Already the uncertainty of the g-factor of hydrogenlike silicon in 2011 has been dominated by the uncertainty of the electron mass [46]. For further planned bound-electron g-factor measurements an improved electron mass is of great importance.

2.6.2 Electron Mass Measurements in History

Some remarkable achievements in trapping physics of charged particles have been associated with measurements of the electron mass. In this section I will summarize the tremendous experimental progress, which improved the relative uncertainty of the electron mass by more than three orders of magnitudes in the last 40 years, see also fig. 2.9. I will start with the first direct determination of the electron mass in a Penning trap 37 years ago. In such a direct approach, which is the most common measurement principle in high-precision mass spectrometry of charged particles (elementary particles, ions, molecules), the cyclotron frequency ratio of the particle of interest, in this case of the electron $\nu_c^{\mathrm{e}} = \frac{1}{2\pi}\frac{e}{m_e}B$, and a reference particle $\nu_c^{\mathrm{ref}} = \frac{1}{2\pi}\frac{q_{\mathrm{ref}}}{m_{\mathrm{ref}}}B$ is measured in a homogeneous magnetic field:

$$m_e = \frac{e}{q_{\mathrm{ref}}}\frac{\nu_c^{\mathrm{ref}}}{\nu_c^{\mathrm{e}}} m_{\mathrm{ref}}, \tag{2.15}$$

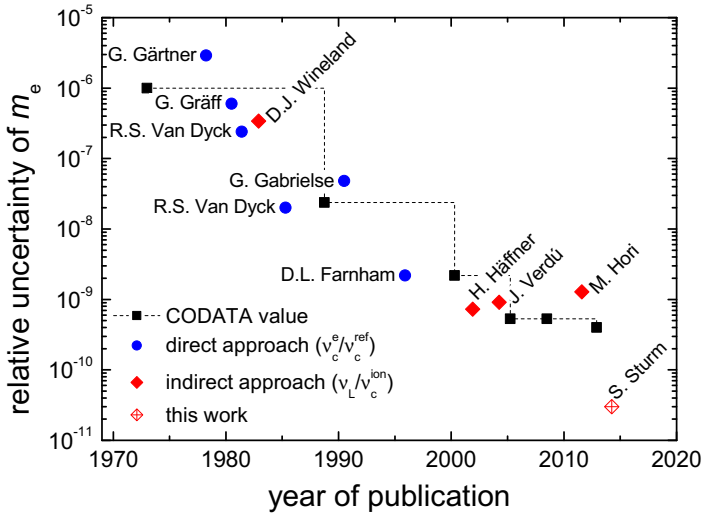

Figure 2.9: A historical overview of the relative uncertainties of the electron mass measurements in the last four decades. Blue markers: Direct measurements of the cyclotron frequency ratio $\nu_c^{\mathrm{ref}}/\nu_c^{\mathrm{e}}$ [69, 70, 71, 72, 73]. Red markers: Indirect measurements of the Larmor-to-cyclotron frequency ratio $\nu_L/\nu_c^{\mathrm{ion}}$ [55, 56, 74, 75, 76, 77]. Black markers: Literature values by the CODATA [65, 78, 79, 80, 81, 82].

where e and q_{ref} are the charge states of the electron and of the reference particle, respectively, and m_{ref} is the mass of the reference particle, which must have a smaller relative uncertainty than the electron mass. For the electron mass this direct approach has been applied for the first time by G. Gärtner and E. Klempt in 1978 [69]. They loaded alternately clouds of a few thousand protons and a few thousand electrons into a Penning trap and measured in a destructive manner the particle loss by resonant cyclotron excitations. In the following 17 years this direct measurement principle has been improved, reducing the size of the particle clouds and optimizing the frequency detection techniques. In this context four papers have to be mentioned: (1) In 1980 G. Gräff, H. Kalinowsky and J. Traut [70] introduced a time-of-flight (ToF) technique to measure the electron-proton mass ratio. (2) In 1981 R. S. Van Dyck Jr. and P.B. Schwinberg used for the first time non-destructive radio frequency (rf) resonance techniques, [71]. They alternately confined clouds of about 10 electrons and 40 ions in the same magnetic field of a Penning trap and detected the induced image charges of the excited clouds. (3) In the following years R. S. Van Dyck Jr. and colleagues improved their experimental setup [72]. (4) In 1995 D.L. Farnham, R.S. Van Dyck Jr. and P.B. Schwinberg published their last direct measurement of the electron mass, by measuring the cyclotron frequencies of a single carbon nucleus ($^{12}C^{6+}$) and a small electron cloud (5-13 electrons) via non-destructive rf-resonance detection techniques [73]. Their measurement principle has been limited by the large relativistic shift of the electron and the corresponding large uncertainty of the electron cyclotron frequency due

to the smallness of the electron mass.
In parallel to this direct approach, D.J. Wineland, J.J. Bollinger and W.M. Itano developed an alternative approach for precision mass spectrometry in Penning traps already in 1982 [74]. They measured on the one hand the cyclotron frequency of a small cloud of lithium-like $^9Be^+$ ions, using a laser-beam fluorescence technique, and on the other hand a hyperfine transition of these ions via an rf-optical double-resonance technique. For the determination of the electron mass they had to rely on theoretical predictions for the bound-electron g-factor.
Before I will come to the state-of-the-art measurement principle for the electron mass, which has been developed within the group of Günter Werth, I want to mention two further, more exotic measurements of the electron mass: (1) In the context of a CPT test, the masses of protons and antiprotons have been measured by Gerald Gabrielse and colleagues in 1990 [75]. They alternatively trapped small clouds of protons and antiprotons in a cylindrical Penning trap. Here, they measured also the mass ratios antiproton-to-electron and proton-to-electron, determining in that way also a value of the electron mass. (2) In 2011 Masaki Hori and colleagues performed two-photon laser spectroscopy of antiprotonic helium, a bound-state including a helium nucleus, an antiproton and an electron. Relying on matter-antimatter symmetry, $m_{\bar{p}} = m_{\mathrm{p}}$, they derived a value for the electron mass [76].

2.6.3 State-of-the-art Measurement Principle of the Electron Mass

In the beginning of this millennium, Günter Werth, Heinz-Jürgen Kluge and Wolfgang Quint presented an improved and advanced variant of the indirect approach to circumvent the determination of the cyclotron frequency of the free electron and the corresponding large relativistic shifts. Instead of measuring the cyclotron frequency of the free electron ν_c^e, the electron was bound to a light nucleus and the ratio between the Larmor frequency of the bound electron and the cyclotron frequency of the hydrogenlike ion has been measured, exactly like for the determination of the bound-electron g-factor, see section 2.4. Relying on calculations for the bound-electron g-factor, eq. (2.13) can be resolved to the electron mass:

$$m_e = \frac{g_{theo}}{2}\frac{e}{q_{ion}}\frac{v_c}{v_L}m_{ion} = \frac{g_{theo}}{2}\frac{e}{q_{ion}}\frac{m_{ion}}{\Gamma}. \tag{2.16}$$

Due to the $(Z\alpha)^5$ scaling of the higher-order two-loop QED corrections, which dominate the uncertainty of bound-electron g-factor calculations for hydrogenlike ions, see fig. 2.3, it is favorable to use light nuclei. For the first time this measurement principle has been used by Hartmut Häffner and colleagues in 2001, in the group of Günter Werth. Here, they determined the Larmor-to-cyclotron frequency ratio of hydrogenlike carbon [83]. Two years later José Verdú and colleagues measured also the Larmor-to-cyclotron frequency ratio of hydrogenlike oxygen [56]. Both measurements have already been mentioned in the context of historical bound-electron g-factor measurements in section 2.5.
In this thesis the measurement on hydrogenlike carbon is repeated with a significantly improved experimental setup, which enables a 25-fold improvement in comparison to the former measurement on hydrogenlike carbon.
We have also chosen hydrogenlike carbon, since the atomic mass of carbon ^{12}C defines

the atomic mass unit and thus has no uncertainty. In table 2.2 the binding energies of carbon ^{12}C are listed. Since for the first ionization energy no uncertainty is listed in [84]

Table 2.2: Binding energies of atomic carbon, ^{12}C from the *NIST Atomic Spectra Database*[89]

ionization state	binding energy (eV)
I [84]	11.260 30
II [85]	24.384 5 (9)
III [86]	47.887 78 (12)
IV [87]	64.493 58 (19)
V [88]	392.090 49 (3)

and a further calculated value in [90] deviates by 0.7 meV, we assume a conservatively estimated error of 1 meV for the first ionization state. With a total binding energy of $E_{\text{bind}} = 540.116\,6\,(14)\,\text{eV}$ and the conversion factor of $1\,\text{u} = 931.494061(21) \cdot 10^6\,\text{eV}/c^2$ [65] the mass of $^{12}\text{C}^{5+}$ is calculated:

$$\begin{aligned} m(^{12}\text{C}^{5+}) &= 12\,\text{u} - 5 \cdot m_e + E_{\text{bind}} \\ &= 11.997\,257\,680\,291\,7\,(18)\,\text{u} \qquad (0.15\ \text{ppt}). \end{aligned} \tag{2.17}$$

2.6.4 State-of-the-art Calculations of the Bound-Electron g-Factor of Hydrogenlike Carbon

In the framework of bound-state QED the g-factor of $^{12}\text{C}^{5+}$ has been calculated with a relative uncertainty of $1.2 \cdot 10^{-11}$: $g = 2.001\ 041\ 590\ 176\ (24)$ [77]. Beyond that, the theoretical uncertainty has been even further reduced by a factor of 5 by estimating the dominant unknown term - the leading higher-order contribution in two-loop QED calculations: $g_{2L}^{\text{ho}}(Z) \approx (\alpha/\pi)^2 (Z\alpha)^5\ b_{50}$ - from the discrepancy between the experimentally and determined g-factor of hydrogenlike silicon, $^{28}\text{Si}^{13+}$, see table 2.3 and supplement of [77]. The final state-of-the-art value for the theoretically predicted bound-electron g-factor value is [77]:

$$g_{\text{theo}}(^{12}\text{C}^{5+}) = 2.001\,041\,590\,179\,8\,(47) \qquad (2.4\ \text{ppt}). \tag{2.18}$$

Table 2.3: Theoretical contributions to the bound-electron g-factor of hydrogenlike carbon $^{12}C^{5+}$. Abbreviations: "h.o.:" higher-order, "SE:" self-energy contribution, "SE-FS:" mixed self-energy and nuclear finite size contribution, "VP-EL:" electric-loop vacuum-polarization contribution, "VP-ML: " magnetic-loop vacuum-polarization contribution, "rad-rec:" leading term of the mixed radiative-recoil contribution [77]

theoretical contributions		$^{12}C^{5+}$
Dirac		1.998 721 345 391 (1)
finite nuclear size		0.000 000 000 407
one-loop QED	$(Z\alpha)^0$	0.002 322 819 466 (1)
	$(Z\alpha)^2$	0.000 000 742 160
	$(Z\alpha)^4$	0.000 000 093 422
	h.o. SE	0.000 000 008 283 (4)
	h.o. SE-FS	-0.000 000 000 002 (2)
	h.o. VP-EL	0.000 000 000 556
	h.o. VP-ML	0.000 000 000 038
$\leq$ two-loop QED	$(Z/\alpha)^0$	-0.000 003 515 108
	$(Z/\alpha)^2$	-0.000 000 001 123
	$(Z/\alpha)^4$	0.000 000 000 060
	h.o.	-0.000 000 000 003 (3)
nuclear recoil	m_e/M	0.000 000 087 725
	rad-rec	-0.000 000 000 068
	h.o.	-0.000 000 000 028
nuclear polarization		0.000 000 000 000
nuclear deformation		0.000 000 000 000
total theory		2.001 041 590 176 (6)

2.7 Testing BS-QED Beyond the Furry Picture

As already specified in the context with bound-electron g-factors, see section 2.3.3, high-precision measurements within the atomic level scheme are sensitive to various nuclear properties, such as the nuclear mass, the nuclear charge distribution, the nuclear spin, the nuclear magnetization distribution and nuclear level schemes. Here, measurements on different isotopes are of particular interest, since the differences of these measurements, the so-called *isotope shifts* (IS), are exclusively caused by the nuclear differences.

2.7.1 Isotope Shift Measurements

High-precision measurements of isotope shifts represent one of the vital investigations in atomic physics [91]. In this context many atomic transitions have been studied with various techniques, e.g. X-ray measurements also in muonic atoms, elastic electron scattering experiments, laser and X-ray spectroscopy and dielectronic recombination measurements. Isotope shifts arise mainly from the combined effects of (1) the finite nuclear mass and (2)

the volume of the nuclear charge distribution[1]. The recoil shift which is also called mass shift (MS) usually dominates the isotope shifts in light atoms and has a large relativistic nuclear recoil contributions in heavy highly charged ions. The nuclear size shift which is also called volume or field shift (FS) is caused by the spatial overlap of the nuclear charge distribution and the electronic wave functions. The FS scales as Z^5 or even Z^6 and thus dominates the isotope shifts in heavy atoms.
A successful test of the relativistic mass shift has been performed by Rosario Soria Orts and colleagues in 2006 [92]. They measured the isotope shift of the magnetic-dipole (M1) transitions of boron- and berilliumlike argon ions at the Heidelberg electron beam ion trap with relative uncertainties of 4.9% and 8.3%.
To my knowledge, the first measurement of an isotope effect in bound-electron g-factors has been performed by W. M. Hughes and H. G. Robinson in 1969 [93]. They measured the bound-electron g-factor ratio (not the difference) of hydrogen (H) and deuterium (D), using optical pumping of rubidium and a spin-exchange detection of H and D atomic Zeeman resonances.

2.7.2 The Isotope Shift of the Bound-Electron g-Factors of Two Different Lithiumlike Calcium Isotopes, $^{40}Ca^{17+}$ and $^{48}Ca^{17+}$

In the second part of my thesis, I will focus on the bound-electron g-factor difference of the lithiumlike isotopes $^{40}Ca^{17+}$ and $^{48}Ca^{17+}$. In the case of ^{40}Ca and ^{48}Ca the nuclear charge radii are surprisingly similar: $r_{\mathrm{nucl}}(^{40}\mathrm{Ca}) = 3.4776(19)$ fm and $r_{\mathrm{nucl}}(^{48}\mathrm{Ca}) = 3.4771(20)$ fm [94], so that the nuclear size contribution basically cancels in the g-factor difference. To 99.96% the g-factor difference is dominated by the recoil contribution.

2.7.3 Theoretical Calculations of the Isotope Shift $\Delta g = g(^{40}Ca^{17+}) - g(^{48}Ca^{17+})$

For ns states the recoil contribution is of pure relativistic origin. The corresponding full relativistic theory can be formulated only in the framework of QED. As already stated in section 2.3.3, the recoil correction is the only contribution, which requires BS-QED calculations beyond the external field approximation, the so-called Furry picture. In a

Table 2.4: Theoretical contributions of the bound-electron g-factor difference of the lithiumlike calcium isotopes $^{40}Ca^{17+}$ and $^{48}Ca^{17+}$ [95].

effects	contributions to $\Delta g/10^{-9}$
nuclear recoil: one-electron non-QED $\sim m_e/m_{\mathrm{nucl}}$	12.246
nuclear recoil: one-electron non-QED $\sim (m_e/m_{\mathrm{nucl}})^2$	-0.006
nuclear recoil: one-electron QED $\sim m_e/m_{\mathrm{nucl}}$	0.123
nuclear recoil: one-electron QED $\sim \alpha(m_e/m_{\mathrm{nucl}})$	-0.009 (1)
nuclear recoil: interelectronic-interaction	-2.051 (25)
finite nuclear size	0.004 (10)
total theory $[\Delta g = g(^{40}Ca^{17+}) - g(^{48}Ca^{17+})]$	10.305 (27)

recent paper the recoil contribution has been evaluated to all orders in $(Z\alpha)$ for the 2s state

1 In principle, also nuclear polarizations contribute to isotope shifts. However, at the present level of precision this contribution can be neglected.

of the calcium isotopes [95]. The corresponding radiative, second-order in (m_e/m_{ion}) and interelectronic interaction (first and higher-orders) recoil corrections have been calculated [96, 97, 98, 99, 100]. The theoretical uncertainty of the recoil contributions is dominated by the uncalculated higher-order relativistic and QED corrections. In table 2.4 the different theoretical contributions to the g-factor difference of $^{40}Ca^{17+}$ and $^{48}Ca^{17+}$ are listed. Since we measured the absolute g-factor values of $^{40}Ca^{17+}$ and $^{48}Ca^{17+}$, I also list the corresponding state-of-the-art g-factor contributions in table 2.5. Although most recent

Table 2.5: Theoretical contributions to the bound-electron g-factors of the lithiumlike calcium isotopes: $^{40}Ca^{17+}$ and $^{48}Ca^{17+}$ [52] and [95].

theoretical contributions	$^{40}Ca^{17+}$	$^{48}Ca^{17+}$
Dirac value (point nucleus)	1.996 426 010 90	
one-loop QED	0.002 325 555 (5)	
two-loop QED	-0.000 003 520 (2)	
interlectronic interaction	0.000 454 290 (9)	
screened QED	-0.000 000 370 (7)	
finite nuclear size	0.000 000 014 41 (2)	0.000 000 014 41 (2)
nuclear recoil	0.000 000 061 85 (15)	0.000 000 051 54 (12)
total theory	1.999 202 042 (13)	1.999 202 032 (13)

progress has been made on the interelectronic interaction contributions, by the rigorous QED evaluation of the second-order contributions (two-photon exchange diagrams) [52], the interelectronic interaction contribution still dominates the theoretical uncertainty.

2.7.4 The Atomic Masses of $^{40}Ca^{17+}$ and $^{48}Ca^{17+}$

The experimental determination of the isotope difference between the bound-electron g-factors of $^{40}Ca^{17+}$ and $^{48}Ca^{17+}$ requires (1) two high-precision frequency ratio measurements of $\Gamma(^{40}Ca^{17+})$ and $\Gamma(^{48}Ca^{17+})$, see eq. (2.13), which will be presented in chapter 6. (2) Above that, high-precision values of the $^{40}Ca^{17+}$ and $^{48}Ca^{17+}$ masses are essential, see also eq. (2.13), which will be summarized in the following.

The mass of $^{48}Ca^{17+}$

In a recent measurement campaign the atomic mass of ^{48}Ca has been directly determined with the Penning trap mass spectrometer SHIPTRAP [101], measuring the cyclotron frequency ratio of singly charged $^{48}Ca^{+}$ ions and C_4^+ carbon clusters as a reference [95]:

$$R = \frac{\nu_c(^{48}Ca^{+})}{\nu_c(C_4^+)} = \frac{m(C_4^+)}{m(^{48}Ca^{+})} = 1.000\,990\,101\,75\,(39) \qquad (0.39\,\mathrm{ppb}). \tag{2.19}$$

Both cyclotron frequencies are determined as the sum of the two trap radial-motion frequencies, see eq. (3.12). For this purpose small clouds ($\leq$5 ions) of $^{48}Ca^{+}$ and C_4^+ are alternately produced with a laser-ablation ion source [102]. They are separately transferred into a preparation Penning trap for cooling and centering via mass-selective buffer-gas cooling [103]. Afterwards, the particular cyclotron frequency is measured in the so-called measurement Penning trap, using the novel Phase-Imaging Ion-Cyclotron Resonance tech-

nique (PI-ICR) [104, 105].
The mass of a C_4^+ cluster is calculated, considering the dissociation energy $E_{\mathrm{diss}} = 18.0(1.7)$ eV [106], the ionization energy $E_{\mathrm{ion}} = 11.0(7)$ eV [107] and the missing electron: $m(C_4^+) = 4 \cdot 12\,\mathrm{u} - 1 \cdot m_e - \Delta m(E_{\mathrm{diss}}) + \Delta m(E_{\mathrm{ion}}) = 47.999\,451\,412\,6\,(20)\,\mathrm{u}$. The mass differences between all three possible cluster structures – linear, rhombus and triangular pyramidal – are already covered by the uncertainties of the dissociation and ionization energies. For the determination of the mass of lithiumlike calcium $^{48}Ca^{17+}$ we have to correct the mass of singly charged calcium: $m(^{48}Ca^{1+}) = R/m(C_4^+)$ by the 16 missing electron masses and the corresponding binding energies: $\Delta m(E_{\mathrm{bind}}) = 7.2438(43) \cdot 10^{-6}$ u [89][1]. Here, the relative isotope dependence of the binding energy is smaller than $3 \cdot 10^{-12}$ [2]. Finally we extract the mass of $^{48}Ca^{17+}$ [95]:

$$m(^{48}Ca^{17+}) = m(^{48}Ca^{1+}) - 16 \cdot m_e + \Delta m(E_{\mathrm{bind}}) = 47.943\,204\,044\,(19)\,\mathrm{u} \quad (0.4\,\mathrm{ppb}). \quad (2.20)$$

The mass of $^{40}Ca^{17+}$

The masses of $^{40}Ca^{17+}$ and $^{40}Ca^{19+}$ have been measured directly by Szilard Nagy and colleagues in 2006 at the SMILETRAP Penning trap mass spectrometer [109], using a time-of-flight technique and H_2^+ ions as a reference. The atomic mass of ^{40}Ca which has been published in the atomic mass evaluation (AME) 2012 [110] is based on these two measurements, corrected by the masses of the missing electrons and their binding energy. Here, calculated binding energies from [111] have been used: 6732.139 eV for the lithiumlike ion and 13017.129 eV for the hydrogenlike ion. Calculating backwards from the AME 2012 value, $m(^{40}Ca) = 39.962\,590\,864\,(22)$ u, we determine the mass of a lithiumlike ^{40}Ca ion:

$$m(^{40}Ca^{17+}) = 39.953\,272\,233\,(22)\,\mathrm{u} \qquad (0.6\,\mathrm{ppb}). \quad (2.21)$$

This value slightly deviates from the value published in [109], since the mass of hydrogen changed by $1.6 \cdot 10^{-9}$ u, comparing AME 2003 and AME 2012.

1 Binding energies from NIST table [89]: $E_{\mathrm{bind}} = 18804(4) - 11756.4449(80) = 6747.5(4.0)$ eV and $1\,\mathrm{u} = 931\,494\,061\,(21)\,\mathrm{eV/c^2}$.

2 In general the binding energies of different isotopes varies due to their different masses (mass shift) and their different charge distributions (field shift). For calcium the field shift dominates, which scales with Z^5 to Z^6 [91]. Since the binding energy of a 1s electron in uranium differs by 200 eV between a hypothetical point-charge distribution and the measured charge distribution [108], the field shift for 1s electrons in calcium isotopes should be smaller than $\Delta m/m = 200\,\mathrm{eV}/92^5 \cdot 20^5/40\,\mathrm{GeV} = 2.6 \cdot 10^{-12}$. For 2s electrons this effect is even smaller.

CHAPTER 3

Penning Trap Physics

Our high-precision measurements of the Larmor-to-cyclotron frequency ratios Γ require single trapped, cooled ions in close-to-ideal vacuum. State-of-the-art trapping and high-precision measurement techniques with stable ions will be introduced in this chapter. These techniques allow us to work with the same single ion for the complete measurement period. In the beginning, section 3.1, fundamental concepts of Penning trap physics, e.g. the dynamics in an ideal (3.1.1), but also in a real Penning trap with intrinsic trap imperfections will be outlined (3.1.2). In section 3.2, I will summarize a non-destructive detection method for the determination of the eigenfrequencies at low temperature by measuring the induced image currents on the trap electrode surfaces. Aside from the determination of the eigenfrequencies, this technique enables at the same time a very efficient way of cooling the ion. General possibilities to modify the eigenmotions of the confined ion by for example excitation or mode-coupling will be explained in section 3.3. In section 3.4, further concepts of eigenfrequency measurement, e.g. phase-sensitive techniques, will be introduced. So far, aiming for the cyclotron frequency of the ion, in the last part of this chapter, section 3.5, the determination of the Larmor frequency will be discussed.

3.1 Trapping Charged Particles

Already 23 years before Maxwell formulated the classical field theory of electromagnetism Samuel Earnshaw proved in 1842 that there is no single electrostatic or magnetostatic field configuration that can maintain a charged particle in a stable stationary equilibrium (Earnshaw's Theorem) [112].

At present, mostly two different concepts are applied for the trapping of electrically charged particles in small volumes, a few cubic centimeters or smaller[1]: (1) In 1953 Wolfgang Paul and Helmut Steinwedel developed the concept of trapping charged particles in the center of an oscillating quadrupole electric potential, which nowadays is called the *Classical Paul Trap* [113]. Already in 1954 the first Paul trap has been realized [114]. (2) In 1959 Hans Georg Dehmelt used for the first time a superposition of an electrostatic and a magnetostatic

1 For completion, we also mention the trapping of electrically charged particles in storage rings, which require usually circumferences of at least a few meters up to 27 km.

field to confine electrons for several seconds [115]. He named this trapping apparatus after Frans Michel Penning who had proposed the fundamental concept already in 1936, when he constructed a vacuum gauge [116]. In 1949 for the first time John Robinson Pierce proposed such a field configuration for the trapping of charged particles [117]. In the field of high-precision physics with charged particles *Penning traps* have two major advantages towards Paul traps: At first, since the field configuration is static no micromotion occurs which would evoke a heating of the particle. The second advantage is given by the stability of the homogeneous magnetostatic field generated by a superconductive magnet, which enables high-precision measurements of the trapped ion's cyclotron frequency.

3.1.1 The Ideal Penning Trap

An ideal Penning trap is a superposition of two static fields (1) a homogeneous magnetic field for radial confinement and (2) an electric quadrupole potential for axial confinement of electrically charged particles[1]. To generate an electrostatic quadrupole potential, at least three hyperbolic electrodes are required. The central electrode, the so-called *ring electrode*, is negatively charged and the two *endcap* electrodes are equally positively biased, see fig. 3.1. An ideal quadrupole potential would require hyperbolically shaped electrodes

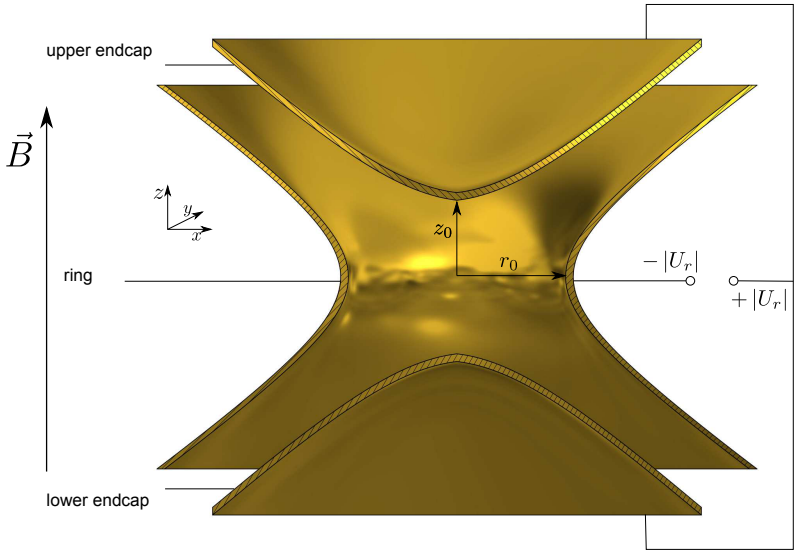

Figure 3.1: Cross section of an ideal Penning trap. An electrostatic quadrupole potential is generated by three hyperbolically shaped electrodes: the ring electrode (central electrode) and two endcap electrodes (upper and lower electrode) with $r_0 = \sqrt{2}z_0$. This setup is placed in a homogeneous magnetic field B. Removing the magnetostatic field and replacing the electrostatic field by an oscillating electric field, such an electrode configuration would represent a classical Paul trap.

1 In a Penning trap, different numbers and even different species of charged particles can be confined at the same time. In this thesis, we focus on single trapped ions.

with infinite size. The homogeneous magnetic field, pointing in axial direction,

$$\vec{B} = B_0 \cdot \vec{e_z} \tag{3.1}$$

confines the electrically charged particle in the radial x / y plane on a circular orbit. In cylindrical coordinates the electric quadrupole potential has the following form:

$$\Phi(z,\rho) = \frac{|U_r|C_2}{2d_{char}^2}\left(z^2 - \frac{\rho^2}{2}\right), \tag{3.2}$$

where $\rho \equiv \sqrt{x^2+y^2}$. U_r is the negative electric voltage applied to the ring electrode and $d_{char} \equiv \sqrt{1/2(z_0^2 + r_0^2/2)}$ is a *characteristic trap length*, such that C_2 is a dimensionless constant. In the case of a hyperbolic Penning trap with $r_0 = \sqrt{2}z_0$, C_2 equals -0.5, see also 3.18.

The Confined Motion

In the following section, the classical, non-relativistic motion in an ideal Penning trap is formulated for a single ion with mass m_{ion} and electric charge q_{ion}. Relativistic corrections will be applied in section 3.3.2.
In the axial direction, which in this thesis will always match with the z-axis, the ion is exposed to an attractive harmonic electrostatic potential. The corresponding equation of motion

$$m_{\text{ion}}\ddot{z} = -\frac{q_{\text{ion}}U_rC_2}{d_{char}^2}z \tag{3.3}$$

describes a one dimensional harmonic oscillation with eigenfrequency[1]

$$\omega_z = \sqrt{\frac{q_{\text{ion}}U_rC_2}{m_{\text{ion}}d_{char}^2}}, \tag{3.4}$$

the so-called *axial frequency*. The total axial energy amounts to

$$E_z = \frac{1}{2}m_{\text{ion}}\omega_z^2 z_0^2, \tag{3.5}$$

where z_0 is the maximal axial amplitude. In the radial directions, the ion senses both, a confining magnetic force and a deconfining electric force:

$$m_{\text{ion}}\begin{pmatrix}\ddot{x}\\ \ddot{y}\end{pmatrix} = q_{\text{ion}}B_0\begin{pmatrix}0 & 1\\ -1 & 0\end{pmatrix}\begin{pmatrix}\dot{x}\\ \dot{y}\end{pmatrix} + \frac{q_{\text{ion}}U_rC_2}{2d_{char}^2}\begin{pmatrix}x\\ y\end{pmatrix}. \tag{3.6}$$

These radial equations of motion can be diagonalized, see for example [118, Appendix A], so that the radial movement consists of a superposition of two circular harmonic

1 Frequencies are quoted sometimes as ordinary frequencies ν or angular frequencies $\omega = 2\pi\nu$.

eigenmotions: (1) the modified cyclotron motion with the *modified cyclotron frequency* ω_+ and the modified cyclotron radius r_+ and (2) the magnetron motion with the *magnetron frequency* ω_- and the magnetron radius r_-:

$$\begin{pmatrix} x \\ y \end{pmatrix} = r_+ \begin{pmatrix} \cos(\omega_+ t + \phi_+) \\ \sin(\omega_+ t + \phi_+) \end{pmatrix} + r_- \begin{pmatrix} \cos(\omega_- t + \phi_-) \\ \sin(\omega_- t + \phi_-) \end{pmatrix}, \tag{3.7}$$

where $\omega_\pm$ can be expressed in terms of the axial frequency and the *free cyclotron frequency*[1] $\omega_c = q_{\text{ion}}/m_{\text{ion}}B$:

$$\omega_\pm = \frac{1}{2}\left[\omega_c \pm \sqrt{\omega_c^2 - 2\omega_z^2}\right]. \tag{3.8}$$

The term beneath the square root sets a stability criterion for Penning traps:

$$\omega_c > \sqrt{2}\omega_z \qquad \text{or} \qquad B_0^2 > 2\frac{m_{\text{ion}}\, U_r\, C_2}{q_{\text{ion}}\, d_{char}^2}. \tag{3.9}$$

In fig. 3.2 the ion's orbit in a Penning trap and its splitting into three independent

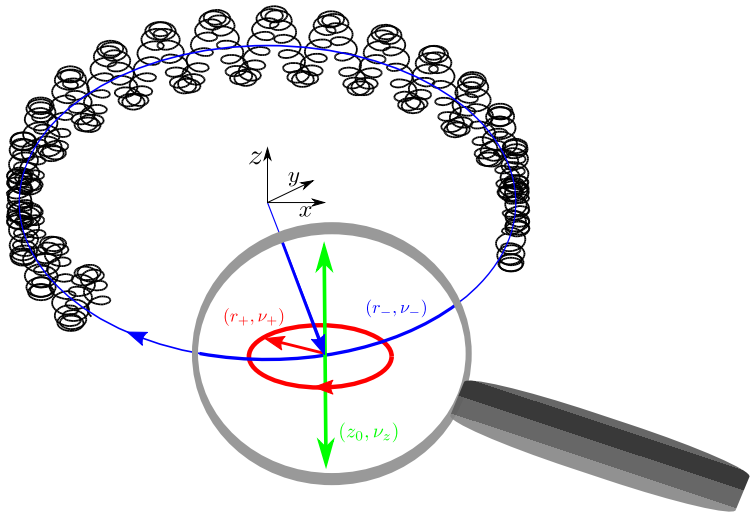

Figure 3.2: Section of an ion's trajectory in a Penning trap. The ion motion can be split into three eigenmotions: (1) the axial motion (green, z_0, ω_z), (2) the fast modified cyclotron motion (red, r_+, ω_+) and (3) the slow magnetron motion (blue, r_-, ω_-). For a distinct illustration of the confined motion, the following artificial parameters have been chosen: $\nu_z = 3$ Hz, $\nu_c = 40$ Hz, $z_0 = 1 \cdot 10^{-6}$ m, $r_+ = 5 \cdot 10^{-6}$ m and $r_- = 1 \cdot 10^{-4}$ m.

eigenmotions is illustrated.

1 In the following, the cyclotron frequency, ω_c, is called the *free cyclotron frequency* in contrast to the *modified cyclotron frequency* ω_+. This terminology is widely used in the Penning trap community.

Considering ordinary field parameters of a few Volt at the ring electrode ($U_r \approx -7\,\mathrm{V}$), zero Volt at the endcap electrodes and a magnetic field of a few Tesla ($B \approx 3.7\,\mathrm{T}$) the following eigenfrequency relations hold for particles with q/m between $\approx 0.5\,\mathrm{e/u}$ for highly charged ions and also $\approx 1\,\mathrm{e/u}$ for protons:

$$\omega_+ \gg \omega_z \gg \omega_-. \tag{3.10}$$

Under these conditions, the magnetron frequency depends approximately linearly on the electric voltage of the ring electrode, $\nu_- \propto U_r$, and the modified cyclotron frequency depends approximately linearly on the magnetic field strength, $\nu_+ \propto B$.
In an ideal Penning trap the three eigenfrequencies are correlated as follows:

$$\omega_z^2 = 2\omega_+\omega_-. \tag{3.11}$$

Finally, we are interested in the determination of the free cyclotron frequency of the ion. In an ideal Penning trap the free cyclotron frequency can be derived from the two radial eigenfrequencies:

$$\omega_c = \omega_+ + \omega_-. \tag{3.12}$$

Not requiring a time consuming measurement of the axial frequency, this relation is widely used in on-line mass measurement experiments.
The kinetic energies of the two radial motions are, see again [118, Appendix A]:

$$E_+ = \frac{1}{2} m_{\mathrm{ion}} \omega_+ (\omega_+ - \omega_-) r_+^2 \approx \frac{1}{2} m_{\mathrm{ion}} \omega_+^2 r_+^2, \tag{3.13}$$

$$E_- = \frac{1}{2} m_{\mathrm{ion}} \omega_- (\omega_- - \omega_+) r_-^2 \approx -\frac{1}{4} m_{\mathrm{ion}} \omega_z^2 r_-^2. \tag{3.14}$$

The magnetron motion is metastable, since its energy is almost purely potential and decreases with increasing magnetron radius. In that way, the magnetron entropy increases with decreasing energy giving rise to a negative magnetron temperature, see also section 3.3.2.
In a quantum mechanical description, the three harmonic eigenmotions can also be treated as three independent quantized oscillations. The quantized energy eigenvalues have the following form [119]:

$$E_z = \left(n_z + \frac{1}{2}\right) \hbar\omega_z, \tag{3.15}$$

$$E_+ = \left(n_+ + \frac{1}{2}\right) \hbar\omega_+, \tag{3.16}$$

$$E_- = -\left(n_- + \frac{1}{2}\right) \hbar\omega_-, \tag{3.17}$$

where n_z, n_+, $n_- \in \mathbb{N}_0$ are the quantum numbers. Our typical ion energies will be discussed in section 3.3.2. The arising large quantum numbers (> 100000), listed in table 3.5, will

illustrate the classical regime of the ion's motion.

3.1.2 Penning Trap Imperfections

In a real Penning trap the field configurations will always deviate from the desired ideal field configurations for a number of reasons:

- **Electric field imperfections:** (1) Generally, it is not possible to design an ideal quadrupole potential with a finite number of electrodes or electrodes of finite size. (2) The dimensions of the electrodes deviate from the ideal design due to machining imperfections during the assembling (in our case: $\approx 10\,\mu m$). (3) In the present trap design the electrodes are misplaced and misaligned in particular by the cooling process from room temperature to cryogenic temperatures ($T = 4.2\,K$), due to the different thermal shrinking of the electrodes and the spacers between the electrodes (in our case: $\approx 20\,\mu m$). (4) Furthermore, the applied voltages deviate and fluctuate from the ideal static specification (voltage fluctuations: $\delta U/U < 6 \cdot 10^{-8}$ in eight minutes). (5) In addition, the potential on the electrode surfaces varies due to patch potentials, which occur when the surface material is not uniform or there are islands of impurities, e.g. islands of insulating layers, on the electrode surfaces. These insulating islands can be caused by frozen rest gas, which can trap unwanted ion species during the ion creation process, see section 4.3.1.
- **Magnetic field imperfections:** The magnetic field is generated typically by a superconducting magnet, which consists of a large solenoidal coil and a couple of smaller shimming coils. They have machining or charging imperfections and are able to cancel only some higher-order magnetic field components but not all. Besides, the materials of the trap and the surrounding always have some residual magnetic susceptibility, which influences the magnetic field. Their susceptibility fluctuates due to pressure and temperature fluctuations, see section 4.2.2.
- **Imperfections of the combination of the electric and magnetic field:** Furthermore, the symmetry axis of the electrostatic potential and the direction of the magnetic field can be misaligned, which disturbs the relation for the free cyclotron frequency in eq. (3.11).

All these imperfections have an impact on the motion of the ion. In the following three subsections I will discuss the first-order eigenfrequency shifts due to cylindrically symmetric imperfections of the electric field and the magnetic field.

Electric Field Imperfections

Even though in a real trap cylinder symmetry is broken, for example by vertically split electrodes, which are necessary for the radial excitation and frequency detection, see section 3.3.2, the dominant electrostatic imperfections are still cylindrically symmetric. Therefore, the electric potential along the z-axis can be decomposed in even powers of z to study its dominant deviations:

$$V(z) = \frac{1}{2} U_r \sum_{i=0,2,4,\ldots}^{\infty} C_i \frac{z^i}{d_{char}^i}. \tag{3.18}$$

In this decomposition the coefficients C_i's are dimensionless parameters, set by the trap design and the applied voltages. Since in high-precision Penning traps all three eigenmotions are cooled, see section 3.3.2, the motional amplitudes are primarily small. In that way, the dominant correction of the electric potential is given by the lower-order imperfections, essentially C_4, which shifts the frequencies in the following way [13]:

$$\begin{pmatrix} \delta\nu_+/\nu_+ \\ \delta\nu_z/\nu_z \\ \delta\nu_-/\nu_- \end{pmatrix} = \frac{6C_4}{q_{\text{ion}}U_r C_2^2} \begin{pmatrix} \frac{1}{4}(\nu_z/\nu_+)^4 & -\frac{1}{2}(\nu_z/\nu_+)^2 & -(\nu_z/\nu_+)^2 \\ -\frac{1}{2}(\nu_z/\nu_+)^2 & \frac{1}{4} & 1 \\ -(\nu_z/\nu_+)^2 & 1 & 1 \end{pmatrix} \cdot \begin{pmatrix} E_+ \\ E_z \\ E_- \end{pmatrix}. \quad (3.19)$$

In [120] universal formulas for the first-order frequency shifts in all even orders of C_i have been derived:

$$\frac{\delta\nu_z}{\nu_z} = \frac{(2n)!}{2^{2n}d^{2n-2}} \frac{C_{2n}}{C_2} \sum_{k=1}^{n-1} \sum_{p=0}^{k} \frac{(-1)^k (n-k) r_+^{2p} r_-^{2(k-p)} z^{2(n-k-1)}}{[(n-k)!p!(k-p)!]^2}, \quad (3.20)$$

$$\frac{\delta\nu_\pm}{\nu_\pm} = \frac{\pm\omega_\mp}{\omega_+ - \omega_-} \frac{(2n)!}{2^{2n-1}d^{2n-2}} \frac{C_{2n}}{C_2} \sum_{k=1}^{n} \sum_{p=0}^{k-1} \frac{(-1)^k (p+1) r_\pm^{2p} r_\mp^{2(k-1-p)} z^{2(n-k)}}{[(n-k)!(k-p-1)!(p+1)]^2}. \quad (3.21)$$

In contrast to the eigenfrequencies of an ideal Penning trap, all these frequency corrections depend on the energies/amplitudes of the eigenmotions. Elaborated trap designs, see section 3.1.3 and especially chapter 7, and, in addition, very small amplitudes minimize these shifts.

Magnetic Field Imperfections

With the same assumptions made for the electric field imperfections, the dominant frequency shifts, which arise from magnetic field imperfections, are generated by the lower-order terms of the magnetic field. With an axial series-expansion of the magnetic field:

$$B(z) = \sum_{i=0,1,2,..}^{\infty} B_i z^i \quad (3.22)$$

the symmetric leading-order correction is:

$$\begin{pmatrix} \delta\nu_+/\nu_+ \\ \delta\nu_z/\nu_z \\ \delta\nu_-/\nu_- \end{pmatrix} = \frac{B_2}{B_0 m_{\text{ion}}(2\pi\nu_z)^2} \begin{pmatrix} -(\nu_z/\nu_+)^2 & 1 & 2 \\ 1 & 0 & -1 \\ 2 & -1 & -2 \end{pmatrix} \cdot \begin{pmatrix} E_+ \\ E_z \\ E_- \end{pmatrix}. \quad (3.23)$$

A linear gradient of the magnetic field B_1 shifts the center of the ion motion in axial direction due to the force acting on the magnetic moment generated by the radial motions. In that way, B_1 shifts the free cyclotron frequency. Analytical expressions of eigenfrequency shifts due to higher-order magnetic field imperfections can also be found in [120]. Again, all these frequency shifts depend on the energy of the ion.

For the detection of the electron spin-state and the measurement of the ion's energies, we take even advantage of magnetic eigenfrequency shifts, by introducing a particular large

magnetic field imperfection B_2, also stated as a *magnetic bottle*, into our Penning trap setup. More details will be given in section 3.5.

Field Tilts and Ellipticity - The Invariance Theorem

The determination of the free cyclotron frequency via eq. (3.12): $\omega_c^* = \omega_+ + \omega_-$ only holds for ideal Penning traps. Especially, this equation depends on tilts between the magnetic and electric field, since it determines only the axial component of the magnetic field, but not the total magnetic field. In 1982 Lowell S. Brown and Gerald Gabrielse derived an equation, the so-called *invariance theorem*, which cancels such trap imperfections [121]:

$$\omega_c = \sqrt{\omega_+^2 + \omega_z^2 + \omega_-^2}. \tag{3.24}$$

More precisely, eigenfrequency shifts due to a misalignment between the electric and magnetic field and moreover radial ellipticity of the ion trajectory are annulled. In this thesis, the invariance theorem will be used persistently to calculate the free cyclotron frequency of the ion.
Consequently, the difference between these two equations, eq. (3.12) and eq. (3.24), is sensitive to the angle of the tilt θ (°) and the corresponding eccentricity of the ellipsoidal ion motion ε:

$$\omega_c^* - \omega_c = \omega_- \left(\frac{9}{4} \left(\theta \frac{\pi}{180^\circ} \right)^2 - \frac{1}{2}\varepsilon^2 \right). \tag{3.25}$$

In table 3.1 our measured tilts are listed for the various ions, assuming vanishing ellipticities $\varepsilon = 0$. In general, these tilts are smaller than 0.2°, which confirms a proper alignment of our experimental setup.

Table 3.1: Measured tilts of our two measurement traps, assuming a vanishing ellipticity. Between the various measurement campaigns, the experimental setup has been replaced and relocated from the superconducting solenoidal magnet several times.

ion	PT-θ (°)	AT-θ (°)
$^{12}C^{5+}$ (see table 3.3)	0.18(2)	0.42(21)
$^{40}Ca^{17+}$	0.11(3)	–
$^{48}Ca^{17+}$	0.09(3)	–

3.1.3 A Real Penning Trap - Our Trap Design

Instead of using a hyperbolic electrode geometry, as introduced for the ideal Penning trap geometry in the previous section 3.1.1, we use cylindrically shaped electrodes for essentially three reasons: (1) Cylindrical objects can be produced with much higher precision than hyperbolic objects[1]. (2) Ion transport along the axial symmetry axis of the trap is significantly easier. (3) The required microwave excitation for the electron spin-drive, see section 3.5, can be coupled from the top of the trap via a microwave horn.

1 The present electrodes have a machining precision of ±10 µm, nowadays ±5 µm are possible.

Aiming for a higher harmonicity of the electric potential, our Penning trap is segmented into five cylindrical electrodes, instead of only three: (1) A ring electrode, which fixes the axial frequency by the setting of the ring voltage U_r; (2) two correction electrodes (one complete and one vertically split electrode, see fig. 3.3(a)) (U_{cor}), which can be used to shape the electric potential, see below, and (3) two grounded endcap electrodes.
In the present trap design, the radius r and the ring voltage U_r have been adjusted in combination with the eigenfrequency detection techniques, especially the axial resonator, see section 3.2.2. The distances between the electrodes $dd = 140\,\mu\mathrm{m}$ have been kept as small as possible. Finally, in case of a Penning trap with five cylindrical electrodes, the following five parameters can be adjusted, to optimize the harmonicity of the electric potential:

- the length of the ring electrode l_r,
- the lengths of the correction electrodes l_c and
- the voltages applied to the correction electrodes U_{cor}.

Requiring a symmetric potential in axial direction, the correction electrodes must have the same lengths l_c and the same voltages: $U_{\mathrm{cor}} \equiv U_{\mathrm{uc}} = U_{\mathrm{lc}}$. In the Penning trap community the correction voltage is usually expressed by the *tuning ratio*: $TR \equiv U_{\mathrm{cor}}/U_r$. The three dimensions: l_r, l_c and TR could be chosen in a way that the three leading-order terms of the anharmonic contributions of the electric potential: C_4, C_6 and C_8, see eq. (3.18), vanish. Nevertheless, due to practical reasons, these parameters are optimized in the following way:

- Only the first two leading-order terms of the anharmonic contributions of the electric potential are canceled: $C_4 = C_6 = 0$ [122]. Such a trap design is called *compensated*.
- In addition, C_2 and in that way also the axial frequency, see eq. (3.4), should not depend on the applied correction voltage U_{cor}. This so-called *orthogonality criterion* is essential for an easier handling of the electric potential during the on-line trap optimization, see section 4.3.2. Expressing C_2 in terms of the tuning ratio:

$$C_2 = E_2 + TR \cdot D_2 \tag{3.26}$$

  orthogonality is equivalent to the demand of $D_2 = 0$.

For our present trap design, we define the characteristic trap length parameter, introduced in eq. (3.4), as: $d_{\mathrm{char}} \equiv \sqrt{1/2(z_0^2 + r^2/2)}$, where $z_0 \equiv l_r/2 + dd + l_c + dd$. In fig. 3.3(a) our trap design is presented together with the geometrical dimensions in table 3.3(b).
In table 3.2 the leading-order coefficients of the theoretically predicted electric potential are summarized. A detailed explanation of these calculations will be given in the last chapter of this thesis, chapter 7, where also a further improved trap design will be represented.
Due to a flaw during the optimization process of the present trap design, our trap is not completely compensated. For this reason, the tuning ratio in table 3.2 is always chosen in a way, that $C_4 = 0$, whereas $C_6 \neq 0$.
In section 3.5 the request of two spatially separated Penning traps in our experimental

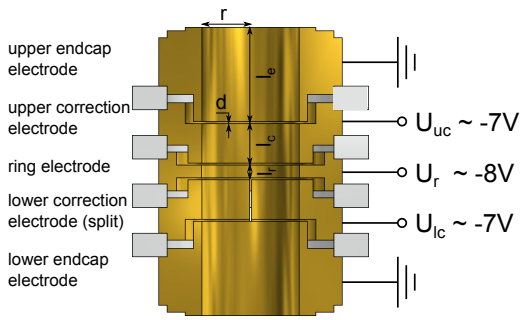

(a)

electrode dim. (mm)	
r	3.5
l_r	0.92
l_c	2.85
l_e	6.8
dd	0.14
char. trap parameter: (mm)	
d_{char}	3.083

(b)

Figure 3.3: The present Penning trap design. (a) Cross section of our Penning trap. The five electrodes are represented in gold and the isolation spacers in gray. The lower correction electrode is vertically split into two parts. (b) List of the electrode dimensions.

Table 3.2: Dimensionless, leading-order coefficients of the theoretically predicted electric potential of our present trap design.

coefficient of the electric potential	value
C_2	-0.5503765
D_2	$6.8 \cdot 10^{-4}$
C_4	0
D_4	-0.62
C_6	-0.012
D_6	0.50

setup is motivated by different magnetic field configurations and different axial resonators. In table 3.3 the eigenfrequencies of a single $^{12}C^{5+}$ ion in these two Penning traps (the so-called precision trap (PT) and the analysis trap (AT)) are summarized.

Table 3.3: Field dimensions and eigenfrequencies for a $^{12}C^{5+}$ ion in the precision trap and the analysis trap.

	precision trap (PT)	analysis trap (AT)
magnetic field (B_0)	3.764 T	3.708 T
ring voltage (U_r)	-7.634 V	-3.0135 V
tuning ratio (TR)	0.87996	[a]
ν_+	24 081 134 Hz	23 730 015 Hz
ν_z	670 964 Hz	412 320 Hz
ν_-	9347.2 Hz	3582.6 Hz

[a] Asymmetric voltage has been used to shift the ion in axial direction: $U_{uc} = -2.37253$ V and $U_{lc} = -2.47253$ V, see section 4.1.5.

3.2 Induced Image Charge Detection

In the previous section (3.1) the two static fields of a Penning trap have been introduced and their impact on the motion of a trapped ion has been studied. In the following section I discuss at first the influence of the ion on the trap electrodes, which induces image charges on their surfaces fulfilling Maxwell's equations. Subsequently, the induced image currents of the moving ion are quantified (3.2.1), which can be translated into a measurable voltage by a large resistance generated by a resonator (3.2.2). Finally, the dynamics between the resonator and the ion enables an elegant detection technique for the axial frequency (3.2.3). In the last subsection we discuss the impact of the induced image charges on the eigenfrequencies of the ion (3.2.4).

3.2.1 The Induced Image Currents

The Shockley–Ramo theorem from 1939 [123] quantifies the instantaneous electric current i_{ind} induced by a moving ion with charge q_{ion} and velocity $\vec{v}_{\text{ion}}$ in the vicinity of an electrode, see fig. 3.4(a):

$$i_{\text{ind}} = q_{\text{ion}} \vec{v}_{\text{ion}} \vec{E}_w(\vec{r}_{\text{ion}}(t)). \tag{3.27}$$

The so-called weighting field $\vec{E}_w(\vec{r}_{\text{ion}}(t)) \equiv \vec{E}(\vec{r}_{\text{ion}}(t))/U_{\text{el}}$ is the electric field of the electrode at the position of the ion $\vec{E}(\vec{r}_{\text{ion}}(t))$ divided by the potential of the electrode U_{el}, assuming that the ion is absent and all other neighbouring electrodes are grounded.
In the following, I focus on the axial ion motion in a Penning trap, which induces image currents for example on the upper correction electrode, see fig. 3.4(b). The electric potential of that electrode can be approximated linearly in the range of the axial motion (indicated in red), similar to the electric potential of a plate capacitor. That way, the ion senses permanently the constant weighting field of the upper correction electrode. In the Penning trap community the inverse of this weighting field is also referred to as the *effective electrode*

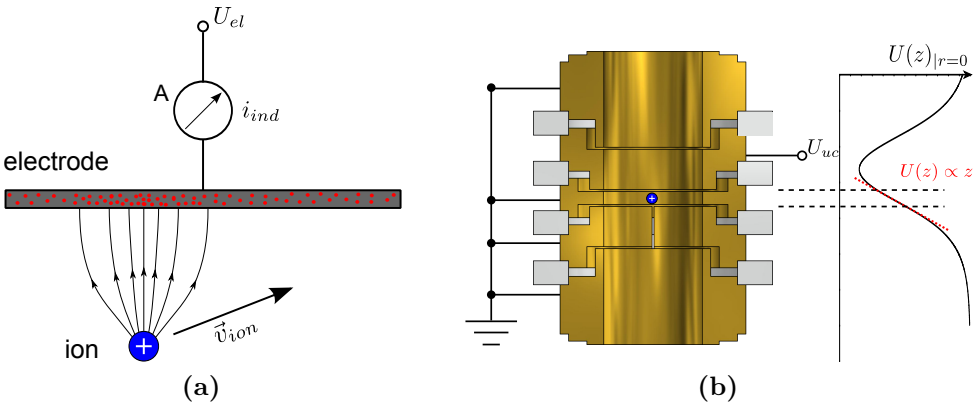

Figure 3.4: Illustration of the induced image charges by a moving electrically charged particle. (a) A moving ion with charge q_{ion} and velocity $\vec{v}_{\text{ion}}$ induces an image current i_{ind} on an electrode with voltage U_{el}. (b) Linear approximation (shown in red) of the electric potential generated by the upper correction electrode of a cylindrical Penning trap, which provides a constant weighting field in the range of the axial ion motion. For details see text.

distance, D:

$$D \equiv \frac{1}{E_w}|_{z=0,r=0} = U_{\mathrm{el}} / \frac{\partial U_{\mathrm{el}}}{\partial z}|_{z=0,r=0}. \tag{3.28}$$

Finally the induced current in eq. (3.27) can be calculated as follows:

$$i_{\mathrm{ind}}(t) = \frac{q_{\mathrm{ion}}}{D}\dot{z}(t) \;\rightarrow\; i_{\mathrm{ind}}^{\mathrm{rms}} = \frac{q_{\mathrm{ion}}}{D} z_{\mathrm{rms}}\omega_z = \frac{q_{\mathrm{ion}}}{D}\frac{z_0}{\sqrt{2}}\omega_z. \tag{3.29}$$

In our trap, we use one of the correction electrodes to detect the axial signal. It has an effective electrode distance of $D = 7.38\,\mathrm{mm}$. Considering a hydrogenlike carbon ion $^{12}C^{5+}$ at an axial frequency of $\nu_z = 670\,\mathrm{kHz}$ and an axial amplitude of $z_{\mathrm{rms}} = 12\,\mu\mathrm{m}$, see table 3.5, the induced current is in the order of: $i_{\mathrm{ind}}^{\mathrm{rms}} \approx 5\,\mathrm{fA}$.
Applying Ohm's law $U = R \cdot I$ this tiny current can be transferred into a measurable voltage u_{ind}. The required large resistance R will be generated by a tuned tank circuit parallel to the trap, which is in resonance with the axial frequency.
In principle, the same detection principle can be used for the radial eigenfrequencies, using a split cylindrical electrode, which generates a radial weighting field.

3.2.2 The Axial-Resonator - a Parallel Tank-Circuit

Since the axial motion of the trapped ion induces an alternating current which is transferred into a measurable alternating voltage by a parallel tank circuit, we focus on the impedance, Z, rather than exclusively on the ohmic resistance, to describe the phase differences between currents and voltages as an angle difference in the complex coordinate system. Consequently Ohm's law has the following structure:

$$u(t) = Z \cdot i(t). \tag{3.30}$$

The heart of the detection system consists of a resonator connected with the complete upper correction electrode. In the representation of a lumped circuit the trap electrodes

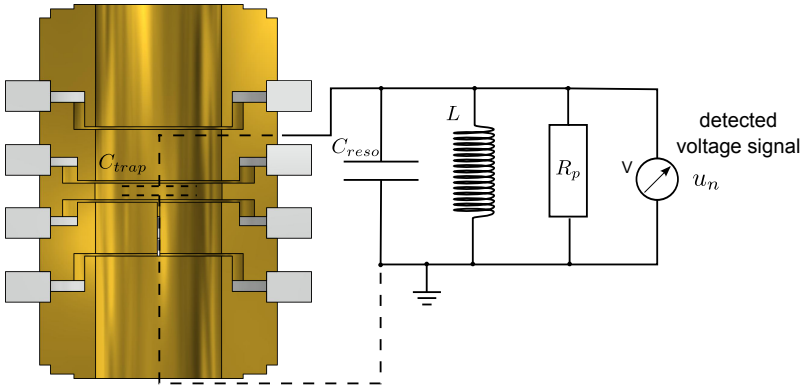

Figure 3.5: Lumped circuit of the axial detection system, including two parallel capacities C_{trap} and C_{reso}, an inductance L and an ohmic resistance R_p.

constitute a capacitance C_{trap} and the resonator is described as a parallel tank circuit with

capacitance C_{reso}, inductance L and ohmic resistance R_p, see fig. 3.5. The total capacitance C is generated from the adjacent electrodes in the trap, the surrounding of the resonator (resonator box) and the intrinsic coil capacitance. The inductance originates primarily from a coil with solenoidal geometry [13]. The finite ohmic resistance R_p is caused by the skin effect, the proximity effect, ohmic losses in the conducting environment and dielectric losses in the isolating environment, which are summarized in [124].
The total impedance of the detection system without any trapped ion has the following form:

$$Z_{LC}^{-1} = Z_L^{-1} + Z_C^{-1} + R_p^{-1} \tag{3.31}$$

$$= \frac{1}{i\omega L} + i\omega C + \frac{1}{R_p} \tag{3.32}$$

$$= \frac{1}{R_p}\left[1 + iQ\left(\frac{\omega}{\omega_{res}} - \frac{\omega_{res}}{\omega}\right)\right]. \tag{3.33}$$

Q denotes the quality factor, also called Q-value: $Q \equiv \nu_{res}/\Delta\nu$, where $\Delta\nu$ is the full width at half maximum (FWHM) of the frequency spectrum of the thermal noise of the resonator. More precisely, $\Delta\nu$ is the FWHM of the real part of the impedance: $\text{Re}(Z_{LC}(\omega))$[1]. At the resonance frequency $\omega_{\text{res}} = \frac{1}{\sqrt{LC}}$ the resistance is maximal and the reactance, the imaginary part of the impedance, vanishes:

$$Z_{LC}(\omega = \omega_{res}) = R_p = \frac{Q}{\omega_{res} C} = Q\omega_{res} L. \tag{3.34}$$

To optimize the signal strength, $\text{Re}(Z_{LC}(\omega))$ can be maximized by adjusting the trap potential in a way that the axial frequency of the ion corresponds to the resonance frequency of the resonator. Furthermore the resonator itself should have a high Q-value, low capacitance and a large inductance to generate a large R_p. In an ideal parallel tank circuit R_p would be infinitely large. The characteristics of the present axial resonators are summarized in table 3.4. Further information can be found in the thesis of Sven Sturm [13].

Table 3.4: Characteristics of the axial resonators of the precision trap (measured with $^{12}C^{5+}$) and the analysis trap (measured with $^{48}Ca^{17+}$). The values of the inductances have been derived from the thesis of Sven Sturm [13].

	precision trap (PT)	analysis trap (AT)
resonance frequency, ν_{res}	670890(4) Hz	411832 kHz
Q-value	670(20)	3280
inductance, L	1.5 mH	5.36 mH
parallel resistance, R_p	4.24 MΩ	45.5 MΩ

1 In dB units the FWHM of a power ratio corresponds to the $10 \cdot \log_{10}(0.5) \approx -3$dB-width.

The Thermal Noise Spectrum of a Resonator

In this section, the line-shape model for the noise spectrum of the detection system is discussed without ions in the trap.
The only measurable electronic signal of a conductor which always occurs regardless of the applied voltage is the thermal noise, also called the *Johnson Noise* or *Johnson-Nyquist Noise*. It has been observed for the first time by John Bertrand Johnson in 1926 [125] and has been modeled by Harry Nyquist in 1928 when he formulated the fluctuation-dissipation theorem [126]. For any electronic conductor it is characterized by the rms voltage u_n at a frequency bandwidth $\Delta\nu$:

$$u_n = \sqrt{4k_B T Re(Z)\Delta\nu}. \tag{3.35}$$

Remarkably, it only depends on the ohmic resistance $Re(Z)$ and the temperature T of the conduction electrons. Without any applied feedback or significant noise source these electrons are in thermal equilibrium with the lattice of the conductor and thus also with the ambient temperature. Except for the resistance, the thermal noise is independent of any other property of the conductor or its geometry.
Combining eq. (3.35) and eq. (3.31), the rms voltage spectrum of our detection system has the following form, after the application of a fast Fourier transformation (FFT):

$$u_n^{\mathrm{res}}(\omega) = \sqrt{\frac{4k_B T \Delta\nu R_p}{1 + Q^2\left(\frac{\omega_{\mathrm{res}}}{\omega} - \frac{\omega}{\omega_{\mathrm{res}}}\right)^2}}, \tag{3.36}$$

where $\Delta\nu$ corresponds to the frequency resolution of the FFT.

Signal Amplification

The resonator signals of the experimental setup are amplified in two stages, before the signal is Fourier analyzed, for the first time already at the cryogenic level, but also once more at room temperature.
In addition to the thermal noise of the resonator, we consider three more effects for the final detected line-shape: (1) The amplifier adds an additional thermal noise term u_n^{ampl}, which in first-order is frequency independent. (2) Moreover, the transfer function of the detection system has a slight frequency dependence with slope κ_{det} and (3) furthermore the complete signal itself is amplified by a factor A. Thus the finally detected rms-voltage has the following form:

$$\begin{aligned} u_{\mathrm{n}}^{\mathrm{final}}&(\omega|A,u_n^{\mathrm{ampl}},\kappa_{\mathrm{det}},T,\Delta\nu,Q,\omega_{\mathrm{res}},R_p) \\ &= A\cdot(1+\kappa_{\mathrm{det}}(\omega-\omega_{\mathrm{res}}))\cdot\sqrt{(u_n^{\mathrm{res}}(\omega|T,\Delta\nu,Q,\omega_{\mathrm{res}},R_p))^2+(u_n^{\mathrm{ampl}})^2}\ (\mathrm{Vrms}) \\ &= 10\log_{10}\left[\widetilde{A}\cdot\mathrm{Re}(Z(\omega|Q,\omega_{\mathrm{res}},R_p)/R_p)+(\widetilde{u}_n^{\mathrm{ampl}})^2\right]+\widetilde{\kappa}_{\mathrm{det}}\cdot(\omega-\omega_{\mathrm{res}})\ (\mathrm{dBVrms}). \end{aligned} \tag{3.37}$$

In the second line some parameters are redefined and formulated in decibel scaling[1]: $\widetilde{A} \equiv A^2 4 k_B T \delta\nu R_p$, $\widetilde{u}_n^{\text{ampl}} \equiv A u_n^{\text{ampl}}$ and $\widetilde{\kappa}_{\text{det}} \equiv 20 \cdot \kappa_{\text{det}} / \log(10)$. The parameters Q, ω_{res}, $\widetilde{u}_n^{\text{ampl}}$ and $\widetilde{\kappa}_{\text{det}}$ are extracted from the recorded frequency spectra of the resonator by a fitting routine and fixed for the complete data analysis, see section 4.3.2. Some of these fit values, e.g. Q and ω_{res} have been already presented in table 3.4.

3.2.3 Interaction Between the Trapped Ion and the Resonator

In this section, the interaction of a single trapped ion and the resonator is studied.
The tiny electric potential on the detection electrode, which is created by the induced image charges and the large resistance of the resonator, generates an additional force acting on the ion. Assuming the same linear approximation of the electric field as in eq. (3.28), the additional force acting on the ion has the following form:

$$F_z = -q_{\text{ion}} E_z \overbrace{\approx}^{3.28} -\frac{q_{\text{ind}}}{D} u_{\text{ind}} \overbrace{=}^{3.30} -\frac{q_{\text{ind}}}{D} Z_{LC} i_{\text{ind}} \overbrace{\approx}^{3.29} \underbrace{-\frac{q_{\text{ind}}^2}{D^2} Z_{LC}}_{\equiv 2\gamma m_{ion}} \dot{z}. \tag{3.38}$$

The differential equation of the harmonic axial movement (3.3) is extended to an equation of motion of a damped harmonic oscillator:

$$0 = \ddot{z} + 2\gamma \dot{z} + \omega_z^2 z, \tag{3.39}$$

whose damped solution can be described by:

$$z(t) = z_0 e^{-\lambda t}, \text{ where: } \lambda = \gamma - i\sqrt{\omega_z^2 - \gamma^2}. \tag{3.40}$$

In contrast to a common damped oscillator the damping constant γ, depending on the impedance of the resonator, is not a real but a complex constant leading to an additional shift of the eigenfrequency of the ion:

$$\omega_z^* = \text{Im}(\lambda) \approx \omega_z - \text{Im}(\gamma). \tag{3.41}$$

In fig. 3.6 the relative shift of the axial frequency of a $^{12}C^{5+}$ ion in the precision trap is presented. It is called *image current shift* [13].
The real part of $\lambda_{1,2}$ which is in very good approximation $\text{Re}(\lambda_{1,2}) \approx \text{Re}(\gamma)$ damps the axial motion of the ion. Its amplitude exponentially decreases $\propto \exp(-\text{Re}(\gamma)t)$ with the so-called cooling time constant[2]:

$$\tau(\omega_z) \equiv \frac{1}{2\text{Re}(\gamma)} = \frac{m_{\text{ion}} D^2}{q_{\text{ion}}^2 \text{Re}(Z_{LC}(\omega_z^*))}. \tag{3.42}$$

1 For an amplitude ratio: $1\,\text{dBVrms} = 20 \log_{10}(1\,\text{Vrms})$.
2 The cooling time constant τ is defined in a way that the axial energy ($\propto z_0^2$) has a damping of $\propto \exp -t/\tau$.

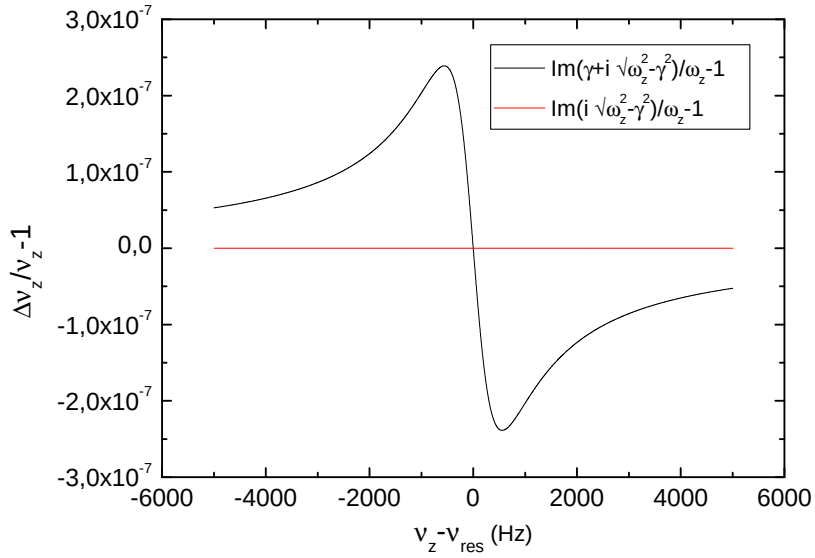

Figure 3.6: Relative deviation of the axial frequency due to the image current shift ($^{12}C^{5+}$ in precision trap). In black: complete shift; in red: only the squared correction $\mathrm{Im}(i\gamma^2)$ is plotted which can be neglected with respect to the correction $\mathrm{Im}(\gamma)$.

We define $\widetilde{\tau} \equiv \tau(\omega_z^* = \omega_{\mathrm{res}} = \omega_z)$. Considering a single $^{12}C^{5+}$ ion, which is in resonance with the axial tank circuit, its axial cooling time constant in the precision trap is $\widetilde{\tau} = 331(15)$ ms and in the analysis trap $\widetilde{\tau} = 37(5)$ ms. In this way, the axial mode of the trapped ion thermalizes within a few seconds with the conductor electrons of the resonator, which are again in thermal equilibrium with the lattice of the resonator material. The resonator itself is thermalized with the neighbouring thermal bath of liquid helium. The boiling temperature of liquid helium at normal pressure is 4.2 K. When the axial motion is in thermal equilibrium with the resonator, the axial energy is Boltzmann distributed at the temperature $T_z = T_{\mathrm{Resonator}}$:

$$\rho(E_z) = \frac{1}{k_B T_z} e^{-\frac{E_z}{k_B T_z}}. \tag{3.43}$$

The averaged axial energy is:

$$< E_z >= k_B T_z. \tag{3.44}$$

This so-called *resistive cooling* method has been first applied by David J. Wineland and Hans G. Dehmelt [127].

The equation of motion 3.39 can also be expressed in terms of the induced current:

$$u_{\mathrm{ind}} = \underbrace{\frac{m_{\mathrm{ion}} D^2}{q_{\mathrm{ion}}^2}}_{\stackrel{\mathrm{def}}{=} L_{\mathrm{ion}}} \partial_t i_{\mathrm{ind}} + \underbrace{\frac{m_{\mathrm{ion}} \omega_z^2 D^2}{q_{\mathrm{ion}}^2}}_{\stackrel{\mathrm{def}}{=} C_{\mathrm{ion}}^{-1}} \int i_{\mathrm{ind}} dt \tag{3.45}$$

$$= L_{\mathrm{ion}} \partial_t i_{\mathrm{ind}} + C_{\mathrm{ion}} \int i_{\mathrm{ind}} dt. \tag{3.46}$$

The first term can be associated with the voltage of an inductance and the second term with the voltage of a capacitance. In this way, the axial dynamics of the ion in presence of the resonator can be understood as a serial tank circuit with the impedance:

$$Z_{\mathrm{ion}} = i\omega L_{\mathrm{ion}} + \frac{1}{i\omega C_{\mathrm{ion}}} \tag{3.47}$$

$$= i\omega R_p \widetilde{\tau} \left(1 - \frac{\omega_z^2}{\omega^2}\right) \tag{3.48}$$

and the resonance frequency: $\omega_z = \frac{1}{\sqrt{L_{\mathrm{ion}} C_{\mathrm{ion}}}}$.

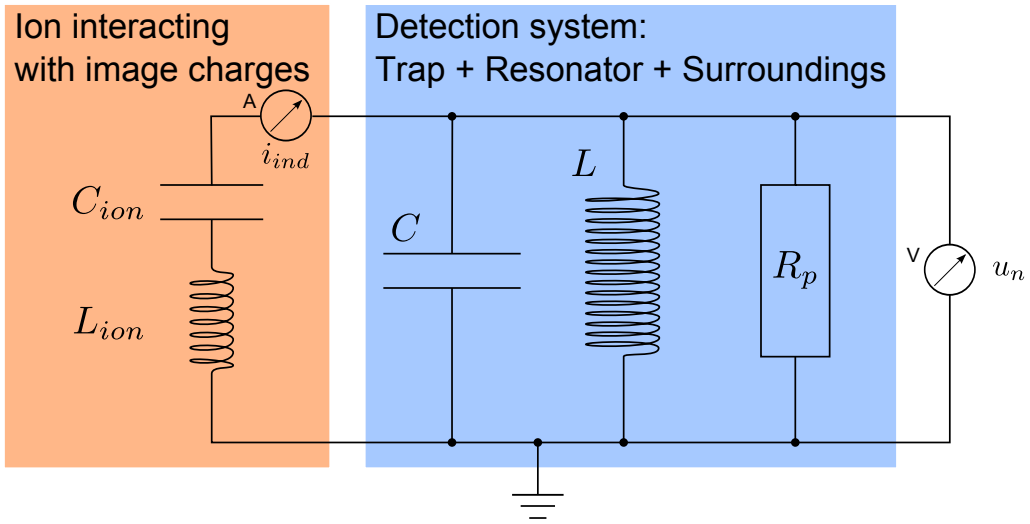

Figure 3.7: Lumped circuit of the detection system including the interaction with the ion. A serial tank circuit represents the interaction between the ion and the induced image charges. A parallel tank circuit describes the detection system including the resonator, resonator box and the detection electrode.

To study the thermal noise spectrum of the thermalised ion and the complete detection system, illustrated in fig. 3.7, the complete impedance is calculated by combining equation

3.34 and 3.47:

$$Z_{\mathrm{tot}} = \frac{1}{\frac{1}{Z_{LC}} + \frac{1}{Z_{\mathrm{ion}}}} \tag{3.49}$$

$$= \left[\frac{1}{R_p} \left(1 + iQ \left(\frac{\omega}{\omega_{\mathrm{res}}} - \frac{\omega_{\mathrm{res}}}{\omega} \right) \right) + \frac{1}{i\omega R_p \widetilde{\tau} \left(1 - \frac{\omega_z^2}{\omega^2} \right)} \right]^{-1} \tag{3.50}$$

$$= R_p \frac{\omega_{\mathrm{res}} \omega (\omega^2 - \omega_z^2)}{\omega_{\mathrm{res}} \omega (\omega^2 - \omega_z^2) + iQ(\omega^2 + \omega_{\mathrm{res}}^2)(\omega^2 - \omega_z^2) - i\omega_{\mathrm{res}} \omega^2 / \widetilde{\tau}} \tag{3.51}$$

For the thermal noise spectrum only the real part of the impedance is required:

$$\mathrm{Re}(Z_{\mathrm{tot}}) = R_p \frac{\left(\omega_{\mathrm{res}} \omega (\omega^2 - \omega_z^2) \right)^2}{\left(\omega_{\mathrm{res}} \omega (\omega^2 - \omega_z^2) \right)^2 + \left(Q(\omega^2 + \omega_{\mathrm{res}}^2)(\omega^2 - \omega_z^2) - \omega_{\mathrm{res}} \omega^2 / \widetilde{\tau} \right)^2}. \tag{3.52}$$

The final line-shape is derived by inserting the real part of the impedance (3.52) into (3.35) to derive u_n^{dip}, the Johnson noise including thermalized ion signal. At last, the final noise spectrum is derived by replacing u_n^{res} with u_n^{dip} in eq. (3.37):

$$\begin{aligned} u_{\mathrm{n}}^{\mathrm{dip}}(\omega, |\omega_z, \widetilde{A}, \widetilde{\tau}, Q, \omega_{\mathrm{res}}, \widetilde{u}_n^{\mathrm{ampl}}, \widetilde{\kappa}_{\mathrm{det}}) \\ = 10 \log_{10} \left[\widetilde{A} \cdot \mathrm{Re}(Z_{\mathrm{tot}}(\omega | \omega_z, \widetilde{\tau}, Q, \omega_{res}, R_p)/R_p) + (\widetilde{u}_n^{\mathrm{ampl}})^2 \right] \\ + \widetilde{\kappa}_{\mathrm{det}} \cdot (\omega - \omega_{\mathrm{res}}) \ (\mathrm{dBVrms}). \end{aligned} \tag{3.53}$$

In fig. 3.14(b) the spectrum of a thermalized $^{12}C^{5+}$ ion is shown. At the axial frequency of the ion ($\omega = \omega_z$) the induced current signal shortens the Johnson noise of the resonator

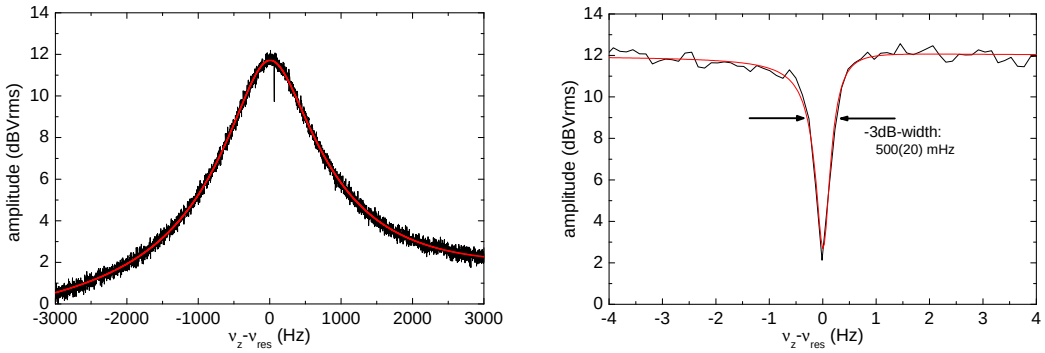

(a) **(b)**

Figure 3.8: Fourier transform of the axial resonator of the precision trap. (a) Thermal noise spectrum of the PT resonator (black) and line-shape fit (red, see eq. (3.37)). (b) Dip signal of a the thermalized $^{12}C^{5+}$ ion (black) and the line-shape fit (red, see eq. (3.53)) in the PT.

($Re(Z_{\mathrm{tot}}) = 0$). We call it a *dip signal*.
The axial frequency ω_z is finally measured by fitting ω_z, $\widetilde{A}$, and $\widetilde{\tau}$ to the noise spectrum of a thermalized dip signal, using eq. (3.53) as the line-shape model. Before the resonator parameters Q, ω_{res}, $\widetilde{u}_n^{\mathrm{ampl}}$, and $\widetilde{\kappa}_{\mathrm{det}}$ have been fixed, by fitting the resonator line-shape in eq. (3.37) to the detected noise spectrum of the resonator without any ion. It is remarkable, that the axial frequency, derived by the axial dip fit, is not shifted by the image current effect, introduced in eq. (3.41).
The -3 dB width of the dip $\Delta\nu_z$ is correlated with the cooling time constant of the ion τ and the number of ions, N[1], in the trap [128]:

$$\Delta\nu_z = \frac{N}{2\pi}\frac{1}{\tau}. \tag{3.54}$$

The uncertainty of the measured axial frequency due to the fitted resonator parameters will be discussed in section 4.3.2.

3.2.4 The Image Charge Shift

At the end of this section, I focus on the additional electric field, generated by the induced image charges on the inner electrode surfaces. Due to the intrinsic axial symmetry, only the two radial motions are modified by its back action on the trapped ion. Already in 1989 this effect, the so-called *image charge shift*, has been experimentally determined by Robert S. Van Dyck Jr. and colleagues. In a compensated hyperbolic Penning trap, they measured the number dependency (1-1000 ions) of the radial eigenfrequency shifts of various ions with a relative uncertainty of 17% [129]. Assuming the electrode surfaces as an infinite cylinder Harmut Häffner calculated this effect in the course of his thesis [128]:

$$\delta\nu_{\pm} \approx \mp\frac{m_{\mathrm{ion}}\omega_c}{4\pi\varepsilon_0 r^3 B_0^2}, \tag{3.55}$$

where r is the trap radius and B_0 is the homogeneous magnetic field. Applying the invariance theorem 3.24, also the measured free cyclotron frequency is shifted.
In 2013 Martin Kretzschmar and Sven Sturm evaluated the image charge shift for a single hydrogenlike ion in our present Penning trap [130]:

$$\frac{\delta\nu_c}{\nu_c} = 1.92\frac{m_{\mathrm{ion}}}{8\pi\varepsilon_0 r^3 B_0^2}. \tag{3.56}$$

Here, they considered also the horizontal and vertical slits between the electrodes. The corresponding relative uncertainty has been estimated conservatively to 5%, dominated by the uncertainty of the radial offset of the ion position with respect to the trap center due to patch potentials on the electrode surfaces.
It should be noted, that the image charge shift dominates our present systematic shifts and uncertainties which even increases linearly with the ion mass. Fortunately, the shift scales also with the inverse cubic trap radius, providing in the near future a possible significant

1 Only thermalized ions of equal species contribute to the dip signal.

reduction of this effect by using a larger trap, see chapter 7.

3.3 Excitations and Couplings of the Eigenmotions

Several eigenfrequency detection techniques and cooling methods require extrinsically applied oscillating electric fields which modify the state of the ion's eigenmotions. In this section fundamental properties of the dipole, quadrupole and LC excitations[1] are introduced.

3.3.1 The Dipole Excitation

A dipole excitation in axial direction acts with the following force on the ion motion:

$$\vec{F}_{\mathrm{dipol}} = q_{\mathrm{ion}} \begin{pmatrix} 0 \\ 0 \\ 1 \end{pmatrix} A_{\mathrm{dipol}} \sin(\omega_{\mathrm{rf}} t + \varphi_0), \tag{3.57}$$

where A_{dipol} is the amplitude and ω_{rf} is the frequency of the excitation. During the excitation time (the excitation pulse length) this term has to be added as an additional force on the right side of the equation of motion, see eq. (3.3), which describes the axially propagating ion in a Penning trap. Radial dipole excitations either resonantly at $\omega_{\mathrm{rf}} = \omega_+$ or $\omega_{\mathrm{rf}} = \omega_-$ have the same characteristics on the respective eigenmotions as in the axial case.

To perform dipole excitations, additional alternating electric voltages have to be applied on the trap electrodes. For an axial dipole excitation one of the correction or endcap electrodes can be used; for a radial dipole excitation a vertically split electrode has to be chosen.

In fig. 3.9 the axial motion is plotted during a resonant ($\omega_{\mathrm{rf}} = \omega_z$) axial dipole excitation. Depending on the phase relation between the phase of the excited eigenmotion at the starting point of the excitation $\varphi(t_0)$ and the starting phase of the excitation $\varphi_{\mathrm{rf}}(t_0)$ the amplitude immediately increases, if the following phase-relation holds for the excitation and the particle motion: $d\varphi = \varphi(t_0) - \varphi_{\mathrm{rf}}(t_0) = -90°$. Otherwise the motional amplitude firstly linearly decreases, which is called *transient oscillation*, and finally increases in phase with the excitation. A dipole excitation thus can be used to excite the motion and simultaneously to imprint a well-defined phase. During the complete dipole excitation, the phase space of the motion is kept constant. Such a phase space conservation is illustrated in fig. 3.10. Here, the spatial r_+-distributions in the radial x / y plane are indicated as dark gray clouds, before and after the radial dipole excitation pulse at $\omega_{\mathrm{rf}} = \omega_+$.

3.3.2 The Quadrupole Excitation

A quadrupole excitation in the x- and z-direction has the following structure:

$$\vec{F}_{\mathrm{quad}} = q_{\mathrm{ion}} \begin{pmatrix} z \\ 0 \\ x \end{pmatrix} A_{\mathrm{quad}} \sin(\omega_{\mathrm{rf}} t + \varphi_0). \tag{3.58}$$

1 In this context excitation can mean both, real excitation but also deexciation/cooling of an eigenmotion.

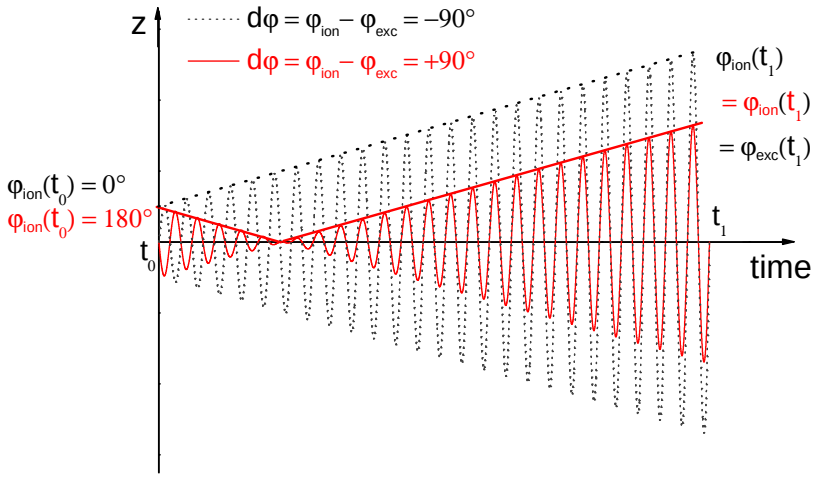

Figure 3.9: Illustration of the axial motion as a function of time, during a resonant axial dipole excitation. In black, the axial eigenmotion and the excitation are initially in phase. In red, they are initially 180° phase shifted. After a short transient oscillation, the axial amplitude linearly increases. In the end of the excitation pulse, the axial phase of the ion always agrees with the phase of the dipole excitation, whereas the amplitudes slightly differ.

Such a field configuration in the z / x plane can be generated via a split endcap or correction electrode. At our experiment, we use one half of the vertically split lower correction electrode, see fig. 3.3(a), which features also small dipole components in the radial and axial directions. These components have been numerically evaluated based on a finite element calculation, using COMSOL [132]:

$$\vec{F}_{\text{quad. real}} \approx q_{\text{ion}} \begin{pmatrix} 64.7 + 38410.1\ \text{m}^{-1} \cdot z \\ 0 \\ 75.7 + 38410.1\ \text{m}^{-1} \cdot x \end{pmatrix} A_{\text{quad}} \sin(\omega' t + \varphi_0). \tag{3.59}$$

In the following, the coupling of the axial and the modified cyclotron motion by a quadrupole excitation is studied in two scenarios: (1) a quadrupole excitation at the upper sideband frequency $\omega_{\text{rf}} = \omega_+ + \omega_z$ and (2) a quadrupole excitation at the lower sideband frequency $\omega_{\text{rf}} = \omega_+ - \omega_z$.

The Upper Sideband ($\omega_{\text{rf}} = \omega_+ + \omega_z$) - A Phase Transfer

A quadrupole excitation in x / z directions at the upper sideband $\omega_{\text{rf}} = \omega_+ + \omega_z$ couples the axial and modified cyclotron motions in the following way: (1) After certain transient oscillations, the amplitudes of both modes increase exponentially. The energy increase can be easily understood on the quantum level. In fig. 3.11(a) the competing processes: the heating process (photon absorption) and the cooling process (stimulated emission) are illustrated. At the upper sideband ($\omega_+ + \omega_z$) the heating process dominates the overall

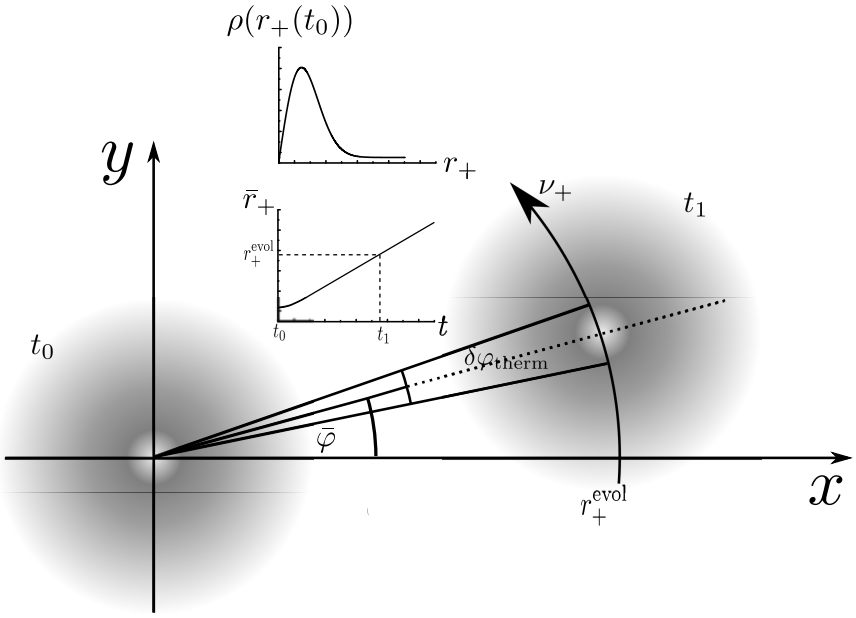

Figure 3.10: Illustration of the spatial r_+-distributions in the radial x/y plane before and after the radial dipole excitation at $\omega_{\text{rf}} = \omega_+$. Since the spread of the thermal r_+-distributions which are represented as dark gray clouds, stays constant, the phase space in the radial plane is conserved during the excitation pulse. In general, the phase-jitter $\delta\varphi_{\text{therm}}$ decreases with an increasing excitation radius r_+^{exc} or a smaller (cooler) radial starting distribution [131].

dynamics, which can be directly derived from the creation and annihilation operators of the quantum harmonic oscillator[1]. (2) Depending on the initial amplitude relation, the motional phase of one mode can be transferred into the other mode, e.g. in the case of $r_+^{\text{init}} > z^{\text{init}}\sqrt{\nu_z/\nu_+}$, the initial modified cyclotron phase is transferred into the axial phase. The combination of both properties - mode amplification and simultaneous phase transfer - triggered the development of a phase-sensitive detection technique of the modified cyclotron frequency at very low energies. This technique, the so-called PnA method, has been developed by Sven Sturm in 2011 [58] and will be introduced and studied in section 3.4.2. Detailed information on the underlying differential equations and corresponding solutions are also given in [58].

The Lower Sideband ($\omega_{\text{rf}} = \omega_+ - \omega_z$)

The coupling of the lower modified cyclotron sideband ($\omega_+ - \omega_z$) and in analogy also the coupling of the the upper magnetron sideband ($\omega_- + \omega_z$) provide three essential applications: (1) cooling of the two radial modes, (2) measurements of both radial eigenfrequencies and (3) measurement of the axial temperature. In the following all three applications are explained.

1 Creation operator: $a_n^\dagger |n\rangle = \sqrt{n+1}\,|n+1\rangle$ and annihilation operator: $a_n |n\rangle = \sqrt{n}\,|n-1\rangle$.

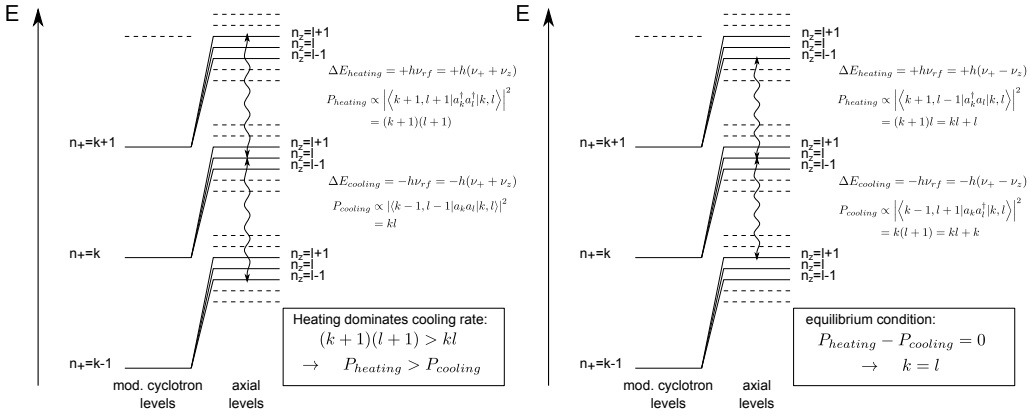

Figure 3.11: Sideband coupling of the modified cyclotron and axial mode. Transition rates in the quantum level scheme are shown in (a) for the upper sideband ($\omega_{\mathrm{rf}} = \omega_+ + \omega_z$) and in (b) for the lower sideband ($\omega_{\mathrm{rf}} = \omega_+ - \omega_z$). In (a) the heating rate dominates. In (b) the cooling and heating rate converge to equal quantum numbers.

Sideband Cooling

For the cooling of the axial mode, the resistive cooling method has been introduced already in section 3.2.3. In principle, also the modified cyclotron mode can be cooled in this way, by using a properly tuned radial resonator. However, resistive cooling cannot be applied to the magnetron mode, since it is metastable. Reduction of the ion's magnetron energy would result in an increase of the magnetron radius until the ion would be lost by hitting the surface of the ring electrode.

In [119] and [133] the quadrupole coupling of one of the radial and the axial motion, e.g. at the sum frequency $(\omega_z + \omega_-)$, a radio frequency (rf), is described in detail. We apply this so-called *rf-sideband cooling* technique also for the modified cyclotron mode, as our low Q cyclotron resonator, see section 4.1.5, has a very large cooling time constant of several 100 seconds $\tau_{\mathrm{cycl}} = 415(100)$ s.

In the quantum mechanical picture which is illustrated in fig. 3.11(b) the generated rf-photon at the frequency $(\nu_+ - \nu_z)$ interacts with the trapped ion in two different ways: (1) It is absorbed by decreasing the axial quantum number by 1 and at the same time increasing the mod. cyclotron quantum number by 1. (2) The photon causes a spontaneous emission by increasing the axial quantum number by 1 and at the same time decreasing the mod. cyclotron quantum number by 1. The two competing rates tend to a convergence of the two quantum numbers: $\langle n_+ \rangle = \langle n_z \rangle$. For the respective equilibrium energies the following relation holds:

$$\langle E_+ \rangle = h\nu_+ \left(\langle n_+ \rangle + \frac{1}{2} \right) = h\nu_+ \left(\langle n_z \rangle + \frac{1}{2} \right) = \frac{\nu_+}{\nu_z} h\nu_z \left(\langle n_z \rangle + \frac{1}{2} \right) = \frac{\nu_+}{\nu_z} \langle E_z \rangle . \quad (3.60)$$

During the complete sideband coupling process the axial mode is kept in thermal equilibrium with the axial resonator via resistive cooling. Only in that way, motional energy of the ion

can be dissipated and also the modified cyclotron mode becomes thermally (Boltzmann) distributed. The temporal dynamics between the rf-sideband coupling and the axial resistive cooling process has been studied in the thesis of José Verdú [118]. The final temperature relation between the two modes is:

$$T_+ = \frac{\nu_+}{\nu_z} T_z. \tag{3.61}$$

A similar relation also holds for the magnetron cooling at the upper sideband ($\omega_z + \omega_-$):

$$\langle E_- \rangle = k_B T_- = \frac{\nu_-}{\nu_z} \langle E_z \rangle = \frac{\nu_-}{\nu_z} k_B T_z. \tag{3.62}$$

Measurement of the Radial Eigenfrequencies
In case both modes, the axial and the modified cyclotron mode, are cold[1], continuous rf-sideband coupling can be used to determine the radial eigenfrequencies by the axial resonator. Considering a resonant coupling at $\nu_{\mathrm{rf}} = \nu_+ - \nu_z$, the system can be regarded in a semiclassical approach as a two-level system[2] interacting with a radiation field, the quadrupole excitation. During the rf-sideband coupling, the energy of both modes is permanently transferred between the two levels and oscillates with the Rabi frequency Ω_0, which depends on the excitation amplitude. Similar to the ac Stark splitting in quantum optics, the initial axial state becomes a superposition of two dressed states due to the modulation of the axial amplitude [134][3]:

$$\begin{aligned} z(t) &= z_0 \sin\left(\omega_z t + \varphi_z\right) \sin\left(2\pi \frac{\Omega_0}{2} t + \varphi_{\Omega_0}\right) \\ &= \frac{1}{2}\left[\cos\left(\left(\omega_z - 2\pi\frac{\Omega_0}{2}\right) t + \left(\varphi_z - \varphi_{\Omega_0}\right)\right) - \cos\left(\left(\omega_z + 2\pi\frac{\Omega_0}{2}\right) t + \left(\varphi_z + \varphi_{\Omega_0}\right)\right)\right], \end{aligned} \tag{3.63}$$

where φ_z and φ_{Ω_0} are some initial phases. In that way, the axial noise dip at ν_z, splits into two dips, with the frequencies: $\nu_{\mathrm{l(eft)}} = \nu_z - \Omega_0/2$ and $\nu_{\mathrm{r(ight)}} = \nu_z + \Omega_0/2$. Such a double-dip spectrum is shown in fig. 3.12. Considering a small detuning δ in the rf-sideband coupling frequency: $\nu_{\mathrm{rf}} = \nu_+ - \nu_z + \delta$ the Rabi frequency is modified $\Omega' = \sqrt{\Omega_0^2 + \delta^2}$ and the two dressed states are not any longer symmetric with respect to the original state, but also shifted: $\nu_{\mathrm{l}} = \nu_z - \delta/2 - \Omega_0/2$ and $\nu_{\mathrm{r}} = \nu_z - \delta/2 + \Omega_0/2$. This effect is often denoted as avoided crossing. Measuring in a double-dip spectrum ν_l, ν_r at a coupling frequency $\nu_{\mathrm{rf}} = \nu_+ - \nu_z + \delta$ and measuring before or afterwards the axial frequency ν_z, the modified cyclotron frequency can be determined:

$$\nu_+ = \nu_{\mathrm{rf}} - \nu_z + \nu_l + \nu_r. \tag{3.64}$$

1 A mode is denoted as *cold*, when it has been thermalized by the axial resonator.
2 One level: Motional energy is maximal in the axial mode, minimal in the modified cyclotron mode. Other level: Motional energy is minimal in the axial mode, maximal in the modified cyclotron mode.
3 $z(t)$ is modulated with the frequency $\Omega_0/2$, since the energy, $E_z \propto z(t)^2$, oscillates with Ω_0.

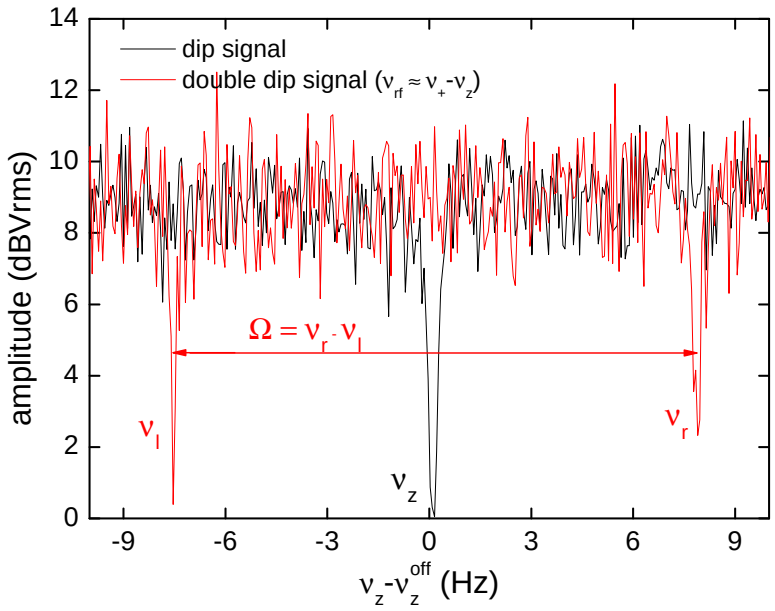

Figure 3.12: Illustration of the continuous sideband coupling at $\nu_{\mathrm{rf}} = \nu_+ - \nu_z$, when both modes are cool. In black, the normal axial dip signal is plotted, which splits into two dips seperated by the Rabi frequency Ω. From the red double-dip spectrum, ν_l and ν_r are measured. In combination with the axial and the coupling frequency, the modified cyclotron frequency can be determined, see text.

It is remarkable, that this relation does not depend on the small detuning δ. In a similar way, also the magnetron frequency can be measured by an axial double-dip spectrum, coupling the axial and magnetron mode at the upper sideband $\nu_{\mathrm{rf}} = \nu_- + \nu_z$:

$$\nu_- = \nu_{\mathrm{rf}} + \nu_z - \nu_l - \nu_r. \tag{3.65}$$

Temperatures of the Eigenmodes and Special Relativity
Regarding a thermalized ion, where all three eigenmodes have been cooled by the axial resonator, the relation between the averaged energies and the corresponding temperatures have been given in eq. (3.44) , eq. (3.61) and eq. (3.62). Relying on eq. (3.5), the square root of the averaged squared maximal axial amplitude is: $< z >\equiv \sqrt{< z_0^2 >} = \sqrt{\frac{k_B T_z 2}{m\omega_z^2}}$. The corresponding averaged radii are given by $< r_+ >= \sqrt{\frac{\nu_z}{\nu_+}} < z >$ and $< r_- >= \sqrt{\frac{2\nu_-}{\nu_z}} < z >$ $= \sqrt{\frac{\nu_z}{\nu_+}} < z >$. For a single $^{12}C^{5+}$ ion in the precision trap the temperatures, averaged energies, averaged amplitude/radii and averaged quantum numbers are summarized in table 3.5. The related measurement method will be explained in section 4.3.2. The con-

Table 3.5: Temperatures, averaged energies, averaged amplitude/radii and averaged principle numbers for $^{12}C^{5+}$ of all three eigenmodes for a single $^{12}C^{5+}$ ion, thermalized by the axial resonator in the PT.

	axial	mod. cycl.	magnetron
temperature (K)	5.44(22)	195(8)	-0.076(4)
amplitude (µm)	21(1)	3.4(1)	3.4(1)
energy (meV)	0.47(2)	16.8(7)	-0.0065(3)
quantum number	170800	170800	170800

verged averaged quantum number of about 170800 justifies a classical treatment of the ion motion. For an axial frequency of 671 kHz the ground-state of the axial motion would require a temperature of $T_z = 16\,\mu K$.

In consideration of the typical energy range, we briefly estimate the impact of the relativistic mass increase. Eigenfrequency shifts due to special relativity have been studied for example in [135] and [119]. Here, we are not interested in the respective relativistic shifts of eigenfrequencies, but in the correction of the free cyclotron frequency:

$$\frac{\delta\nu_c}{\nu_c} = -\frac{\delta m_{\text{ion}}}{m_{\text{ion}}} = -\frac{v^2}{2c^2} \approx -\frac{(\omega_+ r_+)^2}{2c^2} = -\frac{E_+}{m_{\text{ion}}c^2}. \tag{3.66}$$

The velocity of the ion can be approximated to the velocity of the modified cyclotron motion, since for example for a cold $^{12}C^{5+}$ ion:

$$v_+ = 520\,\text{m/s} \gg v_z^{max} = 87\,\text{m/s} \gg v_- = 0.20\,\text{m/s}. \tag{3.67}$$

Although these velocities are quite slow and for a cold $^{12}C^{5+}$ ion also the shift is small ($\delta\nu_c/\nu_c = 1.5 \cdot 10^{-12}$), relativistic corrections will be significant in measurement processes, working with an excited ion, see section 5.1.

3.3.3 LC-Excitation - Electronic Feedback

In addition to the dipole and quadrupole excitation, we use a third excitation type to manipulate the energy of the ion by electronically modifying the temperature and the position of the axial resonator. In the course of the development of the axial ultra-low noise amplifiers, which had a diminutive back-action on the trapped ion, Sven Sturm introduced an active electronic feedback technique at our experimental setup [13]. As depicted in fig. 3.13, active electronic feedback is generated in three steps: (1) In the beginning, the thermal noise of the resonator is amplified in the same way as for the signal detection. (2) In the room temperature region the phases are shifted and the amplitudes are attenuated. (3) Finally, the modified signal is capacitively fed back to the resonator.
In fig. 3.14(a) the dependency of the resonators position and its quality factor is demonstrated for different phase shifts at a fixed attenuation.
In the following three different feedback types are discussed enabling different applications:

- At a phase shift of 180°, also stated as *negative feedback*, the thermal noise level of

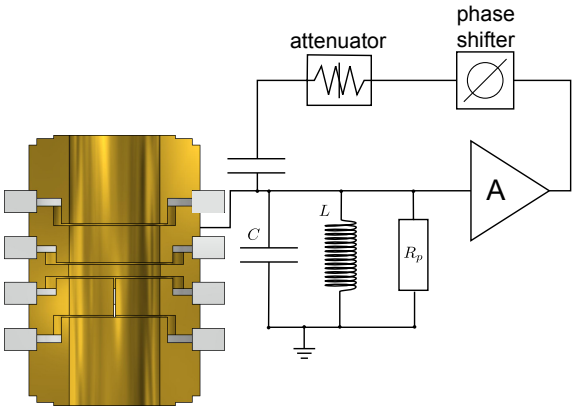

Figure 3.13: Lumped circuit of the feedback loop. For details see text.

the resonator and thus the quality factor decreases, enabling in the AT a 10-fold reduction of the effective temperature of the axial resonator, see thesis of Sven Sturm [13]. The lower temperature limit is given by the electronic noise of the amplifier. In that way, axial ion temperatures in the Kelvin or sub-Kelvin regime are accessible.

- The previous effect can also be reversed, by applying so-called *positive feedback* at a 0° phase shift. Here, the quality factor of the resonator increases, resulting in a stronger coupling of the trapped ion. The enhanced width of the dip-signal enables a faster detection process of the axial frequency. In fig. 3.14(b) the axial AT resonator is shown at different positive and negative feedback strengths.
- At a phase shift of ±90° the quality factor stays constant and the AT resonator can be shifted up to a few line-widths, see fig. 3.14(c). This effect can be understood as a modification of the effective parallel capacitance of the resonator. That way, the cooling time constant of the trapped ion, which is initially in resonance with the resonator, can be significantly enhanced. In the case of a single $^{12}C^{5+}$ ion, the cooling time can immediately be extended by a factor of 15, from ≈ 0.1 s to ≈ 1.5 s, see fig. 3.14(d) without adjustments on the trapping potential.

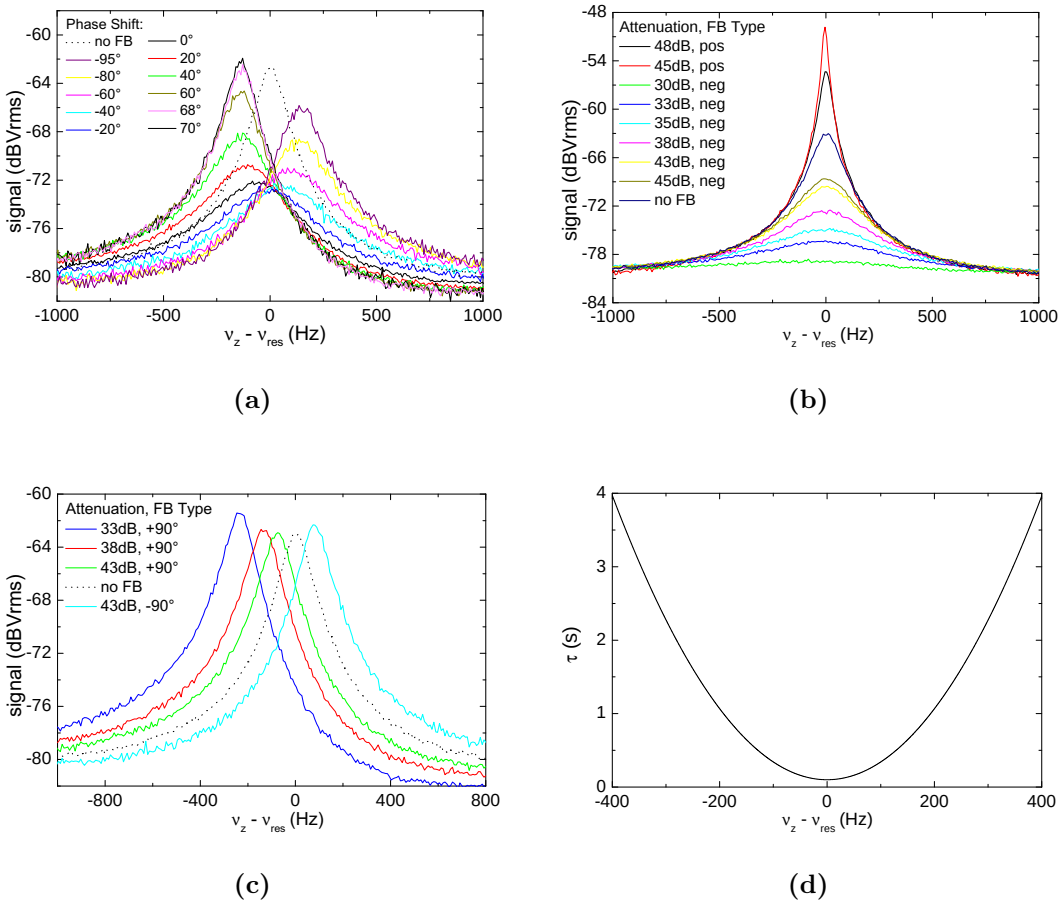

Figure 3.14: Characteristics of the electronic feedback (FB) in the AT ($\nu_{\mathrm{res}} = 411840$). (a) Feedback at different phases and a fixed attenuation. (b) Positive and negative feedback for different attenuations. (c) Illustration of the resonator shift at $\pm 90°$ feedback for different attenuations. (d) Cooling time constant of a single $^{12}C^{5+}$ ion in the AT as a function of the axial frequency with respect to the resonator frequency. Applying 90° feedback, the cooling time constant can be extended without changing the electric trapping potential. For details see text.

3.4 Various Non-Thermalized Eigenfrequency Detection Methods

Up to now, I introduced the dip and the double-dip detection methods, for the determination of the three eigenfrequencies in a Penning trap. These techniques are operated in thermal equilibrium with the axial resonator. Negelecting cooling techniques of the modified cyclotron mode which further reduce the modified cyclotron temperature either by using a cyclotron resonator or laser cooling, the double-dip technique features the smallest energy dependent systematic shifts of all known detection methods in a Penning trap. Nevertheless, a large disadvantage is given by the inevitable time consuming measurement process. Here, one has to average over the Johnson noise of the resonator, which has the following unfavorable scaling with the measurement time t_m : $\delta u_n/u_n \propto 1/\sqrt{t_m}$. We set the measurement time of the axial dip of a single $^{12}C^{5+}$ ion to 3 min to clearly resolve the dip signal. In several situations, faster measurement techniques are preferred, which will be introduced in this section.

3.4.1 Axial Peak Detection

The most straightforward way to detect the axial frequency in an alternative approach to the dip measurement is the frequency detection of the peak signal of the axially excited ion, as represented in fig. 3.15 by the black line. The appropriate measurement sequence is the following: (1) The cold ion is axially excited by a short (≈ 10 ms) dipole pulse at $\nu_{\mathrm{rf}} \approx \nu_z$. (2) Directly thereafter the signal is read out and the axial frequency is extracted from the maximum of the Fourier spectrum. For the detection of a large peak signal, the readout signal length should not be longer than a few cooling time constants; in the PT we usually choose readout times of typically 0.5 to 1 s.
Aiming for a better frequency resolution than by just choosing the frequency-bin with the maximal signal, we use advanced FFT analysis techniques, e.g. zero-padding [136].

Zero-Padding

For a better understanding of zero padding, I will introduce some essential technical details of the frequency analysis. Before we perform the Fourier transformation, we down-mix the axial signal from the several 100 kHz range into the low frequency (audio) range of 0 to 28 kHz. Subsequently the signal is sampled with a sample-rate of $\nu_s = 1/\Delta t = 64$ kHz (total bandwidth), so that we receive a discrete time representation. Then, we apply a fast Fourier transformation (FFT), which is a widely used, very efficient numerical method to calculate a discrete Fourier transform (DFT). The frequency bin-width $\Delta\nu_{\mathrm{bin}}$ of the DFT is the inverse of the total sample time, which in general agrees with the signal length T_s. This binned frequency resolution of $\Delta\nu_{\mathrm{bin}}$ can be improved by the so-called *zero padding*, where a series of zeros is added to the raw signal already in the time domain. By doing so, the total sample time is increased and in that way the frequency bin-width is reduced. In a hand-waving explanation, zero padding can be understood as an advanced interpolation process. Increasing the number of zeros, the Fourier spectrum converges to a sinc-function, the Fourier transform of a rectangular-function, see also fig. 3.15. In particular, this technique improves the frequency resolution in comparison to $\Delta\nu_{\mathrm{bin}}$, if the frequency-bins in the vicinity of the frequency-bin with maximal signal also contain signal information. This effect is often called frequency *bleeding*.

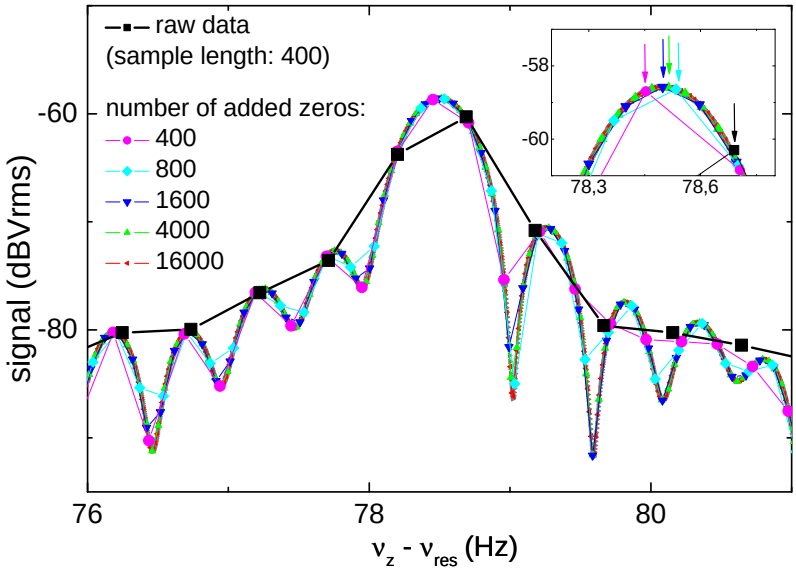

Figure 3.15: Peak signal of a single $^{48}Ca^{17+}$ ion in the AT without (black line) and with zero-padding (other lines). The arrows in the inset indicate the respective maximum, and in that way the determined frequency.

However, due to the fast thermalization of the ion, the precision of such a peak detection has strong limitations. Furthermore, absolute frequency measurements by peak detection are highly unfavourable due to the large energy dependent shifts.

Signal-to-Noise Ratio of a Dip and a Peak Signal

For a quantitative characterization of the quality of a detection system the signal-to-noise ratio (SNR) is widely used. Depending on the choice of the detection method (dip or peak), the optimization of the SNR places different conditions on the axial detection system.

- In case of an axial dip measurement, the detected signal is given in a quiet curious way by the Johnson noise of the resonator, see eq. (3.35). The appropriate noise level, which limits the depth of the dip, is dominated by the voltage noise of the amplifier, u_n^{ampl}. Considering an ion tuned to the resonator, $\nu_z = \nu_{\text{res}}$, the corresponding SNR:

$$\text{SNR}_{\text{dip}} \approx \frac{\sqrt{4k_B T R_p}}{u_n^{\text{ampl}}} \tag{3.68}$$

  can be enhanced in three independent ways: (1) The quality factor, which is proportional to the parallel resistance, could be maximized. (2) The voltage noise of

the amplifier, could be minimized, which has been done by the amplifier design of Sven Sturm: $u_n^{\text{ampl}} = 400\ \text{pV}/\sqrt{\text{Hz}}$ [13]. (3) In principal the temperature could be increased, which, however, is not favourable, since it would cause larger systematic shifts of the eigenfrequencies.

- In case of an axial peak measurement, the SNR is defined as the voltage drop generated by the induced image charges (by the ion) over the thermal noise of the resonator:

$$\text{SNR}_{\text{peak}} \approx \frac{u_{ion}}{u_n} = \frac{q_{\text{ion}}\omega_z\sqrt{R_p t_{sig}}}{D\sqrt{4k_B T}} z_{\text{rms}}, \tag{3.69}$$

where t_{sig} is the signal readout time of about 1 s, see above. Here, I neglect the small voltage noise and current noise contributions of the amplifier, see [13]. Moreover, I still assume an ion in resonance with the resonator $\nu_z = \nu_{\text{res}}$, so that a purely ohmic resistance occurs ($\text{Re}(Z) = R_p$). The SNR_{peak} can be optimized essentially in two ways: (1) The temperature could be decreased. (2) The axial amplitude z_{rms} could be increased, which at some excitation level is limited by the energy dependent shifts, e.g caused by trapping imperfections. It is remarkable, that an increase of parallel resistance ($\propto Q$-value) would not help, since the cooling time constant, which limited the signal readout time, is inversely proportional to the parallel resistance.

3.4.2 Phase-Sensitive Detection Methods

The readout of the axial peak signal does not only provide access to the axial frequency by determining the peak-position in the Fourier spectrum, which has been explained above. Moreover, the complex Fourier spectrum provides also access to the instantaneous phase of the ion, which enables phase-sensitive measurements of the axial frequency. Here, the fundamental measurement principle is the following: From the detection of two subsequent axial phases, $\varphi(t_1)$ and $\varphi(t_2)$, and from the precise knowledge on the elapsed time between these two measurements, also called the *phase evolution time* $T_{\text{evol}} \equiv t_2 - t_1$, the axial frequency can be derived:

$$\nu_z = \frac{\varphi(t_2) - \varphi(t_1)}{360° T_{\text{evol}}}. \tag{3.70}$$

Such a phase-sensitive measurement has two major advantages in comparison to the dip measurements:

1. The relative uncertainty of the frequency features an optimal inverse scaling with the measurement time T_{evol}:

$$\frac{\delta\nu}{\nu} = \frac{\delta\varphi}{360° \ \nu \ T_{\text{evol}}}. \tag{3.71}$$

Here, $\delta\varphi = \sqrt{(\delta\varphi(t_1))^2 + (\delta\varphi(t_2))^2}$ is the phase uncertainty, often also called *phase jitter*.

2. In general, we derive the phase from the FFT-bin with the largest amplitude, so that

we do not require a line-shape model for some fitting routine, as it is the case for a dip spectrum. In this way, model dependent systematic shifts and uncertainties are avoided.

In the following two different phase-sensitive detection techniques are introduced.

Phase-Sensitive Detection of Axial Frequency Fluctuations

Temporal axial frequency fluctuations or small ν_z-shifts can be determined by a subsequent repetition of the following measurement process, which is also illustrated in fig. 3.16: (1) In the beginning, the phase of the axial ion motion is set by a short dipole excitation, which at the same time also excites the axial motion. The so-called *imprinted phase* is

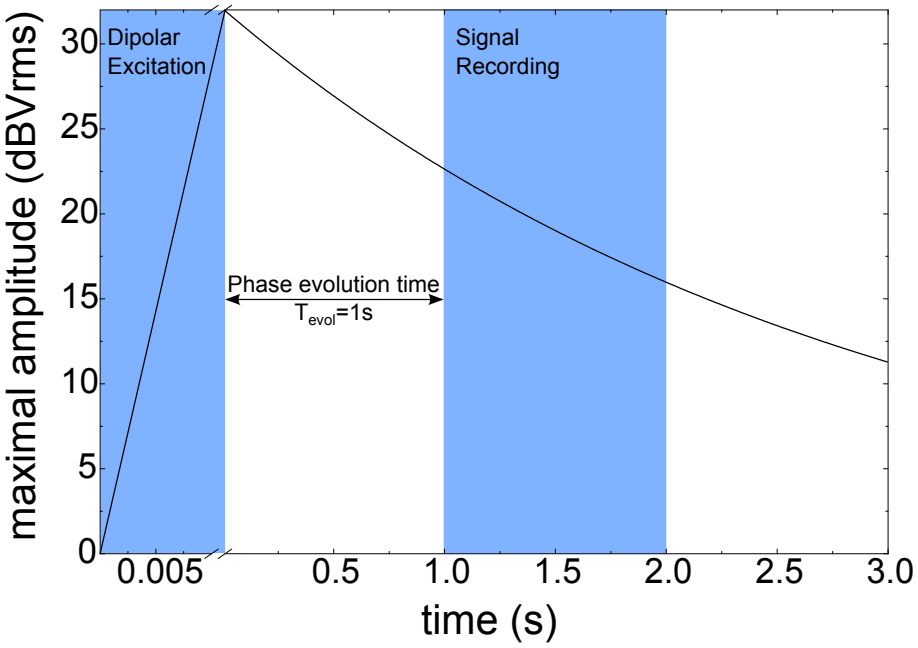

Figure 3.16: Axial phase detection scheme. During the axial dipole excitation pulse of 10 ms the axial amplitude linearly increases and the phase is imprinted. Immediately after the excitation the amplitude decreases exponentially caused by the thermalization with the axial resonator. After a phase evolution time of 1 s the signal is read out and the axial phase is extracted from the complex Fourier transformation. The indicated amplitudes and cooling time constant correspond to a $^{40}Ca^{17+}$ ion in the AT.

mainly given by the pulse length and the starting phase of the dipole excitation, see fig. 3.9 Aside from an intrinsic thermal phase jitter, which will be discussed in section 4.5.1, such a phase imprint is a highly reproducible process. (2) The axial phase freely evolves with the present axial frequency for a fixed time T_{evol}. (3) Finally, the peak signal is read out and the phase is extracted from the complex Fourier spectrum.
Subsequent repetitions of exactly the same measurement process enable the determination of frequency differences:

$$\Delta\nu = \frac{\Delta\varphi}{360^\circ\, T_{\mathrm{evol}}}. \tag{3.72}$$

In contrast to eq. (3.70), here, we do not measure the phase difference of the starting and the end phase, since we can set the starting phase, but we do not know its value. Instead, we consider the phase difference $\Delta\varphi$ of two subsequent measurement cycles.
A small frequency uncertainty requires a long phase evolution time, which in this case is limited in two different ways: (1) A proper phase detection requires a large SNR, which decreases with time due to the permanent resistive cooling. However, the cooling time constant can be enhanced by adjusting the ions on the wings of the thermal resonator spectrum and not on the resonator centre, see also fig. 3.14. (2) Unfortunately the complex Fourier spectrum does not deliver the absolute phase of the ion: $\varphi_{\mathrm{abs}} = \omega_z T_{\mathrm{evol}}(180°/\pi)$, but the phase modulo 360° [1]:

$$\varphi_{\mathrm{meas}} = \varphi_{\mathrm{abs}} - n \cdot 360°, \tag{3.73}$$

where $n \in \mathbb{N}$ is the phase evolution number. To prevent phase ambiguities, great care has to be taken, that at long and fixed phase evolution times, the phase fluctuations in subsequent measurement cycles are smaller than ±180° or, in other words, that the fluctuations of the phase evolution number are well below one.

Phase-Sensitive Detection of the Modified Cyclotron Frequency

Using the invariance theorem, see eq. (3.24), the three eigenfrequencies contribute with different relevances to the uncertainty of the free cyclotron frequency. Based on their different sizes, for $^{12}C^{5+}$ see table 3.3, the contribution of the modified cyclotron frequency uncertainty is $\nu_+/\nu_z \approx 36$ times larger than the contribution of the axial frequency uncertainty and even $\nu_+/\nu_- \approx 2576$ times larger than the contribution of the magnetron frequency uncertainty. For this reason the modified cyclotron frequency has to be measured with the highest precision. For a fast detection of the modified cyclotron frequency at low energies, a dedicated phase-sensitive technique, the PnA (Pulse and Amplify) method, is used [58].
In the following, I introduce the central building block of this method, the five-step *PnA-cycle*, which is illustrated in fig. 3.17.

1. **First PnA pulse:** Starting with a thermalized ion, the phase of the modified cyclotron motion is set by a short (10 ms) radial dipole excitation at the expected modified cyclotron frequency, $\nu_{\mathrm{rf}} \approx \nu_+$, so that in each PnA-cycle the ion has the same imprinted modified cyclotron phase. An illustration of the phase space dynamics during the first PnA pulse has been shown in fig. 3.10.
2. **Phase evolution time:** In the following, the modified cyclotron mode is completely decoupled from any detection system. The phase of this mode freely evolves for a phase evolution time T_{evol} of typically 5 s at a motional radius of $r_+^{\mathrm{evol}} \approx 13$ µm or larger.
3. **Second PnA pulse:** Subsequently, a quadrupole pulse at the expected upper sideband, $\nu_{\mathrm{rf}} = \nu_+ + \nu_z$, parametrically excites the axial and the modified cyclotron mode

1 In this thesis, phases will always be denoted in degree and not in radian.

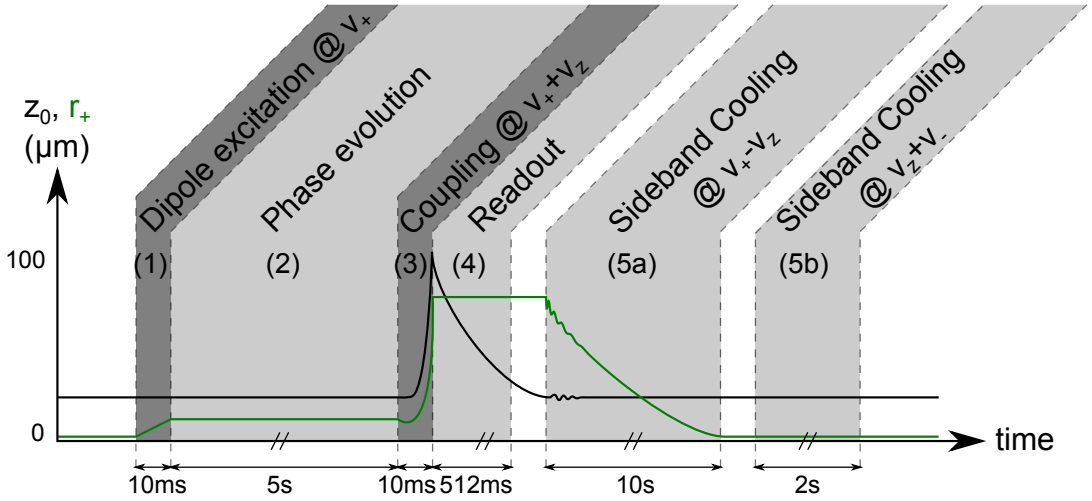

Figure 3.17: Schematic of the phase-sensitive detection technique PnA (Pulse and Amplify) [58]. The five-step PnA-cycle is illustrated by the progressions of the axial amplitude (black line) and the modified cyclotron radius (green line) [131]. For details see text.

for about 10 ms. If at the beginning of the second PnA pulse $r_+^{\text{evol}} > z\sqrt{\nu_z/\nu_+}$, the phase information of the modified cyclotron mode is transferred into the phase of the axial mode during the pulse. Simultaneously both amplitudes increase exponentially. Detailed information, e.g. the differential equations and the corresponding solutions, are given in [58]. The phase space dynamics of the second PnA pulse is illustrated in fig. 3.18.

4. **Signal readout:** Right after the second pulse, the excited ion is detected as an axial peak signal above the thermal noise spectrum of the axial resonator. The readout time is typically 512 ms, which corresponds roughly to two times the axial cooling time constant of a $^{12}C^{5+}$ ion. From the complex amplitudes of the Fourier transform, we determine the axial phase of the ion, which contains the modified cyclotron phase information.

5. **Cooling:** Finally, both radial modes are thermalized via rf-sideband couplings to the axial resonator. For the modified cyclotron mode, $\nu_{\text{rf}} = \nu_+ - \nu_z$, the coupling time is of the order of 10 s and for the magnetron mode, $\nu_{\text{rf}} = \nu_- + \nu_z$, the coupling time is about 2 s.

As previously explained, a phase-sensitive frequency determination requires at least two phase measurements at two different point of times. Here, the starting phase is measured with very short evolution times of $T_{\text{evol}}^{\text{start}} = 10\,\text{ms}$. At these short time scales, magnetic field fluctuations, which dominate the phase jitter on long time scales, are negligible with respect to the intrinsic sources of phase jitter: the thermal and the readout jitter, which will be introduced and analyzed in section 4.5.1. We repeat these 10 ms-PnA-cycles six times, to reduce the statistical uncertainty of the starting phase. As the frequency uncertainty scales inversely with the measurement time $T_{\text{evol}}^{*} = T_{\text{evol}}^{\text{final}} - T_{\text{evol}}^{\text{start}}$, the phase evolution time

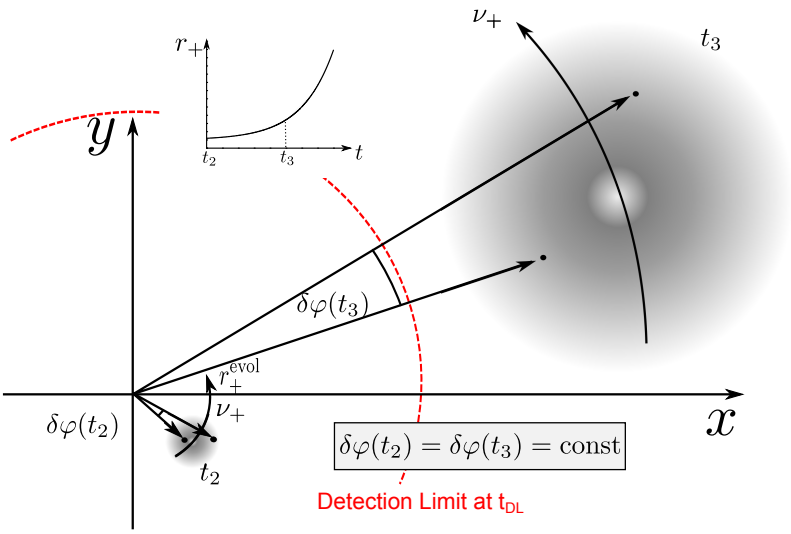

Figure 3.18: Radial phase space dynamics of the second PnA pulse. The small cloud at a radius r_+^{evol} indicates the phase space distribution after the phase evolution. During the second PnA pulse at $\nu_{\mathrm{rf}} = \nu_+ + \nu_z$, the modified cyclotron radius and the axial amplitude increase exponentially and the phase-spread scales with r_+, so that no additional phase jitter arises. If $r_+^{\mathrm{evol}} > z\sqrt{\nu_z/\nu_+}$, the phase information of the modified cyclotron mode is transferred into the axial mode. The inset illustrates the exponential increase of the modified cyclotron radius during the second PnA pulse. For more details, see text.

$T_{\mathrm{evol}}^{\mathrm{final}}$ of the second phase measurement should be as long as possible.
Since phases can only be determined modulo a factor of 360°, an appropriate phase unwrapping is required to determine the absolute phase: $\varphi_{\mathrm{abs}} = n \cdot 360° + \varphi_{\mathrm{meas}}$, where n is an integer. With the knowledge of ν_+ from a previous *double-dip* measurement and the starting phase from the 10 ms-PnA cycles, the phase evolution number, n, can be predicted for longer phase evolution times:

$$n(T_{\mathrm{evol}}^*) = \left[\varphi_{10\ \mathrm{ms}} + 360° \cdot \nu_+^{\mathrm{DD}} \cdot (T_{\mathrm{evol}}^* - 10\ \mathrm{ms})\right] /360°. \tag{3.74}$$

For a proper phase unwrapping the predicted uncertainty of the phase evolution number should be well below 1, see fig. 3.19. In this plot the gray band illustrates the extrapolated phase evolution number uncertainty in dependence of the phase evolution time, given by six 10 ms-PnA-cycles and the frequency uncertainty from a previous 3 min double-dip measurement. This estimated phase uncertainty is subsequently reduced by PnA cycles with phase evolution times of 1 s (cyan), 2 s (red) and 5 s (green). For example at a phase evolution time of 5 s the uncertainty δn based on the uncertainties of ν_+^{DD} and $\varphi_{10\ \mathrm{ms}}$ (gray band) is roughly halved by the 2 s PnA measurement (red band). The maximal phase evolution time and thus the frequency uncertainty are limited by magnetic field fluctuations, which cause a significant probability for phase unwrapping errors ($3{\cdot}\delta\varphi > 180°$) at phase evolution times larger than 8 s. In fig. 3.19 magnetic field fluctuations have been

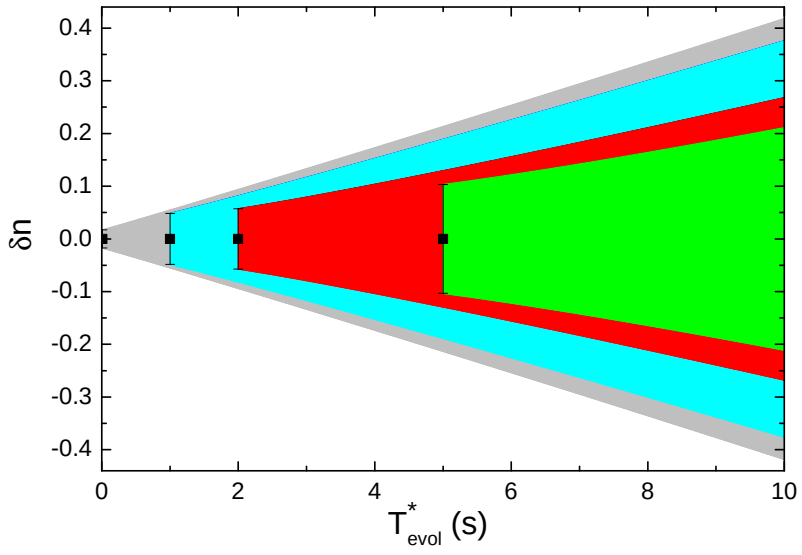

Figure 3.19: The principle of phase unwrapping. The colored error-bands illustrate the uncertainty of the phase evolution number δn as a function of the phase evolution time. The gray band is determined by the phase uncertainty of the six 10 ms-PnA-cycles and the frequency uncertainty from a previous 3 min double-dip measurement. This extrapolated δn is subsequently reduced by PnA phase measurements with phase evolution times of 1 s (cyan), 2 s (red) and 5 s (green). For further details see text.

also considered, resulting in a slight non-linear increase of the phase evolution number uncertainty.Such fluctuations will be separately analyzed in section 4.5.1.
In comparison to the double-dip measurement of ν_+, which requires a long averaging time of about 3 min and reaches a relative Allan deviation of $\delta\nu_+/\nu_+ = 2 \cdot 10^{-9}$, the PnA method requires only a measurement time of 5-10 s[1] to reach an exceptionally small relative Allan deviation of $\delta\nu_+/\nu_+ \approx 5 \cdot 10^{-10}$, see also figure 4.19.
In contrast to the double-dip technique no line-shape model is required. In comparison to other phase-sensitive methods (PnP) [133], the phase evolution proceeds at notably small kinetic energies, leading to significantly smaller systematic shifts [13]. Moreover, considering PnA, systematic shifts linearly depend on the modified cyclotron temperature, which can be decreased by improved cooling techniques for the modified cyclotron mode, e.g. by using a high-Q cyclotron resonator. However, this improvement cannot be used in case of PnP.

1 Here, I neglect the complete preparation time, which comprises the time of the double-dip measurement, the six 10 ms-PnA cycles, the phase unwrapping PnA-cycles (1 s and 2 s) and especially the cooling time of the modes between these cycles.

3.5 Larmor Frequency Determination

In the last section of this introductory chapter on the essential theoretical and methodical knowledge in Penning trap physics, I will introduce a technique to determine the Larmor frequency. Since at the accessible measurement time scale of 5 to 10 s, the relative magnetic field fluctuations are in the order $5 \cdot 10^{-10}$, see section 4.5.1, and the relative resonance-width of a coherent spin-flip excitation of about $1 \cdot 10^{-12}$ is much smaller[1], only an incoherent Rabi-like spin-flip excitation at the sought-after Larmor frequency is possible. For that reason, we measure the spin-flip probability by probing the Larmor transition at different Larmor frequencies ν_{MW} and each time simultaneously determining the magnetic field by measuring the modified cyclotron frequency via PnA. To determine the success of such a spin-flip drive the spin state of the bound electron has to be detected before and afterwards.

3.5.1 The Continuous Stern-Gerlach Effect

Hans Dehmelt developed a technique which he called the *continuous Stern-Gerlach effect* to determine the spin state of a single free or bound electron [137]. In a Penning trap, in our case the analysis trap (AT), see also section 4.1.5, he introduced a strong magnetic inhomogeneity, a so-called *magnetic bottle*, which generates an additional magnetic potential in axial direction:

$$U_{mag} = -\mu_z B_z \approx -\mu_z (B_0 + B_2 z^2), \tag{3.75}$$

where $\mu_z = -g\mu_B s_z/\hbar$ and $s_z = \pm 0.5\hbar$. Here, we only focus on a the dominating leading-order inhomogeneity B_2, which results in a harmonic potential. The resulting axial force:

$$F_{z,B2} = 2\mu_z B_2 z = \pm g\mu_B B_2 z \tag{3.76}$$

depends on the magnetic moment of the electron and thus on its spin state. This harmonic magnetic force sums up with the harmonic electronic trapping force. In this way, the axial frequency slightly depends on the spin state of the bound electron:

$$\omega_z = \sqrt{w_{z,0}^2 \pm \frac{g\mu_B B_2}{m_{\mathrm{ion}}}} \approx \omega_{z,0} \pm \frac{g\mu_B B_2}{2 m_{\mathrm{ion}} \omega_{z,0}}. \tag{3.77}$$

At an axial frequency of 412 kHz and a magnetic bottle of $B_2 = 10.5\ (4) \cdot 10^3\ \mathrm{T/m^2}$ the spin state dependence is of the order of $\Delta\nu_z = \pm 1$ Hz; for more precise numbers see also table 3.6.

For the determination of our magnetic bottle B_2 in the analysis trap, I measured the magnetic field strength at different axial ion positions, see fig. 3.20. Here, a specific burst technique has been applied for the determination of the modified cyclotron frequency in such a large magnetic inhomogeneity. This method has been explained in detail in the

1 For a coherent spin-flip drive at $\nu_L \approx 105$ GHz and a Rabi frequency of 0.1 Hz the relative width of the Rabi resonance is: $(0.1\ \mathrm{Hz}/105\ \mathrm{GHz}) \approx 1 \cdot 10^{-12}$, see also section 4.5.

Table 3.6: Axial frequency jumps in the AT caused by spin-flips, in dependence of the ion species.

ion	$\Delta\nu_z^{\mathrm{sf}}$ [mHz]
$^{12}C^{5+}$	580(20)
$^{40}Ca^{17+}$	170(10)
$^{48}Ca^{17+}$	140(10)

thesis of Anke Kracke [14]. The four asymmetric voltage configurations for the chosen ion

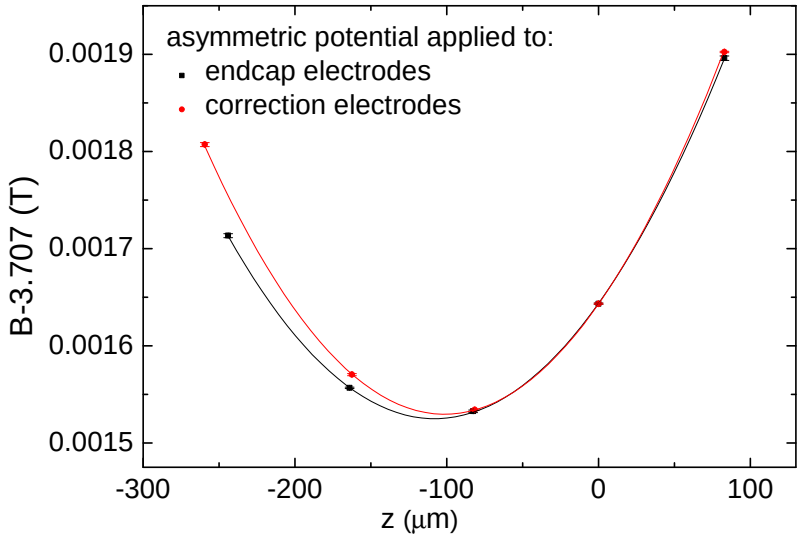

Figure 3.20: Magnetic bottle in the AT to determine the spin state, measured with a single $^{40}Ca^{17+}$ ion. Parabola functions have been fitted to extract the size of the magnetic bottle. For details see text.

positions have been calculated numerically, based on COMSOL simulations. So far, it is not completely understood, why the size of the magnetic bottle slightly depends on the kind of voltage configuration, either applying the asymmetric voltage to the endcap electrodes: $B_2^{\mathrm{endcap}} = 10164\ (70)\,\mathrm{T/m^2}$ or at the correction electrodes: $B_2^{\mathrm{corr}} = 11051(70)\,\mathrm{T/m^2}$. In the following, we use the averaged value of $B_2 = 10.5\ (4)\cdot 10^3\,\mathrm{T/m^2}$, whose uncertainty includes both measured values. Furthermore it is remarkable, that the center of the magnetic bottle is shifted by roughly 100 µm, which is most probably caused by patch potentials on the electrode surfaces.

To determine the spin state, we use two different axial frequency detection techniques, due to the different spin-flip sizes, which inversely scale with the ion mass, see eq. (3.77) and table 3.6:

- For the single $^{12}C^{5+}$ ion the spin-flip is large ($\Delta\nu_z = 580(20)$ mHz), see fig. 3.21, and we determine the axial frequency by measuring the axial peak frequency with zero padding, see section 3.4.1. This technique is very robust and fast.

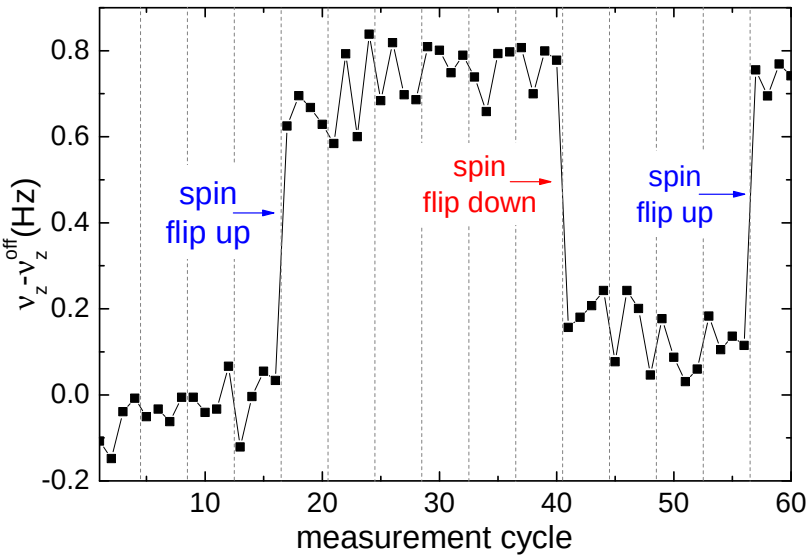

Figure 3.21: Spin-flip detection of a single $^{12}C^{5+}$ ion in the analysis trap. We derive the axial frequency as an average value of four subsequent axial peak measurements. This technique has been introduced in section 3.4.1. Between these blocks of four measurements, at the positions of the gray doted vertical lines, we try to induce spin-flips by a resonant MW-excitation at maximal power. Such a spin-flip drive lasts for 30 s. For a single $^{12}C^{5+}$ ion the axial frequency jump is about 580(20) mHz and can be clearly resolved.

- Due to the heaviness of $^{40}Ca^{17+}$ and especially $^{48}Ca^{17+}$ the axial frequency jumps are particular small, 140 (10) mHz for a $^{48}Ca^{17+}$ ion. Here, we detect the axial frequency jump by measuring subsequently axial phases. This technique has been introduced in section 3.4.2.

3.5.2 Systematic Shifts of the Larmor Frequency

Similar to the frequency shifts of the three eigenmotions, also the Larmor frequency has to be corrected for magnetic inhomogeneities and special realtivity.

Magnetic Imperfections

It is remarkable, that the relative Larmor frequency shift caused by the relevant leading-order magnetic imperfection B_2 is calculated in the same way as for the modified cyclotron frequency, compare with eq. (3.23):

$$\delta\nu_L/\nu_L = \frac{B_2}{B_0 m_{\mathrm{ion}}\omega_z^2}\left(-(\omega_z/\omega_+)^2 E_+ + E_z - 2E_-\right). \tag{3.78}$$

Special Relativity

The effect of special relativity is slightly more complicated than for the free cyclotron frequency, see section 3.3.2, which is completely described in the reference frame of the laboratory. The spin dynamics and thus the formula for the Larmor frequency, see eq. (2.11), is valid in the reference frame of the ion, so that the magnetic field in this reference frame has to be considered. The general formula for a boosted magnetic field is:

$$\vec{B}' = \gamma \left(\vec{B} - \frac{\vec{v} \times \vec{E}}{c^2} \right) - (\gamma - 1) \frac{\vec{B}\vec{v}}{\vec{v}^2} \vec{v}. \tag{3.79}$$

The last term can be neglected since the largest velocity, the velocity of the modified cyclotron motion v_+, see eq. (3.67), is orthogonal to the magnetic field. The second term, which describes a motional magnetic field, is generated mainly by the modified cyclotron velocity and the electric field in radial direction. At the present level of precision it can be neglected, since for example for a single $^{12}C^{5+}$ ion at a temperature of $T_+ \approx 3000\,\mathrm{K}$[1] the radial electric field is $2.7\,\mathrm{V/m}$ [2] and thus such a magnetic field shift is of the order of: $(B_{\mathrm{motional}} - B_0)/B_0 = 7 \cdot 10^{-14}\,\mathrm{T}$. In this approximation, the Larmor frequency in the reference frame of the ion is given by: $\omega_L' = \gamma \omega_L$. Finally, the spin dynamics has to be transformed into the reference frame of the lab to compare with the cyclotron frequency. It is a double Lorentz boost (rotation of electron spin and rotation of the ion), also called *Thomas Precession*, which can be written as, see also [13]:

$$\omega_L = \omega_L'/\gamma + (1-\gamma)\omega_c \approx \omega_L^0 - \beta^2/2\omega_c = \omega_L^0 - \delta\nu_c \qquad \rightarrow \qquad \frac{\delta\nu_L}{\nu_L} = \frac{\delta\nu_c}{\nu_c}\frac{\nu_c}{\nu_L} \tag{3.80}$$

This shift is a factor $\frac{\nu_L}{\nu_c} \approx 4200$ smaller than the relativistic shift of the free cyclotron frequency. In that way the complete relativistic shift does not cancel in the measured frequency ratio Γ.

1 $T_+ \approx 3000\,\mathrm{K}$ corresponds to a typical modified cyclotron radius of $r_+ = 14\,\mu\mathrm{m}$ during the PnA phase evolution time.

2 Calculated by a COMSOL simulation.

CHAPTER 4

Towards the Measurement of the Larmor-to-cyclotron Frequency Ratio

After introducing in the previous chapter 3 the underlying principles of non-destructive high-precision Penning trap measurements with single, highly charged particles, in the present chapter I will focus on our specific experimental setup and the technical information, which are essential for the understanding of the complete high-precision measurement process on the Larmor-to-cyclotron frequency ratio. In section 4.1 I will start with an overview on the experimental setup, where I will briefly summarize the various hardware components. In the subsequent section 4.2 the currently applied stabilization systems will be studied. Here, a special focus is set on superconducting self-shielding coils which reduce the impact of external magnetic field fluctuations. This concept will be extended from a one dimensional compensation of magnetic field fluctuations to a compensation in all three spatial dimensions. Dedicated numerical calculations on transversal self-shielding coils will be presented. In the following section 4.3 all preparatory procedures and measurements are discussed, e.g. the creation process of a single highly charged ion, the optimization of the electrostatic trapping fields, the measurement of the ion temperature and finally the determination of the axial resonator parameters, which are required for the line-shape model of the axial dip signal. Afterwards, in section 4.4, the automated measurement process for the determination of the Γ-resonance is explained step-by-step. In the last part of this chapter, section 4.5, I will discuss the line-shape model of the Γ-resonance. Here, a special focus is set on the various phase jitters of the PnA measurement process.

4.1 Experimental Setup

Almost all components of the current experimental setup which are directly related to the Larmor-to-cyclotron frequency ratio measurement have been designed and assembled by the previous PhD students Birgit Schabinger [138], Sven Sturm [13] and Anke Kracke [14]. Since then, only minor changes have been taken, e.g. a simplification of the technical realization of the PnA method and the implementation of an axial compensation coil by Anke Kracke, see below. However, for a profound understanding of the electron mass determination and the g-factor measurements of the two different calcium isotopes, I will briefly summarize all the relevant experimental features. Here, I start with the outer components and step-by-step approach the heart of the experiment, the triple Penning trap tower.

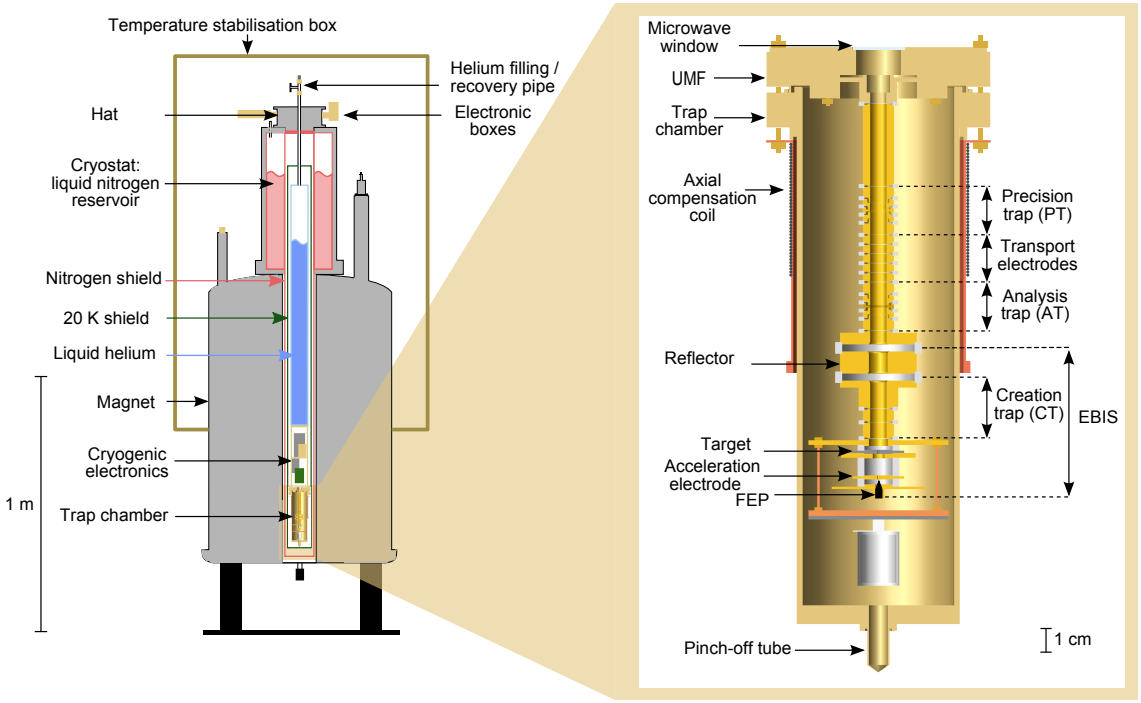

Figure 4.1: Illustration of the experimental setup (modified from [14]). On the left side the superconducting magnet by Oxford Instruments is sketched in gray, including the experimental setup. On the right side, the hermetically sealed, cryogenic trap chamber is shown, which contains the complete trap tower, including the precision trap (PT), the analysis trap (AT) and the creation trap (CT). For details see text.

4.1.1 The Magnet and the Cooling Reservoirs

Some of the larger constituents of the experimental setup, e.g. the magnet, the cooling reservoirs, the microwave waveguides as well as many parts of the experimental stages have been adopted from a collaboration between the former Experimental Particle and Astroparticle Physics (ETAP) group of Günter Werth and the atomic physics division of GSI (Wolfgang Quint, H.-Jürgen Kluge), which performed bound-electron g-factor experiments in the turn of the millennium, see e.g. the doctoral thesis' of Stefan K.-H. Stahl [124], Nikolaus H. Hermanspahn [139], Hartmut Häffner [128] and José Verdú [118]. The homogeneous magnetic trapping field is generated by a superconducting NMR magnet from Oxford Instruments, which has a design field strength of 6 T. The magnet has been ordered and charged by Wolfgang Quint and coworkers in 1995. Since then the superconducting currents deliver a field of nominally 3.76 T in the lower part of its vertical

warm bore of the magnet [1, 2] (bore diameter: 126 mm).
In addition to the superconducting magnet, we also cool the experimental apparatus itself to cryogenic temperatures for a number of reasons:

- In section 4.4 it will be explained, that the high-precision measurement of the Larmor-to-cyclotron frequency ratio requires a trapping time of at least a few weeks. Only the freeze-out of the residual gas at temperatures of a few Kelvin (cryo-pumping of the vacuum) enables to reach eXtremely High Vacuum (XHV) $< 10^{-12}$ mbar. Due to negligible charge-exchange rates with restgas atoms we obtain long storage times of single highly charged ions.
- Furthermore, we cool the ion for essentially two reasons:
  - To reduce the energy dependent systematic frequency shifts and uncertainties, e.g. the dominant frequency shifts due to imperfections of the electric and magnetic fields, see section 3.1.2, or the relativistic corrections, see section 3.3.2, we need to work at small amplitudes.
  - Using phase-sensitive eigenfrequency detection methods, e.g. the PnA method, a cooled thermal amplitude distribution in the beginning of the measurement decreases the phase jitter during the phase imprint, see also fig. 3.10. This temperature dependent phase jitter will be explained and analyzed in section 4.5.1.

  To cool the ion in our experimental apparatus, we exclusively use the resistive cooling technique, introduced in section 3.2.3. Here, the axial motion of the ion thermalizes with the axial resonator, which itself has to be cooled by a thermal bath. In our case, the bath is given by the liquid helium reservoir of the experimental apparatus, see below.

The cooling system of the apparatus includes an outer liquid nitrogen reservoir and an inner reservoir of liquid helium at normal pressure with boil-off temperatures of 77 K for nitrogen and 4.2 K for helium. To reduce the thermal radiation and thus the evaporation rate of the helium, a 20 K-shield is set in a 10^{-7} mbar vacuum between these reservoirs, see fig. 4.1. This shield is only fixed to the filling / recovery pipe of the helium reservoir of the apparatus.

4.1.2 Electronic Components

The complete experimental setup, including the helium reservoir of the apparatus, is placed within the bore of the magnet. Only the so-called *hat flange* of the setup, see fig. 4.2, is mounted on top of the nitrogen cryostat, which itself sits above the magnet, see fig. 4.1. The only stiff connection between the hanging apparatus and the hat flange is given by

1 Replacing the experimental apparatus from the magnet, the inner bore of the solenoid is filled with air and in that way it is *warm*. The cooling of our cryogenic experimental apparatus which is placed within the bore requires additional liquid nitrogen and helium reservoirs.

2 The magnetic field distribution has been measured with a NMR-probe along the symmetry axis (z-axis) of the magnet, see e.g. [14]. The homogeneous field region is generated in the lower part of the vertical bore on an axial section of about 15 cm.

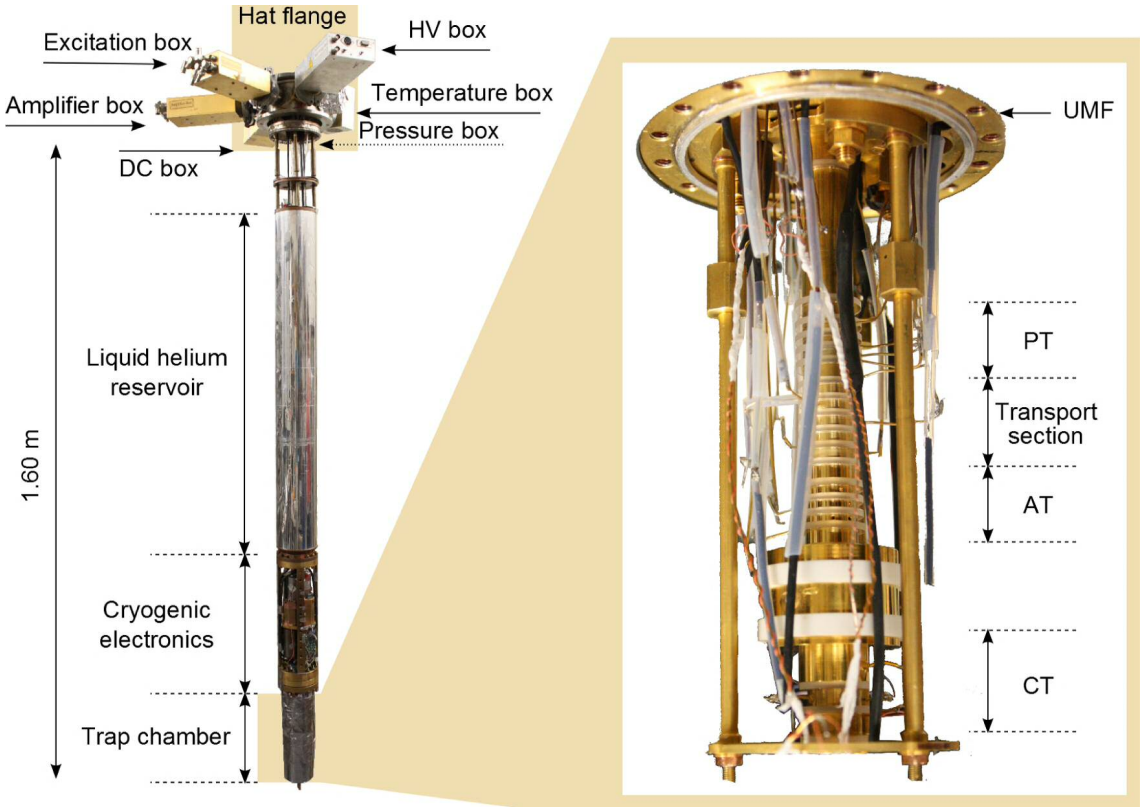

Figure 4.2: Photos of the experimental setup. On the left side the apparatus is shown, which is placed in the bore of the magnet. On the right side, a picture of the wired triple Penning trap tower is shown. In the lower part of the right photo the target, the acceleration electrode and the FEP are missing, compare with fig. 4.1 and fig. 4.8.

the steel pipe for the helium filling and recovery. The hat flange itself contains six smaller lateral flanges with the following attached electronic boxes:

- **The amplifier box:** The built-on *BS1-12*, developed by Stefan Stahl [124], delivers the voltage for all cryogenic amplifiers, the control voltages for the miniature-EBIS, CT and electric switches. With the so-called cryo-switch, implemented by Sven Sturm [13], the dipole and quadrupole excitation lines can be actively grounded close to the trap chamber in the cryogenic part, which has been essential for the axial frequency stability in the analysis trap. Furthermore, all the three signal lines: the axial signals of the PT and the AT and the cyclotron signal of the PT pass the amplifier box. Here, both axial signal lines are down-converted from 671 kHz in the PT and 412 kHz in the AT to "audio" frequencies 0 to 28 kHz. An Agilent 33250A function generator[1] is used as a local oscillator. In the room temperature lab region all signal lines are amplified once more before the Fourier analysis and the recording is performed by

1 Since 2014, electronic instruments by Agilent Technologies spun-off into Keysight Technologies.

the SR1 Audio Analyzer (Stanford Research Systems).

- **The excitation box:** All three excitation lines pass the feedthroughs of the excitation box:
  - The axial dipole excitation line, see also section 3.3.1, is connected to the lower endcap in the PT and the upper endcap in the AT. In the PT, this excitation is only used during the cleaning process, see section 4.3.1. In the AT, the dipole excitation has been used for the axial peak detection of the $^{12}C^{5+}$ ion. The corresponding excitation signal is also generated by an Agilent 33250A function generator.
  - The quadrupole excitation line, see also section 3.3.2, is connected to one half of the split correction electrodes in both traps. The excitation signal is generated by the two channel function / arbitrary waveform generator Agilent 33522A. The PnA cycle, see section 3.4.2, is programmed as a simultaneously started superposition of two arbitrary waveforms: Channel one only performs the first PnA pulse. The pulse sequence of channel two includes at first a waiting time for the first PnA pulse and the phase evolution time and subsequently the programmed second PnA pulse. Both channels are combined by a power splitter / combiner of Mini-Circuits, ZSC-2-2+.
  - The LC excitation line is capacitively connected to both axial resonators, see fig. 3.13 and section 3.3.3. Since the required feedback amplitudes differ in the two measurement traps we use two separate function generators, both Agilent 33250A, with different attenuators. The axial signal, which has been amplified at room temperature, is mixed by the respective phase shifted signal via frequency mixers ZP-3 (0.15 − 400 MHz) by Mini-Circuits[1]. Before it passes the feedthrough of the excitation box, the signal is high-pass filtered at a cutoff frequency of 300 kHz (RC-filter).

  For galvanic isolation all excitation lines contain rf-transformers by Mini-Circuits (FTB-1-6*) in the proper frequency range. Furthermore, for the excitation and signal lines, we use persistently coaxial cables with an impedance of 50Ω. In addition, the excitation box also contains the voltage supply line of a heating resistance, which is used to discharge the superconducting axial compensation coil by a local heating of the coil wire over the critical temperature, see also section 4.2.1.
- **The DC box:** On top of this box the high-precision voltage source UM1-14 by Stahl Electronics is placed. It provides all trapping and transport voltages from 0 up to −14 V. This power supply has been explained in various previous thesis', see e.g. [138] or [13]. In the relevant measurement time span of about eight minutes[2] the

1 The used frequency mixers are double-balanced passive diode mixers, also denoted as ring modulators.
2 The exact measurement process will be explained in section 4.4. In the PT, the axial frequency is determined from two dip measurements with averaging times of 200 s. In between these measurements PnA cycles are performed for about 300 s. The standard deviation of the axial frequency differences is $\sigma(\nu_z^I - \nu_z^{II}) = 29\,\text{mHz}$.

axial frequency fluctuates by 21 mHz at an absolute frequency of $\nu_z = 671\,\text{kHz}$, which corresponds to relative voltage fluctuations of the ring electrode of $\delta U_r/U_r = 6 \cdot 10^{-8}$. In addition to the UM1-14, also the so-called HVM box is connected to the DC box, which provides voltages between -100 V and 0 V for the three electrodes of the creation trap, see section 4.3.1. All lines, which enter the trap chamber, have been low-pass filtered via RC-filters in the cryogenic electronics section.

- **The HV box:** The high voltage box has been designed by Joseba A. Otamendi [140, 141]. It provides voltages for the miniature electron beam ion source (mEBIS), which will be introduced in section 4.3.1. Electron energies of several keV can be reached. The built-in power supply provides a maximum voltage of 8 kV. Nevertheless, mainly due to the compactness of that box and the accompanying restricted isolation, so far, creeping currents and flash-overs limit the maximum voltage to roughly 5 kV.
- The remaining two boxes: **the pressure box** and **the temperature box** are only relevant for the diagnostics, when the apparatus is cooled down from room temperature to cryogenic temperature. Such cooling procedures happened only a few times during the last 3.5 years. One flange contains the pressure sensor, a compact full range gauge by Pfeiffer Vacuum, to observe the bore vacuum of about $1 \cdot 10^{-7}$ mbar and the other flange provides access to various standard temperature sensors.

4.1.3 The Microwave System

The Larmor frequency of the valence electron in a hydrogenlike but also lithiumlike ion is in the millimeter wave range, e.g. about 105 GHz for a $^{12}C^{5+}$ ion at $B_0 = 3.76\,\text{T}$. The probed microwave excitation is produced by a MW synthesizer, MG3692B by Anritsu, which generates microwaves up to max. 20 GHz. To reach 105 GHz, we multiply the frequency by a factor of six to $75 - 110$ GHz using the S10 MS millimeter wave source module by OML. Subsequently, the microwaves are guided by W-band waveguides into the trap chamber. On that way, two different vacuum barriers are crossed by horn-horn transitions. The vacuum barrier on top of the hat flange consists of a Teflon window and the other barrier in the center of the *Untere Montage Flansch* (UMF) is made up of quartz glass. A detailed description and testing of the waveguide system and the occurring loss of power is given in the diploma thesis of Manfred Tönges, see [142].

4.1.4 The Timing System

For the generation and measurement of frequencies a stable and precise timing is absolutely essential. For this reason, all function generators, the microwave synthesizer, and the Fourier analyzer are locked to a rubidium atomic clock. More precisely, we use a rubidium frequency standard, model FS725 by Stanford Research Systems, which provides a 1 pps (one pulse per second) signal and a 10 MHz output with a relative frequency stability of $2 \cdot 10^{-11}$ on a time scale of 10 s. The 10 MHz output signal is distributed via a dual distribution amplifier, model FS735 by Stanford Research Systems.
For the phase-sensitive measurements, e.g. the PnA method, also the timing between the excitation pulses and for example the signal readout is essential. We program such kind of trigger sequences by the pulse-delay generator, model 555, by Berkeley Nucleonics Corporation (BNC), which provides four different trigger channels: (A) for the quadrupole

excitation, (B) for the dipole excitation and the microwave synthesizer, (C) the axial local oscillator and both feedback oscillators to set the proper feedback phase relation, and (D) the Fourier analyzer, SR1.

4.1.5 The Triple Penning Trap Tower

The requirements of a strongly inhomogeneous magnetic field for the spin-state detection on the one hand, see section 3.5, and an as perfect as possible field homogeneity for the precise eigenfrequency measurements and Larmor frequency scans on the other hand are conflicting. To fulfill these requests, at the end of the nineties, in the group of Günter Werth, Nikolaus H. Hermanspahn and colleagues [139], developed the so-called *double Penning trap technique*, which spatially separates the measurement processes into two Penning traps. For the first time, this measurement concept has been applied by Hartmut Häffner [128] in 2000.

In our present Penning trap setup, both measurement traps are separated by five cylindrical transport electrodes, with a distance of 41 mm between the trap centers, see figure 4.1. In the so-called *analysis trap* (AT) a ferromagnetic ring electrode with a saturation flux density of $B_s = 0.645$ T (nickel) induces a magnetic bottle of $B_2 = 10.5\ (4) \cdot 10^3$ T/m^2 for the spin state detection, as mentioned in section 3.5. The *precision trap* (PT) has a homogeneous magnetic field for the measurement of the eigenfrequencies and the probing of the Larmor precession frequency. The dominant magnetic field imperfections in the PT are caused by the residual magnetic bottle of the AT: $B_1^{\mathrm{PT}} = -13.41(23) \cdot 10^{-3}$ T/m [13] and $B_2^{\mathrm{PT}} = 1.01(0.20)$ T/m^2, see also section 5.3.

Within the trap chamber, the cryo-pumped vacuum pressure is better than 10^{-17} mbar, which we estimate by the trapping time of the ions, see also [139]. Such a pressure corresponds to less than 20 gas atoms in the trap volume. The complete trap tower is enclosed in a cold-welded cryogenic chamber, made from oxygen-free high conductivity (OFHC) copper. An indium-sealed flange, the so-called *Untere Montage Flansch* (UMF), contains all voltage, signal and excitation lines and a quartz glass window, which enables the coupling of the microwaves for the probing of the Larmor precession frequency.

A miniature electron beam ion source and trap (mEBIS/T) is used for the ion production. It contains a third 3-electrode Penning trap, the so-called *creation trap* (CT), which will be explained in section 4.3.1.

All the electrodes have been manufactured by the workshop of the University of Mainz with a precision of ±10µm. They are made out of OFHC copper, having susceptibilities of only $\chi = -6.4 \cdot 10^{-6}$. Reducing the creation of patch potentials by oxidation, the electrode surfaces are protected by a few µm gold layer on top of a few µm silver layer, which prevents the diffusion of the gold atoms. The thickness of both layers amounts to 15 µm. These electrodes are spatially separated and isolated by sapphire rings. Sapphire (Al_2O_3) is a good thermal conductor especially at low temperatures, has a tiny susceptibility of $\chi = -2.1 \cdot 10^{-7}$ and good ac-properties, e.g. a tiny loss tangent ($\tan\delta < 1 \cdot 10^{-4}$ for > 1 MHz). Macor rings are only used for the high-voltage electrodes.

4.2 Environmental Influences and Stabilization Systems

High-precision measurements in Penning traps highly rely on the temporal stability of the applied electric and magnetic fields. The impact of various external disturbances is analyzed and as the need arises has to be stabilized. In the past years, several efforts have been made to minimize these environmental influences at our experimental apparatus. Essentially, in the course of the thesis of Anke Kracke [14] two significant reductions of environmental fluctuations have been achieved:

- The dominant fluctuations of the electrostatic trapping field have been caused by the fluctuations of the ambient temperature due to the temperature dependence of the ultra-stable voltage source, UM1-14. These fluctuations have been reduced by an active temperature stabilization of the affected experimental surrounding. The constructed isolation box is denoted in fig. 4.1. Within the box an active temperature stabilization of less than 10 mK has been reached for time spans of up to one day, enabling for example in the PT temperature generated fluctuations of the axial frequency, which are smaller than 6 mHz, at a total axial frequency of about 687 kHz [14].
- Working at cryogenic temperatures, an elegant way to reduce the impact of homogeneous external magnetic field fluctuations is the concept of a superconducting self-shielding compensation coil, see [143]. During the thesis of Anke Kracke, such a solenoidal coil has been designed and implemented directly in the vicinity of the trap chamber, see fig. 4.1. It compensates locally at the trapping center of the PT external homogeneous magnetic field fluctuations, which point in axial direction. In the following, I will introduce the underlying concept and summarize its present performance, which for the first time has been tested during a measurement of the Larmor-to-cyclotron frequency ratio. Finally, I will extend this idea to compensate also transversal magnetic field fluctuations.

4.2.1 Superconducting Compensation Coils

In 1988 Gerald Gabrielse and Joseph Tan developed the concept of a passive compensation of homogeneous magnetic field fluctuations by using a closed superconducting solenoidal coil [143, 144]. Their idea is based on the fact, that in a superconducting loop external magnetic field fluctuations induce electric currents in a way, that the magnetic flux through the loop $\Phi \equiv \int_A \vec{B} d\vec{A}$ is constant[1]. At first, we consider an uncharged solenoidal closed superconducting coil with $\Phi(t_0) = 0$. Thereupon, a homogeneous disturbance of the external magnetic field B_{ext} occurs parallel to the solenoidal axis. Due to flux conservation:

$$\begin{aligned} \Phi(t_1) = \int_A \left(B_{\text{ext}} + B_{\text{ind}}\right) dA = A \cdot B_{\text{ext}} + A \cdot \langle B_{\text{ind}} \rangle = \Phi(t_0) = 0 \\ \rightarrow \qquad B_{\text{ext}} = -\langle B_{\text{ind}} \rangle \,, \end{aligned} \tag{4.1}$$

1 In case of any superconducting loop, magnetic flux conservation can be easily derived from Maxwell's equation: $\vec{\nabla} \cdot \vec{E} = -\frac{\partial \vec{B}}{\partial t}$ (Faraday's law). Using Stokes' theorem: $\oint_{\partial A} \vec{E} d\vec{s} = \int_A \vec{\nabla} \cdot \vec{E} d\vec{A} = -\int_A \frac{\partial \vec{B}}{\partial t} d\vec{A} = -\frac{\partial}{\partial t}\Phi$. If the wire is closed and superconductive: $\oint_{\partial A} \vec{E} d\vec{s} = 0$ and in that way: $\frac{\partial}{\partial t}\Phi = 0$.

where $\langle B_{\mathrm{ind}} \rangle$ is the averaged induced magnetic field, generated by the coil. Due to linear dependences between the locally induced magnetic field, the induced current and the mean induced magnetic field: $B_{\mathrm{int}}(z) \propto I_{\mathrm{ind}} \propto \langle B_{\mathrm{int}} \rangle$, we introduce a position-dependent proportional factor $b(z)$[1]:

$$B_{\mathrm{ind}}(z) = b(z) \cdot \langle B_{\mathrm{ind}} \rangle = -b(z) \cdot B_{\mathrm{ext}}. \tag{4.2}$$

To quantify the local compensation, we define the shielding factor:

$$\eta(z) \equiv \frac{\text{homogeneous outer disturbance}}{\text{disturbance within the solenoid at z}} = \frac{B_{\mathrm{ext}}}{B_{\mathrm{ext}} + B_{\mathrm{ind}}(z)} = \frac{1}{1 - b(z)}. \tag{4.3}$$

In the case of perfect shielding at a position z: $\eta(z) \to \infty$. Considering the spatial limitations of our experimental setup, Anke Kracke designed a solenoidal self-shielding coil, where $b(z_{\text{PT-center}}) = B_{\mathrm{ind}}(z_{\text{PT-center}}) / \langle B_{\mathrm{ind}} \rangle$ approaches one at the trapping center of the PT.

Compensation in Axial Direction

The calculation and the design of the axial superconducting compensation coil is described in [14]. Placing this coil directly around the trap chamber and fixing it to the UMF, also magnetic field fluctuations caused by the movement of the apparatus with respect to the magnet (by thermal expansions or vibrations) are at least partially compensated. Special design adjustments had to be made due to the relatively short distance between the center of the PT and the UMF which spatially limits the coil in the upper direction.
By applying artificial external magnetic field fluctuations and simultaneously measuring the resulting modified cyclotron frequency variations of a single $^{12}C^{5+}$ ion in the PT with firstly a superconducting and secondly a quenched compensation coil, a shielding factor of 19 has been measured, see also [14]. This axial compensation coil has been mounted after the g-factor measurement of lithiumlike silicon had been finished, so that its performance during a g-factor measurement has been tested for the first time at the Larmor-to-cyclotron frequency measurement of the $^{12}C^{5+}$ ion for the determination of the electron mass. Considering PnA phase evolution times of 10 s and a total PnA cycle time of about 30 s relative magnetic field fluctuations of $\delta B/B = 1.2 \cdot 10^{-9}$ have been measured without the compensation coil. After the assembly magnetic field fluctuations decreased to $\delta B/B = 6 \cdot 10^{-10}$, see fig. 4.19(b). After the completion of the electron mass determination, the apparatus has been warmed up mainly to tune the cyclotron resonator. Here, the compensation coil has been better aligned, so that the magnetic field stability for the $^{48}Ca^{17+}$ ion: $\delta B/B = 3.5 \cdot 10^{-10}$, see fig. 4.19(d), has been further improved. These magnetic field fluctuations will be also analyzed in detail in section 4.5.1. Here, a random walk model of these fluctuations improves by a factor of two by comparing the $^{12}C^{5+}$ and the $^{48}Ca^{17+}$ measurements. However, so far a discrepancy has been observed between the artificially generated, macroscopic magnetic field fluctuations, which yield a shielding factor of 19, and the microscopic fluctuations on short time spans (10 s) with a shielding

1 Here, we are only interested in the magnetic field distribution along the axial / z-direction, where $x = 0$ and $y = 0$.

factor of only 5. A possible explanation will be given in the next section by a combination of an intrinsic tilt of the axial compensation coil and vibrations.

Compensation in Transversal Directions

The following considerations triggered the development of transversal compensation coils. As a starting point, I assume an initially perfectly aligned solenoidal axial compensation coil, see fig. 4.3 (left side) in a perfectly homogeneous magnetic field, B_0. In the following the superconducting coil is tilted by an angle θ with respect to the magnetic field. As a consequence, the coil compensates the reduced magnetic field along the coil axis[1]: $B_{\text{ind}} = -B_{\text{ext}} = B_0(1 - \cos(\theta))$. The absolute magnetic field is increased, since next to the

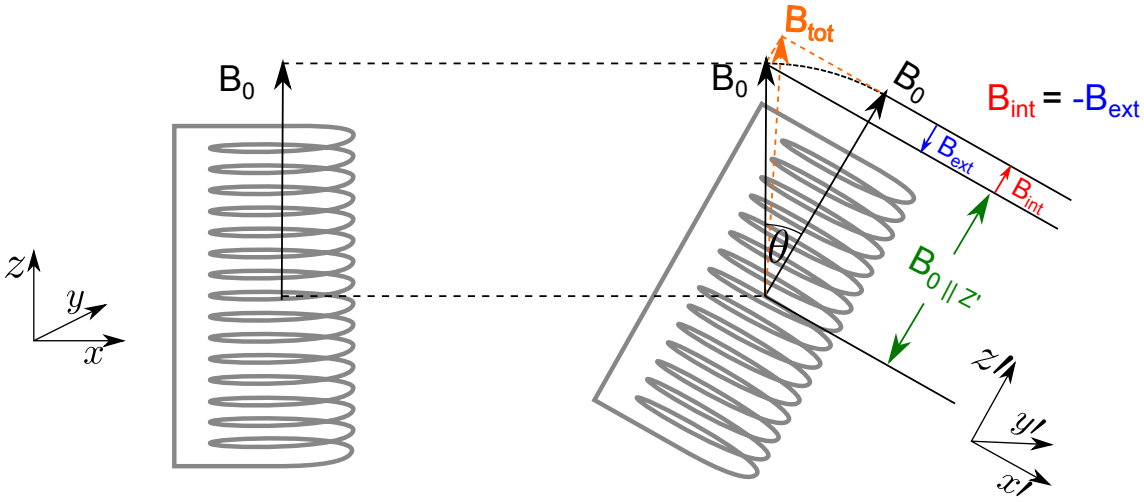

Figure 4.3: Compensation of magnetic field fluctuations by a tilted axial, solenoidal coil. For details see text.

constant magnetic field along the coil axis, an additional $B_{x'} = -B_0 \sin(\theta)$ component of the outer magnetic field occurs, which increases the total magnetic field:

$$|B_{\text{tot}}| = B_0 \sqrt{\sin(\theta)^2 + 1} \approx B_0(1 + \theta^2/2). \tag{4.4}$$

For small angles the relative deviation of the magnetic field is about $\delta B_0/B_0 \approx \theta^2/2$. To explain the currently measured magnetic field fluctuations of $\delta B/B = 4 \cdot 10^{-10}$ via fluctuations of the tilt of the experimental setup placed in the magnet bore, would require angle fluctuations of $\delta\theta = 0.0016°$. Assuming that the complete apparatus with a length of about 1.4 m vibrates as a rigid body, such tilts correspond to radial vibrations of the bottom of the experiment of: 42 µm, which are not realistic, see [14]. However, in case of small initial (static) tilts θ_0, e.g. given by an imperfect alignment of the magnetic field itself or the alignment of the apparatus with respect to the magnetic field, much smaller fluctuating tilts $\delta\theta$ would be required: $\delta B_0/B_0 = (\theta_0 + \delta\theta)^2/2 \approx \theta_0\delta\theta + \text{const}$. For example,

1 Here, I assume perfect shielding: $b = 1 \quad \leftrightarrow \quad B_{\text{ind}} = -B_{\text{ext}}$.

at the measured static tilts of $\theta_0 = 0.1 - 0.2°$, see table 3.1, the present magnetic field fluctuations could be explained by oscillation amplitudes of the bottom of the apparatus of only $160 - 320$ nm. Vibrations of the complete setup might cause these fluctuating tilts. To reduce this effect, in the course of this thesis I worked on the concept of transversal compensation coils.

Design of Transversal Compensation Coils
Complete compensation in transversal direction, requires at least two independent self-shielding coils, which we would place directly around the axial compensation coil, pointing in x- and y-direction. The severe spatial constraints exclude the usage of the relatively simple solenoidal geometries[1]. Several elaborated geometries have been numerically calculated in Matlab. Here, I dynamically[2] subdivided the windings (n segments) as well as the closed area (k segments), which is required for the numerical flux integration, in tiny segments. The magnetic field at a position $\vec{r}$ is calculated as a field superposition by applying to all n wire segments separately the Biot-Savart law. For the following reason the calculation of the magnetic flux the consideration of the wire thickness is of great importance. Focussing on a densely wound coil the magnetic flux in the close vicinity of the wires is rather homogeneous. However, considering a losely wound coil with rather large distances between the wires, the wire thickness has a large impact on the magnetic flux, since e.g. for an infinitely small wire the flux ($\Phi \propto \ln(r)$) would diverge.
The flux concentrator design of the transversal compensation coil, shown in fig. 4.4, considers the following three criteria: (1) The magnetic field strength is concentrated at the center of the PT, in the upper part of the trap chamber. (2) The integration area of the flux is enlarged. (3) The flux itself is reduced. The layout consists of two winding layers on both sides of the trap chamber fixed on a cylinder with an outer radius of 44.4 mm. Each layer contains 30 windings, which are densely wound. The lengths of the straight sections are 25 mm for the small windings and 90 mm for the large windings; the innermost bending radius is 7 mm. The superconducting NbTi wire should have a total radius of 275 µm including a wire isolation with a thickness of 25 µm.

1 Spatial Constraints: At our experimental apparatus, spatial constraints in radial directions are given by the trap chamber, the solenoidal self-shielding coil and the 20 K shield, see fig. 4.1. In numbers: The innermost spatial limitation is given by the trap chamber with an outer radius of 35 mm At the moment, the trap chamber is directly surrounded by the solenoidal self-shielding coil, fixed on an OFHC-copper cylinder with an inner radius of 37.25 mm. The cylinder itself (1 mm) and the winding including insulation (1 mm), enable a mounting cylinder for the inner transversal self-shielding coil with an inner radius of 39.4 mm. The outer limitation is set by the 20 K shielding with an inner radius of 48 mm. Replacing the 20 K shield by at least 15 layers of superinsulation foil, see proton g-factor experiment [145], the absolute outer limit would be given by the nitrogen shield at a radius of 57 mm. In the current setup of the trap tower, the center of the PT is close to the UMF, so that there is a strict limitation in axial direction, e.g. 27.4 mm for the inner transversal self-shielding coil to the top. Also a lower axial limit of about 10 cm is set by the spatially limited homogeneity of the magnetic field.

2 Here, dynamical subdivision means: (1) The size of the winding segments scale with the bending; e.g. straight wire sections do not need to be subdivided. (2) The size of the area segments scale with the change of the magnetic field strength; e.g. the segmentation of the area close to the windings are very dense.

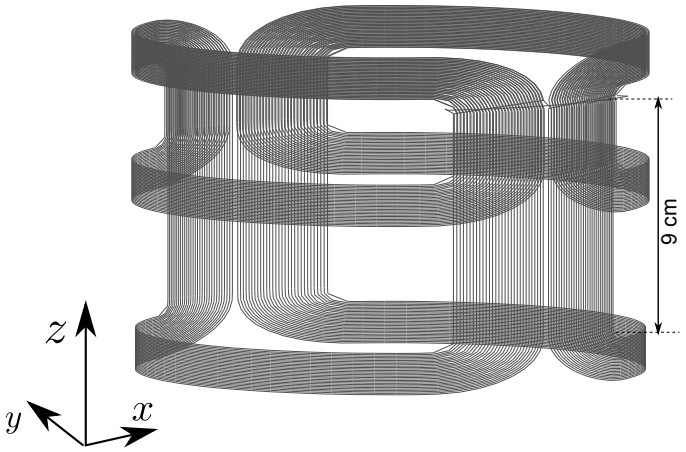

Figure 4.4: Design of an inner transversal self-shielding coil in x-direction. The layout consists of two stacked winding layers of different sizes on both sides of the cylindrical trap chamber. For details see text.

Table 4.1: Robustness analysis of the numerical solution of the inner transversal compensation coil, which is illustrated in fig. 4.4.

parameter	set value	studied tolerances	η range
coil meshing	3.5 mm	±1.5 mm	11.4 – 12.7
meshing parameter[a]	0.02	±0.01	12.1 – 12.3
distance: PT_{centre}-UMF	26.8 mm	±0.8 mm	10.9 – 13.6
number of big windings	30	±1	11.3 – 12.4
number of small windings	30	±1	11.6 – 12.3
straight length of big windings	90 mm	±3 mm	11.0 – 13.5
straight length of small windings	25 mm	±3 mm	11.9 – 12.2
wire radius without isolation	250 µm	±10 µm	11.2 – 13.3
isolation thickness	25 µm	±5 µm	11.7 – 12.7
inner bending	6 mm	±1 mm	11.4 – 12.8
radius of the staging cylinder	40.4 mm	±0.4, (37.25) mm	13.4 – 11.1, (52.3)

a Some specific parameter, which characterizes the meshing size of the integration area.

The calculated shielding factor of 12.1(7) could be dramatically increased by lowering the center of the PT with respect to the UMF, see fig. 4.5. The corresponding outer compensation coil for compensation in y-direction, has a shielding factor of 6.5(7). The specified uncertainty considers the estimated numerical uncertainty, which has been analyzed by varying the segment size of the split windings and the meshing of the integration area. A detailed study of the robustness of this numerical calculation is given in table 4.1.

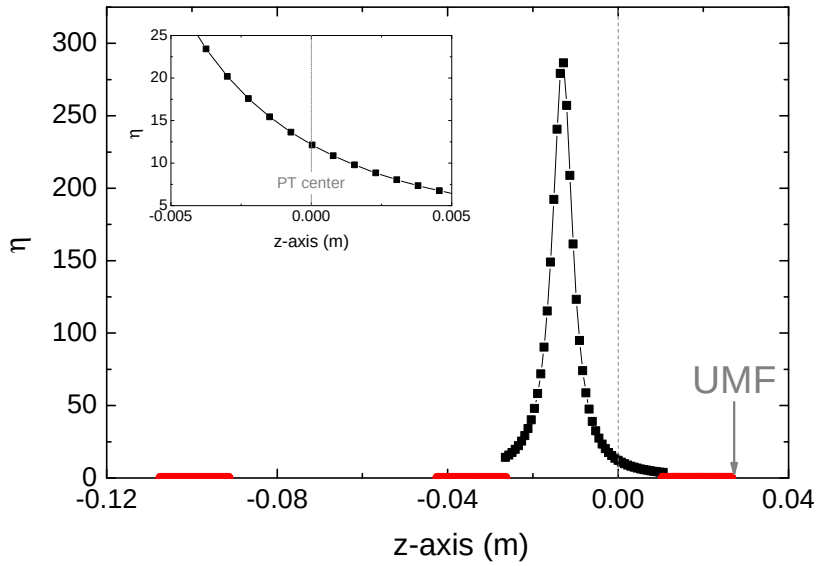

Figure 4.5: Calculated shielding factor of the transversal compensation coil in x-direction as a function of the z-position ($x = y = 0$ m). The corresponding design is shown in fig. 4.4. In red the z-position of the windings are indicated. At $z = 0$ m (dotted line) the center of the PT is located. A larger distance between the UMF and the PT center would significantly increase the shielding factor.

For future major upgrades, where the PT is shifted for a few centimeters with respect to the UMF, transverse shielding factors of about 1000 seem to be feasible also with mono-layer geometries, see fig. 4.6.

Coupling of the Compensation Coils

So far, the compensation coils have been optimized separately. In combination, their mutual interactions have to be considered. The determination of the combined shielding factor requires the knowledge of the total integrated areas A_i, the self-inductances L_{ii}, the mutual-inductances L_{ij} and the factors: $g_i = B_i(\mathrm{PT_{centre}})/I_i$. Here, $B_i(\mathrm{PT_{centre}})$ is the generated magnetic field at the PT-centre when a current I_i is applied. Assigning $i = 1$ to the inner transversal coil, $i = 2$ to the outer transversal coil and $i = 3$ to the axial coil, the combined shielding factor in x-direction is:

$$\begin{aligned}\eta^{-1} =& 1 - g^T L^{-1} A \qquad (4.5)\\ =& 1 - \begin{pmatrix} -1.0\cdot 10^{-3} \\ -1.6\cdot 10^{-8} \\ 0 \end{pmatrix}^T \begin{pmatrix} -1.2\cdot 10^{-3} & -7.4\cdot 10^{-9} & 4.0\cdot 10^{-4} \\ -7.4\cdot 10^{-9} & -1.3\cdot 10^{-3} & 3.7\cdot 10^{-4} \\ 4.0\cdot 10^{-4} & -3.7\cdot 10^{-4} & 5.1\cdot 10^{-3} \end{pmatrix} \begin{pmatrix} 1.1 \\ 1.3 \\ 1.4 \end{pmatrix}\\ =& 1/12.1,\end{aligned}$$

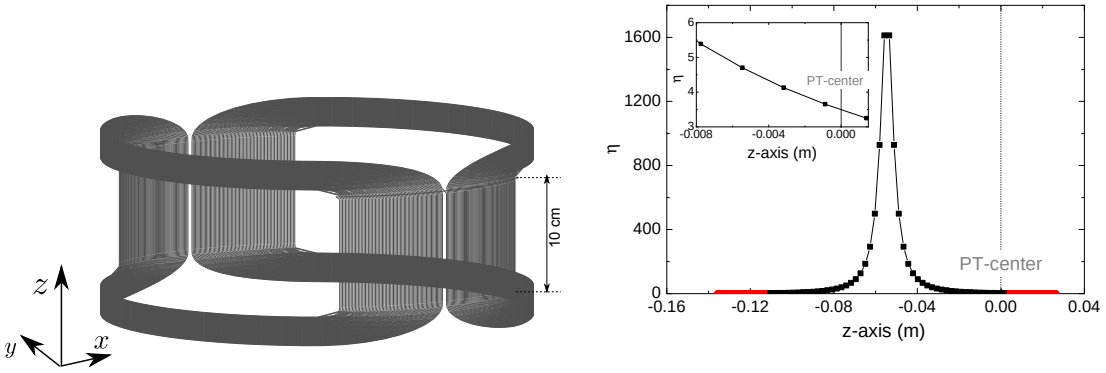

(a) **(b)**

Figure 4.6: Transversal compensation coil with a mono-layer of windings (a). Dimensions: radius of the cylinder: 49 mm; wire radius without isolation: 125 µm, thickness of the wire-isolation: 25 µm, bending radius of the inner most winding: 6 mm, total number of windings: 172 (in one-layer and per side: 86 windings). (b) In the coil center shielding factors larger than 1000 are feasible.

which does not significantly deviate from the former result. Moreover, the couplings with the various shimming coils of the OXFORD magnet have to be considered. Due to the missing knowledge on their positions and inductances, the assembling of the transverse compensation coils has been postponed.

4.2.2 Pressure Study of the Four Cooling Reservoirs

Pressure fluctuations of the boil-off gas in the four liquid gas reservoirs, see section 4.1.1 and fig. 4.1, arise due to a number of reasons: (1) outer room temperature and pressure fluctuations, (2) pressure fluctuations in the helium exhaust line and (3) fluctuations generated during the evaporation process (bubbles). These fluctuations cause an alteration of the boiling temperature and in that way a change of the susceptibilities of the surrounding materials, which finally generate magnetic field fluctuations. Moreover, local pressure fluctuations e.g. in the helium reservoir of the apparatus lead to temperature fluctuations of the evaporated gas, which thereupon generate a fluctuating thermal expansion of the helium recovery pipe. Since the complete apparatus is only fixed by this recovery pipe, the apparatus and especially the nickel ring electrode of the AT move within the bore of the magnet, so that magnetic field fluctuations arise in the Penning traps.
To study the impact of pressure fluctuations artificial pressure variations of up to 20 mbar have been generated by the absolute pressure controller 640A of MKS Instruments. In parallel, the variation of the modified cyclotron frequency has been observed by subsequent double-dip measurements. Data of the nitrogen reservoir of the magnet are plotted in fig. 4.7. The results of all four liquid gas reservoirs are listed in table 4.2. Here, an explicit pressure dependence has been only detected for the nitrogen reservoir of the magnet.
Subsequently the unstabilized pressure variations have been studied for several hours by the

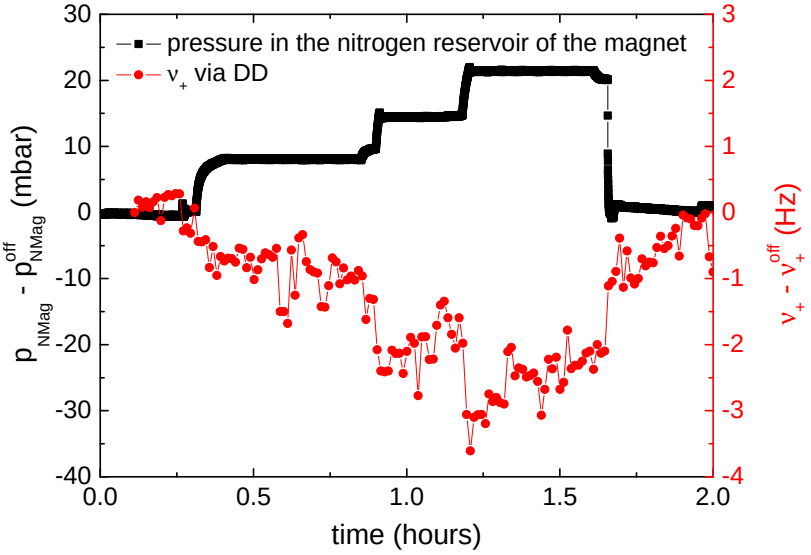

Figure 4.7: Study of the magnetic field fluctuations in dependence of the pressure in the nitrogen reservoir of the magnet (NMag). The stabilized pressure has been increased in three steps, indicated in black. The pressure offset $p^{\text{off}}_{\text{NMag}}$ corresponds to the average air pressure in the lab. Simultaneous to the pressure measurements, the modified cyclotron frequency has been detected in the PT via subsequent double-dip measurements, indicated in red.

Table 4.2: Analysis of the pressure fluctuations in all four liquid gas reservoirs. Axial compensation coil is present.

reservoirs	ν_+ pressure dependence (Hz/bar)
nitrogen magnet (NMag)	118(21)
helium magnet (HeMag)	0(3)
nitrogen apparatus (NApp)	12(18)
helium apparatus (HeApp)	15(17)

pressure transducer, type 220D (MKS Instruments). For both magnet reservoirs pressure fluctuations of 6 µbar have been observed on a time span of 10 s. If we assume a linear extrapolation to small scale pressure fluctuations, the relative magnetic field fluctuations will be smaller than $1 \cdot 10^{-10}$. Consequently, in presence of the solenoidal compensation coil, the observed magnetic field fluctuations are not limited by the unstabilized pressure fluctuations, so that in presence of the axial compensation coil no pressure stabilization is needed at the current level of precision.

4.3 Preparatory Steps and Measurements

4.3.1 Creation of a Single Highly Charged Ion

As mentioned in section 4.1.5, the studied highly charged ions have to be created within the closed trap chamber by a miniature electron beam ion source (mEBIS). Here, electrons are emitted from a single field emission point made out of tungsten. The FEP fires by applying a voltage difference of at least 700 V between the FEP and the acceleration electrode, see fig. 4.8. Setting the reflector electrode to a voltage at least as low as the voltage of the FEP, the emitted electrons start oscillating along the magnetic field lines between the FEP and the reflector forming an oscillating electron beam. Increasing the beam current up to a few 100 nA the beam broadens due to Coulomb repulsion and finally impinges on the target. Different atomic and molecular species are desorbed from the target surface. Some of them diffuse into the electron beam and get ionized. These low charged ions are confined in the creation trap (CT), a simple cylindrical Penning trap, comprising three electrodes, a ring and two endcap electrodes. Further electron-impact ionization produces ions in

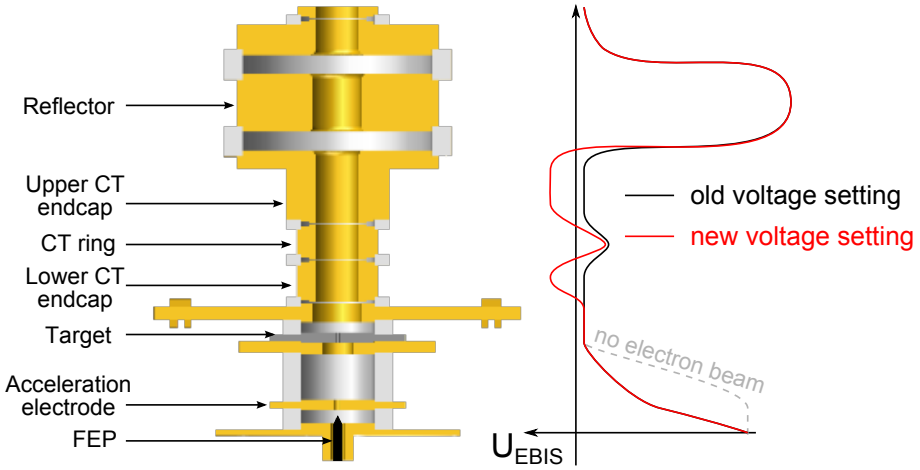

Figure 4.8: Illustration of the miniature electron beam ion source (mEBIS). On the right side, the voltage configurations during the ion production are sketched. The common voltage configuration is shown in black. The modified voltage configuration for the creation of trapped calcium ions with the additionally positively charged endcap electrodes of the CT is indicated in red. The electron beam current is steered by the applied voltage on the acceleration electrode.

higher charge states, in particular lots of carbon, oxygen and silicon ions. The maximal accessible charge states are limited by the voltage difference between the FEP and the ring electrode of the CT. The latter voltage is typically of the order of $U_r^{\mathrm{CT}} \approx -100\,\mathrm{V}$. Technical details and the characterization of the mEBIT as well as an extensive description of the corresponding HV box are given in the theses of Joseba A. Otamendi [140, 141] and Birgit Schabinger [138].

The voltage configurations during the creation process slightly differ with respect to the desired ion species:

- Creation of a single $^{12}C^{5+}$ ion: The chosen energy of the electron beam of 1 keV is well above the ionization threshold of hydrogen-like carbon, $E_{\mathrm{ion}} = 392\,\mathrm{eV}$, see also

table 2.2. Optimizing the ionization cross section, the energy of the electron beam should be a factor 2.5 higher than the desired ionization energy, see [146]. The charge breeding time is in the order of 10 s. In the subsequent analysis of the produced ion cloud usually a few $^{12}C^{5+}$ ions, 2-5 ions, have been detected.

- Creation of lithiumlike calcium ions, $^{40}Ca^{17+}$ and $^{48}Ca^{17+}$: At an ionization energy of 1.1 keV, I used an electron beam energy of about 4 keV. With the common voltage configuration, see fig. 4.8 (black line), it has not been possible to desorb calcium atoms from the target, although we increased the charge-breading time to several minutes. In the end, a modification of the voltage setting of the two endcap electrodes of the CT, applying +85 V instead of 0 V, enabled the production of calcium ions. The CT ring electrode remained at −100 V. Two possible reasons might explain this essential adjustment:
  - After some charge breeding time, the CT is completely filled with ions, so that the CT overflows and several ions are accelerated towards the target. Here, we consider for example a lithiumlike silicon ion which is for some reason produced in great quantities. If such an ion hits the target, the momentum transfer will be a factor 110 larger than the momentum transfer of an electron from the electron beam. This might increase the calcium desorbtion rate.
  - The effective deeper trapping voltage of the CT enables the generation of larger clouds, which might be essential for the charge-breeding of the heavy calcium ions.

  The typical charge breeding time has been one minute. In most of these creation cycles no calcium ions have been detected in the subsequent analysis of the ion cloud. However, in a few cycles up to two lithiumlike calcium ions have been detected.

After the charge breeding process in the CT, the cloud of ions is transported into the PT for the separation of the desired single ion.

Composition of the Target Surface

The natural abundance of ^{40}Ca amounts to 97% and of ^{48}Ca to only 0.19%. To increase the production rate of ^{48}Ca ions, the built-in target contains an enriched calcium isotope mix. The target surface has been produced by the target laboratory of the GSI Helmholtzzentrum für Schwerionenforschung GmbH Darmstadt. In a sputtering process various calcium isotopes have been accumulated on an ultra-pure graphite disk. The exact isotope composition is listed in table 4.3. Great care has to be taken during the installation of the target to protect the target from oxidation processes, see also [138]. As the target disk should mainly consists of carbon (graphite) and calcium atoms, it is remarkable (and until now not completely understood), that we detect a large abundance of silicon ions in the produced ion clouds.

Cleaning Methods - Preparation of a Single Ion

Essentially three different techniques have been applied to clean the trap from the unwanted ion species and at the same time to separate the desired single ion:

Table 4.3: Calcium isotope abundance on the built-in target.

isotope	enriched target	natural abundance
^{40}Ca	78.774%	96.941%
^{42}Ca	3.015%	0.647%
^{43}Ca	0.615%	0.135%
^{44}Ca	9.549%	2.086%
^{46}Ca	0.021%	0.004%
^{48}Ca	8.023%	0.187%

- **B_2-Cleaning:** The most efficient way to clean the setup from unwanted ion species is the highly selective B_2-cleaning technique, which includes the following five steps, developed by Sven Sturm: (1) Via a short radial dipole excitation at the expected modified cyclotron frequency we excite the modified cyclotron motion of the ions in the PT. More precisely, we apply a single frequency sweep with a frequency span of a few 100 Hz and a sweep time of 1 s. During this process, the axial mode of the wanted ion is resistively cooled to a few Kelvin by the tuned axial resonator. (2) Subsequently, we transport the modified ion cloud into the AT. (3) Lowering the electric trapping potential below the thermal axial energy, the unwanted ion species are evaporated, while the wanted ion species remain confined, due to the force acting on their large magnetic moments: $\mu_z^{\mathrm{cycl}} = 0.5 q r_+^2 \omega_+$, which is caused by the large magnetic bottle $B = B_2 z^2$. In order to keep the wanted ion species in the trap, the corresponding axial magnetic energy $E_z^{\mathrm{cycl}} = \mu_z^{\mathrm{cycl}} B_2 z^2$ must be larger than the axial thermal energy $E_z = k_B T_z$. (4) The remaining ions are transported back from the AT into the PT, where (5) their modified cyclotron mode is sideband cooled.
- **Axial Sweeps and Swifts:** In addition to the B_2-cleaning technique, we also perform selective axial dipole excitations and subsequent evaporations of the unwanted ions. This cleaning process can be explained in four steps: (1) The ion cloud is placed in the PT. (2) For an efficient resistive cooling during the cleaning process, the axial frequency of the wanted ion species is tuned to the resonance frequency of the axial resonator by adjusting the trapping voltage. (3) Ions with a different charge to mass ratio are axially excited by dipole frequency sweeps above and below the frequency of the axial PT resonator. The lower limit of the lower frequency span is set by the magnetron frequency (≈ 10 kHz) and the upper limit of the upper frequency span is set by two times the axial frequency (≈ 1.3 MHz). Also the frequency range around the axial resonator of the AT (≈ 412 kHz) is excluded from the sweep, to protect the detection system in the AT. (4) Immediately after these sweeps the trapping potential is lowered for a few seconds to evaporate the excited unwanted ion species. Instead of using several sweeps, also a broad band axial excitation can be programmed as a stored waveform inverse fourier transform (SWIFT), again be limited by the magnetron frequency, the double axial frequency and the frequency ranges of axial resonators of the AT and PT [13].

- **Detection on the Cyclotron Resonator:** After an excitation of the modified cyclotron motion, multiple ions of the desired ion species can be detected as peak signals on the low-Q cyclotron resonator in the PT. Having slightly different motional energies, these ions can be distinguished by their slightly different modified cyclotron frequencies appearing as distinguishable peak signals. Such multiple ions can be selectively removed by a cautious lowering of the trapping potential until a single peak signal / ion remains. The characteristics of the cyclotron resonator are summarized in table 4.4.
  In case of thermalized ions, a further indication of multiple ions of the same species is given by the width of the axial dip signal, as explained in section 3.2.3.

Table 4.4: Characteristics of the PT cyclotron resonator during the electron mass measurement.

cyclotron resonator parameters:	value
Q	120(10)
$\tau(\nu_+)$	415(100) s
ν_{res}	24455(15) kHz
ν_+	24081134 Hz

4.3.2 Preparation of the Precision Trap

After the creation of a single trapped ion, both measurement traps have to be adjusted before the automated measurement of the Γ-resonance is started. In the following, these preparatory measurements are introduced.

Tuning Ratio Optimization

Deviations from the ideal electric quadrupole potential, see eq. (3.19) and eq. (3.20), lead to energy dependent eigenfrequency shifts [119, 120]. As explained in section 3.1.3, in the optimal design of a five-electrode configuration with grounded endcaps, the Penning trap is orthogonal, so that the axial frequency, which is proportional to $\sqrt{C_2}$, does not depend on the tuning ratio (TR), $\mathrm{TR} \equiv U_{\mathrm{cor}}/U_{\mathrm{r}}$. Moreover, the electric potential is doubly compensated: $C_4 = C_6 = 0$. Due to small imperfections of our trap design, only C_4 can be completely nulled, while a tiny C_6 remains. During each ion creation process, the patch potentials on the electrode surfaces in the PT are slightly modified, demanding a tuning ratio optimization right before the automated measurement process starts.
For this purpose, axial frequency shifts, generated by magnetron burst excitations, are studied for different tuning ratios and as a function of the applied burst amplitude, see fig. 4.9. For all three studied ions ($^{12}C^{5+}$, $^{40}Ca^{17+}$ and $^{48}Ca^{17+}$) a two-parameter fit has been used, which describes the axial frequency shifts in dependence of the magnetron burst amplitude:

$$\begin{aligned} \mathrm{d}\nu_z &\approx -\frac{3}{2}\frac{1}{d_{\mathrm{char}}^2}\frac{C_4}{C_2}\nu_z \cdot \kappa^2 \cdot U_{\mathrm{exc}}^2 + 2.8125\,\frac{1}{d_{\mathrm{char}}^4}\frac{C_6}{C_2}\nu_z \cdot \kappa^4 \cdot U_{\mathrm{exc}}^4 \\ &= \mathrm{P1} \cdot U_{\mathrm{exc}}^2 + \mathrm{P2} \cdot U_{\mathrm{exc}}^4. \end{aligned} \tag{4.6}$$

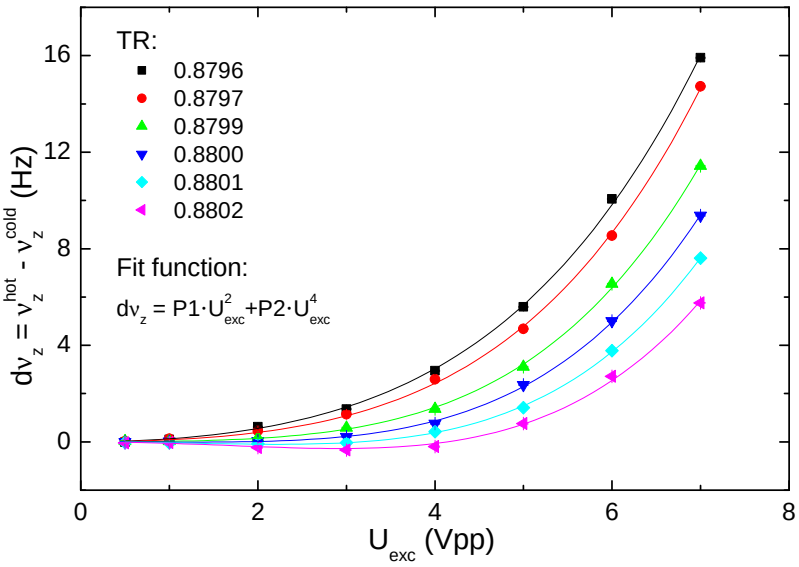

Figure 4.9: Tuning ratio optimization in the PT via magnetron burst excitations. Axial frequency differences between the excited (ν_z^{hot}) and the thermalized (ν_z^{cold}) magnetron modes of a single $^{12}C^{5+}$ ion are plotted as a function of the magnetron burst amplitude U_{exc} ($\propto r_-$) for six different TR's. The excitation pulse length has been fixed to 10 ms.

Here, only the leading-order C_4 and C_6 terms are considered. The magnetron radius is proportional to the magnetron burst amplitude: $\rho_- \equiv \kappa \cdot U_{\mathrm{exc}}$. In figure 4.10(a) the determined fitting parameter P1 is plotted as a function of the TR. As C_4 linearly depends on the TR: $C_4 = E_4 + \mathrm{TR} \cdot D_4$, we extract the optimal TR at $\mathrm{P1} = C_4 = 0$ from a linear fit of P1(TR), shown as a red curve: $\mathrm{TR_{opt}} = \mathrm{TR(P1{=}0)} = 0.8799693(51)$[1].
To determine the magnetron radius as a function of the burst amplitude, we rely on the calculated value of $D_4^{\mathrm{calc}} = -0.616$, the measured $C_2 = -0.5504$, see eq. (3.4), and the slope of the linear fit in fig. 4.9(a), $m_{\mathrm{P1}} = -307(10)$ Hz Vpp^{-2}. During the determination of the electron mass the proportionality constant κ has finally been given by:

$$\kappa = \sqrt{-\frac{2\, m_{\mathrm{P1}} \cdot C_2 \cdot \mathrm{d}_{\mathrm{char}}^2}{3\nu_z D_4}} = 5.1(1) \cdot 10^{-5}\ \mathrm{m/Vpp}. \tag{4.7}$$

At the maximal applied voltage of 7 Vpp, see fig. 4.9, we thus reach magnetron radii of 360(10) µm.

1 This optimized tuning ratio and all numbers in this section have been determined with a single trapped $^{12}C^{5+}$ ion during the preparation of the electron mass measurement. The corresponding numbers for the two calcium measurements will be discussed at the end of the section.

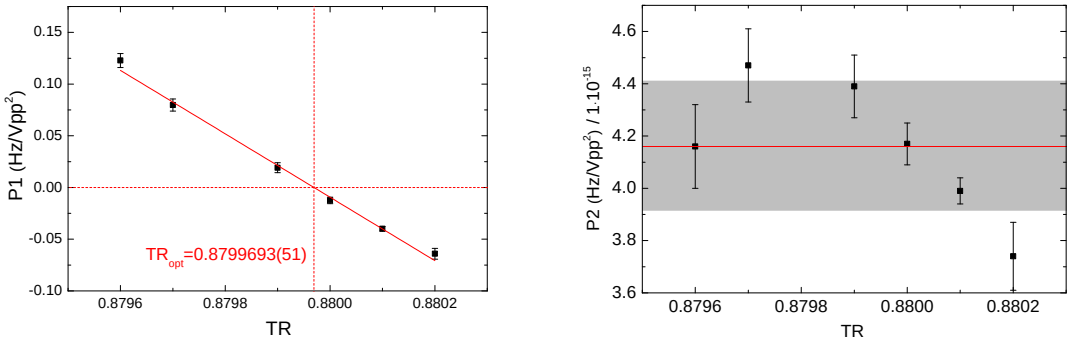

(a) **(b)**

Figure 4.10: Fit parameters of the tuning ratio optimization in the PT measured with a single $^{12}C^{5+}$ ion. Fitting curves of the form $d\nu_z = P1 \cdot U_{exc}^2 + P2 \cdot U_{exc}^4$ have been applied to the measured data shown in fig. 4.9. (a) P1 ($\propto C_4$) is plotted as a function of the TR. The optimized TR is derived by the linear interpolation (red line), where P1 = 0. (b) Here, P2 ($\propto C_6$) is plotted as a function of the TR. A profound model of the P2(TR) distribution could not be derived due to the limited statistics.

In the following, I study the limitations of the fitting model, introduced in eq. (4.6), and three further models, which consider higher-order terms in eq. (3.20):

1. $d\nu_z = P1 \cdot \rho_-^2 + P2 \cdot \rho_-^4$ (used for trap optimization, see eq. (4.6)),
2. $d\nu_z = P1 \cdot \rho_-^2 + P2 \cdot \rho_-^4 + P3 \cdot \rho_-^6$,
3. $d\nu_z = ((0.1578 \cdot C_4 + 7.251 \cdot 10^{-6} \cdot C_6)/0.5504 \cdot \rho_-^2 - 0.03112 \cdot C_6/0.5504 \cdot \rho_-^4) \cdot \nu_z$,
4. $d\nu_z = ((0.1578 \cdot C_4 + 7.251 \cdot 10^{-6} \cdot C_6 + 1.99 \cdot 10^{-10} \cdot C_8)/0.5504 \cdot \rho_-^2 - (0.03112 \cdot C_6 + 2.670 \cdot 10^{-6} \cdot C_8)/0.5504 \cdot \rho_-^4) \cdot \nu_z$.

At first, the axial frequency shifts are calculated analytically[1] for different tuning ratios and different magnetron radii analog to the measured data shown in fig. 4.9. These calculated curves are fitted by using the four different models at different ranges of the magnetron radius. From these fits the optimal ($C_4 = 0$) tuning ratios (TR_{fit}) are derived. In case of the first two fit functions, we approximate $P1 \propto C_4$. The optimal tuning of the calculated data amounts to $TR_{calc} = 0.8669137$[2]. In fig. 4.11 the tuning ratio deviations $\Delta TR = TR_{fit} - TR_{calc}$ are illustrated for the four fitting routines as a function of the largest magnetron radius used during the fitting. Considering only axial frequency shifts at small magnetron excitations ($\rho_- < 150\,\mu m$), the approximation $P1 \propto C_4$ leads to a large

1 The axial frequency shifts are calculated via eq. (3.20). The required higher-order electric field coefficients are calculated analytically, see eq. (7.10). For the axial and the modified cyclotron mode the thermalized amplitude / radius are considered.

2 It is remarkable, that the absolute value of the analytically calculated $TR_{calc} = 0.8669137$ significantly deviates from the experimentally optimized $TR_{meas} = 0.8799693(51)$.

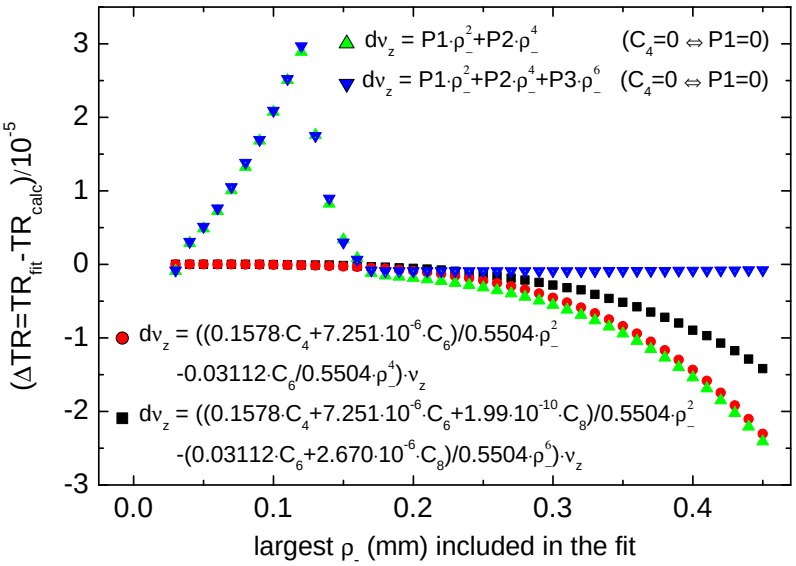

Figure 4.11: Analysis of different models used for the fitting of the data, presented in fig. 4.9. Here, the axial frequency shifts have been calculated analytically for different tuning ratios and different magnetron radii. These calculated curves have been fitted by four different models (green, blue, red and black). From these fits the optimal tuning ratio has been derived $\mathrm{TR_{fit}}$ for different ranges of the magnetron radii. The optimal tuning of the calculated data amounts to $\mathrm{TR_{calc}} = 0.8669137$. For further details see text.

deviation of the determined TR of $\Delta\mathrm{TR} = 3 \cdot 10^{-5}$, which in the future can be reduced by including also the $C_6 \cdot \rho_-^2$ dependence into the fit model , see red and black markers. Including also magnetron excitations larger than 300 µm into the fits, also higher-order terms of the electric potential, e.g. C_8, have to be considered in the fitting routine, see black markers.

For this reason, I add a systematic uncertainty of $1 \cdot 10^{-5}$ to the optimized TR, which has been used during the electron mass measurement. During the complete electron mass measurement period of 3.5 months the optimal TR has only marginally shifted, so that in this case we assume a conservative estimation for the relative uncertainty of the optimal TR of $2 \cdot 10^{-5}$.

The uncertainty of C_4 can be estimated:

$$\delta C_4 = \left| D_4^{\mathrm{calc}} \right| \cdot \mathrm{TR} \cdot 2 \cdot 10^{-5} = 1.1 \cdot 10^{-5}. \tag{4.8}$$

An estimation of C_6 is possible by the fitted P2 value, see figure 4.10(b) and the calculated value of D_4 :

$$C_6 = \frac{\mathrm{P2} \cdot C_4 \cdot d_{\mathrm{char}}^4}{2.8125 \cdot \nu_z \cdot \kappa^4} = -0.016(1). \tag{4.9}$$

It roughly agrees with the predicted value $C_6^{\mathrm{calc}} = -0.012$.
In table 4.5 the optimized TR of all the three studied ions are listed. It is remarkable,

Table 4.5: Optimized tuning ratios of all three ions.

ion	TR
$^{12}C^{5+}$	0.879969(11)
$^{40}Ca^{17+}$	0.879843(57)
$^{48}Ca^{17+}$	0.87680(6)

that the TR of $^{48}Ca^{17+}$ significantly deviates (0.33%) from the TR's of $^{12}C^{5+}$ and $^{40}Ca^{17+}$, which requires large modifications of the patch potentials on the electrode surfaces. As a cross check, I list the used ring voltages and the corresponding magnetron frequencies in table 4.6. With the relation: $\nu_- \propto U_r$, the magnetron frequency of $^{40}Ca^{17+}$ can be predicted

Table 4.6: Ring voltages and measured magnetron frequencies of all the three studied ions.

ion	U_r (V)	ν_- (Hz)
$^{12}C^{5+}$	−7.634	9347.0(2)
$^{40}Ca^{17+}$	−7.4728	9137.5(2)
$^{48}Ca^{17+}$	−8.97854	10967.6(1)

with almost the same deviation via the ring voltage and the magnetron frequency of $^{12}C^{5+}(\Delta\nu_- = 11\,\mathrm{Hz})$, as predicting $^{48}Ca^{17+}$ from the parameters of $^{40}Ca^{17+}(\Delta\nu_- = 11\,\mathrm{Hz})$. Here, no significant deviation of the $^{48}Ca^{17+}$ parameters is observed.

Systematic Uncertainty of the Axial Dip Signal

During the complete measurement period the frequency spectrum of the axial PT resonator has been recorded several times, see e.g. fig. 3.14. Fitting the resonator line-shape model, introduced in eq. (3.53), to these data, the resonator parameters ν_{res}, Q, $\widetilde{u}_n^{\mathrm{ampl}}$ and $\widetilde{\kappa}_{\mathrm{det}}$ have been extracted, see table 4.7.
A clear decrease of the quality factor with time has been observed already in the past.

Table 4.7: Fitted axial resonator parameters in the PT for all the three studied ions.

ion	ν_{res} (Hz)	Q	$\widetilde{u}_n^{\mathrm{ampl}}$ (Vrms)	$\widetilde{\kappa}_{\mathrm{det}}$ (dbVrms/Hz)
$^{12}C^{5+}$	670890(8)	670(40)	1.2(2)	$2.5(8.0) \cdot 10^{-5}$
$^{40}Ca^{17+}$	670145(30)[a]	531(15)	0.95(20)	$3.1(10.0) \cdot 10^{-5}$
$^{48}Ca^{17+}$	670180(8)	503(10)	0.95(20)	$1.8(10.0) \cdot 10^{-5}$

a The uncertainty of the resonator frequency, measured with $^{40}Ca^{17+}$, is exceptionally large, since a drift of the resonator frequency has been observed.

In the previous theses the following Q values have been listed for the axial resonator: 1200 [138] and 950 [13, 14]. These reductions of the quality factor might be explained by accidental overvoltages which damaged the gate of the primary transistor of the axial cryogenic amplifier during the ion creation process, when high voltage is applied to the mEBIS. Furthermore, also the resonance frequency decreased over time.
The dependence of the measured axial frequency on the four resonator parameters has

Table 4.8: Upper table: Axial frequency dependence of the fitted axial resonator parameters in the PT. Lower table: Absolute axial frequency uncertainties caused by the uncertainties of the resonator parameters.

ion	$\frac{d(\nu_z)}{d(\nu_{res})}$	$\frac{d(\nu_z)}{d(Q)}$ (Hz)	$\frac{d(\nu_z)}{d(\widetilde{u}_n^{\mathrm{ampl}})}$ (Hz/Vrms)	$\frac{d(\nu_z)}{d(\widetilde{\kappa}_{\mathrm{det}})}$ (Hz^2/dBVrms)
$^{12}C^{5+}$	$-1.8(5)\cdot10^{-4}$	$1.9(8)\cdot10^{-5}$	$-1.5(4)\cdot10^{-2}$	$-1.0(1.0)$
$^{40}Ca^{17+}$	$-2.70(8)\cdot10^{-4}$	$8.2(2)\cdot10^{-5}$	$-1.6(3)\cdot10^{-2}$	$-1.2(3)$
$^{48}Ca^{17+}$	$-2.26(8)\cdot10^{-4}$	$7.1(2)\cdot10^{-5}$	$-2.5(4)\cdot10^{-2}$	$-2.2(3)$

ion	$\delta\nu_z\vert_{\nu_{res}}$ (mHz)	$\delta\nu_z\vert_Q$ (mHz)	$\delta\nu_z\vert_{\widetilde{u}_n^{\mathrm{ampl}}}$ (mHz)	$\delta\nu_z\vert_{\widetilde{\kappa}_{\mathrm{det}}}$ (mHz)
$^{12}C^{5+}$	1.5(4)	0.8(3)	3.0(8)	0.1(1)
$^{40}Ca^{17+}$	8.1(3)	1.2(1)	3.2(6)	0.1(1)
$^{48}Ca^{17+}$	1.8(1)	0.7(1)	5.0(8)	0.2(1)

been analyzed for each resonator parameter separately. Here, some axial dip spectra have been fitted by the line-shape model, introduced in eq. (3.53), using slightly different values of the studied resonator parameter and keeping the other three resonator parameters fixed at the determined values, listed in table 4.7. The extracted linear dependences of the axial frequency with respect to the altered resonator parameters are specified in table 4.8. From this table and the uncertainties of the resonator parameters, listed in table 4.7, the systematic uncertainty of the line-shape model of the dip signal is calculated. These absolute uncertainties are listed in table 4.9 together with the dip widths of the three ions. The tabulated line widths of the calcium ions, which scale with $q_{\mathrm{ion}}^2/m_{\mathrm{ion}}$, are consistent

Table 4.9: Systematic uncertainty of the axial dip fit caused by the uncertainty of the resonator parameters. In addition, the axial dip width and the corresponding line-splitting (=dip-width/$\delta\nu_z^{\mathrm{sys}}$) are listed for all three studied ions.

ion	$\delta\nu_z^{\mathrm{sys}}$ (mHz)	dip-width (Hz)	line-splitting
$^{12}C^{5+}$	4.5	0.48(2)	107
$^{40}Ca^{17+}$	12	1.23(1)	103
$^{48}Ca^{17+}$	8	1.03(1)	129

with each other. The slight deviation of the calcium line widths, which are predicted from the line width of the $^{12}C^{5+}$ ion (1.6 Hz for $^{40}Ca^{17+}$ and 1.3 Hz for $^{48}Ca^{17+}$), can be explained by the decrease of the quality factor.

Axial Temperature and Calibration of the First PnA Pulse

Thanks to the ergodic theorem, which states, that the energy distribution of a single particle, averaged over long time spans, agrees with the thermal energy distribution of an

ensemble of ions, we can measure the axial temperature of a single trapped ion.
The corresponding measurement cycle, which has also been explained in [13, 14], includes five steps: (1) In the PT the axial and the modified cyclotron mode are sideband coupled for several seconds, so that both, the modified cyclotron mode and the axial mode, thermalize with the axial resonator. (2) The ion is transported adiabatically[1] from the PT into the AT. (3) Here, the axial frequency is measured by a dip. (4) The ion is adiabatically transported back into the PT.
Repeating this cycle several 100 times, each measured axial frequency in the AT is slightly shifted due to different modified cyclotron energies and the corresponding B_2 shift of the axial frequency:

$$\Delta\nu_z^{AT} = \frac{B_2^{AT}}{B_0^{AT}} \frac{E_+}{(2\pi)^2 m_{\text{ion}} \nu_z^{AT}}. \tag{4.10}$$

Due to the sideband coupling in the PT the modified cyclotron energy is Boltzmann distributed in analogy to eq. (3.43): $\rho(E_+) = \frac{1}{k_B T_+} e^{-\frac{E_+}{k_B T_+}}$, so that the axial frequency shift $\Delta\nu_z^{AT} = \nu_z^{AT} - \nu_z^{ATOff}$ is also Boltzmann distributed:

$$\rho(\Delta\nu_z^{AT}) = \rho(E_+)\frac{dE_+}{d(\Delta\nu_z)} = \theta(\nu_z^{AT} - \nu_z^{ATOff}) \cdot \text{K1} \cdot e^{-\text{K1}\cdot(\nu_z^{AT} - \nu_z^{ATOff})}, \tag{4.11}$$

where $\text{K1} \equiv \frac{(2\pi)^2 B_0^{AT} m_{\text{ion}} \nu_z^{ATOff}}{B_2^{AT} k_B T_+}$ and $\theta(\nu_z^{AT} - \nu_z^{ATOff})$ is a Heavyside function. The parameters K1 and ν_z^{ATOff} are extracted via a maximum likeliood fit, see fig. 4.12. The final determined axial temperature of $T_z = 5.5(3)\,\text{K}$ corresponds with the expectation of $4-5\,\text{K}$.
In a very similar way, the first PnA pulse can be calibrated for small excitation amplitudes. Here, only the first pulse of the PnA cycle is performed in the PT. Subsequently the axial frequency shift is measured in the AT. As explained in section 5.1, usually Γ-resonances at different modified cyclotron energies are measured to cancel the frequency shifts due to the relativistic mass increase.

4.3.3 Preparation of the Analysis Trap

Tuning Ratio Optimization

In the AT the axial frequency shifts caused by a magnetron burst excitation would be generated by the dominant electric field imperfection (C_4), but also by the dominant magnetic field imperfection (B_2), which is a factor $B_2^{\text{AT}}/B_2^{\text{PT}} \approx 10400$ larger than in the PT. Nevertheless, axial frequency shifts due to an axial energy increase are only caused by the dominant electric field imperfections, compare eq. (3.19) and eq. (3.23). For this reason, we optimize the tuning ratio in the AT by minimizing the axial frequency shifts, when we dispose the ion at different axial temperatures. Here, we heat the axial resonator by applying white noise via the LC excitation line.

1 An adiabatic transport can be assumed, since the measured temperature does not change when the ion is transported back and forth for several times, before the axial frequency shifts are measured in the AT.

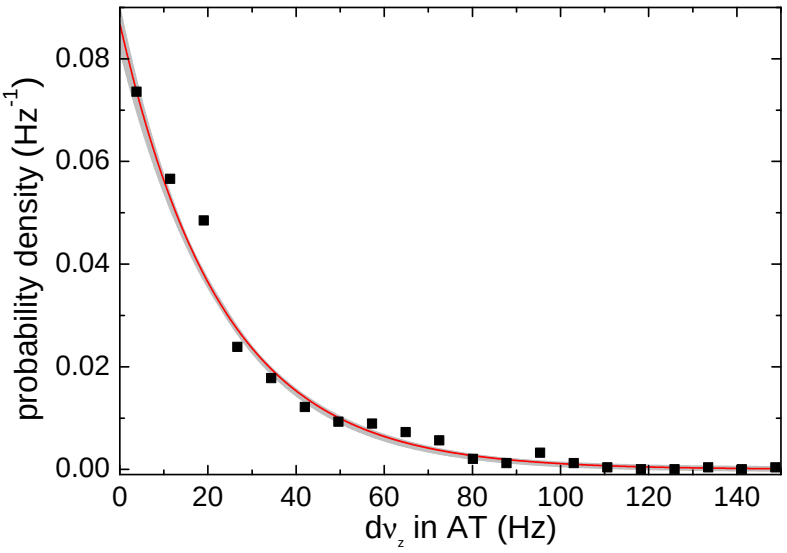

Figure 4.12: Boltzmann distribution of the axial frequency shifts in the AT generated by the large magnetic bottle and the thermal energy distribution of the modified cyclotron mode of a single $^{12}C^{5+}$ ion. To guide the eye, randomly histogrammed data are indicated by the black markers. The temperature is derived from a maximum likelihood fit, shown in red. The gray shaded area covers all possible ML fits within the 1σ uncertainty of K1 and thus T_z. The distribution contains 675 measurement cycles, where no feedback has been applied.

The Magnetic Bottle and Larmor Resonances in the AT

During the complete automated measurement of the frequency ratio Γ we induce the spin-flips in the AT at a fixed MW frequency and maximal MW power. Before we start the measurement, we need to measure the magnetic field in the AT to calculate the Larmor frequency. Besides the axial frequency, which we can easily measure as a dip signal, and the magnetron frequency, measured by a double-dip, in the AT, it is not possible to measure the modified cyclotron frequency by a double-dip, due to the large frequency shifts, generated by the magnetic bottle. Here, we scan the modified cyclotron frequency by applying modified cyclotron bursts at different ν_+ and measuring the size of the axial frequency shifts. A detailed analysis of this measurement method is given in the thesis of Anke Kracke [14]. The measured magnetic bottle has been shown in fig. 3.20.
In fig. 4.13 the Larmor frequency spectrum in the AT is shown at different ion positions and temperatures:

- The gray curve: A symmetric trapping voltage is applied, so that the axial ion position is shifted 75 µm from the center of the magnetic bottle. The ion is in thermal equilibrium with the axial resonator at $T_z \approx 4.5$ K.
- The blue curve: The same symmetric trapping voltage is applied. Additionally,

negative feedback cools the axial motion to $T_z \approx 2.3\,\mathrm{K}$. Also the magnetron motion is further cooled by an axial sideband coupling during the Larmor frequency irradiation.

- The red curve: The ion is moved into the center of the magnetic bottle by applying asymmetric trapping voltages. The negative feedback is applied in the same way as for the blue curve.

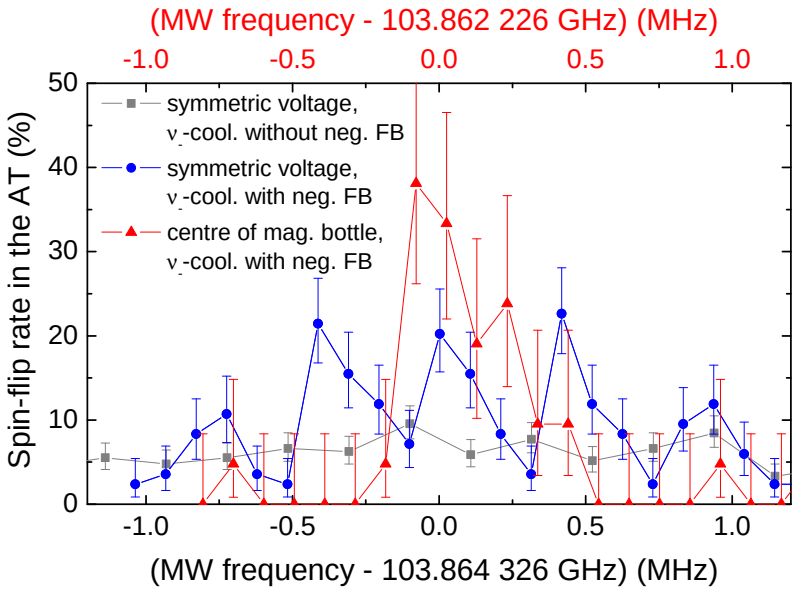

Figure 4.13: Spin-flip rate in the AT for different ion positions and temperatures. The x-axis of the gray and blue curve is given by the lower x-axis and the red curve corresponds to the upper x-axis. For further details see text.

All three Larmor frequency spectra can be interpreted by frequency modulations of the Larmor frequency, which are explained in the following. Instead of a constant magnetic field, the ion senses an oscillating magnetic field due to its movement in the magnetic bottle. Exclusively focusing on the axial motion of the ion and neglecting the radial motions, the magnetic field oscillates with the axial frequency:

$$\begin{aligned} B(t) &= B_0 + B_2 z^2 = B_0 + B_2(z_0 + \delta z(t))^2 \\ &= B_0 + B_2 z_0^2 + 2B_2 z_0 \delta z(t) + B_2 \delta z(t)^2, \end{aligned} \tag{4.12}$$

where z_0 is a fixed shift between the center of the magnetic bottle and the center of the axial motion and $\delta z(t) = z_0' \sin\left(\omega_z t + \varphi_z^0\right)$ is the axial motion of the ion. In that way, the Larmor frequency is not constant, but frequency modulated, which under certain conditions (non-vanishing modulation index) provides a sideband structure. The relation between the

signal strength of the carrier and the sidebands is characterized by the modulation index:

$$\eta \equiv \frac{\text{frequency deviation}}{\text{modulation frequency}} = \frac{\Delta\nu_L}{\nu_z} = \frac{2B_2\delta z z_0 + B_2\delta z^2}{B_0}\frac{\nu_L}{\nu_z} \approx \frac{2B_2\delta z z_0}{B_0}\frac{\nu_L}{\nu_z}. \tag{4.13}$$

For example, the relation between the signal strength of the carrier u_{carrier} and the first sideband u_{1stBand} is given by $u_{\text{carrier}}/u_{\text{1stBand}} = J(0,\eta)/J(1,\eta)$, where $J(0,\eta)$ is the Bessel function of first kind and zeroth order.
In case of the blue curve in fig. 4.13, the $^{12}C^{5+}$ ion has been shifted by $z_0 \approx 75\,\mu\text{m}$, the averaged axial amplitude in presence of negative feedback is about $\delta z \approx 14\,\mu\text{m}$, and $B_2 \approx 10500\,\text{T/m}^2$, $B_0 \approx 3.709\,\text{T}$, $\nu_L \approx 103.86\,\text{GHz}$ and $\nu_z \approx 412\,\text{kHz}$. Here, we derive a modulation index of about $\eta \approx 1.5$. The listed amplitude relations between the carrier,

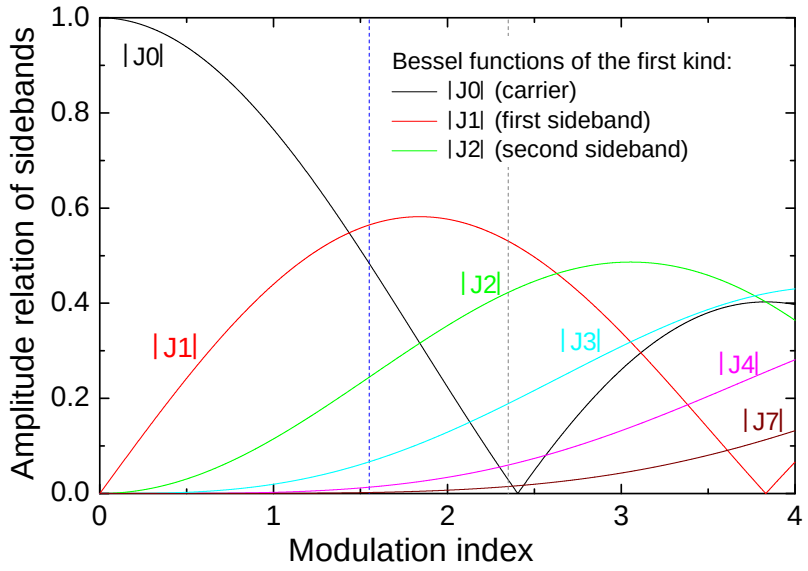

Figure 4.14: Amplitude relations between the carrier and the first sidebands as a function of the modulation index. The vertical blue (gray) line indicates the modulation index of the blue (gray) Larmor frequency spectra in fig. 4.13.

the first and second sideband at $\eta = 1.5$, see the blue vertical curve in fig. 4.14, roughly agree with the observed amplitude relation in fig. 4.13, where the carrier and both first sidebands have the same size and the second sidebands are smaller.
In case of the red curve, the modulation index is close to zero, since $z_0 \approx 0\,\mu\text{m}$ and only the carrier exists. The asymmetric line-shape is given by the Boltzmann distribution of the axial energy.
Also the flat gray curve in fig. 4.13 might be explained firstly by the increased modulation index of the axial motion but also the magnetron motion, where the sideband structure

cannot be resolved.
In that way, the spin-flip rate in the AT can be maximized by adjusting the axial position of the ion in the center of the magnetic bottle. This is a significant improvement compared to the very low spin-flip rate in the AT during the measurement of the bound-electron g-factor measurement on lithiumlike silicon, see the thesis of Anke Kracke [14]. Here, the spin-flip rate in the AT has been only 1%, which significantly elongated the automated measurement period and moreover reduced the statistical uncertainty.

4.4 The Measurement Process

The complete measurement process of the Γ-resonance is automated. All electronic components of the experiment are remotely controlled via GPIB, RS232, USB or Ethernet connections. The steering of the measurement process and the data acquisition is programmed in LabVIEW, a visual programming language from National Instruments. In the following, the operations during one measurement cycle are listed:

1. The measurement cycle is started in the AT to determine the spin state of the bound electron:
   a) In the beginning the proper high-precision voltages are applied to the ring and correction electrodes of the AT, so that the ion oscillates in the center of the magnetic bottle. In this way, the modulation index is reduced and the spin-flip probability maximized, see section 4.3.3. All other electrodes are grounded.
   b) For several seconds the magnetron mode is cooled via axial sideband coupling. At the same time negative feedback is applied.
   c) Since the axial frequency jump generated by the spin-flip of the bound electron scales inversely with the ion mass, $\Delta\nu_z^{\mathrm{sf}} = 580\,\mathrm{mHz}$ for $^{12}C^{5+}$, $\Delta\nu_z^{\mathrm{sf}} = 170\,\mathrm{mHz}$ for $^{40}Ca^{17+}$, $\Delta\nu_z^{\mathrm{sf}} = 140\,\mathrm{mHz}$ for $^{48}Ca^{17+}$, see table 3.6, different frequency measurement techniques are used for an efficient spin-state resolution:
      i. $^{12}C^{5+}$ measurement: It is sufficient to use the axial peak detection including zero-padding, which is explained in section 3.4.1. Reducing the statistical error, this method is repeated six times and the average value of the axial frequency is derived (40 s).
      ii. $^{40}Ca^{17+}$ and $^{48}Ca^{17+}$ measurements: For a proper resolution of axial frequency jumps below 200 mHz, a phase-sensitive detection method has been applied, which is explained in section 3.4.2.
         A. After the arrival of the ion in the AT, the voltages are chosen in a way that the ion is placed about 500 Hz above the resonator frequency to increase the cooling time constant. Initially, the axial frequency is determined by measuring the frequency spectrum of the dispersive dip. Afterwards, the trapping voltage is adjusted, so that the axial frequency is always the same in each measurement cycle. In that way, we persistently use the same FFT-bin, for the readout of the axial phase.

B. The measurement time of the axial phase is chosen in a way, that a spin-flip would induce an axial phase shift of about 60°. E.g. for $^{48}Ca^{17+}$ the measurement time is $\Delta\varphi/(360°\Delta\nu_z^{sf}) = 1/(6 \cdot 0.14\,\text{Hz}) = 1.2\,\text{s}$. Working with signal readout times of 512 mHz, the phase evolution time is about 0.95 s. For a further increase of the cooling time constant, during the phase evolution time the axial resonator is shifted several 100 Hz applying 90° feedback. This measurement cycle is repeated four times. Finally, the four measured phases are unwrapped and averaged.

d) Subsequently, for 30 s we try to induce electron spin-flips by injecting microwaves with maximal accessible power at the expected Larmor frequency. During this time negative feedback is applied. In this way, the modulation index is reduced and the spin-flip probability maximized.

e) Afterwards, the axial frequency is detected, as explained in item 1c. In case the axial frequency has shifted more than $\pm\Delta\nu_z^{sf}/2$, we detect an axial frequency jump, which is caused by a spin-flip, arising from the continuous Stern-Gerlach effect. From the algebraic sign of the jump, we determine the spin state and continue the measurement cycle with the transport into the PT, see item 2. In case we do not observe an axial frequency jump, we repeat the MW irradiation in item 1d and the axial frequency in item 1c until a spin-flip is observed.

2. Knowing the spin state of the bound electron, the ion is adiabatically transported from the AT to the PT.

3. Measurement of one frequency ratio Γ^* in the PT:

a) In the beginning, the proper high-precision voltage is applied to the ring and correction electrodes of the PT. All other electrodes are grounded. Then, both radial modes are cooled via axial sideband coupling, each for several seconds.

b) At first, we determine the modified cyclotron frequency from a double-dip signal ν_+^{DD}, see section 3.3.2. Here, we average over 25 successively recorded Fourier spectra, each derived from an 8 s readout signal, so that the total measurement time is 200 s.

c) Subsequently the axial frequency ν_z^I is measured via a dip-signal, see section 3.2.3. Again, we use a total averaging time of $25 \cdot 8\,\text{s} = 200\,\text{s}$.

d) Then the PnA cycle, described in section 3.4.2 is realized 10 times with the following phase evolution times: $6 \times 10\,\text{ms}, 1\,\text{s}, 2\,\text{s}, 2 \times 5\,\text{s}$.

i. Measurement of the starting phase: The 10 ms measurements determine the starting phase. They can be repeated to reduce the statistical uncertainty, since magnetic field fluctuations can be neglected at these time scales.

ii. Phase unwrapping: The double-dip measurement, as well as the 1 s and 2 s PnA cycles are essential for a proper phase unwrapping.

iii. Measurement of the present magnetic field: The first 5 s measurement determines the current modified cyclotron frequency and thus the magnetic field.

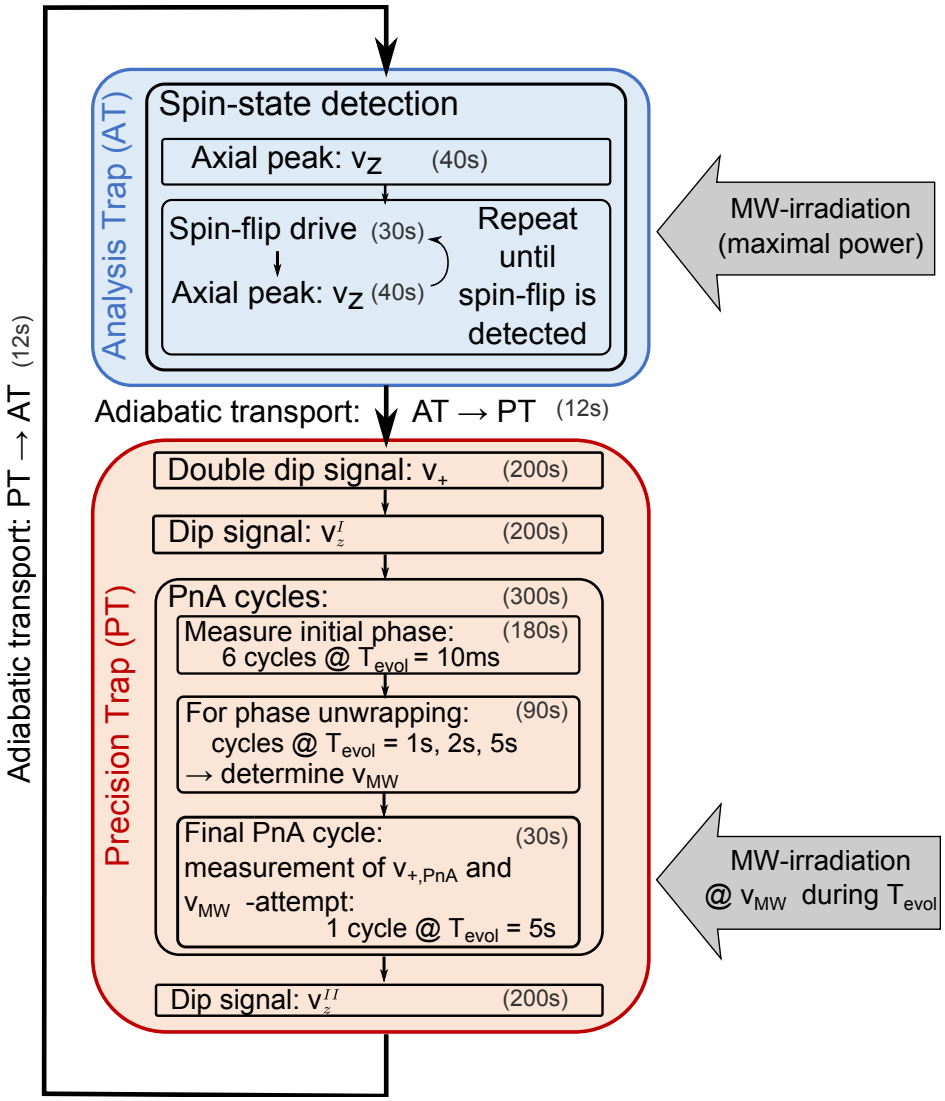

Figure 4.15: Flow chart of the measurement cycle [131]. For details see text.

iv. Probing the Larmor frequency and simultaneously measuring the magnetic field: From the first 5 s PnA measurement the scanning frequency ν_{MW} of the microwave field is derived, which is injected during the second 5 s PnA measurement. Since the probing of the Zeeman transition at ν_{MW} and the measurement of the modified cyclotron frequency, ν_+^{PnA}, happen at the same time during the last PnA cycle, magnetic field fluctuations cancel to a large extent in the obtained ratio of the frequencies[1].

e) To consider changes of the trapping voltage during the PnA cycles a further

1 Sometimes also phase evolution times of 10 s have been applied during the last PnA cycle.

dip-signal ν_z^{II} is measured for an interpolation of the axial frequency, $\nu_z = (\nu_z^I + \nu_z^{II})/2$. From ν_+^{PnA}, ν_z and ν_- from previous measurements[1] we calculate the free cyclotron frequency: $\nu_c = \sqrt{\nu_{\mathrm{PnA},+}^2 + \nu_z^2 + \nu_-^2}$. In combination with the probed Larmor frequency ν_{MW} we determine a frequency ratio: $\Gamma^* = \nu_{\mathrm{MW}}/\nu_c$.

4. Finally, the ion is transported back to the AT and the spin state is determined in the same way as in the beginning of the cycle, see item 1. At each measurement cycle we determine one frequency ratio Γ^* and the corresponding binary information, whether the attempt to flip the spin in the PT was successful or not.

During the electron mass measurement the whole measurement cycle, which is also illustrated in fig. 4.15, took typically 25 min.
This measurement sequence is repeated several 100 times for one to two weeks. During that time, we enter the lab only for the filling of the liquid gas reservoirs. Due to temperature drifts, which occur during and after the filling, measurement cycles which have been performed after the filling for about 4 hours are removed from the final data analysis (data cuts).
In the final analysis the spin-flip probability is analyzed as a function of the measured frequency ratios Γ^*, see fig. 4.20. Here, the modified cyclotron energy of the single $^{12}C^{5+}$ ion amounts to $E_+ = 0.26(2)$ eV ($r_+^{\mathrm{evol}} = 13.4(6)$ µm) during the PnA phase evolution time of $T_{\mathrm{evol}} = 10$ s. The line-shape of this so-called Γ-resonance is discussed below. Since the phase jitter of the modified cyclotron mode represents the main contribution to this line-shape, we discuss it separately in the following section.

1 The contribution of ν_- to ν_c is very small and only an occasional measurement is required.

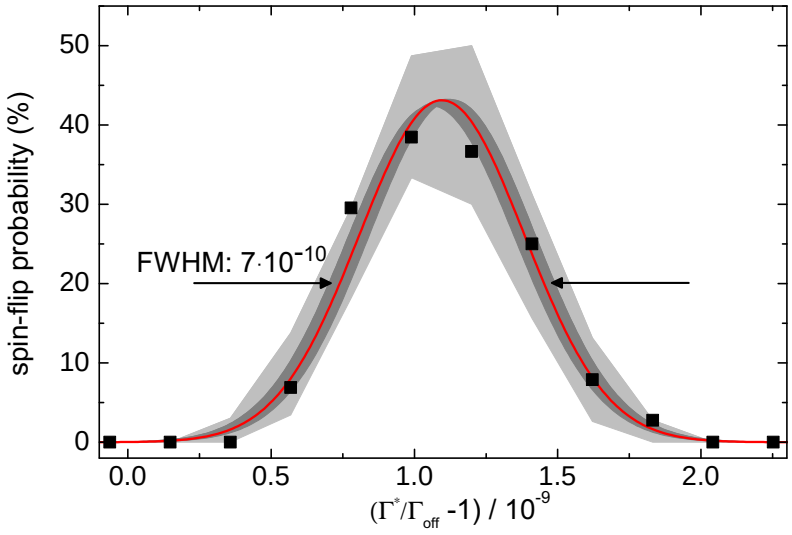

Figure 4.16: A Γ-resonance represents the spin-flip rate in the PT in dependence of the measured frequency ratio Γ^*. Here, the frequency ratios of $^{12}C^{5+}$ are scaled by a constant: $\Gamma_{\text{off}} = 4376.210497791$. To guide the eyes, randomly histogrammed data are indicated by the black markers. The final Γ value is extracted from the maximum-likelihood (ML) fit-routine shown in red line. The corresponding line-shape model is discussed in section 4.5. The dark gray area covers all possible ML line-shapes within the 1σ uncertainty of the final Γ value. The bright gray area illustrates the binomial uncertainty of the histogrammed data based on the spin-flip probability of the ML-fit. The resonance includes 53 measurement cycles, which feature a spin-flip in the PT, and 544 measurement cycles featuring no spin-flip in the PT (adopted from [77]).

4.5 Line-Shape Model of the Γ-Resonance

The line-shape model of the Γ-resonance requires a detailed understanding of the composition of the modified cyclotron phase jitter, which emerges during the PnA measurement. As a phase jitter we define the standard deviation of subsequently measured phase differences divided by the square root of two: $\delta\varphi = \text{std}(\text{diff}(\varphi))/\sqrt{2}$, which is often also termed as Allan deviation.

4.5.1 Sources of the Modified Cyclotron Phase Jitter

The PnA measurement of ν_+ is limited by the jitter of the detected modified cyclotron phase, see eq. (3.71). For further improvements of the ν_+ determination, it is of great importance to study the sources of this jitter. For a profound explanation of the presently observed phase jitter we consider essentially three different sources: (1) an intrinsic thermal jitter, (2) an intrinsic technical phase detection uncertainty and (3) a magnetic field jitter. In the following these three different types of phase jitter are studied separately.

The Intrinsic Thermal Phase Jitter

The intrinsic thermal phase jitter of the first PnA pulse - a radial dipole excitation of the modified cyclotron motion - has been briefly mentioned in fig. 3.10. In that scheme the initial thermal energy distribution of the modified cyclotron mode is indicated by the gray cloud at time t_0. The measured phase jitter depends on this Boltzmann distribution in two different ways:

- In principle, the radial spread of the ion generates a phase jitter right after the first PnA pulse is applied, which is denoted as $\delta\varphi_{\mathrm{therm}}$ in fig. 3.10. In table 4.11 (5^{th} column) this jitter has been calculated for different modified cyclotron energies, assuming an initial temperature of about $T_+ = 130\,\mathrm{K}$. In principle, the jitter could be reduced by a better, improved cooling of the initial ion motion, e.g. by using a cyclotron resonator, or by an increase of the excitation strength of the first PnA pulse. The latter way, however, is not favorable, since higher modified cyclotron energies during the phase evolution time lead to larger systematic shifts with larger systematic uncertainties.
- Furthermore, the thermal distribution of the modified cyclotron radius leads to different modified cyclotron energies during the phase evolution time. Therefore different energy dependent phase shifts occur, e.g. due to C_4, C_6, B_2 and special relativity. This effect increases linearly with the evolution time. At very small phase evolution times, e.g.: 10 ms, even for the highest excitation energies these shifts are negligible with respect to the other sources of phase jitter. For a phase evolution time of 5 s these phase jitters are summarized in table 4.10. They are calculated for a single $^{12}C^{5+}$ ion at the largest applied modified cyclotron radius of $r_+ = 90(4)\,\mu\mathrm{m}$ and a conservative estimation of the axial temperature $T_z = 5\,\mathrm{K}$ during the sideband cooling. In comparison to the absolute value of the measured phase jitter of at least 10°, see table 4.11 (7th column), these jitters can be completely neglected.

Table 4.10: Thermal phase jitter of the modified cyclotron mode of a single $^{12}C^{5+}$ ion after 5 s phase evolution time and at a radius of $r_+ = 90(4)\,\mu\mathrm{m}$, caused by the leading-order magnetic and electric inhomogeneity and special relativity.

effect	$\delta\varphi(°)^a$
B_2	2.3(1)
spec. relat.	2.3(1)
residual C_4	0.02(2)
C_6	0.04(1)

a Throughout this thesis phase jitters are presented as the standard deviation of the phase differences of subsequent PnA cycles divided by the square root of two.

A third source of thermal phase jitter could arise from the second PnA pulse. Nevertheless, since $r_+^{\mathrm{evol}} > z\sqrt{\nu_z/\nu_+} = 3.3\,\mu\mathrm{m}$ during the phase evolution time, no significant phase jitter is mixed-in by the parametric second PnA pulse, see fig. 3.18.

The Technical Phase Detection Uncertainty

The technical readout phase jitter arises during the readout process of the axial peak signal. Since it is completely independent of the motion of the ion, we studied this effect by inducing an artificial peak signal a few kHz next to the axial resonator of the PT (≈ 630 kHz) via the quadrupole excitation. The peak signal has been generated by an exponentially decreasing sine signal, simulating a thermalizing excited ion. The readout signal has the usual length of 512 ms. Similar to the cooling time constant of a single $^{12}C^{5+}$ ion, the exponential modulation had a decay constant of 260 ms. The phase detection uncertainty scales with the signal-to-noise ratio of the peak signal, see fig. 4.17. The white

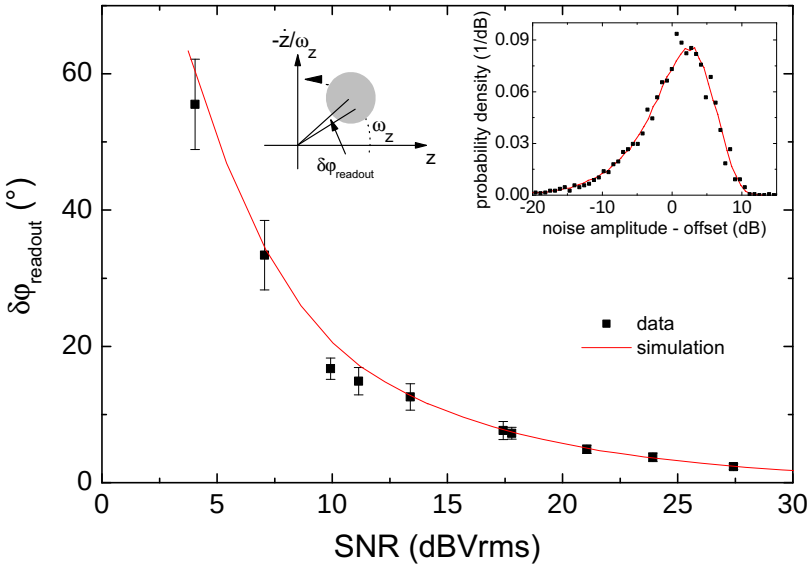

Figure 4.17: Measurement of the intrinsic technical phase detection uncertainty by an artificially generated, exponentially decreasing sine signal ($\tau = 260$ ms $\approx 0.5 \cdot$ signal length) for different signal-to-noise (SNR) ratios. The numerically predicted detection uncertainty (red line) is in reasonable agreement with the data. This prediction relies on the distribution of the noise amplitudes, see gray cycle in the left inset, which is also in good agreement with the expectation, see right inset [131].

noise of both the real and imaginary part of the fast Fourier spectrum leads to a probability density of the noise amplitude of a single FFT-bin shown in the right inset in fig. 4.17. The subsequent numerical prediction of the phase detection uncertainty (red line in fig. 4.17) is in reasonable agreement with the data (black markers).
An unfavorable axial peak position with respect to the FFT-binning, the so-called frequency bleeding, might reduce the apparent SNR. In case that the peak-signal *bleeds* likewise into two FFT-bins the SNR is reduced by maximally 3 dB. The phase detection uncertainty can be diminished by a larger SNR, which in the future might be achieved by a resonator with a higher quality factor or by a larger excitation during the second PnA pulse. The excitation

strength is limited by higher-order electric field imperfections [120] in combination with the initial thermal distribution of the amplitudes, which shift the axial frequency out of the readout bin.

Predicting the Phase Jitter of the Measured 10 *ms PnA Cycles*

The combination of the thermal and the readout phase jitter has been studied in PnA cycles with short phase evolution times of 10 ms. In fig. 4.18(a) and (c) the Gaussian distributed phase differences of subsequent PnA measurements are histogrammed for different modified cyclotron radii during the phase evolution time of $r_+^{\mathrm{evol}} = 30(2)$ µm and $r_+^{\mathrm{evol}} = 90(4)$ µm. In table 4.11 the measured phase jitters (6$^{\mathrm{th}}$ column) are listed for different modified cyclotron radii (1$^{\mathrm{st}}$ column, determined by the first PnA pulse) of $^{12}C^{5+}$ and $^{48}Ca^{17+}$ ions and the measured averaged SNR (2$^{\mathrm{nd}}$ column, determined by the second PnA pulse). The readout jitter, also stated as phase detection uncertainty (3$^{\mathrm{rd}}$ column), is calculated

Table 4.11: Analysis of the 10 ms phase jitter for a single $^{12}C^{5+}$ and $^{48}Ca^{17+}$ ion. Comparison between the modeled phase jitter (the squared sum of the thermal jitter and the phase detection uncertainty) and the measured phase jitter in dependence on the radius and the measured SNR [131].

	r_+^{evol}(µm)	avg-SNR (dB)	readout jitter (°)	thermal jitter (°)	modeled jitter (°)	measured jitter (°)
$^{12}C^{5+}$	13(1)	13.4(1)	13.8(1.7)	9.0(3)	16.5(1.5)	23.3(5)
	30(2)	13.0(2)	14.6(1.8)	3.9(2)	15.1(1.7)	15.8(5)
	36(2)	15.3(2)	10.3(1.3)	3.4(2)	10.9(1.2)	14.2(1.0)
	54(3)	11.0(2)	18.2(2.2)	2.2(2)	18.3(2.2)	16.6(1.1)
	90(4)	15.8(3)	12.4(1.5)	1.3(1)	12.4(1.5)	11.8(1.1)
$^{48}Ca^{17+}$	8(1)	17.7(2)	8.0(1.0)	9.5(9.9)	12.4(7.6)	15.8(7)
	14(1)	17.5(2)	8.4(1.0)	5.6(2.5)	10.1(1.6)	11.4(9)
	76(6)	18.1(3)	7.8(1.0)	1.0(1)	7.8(1.0)	7.0(4)
	109(8)	17.4(2)	8.9(1.1)	0.7(1)	8.9(1.1)	10.3(7)
	162(12)	15.2(4)	11.9(1.5)	0.5(1)	11.9(1.4)	34.5(3.8)

by determining the SNR of each measurements cycle separately using the fit-function in fig. 4.17. Afterwards the readout jitter is averaged. The final modeled phase jitter (5$^{\mathrm{th}}$ column), which is the squared sum of the calculated readout jitter (3$^{\mathrm{rd}}$ column) and the calculated thermal jitter (4$^{\mathrm{th}}$ column), is in reasonable agreement with the data. Significant deviations only occur at very small and very high energies. At very high energies this discrepancy might be explained by trap imperfections, which generate axial frequency shifts in a way, that the maximal peak signal jitters between different FFT-bins. In this case, the phase readout of a single fixed FFT-bin is not appropriate any longer.

The Magnetic Field Related Phase Jitter

During the phase evolution time an additional phase jitter is generated by the magnetic field fluctuations. The time dependent behavior of these fluctuations can be modeled by a

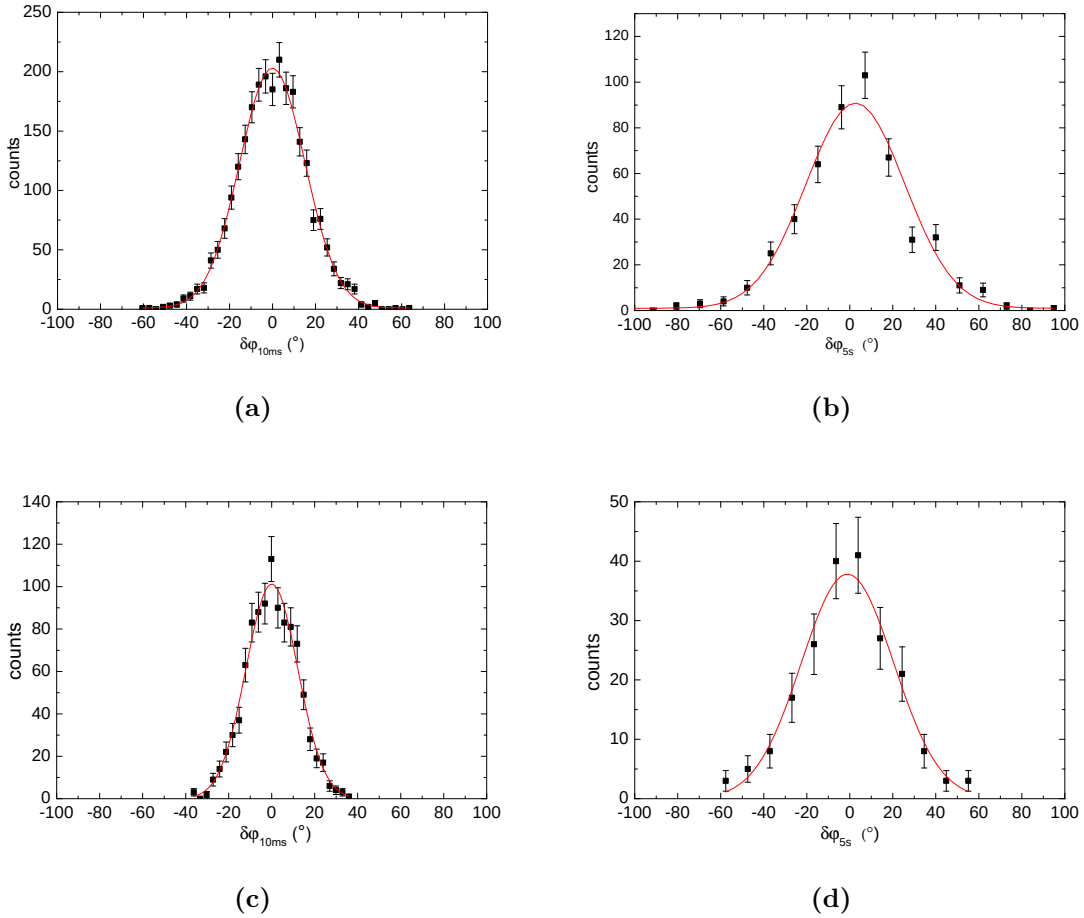

Figure 4.18: Histogrammed phase differences of subsequent PnA cycles ($\delta\varphi = \mathrm{diff}(\varphi_z)/\sqrt{2}$) at small modified cyclotron energies ($r_+^{\mathrm{evol}} = 30(2)$ µm) of a single $^{12}C^{5+}$ ion with phase evolution times of $T_{\mathrm{evol}} = 10$ ms (a) and $T_{\mathrm{evol}} = 5$ s (b). In (c) and (d) similar distributions are shown measured at a larger modified cyclotron radius of $r_+^{\mathrm{evol}} = 90(4)$ µm. All distributions have a Gaussian[a] line-shape (red line) [131].

a The Shapiro-Wilk test has been applied, which is a parametric hypothesis test [147]. The considered null hypothesis is, that the studied data set is Gaussian distributed with unspecified mean and variance. The calculated p-value describes the probability of observing the given result by chance, given that the null hypothesis is true. In fig. 4.18(a) the p-values is 8.6 % and in (b) only 6.3%. In that way, the null hypothesis is not rejected at a significance level of 5%.

random walk of the magnetic field, the corresponding standard deviation is given by:

$$\delta B \propto \delta\nu_+ \propto \sqrt{T_{\text{cycle}}}, \tag{4.14}$$

where $T_{\text{cycle}} \equiv T_{\text{evol}} + T_{\text{cooling}}$ is the time period of a complete PnA cycle, mainly composed of the phase evolution time of $T_{\text{evol}} = 10\,\text{ms}$ to 5 s and the cooling time T_{cooling} of all eigenmotions. During the measurement of the electron mass the cooling time has been 25 s and for the g-factor measurement on the calcium ions it has been 29 s. In combination with the model of the 10 ms phase jitter (readout jitter + thermal jitter), the total phase jitter has the following form:

$$\begin{aligned}\delta\varphi_+^{\text{tot}} &= \text{std}(\text{diff}(\varphi_+^{\text{meas}}))/\sqrt{2} \\ &= \sqrt{2(\delta\varphi_+^{10\text{ms}})^2 + (A\sqrt{T_{\text{cycle}}}\cdot 360^\circ \cdot T_{\text{evol}})^2}/\sqrt{2}.\end{aligned} \tag{4.15}$$

In fig. 4.19 the phase jitter of the modified cyclotron mode of $^{12}C^{5+}$ (a) and $^{48}Ca^{17+}$ (c) is plotted versus the phase evolution time of the PnA method. From these data the random walk constant A is extracted. The corresponding fit-functions are shown in red. For $^{48}Ca^{17+}$ ($A_{^{40}Ca^{17+}} = 0.00149(2)\,\text{s}^{-1.5}$) this constant is a factor of two smaller than for $^{12}C^{5+}$ ($A_{^{12}C^{5+}} = 0.00339(7)\,\text{s}^{-1.5}$), which might be explained by the better aligned axial compensation coil, as already mentioned in section 4.2.1. The right graphs of fig. 4.19 illustrate the corresponding relative magnetic field jitter $\delta B/B = \delta\varphi_+^{\text{tot}}/\nu_+/360^\circ/T_{\text{evol}}$. The optimal phase evolution time for a minimal frequency jitter is 8.3 s for $^{12}C^{5+}$ and 10 s for $^{48}Ca^{17+}$.

4.5.2 The Combined Line-Shape Model

The fundamental mechanism for a spin-flip transition is described by a Rabi oscillation of a quantized two level system (spin-up and spin-down state). The transition frequency, the Rabi frequency Ω, scales linearly with the drive amplitude. For a close-to-resonant drive of the Larmor frequency, ω_{L_0}, with the frequency $\omega_{\text{MW}} = \omega_{L_0} + \Delta$, where Δ is an offset, the Rabi frequency is modified $\Omega' \equiv \sqrt{\Omega^2 + \Delta^2}$ and the probability for a spin-flip is given by:

$$p_\uparrow(t) = \frac{\Omega^2}{\Omega'^2}\sin^2\left(\frac{\Omega' t}{2}\right). \tag{4.16}$$

Some conditions of our experiment, e.g. the existing magnetic field fluctuations, prohibit coherent Rabi oscillations of the electron spin on the time-scale of a cyclotron frequency measurement. As a starting point for the construction of a line-shape model of the Larmor resonance we thus use the time averaged value of the squared sine term:

$$p_{\text{sf}} = \frac{1}{2}\frac{\Omega^2}{\Omega^2 + \Delta^2}. \tag{4.17}$$

The spin-flip probability p_{sf} has a symmetric line-shape and saturates at a value of 0.5 for large Rabi frequencies. However, in the following we will exclusively focus on line-shapes well below saturation.

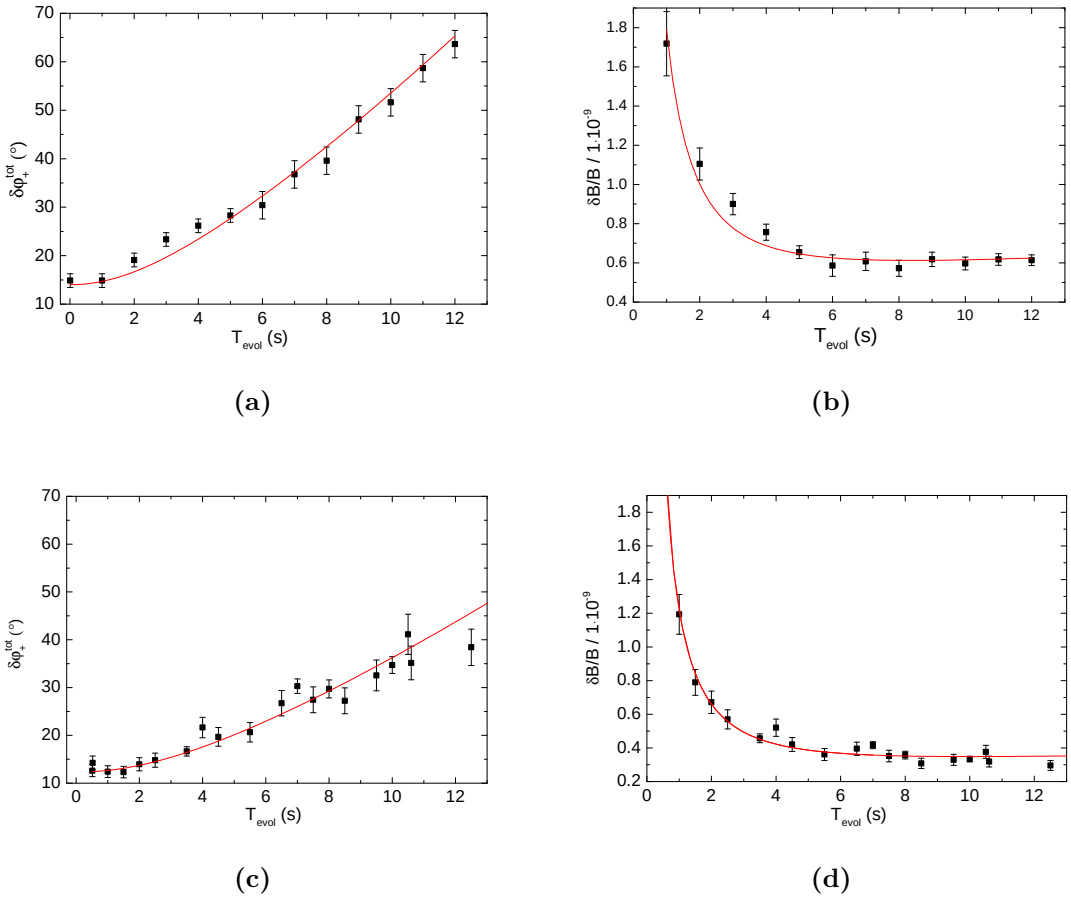

Figure 4.19: Study of the magnetic field jitter. PnA measurement of the magnetic field jitter in the PT with $^{12}C^{5+}$ at $r_+ = 30(2)$ µm (a,b) and $^{48}Ca^{17+}$ at $r_+ = 14(1)$ µm (c,d). The plots (a) and (c) present the phase jitter versus the phase evolution time and the plots (b) and (d) the corresponding relative jitter of the modified cyclotron frequency. The fit-functions (red lines) rely on a random walk model of the magnetic field. For further details see text and [131].

To take care of magnetic field drifts and fluctuations, we probe the spin-flip transition at the fixed frequency ω_{MW} and simultaneously measure the modified cyclotron frequency, ω_+^{PnA}, which requires a line-shape model in dependence on the measured frequency ratios, $\Gamma^* = \omega_{\mathrm{MW}}/\omega_c$:

$$p_{\mathrm{sf}}(\Gamma^*) = \frac{1}{2}\frac{\Omega^2}{\Omega^2 + \omega_{c_0}^2(\Gamma_0 + \delta\Gamma_0 - \Gamma^*)^2}, \tag{4.18}$$

where $\Gamma_0 = \frac{\omega_{L_0}}{\omega_{c_0}}$ is the final value of interest and $\delta\Gamma_0$ are systematic shifts. For clarity reasons we ignore any systematic shifts for a moment. They will be summarized in table 5.2 for the measurement of the single $^{12}C^{5+}$ ion and in table 6.1 for the calcium ions. Here,

we focus exclusively on four independent frequency jitters, which modify the shape of the Γ-resonance:

- The continuous thermalization of the axial mode during the 5 s measurement process affects the cyclotron and the Larmor frequency mainly caused by the leading-order inhomogeneity of the magnetic field, B_2. Since the measured modified cyclotron frequency is an average over the phase evolution time, only the Larmor frequency jitter alters the shape of the resonance, which causes the dominant asymmetric contribution of the line-shape (E_z-B_2 asymmetry), see also the thesis of Verdú [118]:

$$p_{\mathrm{sf}}(\Gamma^*) = \frac{1}{2}\int_0^\infty \frac{\Omega^2}{\Omega^2 + \omega_{c_0}^2\left(\Gamma_0 + \alpha_{\mathrm{B2}}\cdot(E_z - \bar{E}_z) - \Gamma^*\right)^2}\frac{1}{k_B T_z} e^{-\frac{E_z}{k_B T_z}}\,\mathrm{d}E_z, \quad (4.19)$$

  where $\alpha_{\mathrm{B2}} \equiv B_2\cdot(B_0\cdot\omega_z^2\cdot m_{\mathrm{ion}})^{-1}\cdot(\omega_{L_0}/\omega_{c_0})$. Due to the same, but averaged effect in the modified cyclotron frequency, which is considered by the averaged term $-\alpha_{\mathrm{B2}}\cdot\bar{E}$, the difference between the maximum and the mean value of the line-shape is small. For an axial temperature of $T_z = 3.6\,\mathrm{K}$ and a spin-flip probability of about 30% the relative effect is:

$$\frac{\Gamma_{\mathrm{mean}} - \Gamma_{\mathrm{max}}}{\Gamma_{\mathrm{max}}} \approx 3\cdot 10^{-13}. \quad (4.20)$$

- Since the modified cyclotron frequency has Gaussian distributed thermal and readout jitters of $\delta(\varphi_{10\mathrm{ms}}) \approx 14(1)^\circ$ (for $^{12}\mathrm{C}^{5+}$), see fig. 4.18(a) and the 5$^{\mathrm{th}}$ column of table 4.11, also the measured Γ^* has the same relative jitter contribution, which has to be considered in the line-shape model by a Gaussian convolution.
- A further jitter of the measured Γ^* values is caused by the random walk of the magnetic field during the measurement, see figure 4.19(b). In case of a $^{12}\mathrm{C}^{5+}$ ion and phase evolution time of 5 s, we have: $\delta\varphi_+^{\mathrm{rw}} = A\cdot 360^\circ\cdot\sqrt{5\,\mathrm{s}}\cdot 5\,\mathrm{s}/\sqrt{2} = 10(1)^\circ$, where: $A = 0.00339(7)\,\mathrm{s}^{-1.5}$. In a good approximation this jitter can be convoluted in the same way as the thermal and readout jitters. In total the Gaussian phase jitters cause a relative uncertainty of the modified cyclotron frequency:

$$\delta\nu_+/\nu_+ = \frac{\sqrt{7/6(\delta\varphi_{10ms})^2 + (\delta\varphi_{\mathrm{rw}})^2}}{360^\circ\cdot\nu_+\cdot T_{\mathrm{evol}}} \approx 4(1)\cdot 10^{-10}. \quad (4.21)$$

  The factor 7/6 originate from the six averaged 10 ms PnA cycle and the final 5 s PnA cycle.
- Another jitter of the measured free cyclotron frequency is caused by the measurement of the axial frequency. The fluctuations of the two axial dip measurements (before and after the PnA cycles) amounts to 30 mHz. With an uncertainty of $\delta\nu_z = 15\,\mathrm{mHz}$ for the interpolated axial frequency, the final relative jitter of the free cyclotron frequency is: $1.7\cdot 10^{-11}$, which can be neglected in the line-shape model of the Γ-resonance.

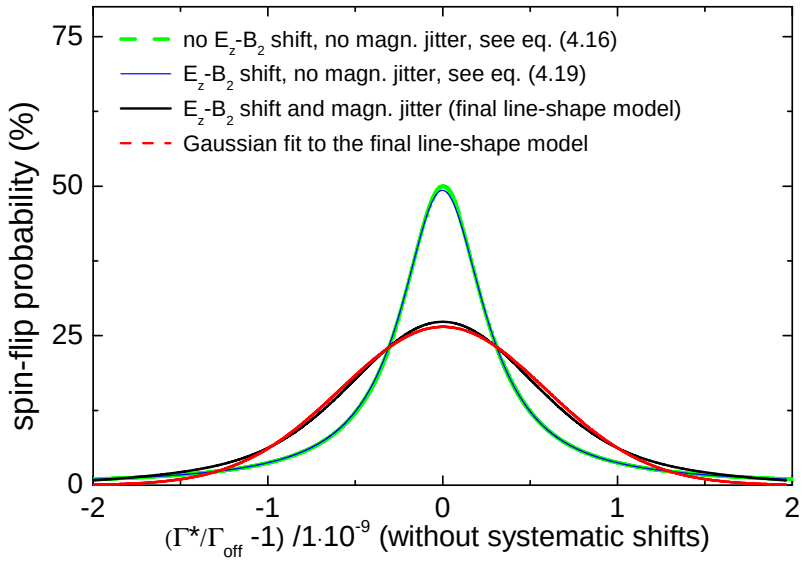

Figure 4.20: Analysis of the line-shape model of the Γ-resonance: In green: The pure, averaged Rabi resonance is shown with a Rabi frequency of $\Omega = 30\,\text{Hz}$ (see equation (4.16)). In blue: An additional E_z-B_2 asymmetry with $T_z = 3.6\,\text{K}$ (see equation (4.19)) is added. In black: The complete line-shape model is shown, also including the Gaussian phase jitter of $4 \cdot 10^{-10}$. In red: A Gaussian distribution is fitted to the complete line-shape model [131].

In figure 4.20 the different contributions of the line-shape model are presented: (1) The pure averaged Rabi resonance with a Rabi frequency of $\Omega = 30\,\text{Hz}$ is plotted (green line, eq. (4.16)). (2) An E_z-B_2 asymmetry with $T_z = 3.6\,\text{K}$ is added (blue line, eq. (4.19)). (3) The complete line-shape model is shown, also including the convoluted Gaussian phase jitter of $\delta\Gamma^*/\Gamma = 4 \cdot 10^{-10}$ (black line).
Finally the complete line-shape model of the Γ-resonance is compared with a Gaussian distribution (red line). The deviation between the centroid of the line-shape model and the mean value of the Gaussian fit is only $1 \cdot 10^{-13}$. For that reason the Gaussian line-shape approximation is justified, as long as the maximal spin-flip probability is well below the saturation value of 50%. The characteristic model parameters, the maximal spin-flip probability of $\approx 27\%$ and the full width at half maximum (FWHM) of $\approx 1.3 \cdot 10^{-9}$ are in good agreement with the measured Γ-resonances, which have maximal spin-flip rates of 25-45% and FWHM's of $0.7\text{-}1.35 \cdot 10^{-9}$. The rather smaller resonance widths of the measured data might be explained by a partial cancellation of the magnetic field jitter in the measured frequency ratio Γ^*.

Finally the Gaussian line-shape,

$$\mathcal{G}(\Gamma^*;\mathrm{sf}_0,\Gamma_{\mathrm{res}},\sigma_\Gamma) \equiv \frac{\mathrm{sf}_0}{2\pi\sigma_\Gamma^2} e^{-\frac{(\Gamma^*-\Gamma_{\mathrm{res}})^2}{2\sigma_\Gamma^2}}, \tag{4.22}$$

is applied as a maximum-likelihood fit to the data, see [13]:

$$\begin{aligned}\log\left[\mathcal{L}(\mathrm{sf}_0,\Gamma_{\mathrm{res}},\sigma_\Gamma)\right] = &\sum_{i=1}^{N_{\mathrm{Sf}}} \log(\mathcal{G}(\Gamma^{*,\mathrm{Sf}}(i);\mathrm{sf}_0,\Gamma_{\mathrm{res}},\sigma_\Gamma)) + \\ &\sum_{j=1}^{N_{\mathrm{NonSf}}} \log(1-\mathcal{G}(\Gamma^{*,\mathrm{NonSf}}(j);\mathrm{sf}_0,\Gamma_{\mathrm{res}},\sigma_\Gamma)),\end{aligned} \tag{4.23}$$

extracting the desired mean value Γ_{res}, the maximal spin-slip rate (sf_0) and the width of the resonance (σ_Γ). A typical Γ-resonance has been shown in fig. 4.20. Here, the red line represents the maximum-likelihood fit, the dark gray area is the error band of the mean value, the black markers illustrate binned data and the bright gray area the binomial prediction band of the binned data with the probability given by the maximum-likelihood fit.

CHAPTER 5

Determination of the Atomic Mass of the Electron

In the present chapter, I will present the measurement results of the atomic electron mass, which have been published in [77]. An extensive paper focusing in detail on the line-shape model of the Γ-resonance, see section 4.5, as well as on all the reviewed systematic shifts has been recently accepted [131]. In the beginning of this chapter, in section 5.1, I will introduce the data sets considered in the final analysis, which include measurement runs of three independently produced, single $^{12}C^{5+}$ ions measured at different modified cyclotron energies. In the end of section 5.1, I will specify the extrapolated statistical Γ value at zero modified cyclotron energy, featuring a relative precision of $2.3 \cdot 10^{-11}$. In the following section, section 5.2, I will summarize the various systematic shifts and the corresponding uncertainties. Finally, in section 5.4, I will combine our measured frequency ratio with the predicted g-factor and the ion mass of $^{12}C^{5+}$ to quantify the atomic mass of the electron with a relative uncertainty of $2.8 \cdot 10^{-11}$.

5.1 Statistical Γ-Value

Regarding the high-precision measurement of the Γ-ratio of $^{12}C^{5+}$, the data acquisition has been accomplished within 4.5 months, starting in the end of November 2012. At that time various Γ-resonances have been measured at different modified cyclotron energies during the PnA phase evolutions, see for example fig. 4.20 and fig. 5.1. To minimize the probability of the very unlikely scenario, that we have worked not only with one single trapped $^{12}C^{5+}$ ion, but in presence of other unwanted trapped ions, we removed the studied $^{12}C^{5+}$ ion two times on purpose during the data acquisition and subsequently prepared further single trapped $^{12}C^{5+}$ ions. A list of all selected measurement runs is given in table 5.1. It only contains data sets with at least 30 detected spin-flips in the PT. In total, 3096 measurement cycles / Γ^* measurements are considered in the final analysis. With an averaged measurement cycle time of half an hour and four hours per day, which have to be cut out due to the filling of the cryogenic reservoirs, the pure measurement time amounts to 11 weeks.

To map out relativistic frequency shifts, see section 3.5.2, Γ-resonances have been recorded at different modified cyclotron energies. In fig. 5.2 the fitted central values of all Γ-resonances are plotted as a function of the excitation strength of the first PnA pulse, which is proportional to the energy of the modified cyclotron mode during the phase evolution

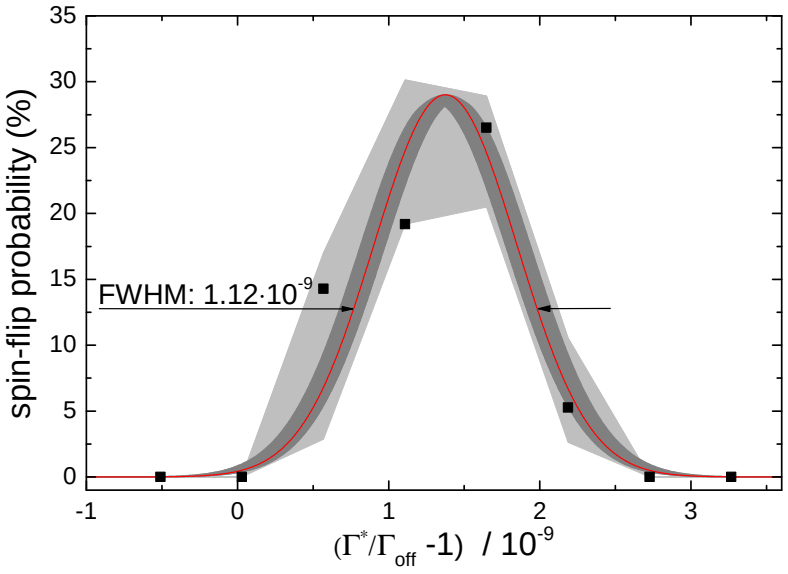

Figure 5.1: Γ-resonance measured with a single $^{12}C^{5+}$ ion at a modified cyclotron energy of $E_+ = 4.2(5)$ eV ($r_+^{\mathrm{evol}} = 54(3)$ µm) during the PnA phase evolution time of $T_{\mathrm{evol}} = 5$ s. The resonance includes 43 measurement cycles which feature a spin-flip in the PT and 236 measurement cycles featuring no spin-flip in the PT. For the description of the denoted error bands, see fig. 4.20 [131].

Table 5.1: List of all measurement runs used for the electron mass determination. Only measurement runs with more than 30 induced spin-flips in the PT are considered. In the first column the name of the $^{12}C^{5+}$ ion (I, II or III) is denoted. The second column contains the amplitude of the first PnA pulse, which is proportional to the modified cyclotron energy. Mapping out relativistic frequency shifts by a linear extrapolation to zero modified cyclotron energy, see fig. 5.2, most data has been recorded at low modified cyclotron energies.

ion	U_{exc} (Vpp)	# sf-cycles	# all cycles
III	0.075	245	1763
II, III	0.17	66	724
I	0.2	33	128
III	0.3	43	279
III	0.5	35	202

time. The observed linear energy dependence is mainly given by the relativistic shift of the modified cyclotron frequency:

$$(\delta\Gamma/\Gamma)_{\mathrm{relat}} \approx \delta\nu_c/\nu_c \approx \delta\nu_+/\nu_+ \approx E_+/(m_{\mathrm{ion}}c^2) \approx 8.9 \cdot 10^{-11}\,\mathrm{eV}^{-1} \cdot E_+. \tag{5.1}$$

Minor contributions to the slope of the linear extrapolation in fig. 5.2 are caused by trap imperfections: (1) A tiny contribution is given by the leading-order electric field imperfection, the uncertainty of C_4: $\delta C_4 \approx 1.1 \cdot 10^{-5}$, see eq. (4.8) and eq. (3.19): $(\delta\Gamma/\Gamma)_{C_4} \approx 6C_4\nu_z^4/(q_{\text{ion}}U_r C_2^2 4\nu_+^4)E_+ \approx 8.9 \cdot 10^{-13}\,\text{eV}^{-1} \cdot E_+$, which is about two orders of magnitude smaller than the relativistic shift. (2) The contribution of the leading-order magnetic field imperfections (B_2) basically cancels, see eq. (3.23). A residual effect: $(\delta\Gamma/\Gamma)_{B_2} \approx 6.5 \cdot 10^{-14}\,\text{eV}^{-1} \cdot E_+$ is more than three orders of magnitude smaller than the relativistic shift.
The linearly extrapolated Γ value at zero modified cyclotron energy is[1, 2]:

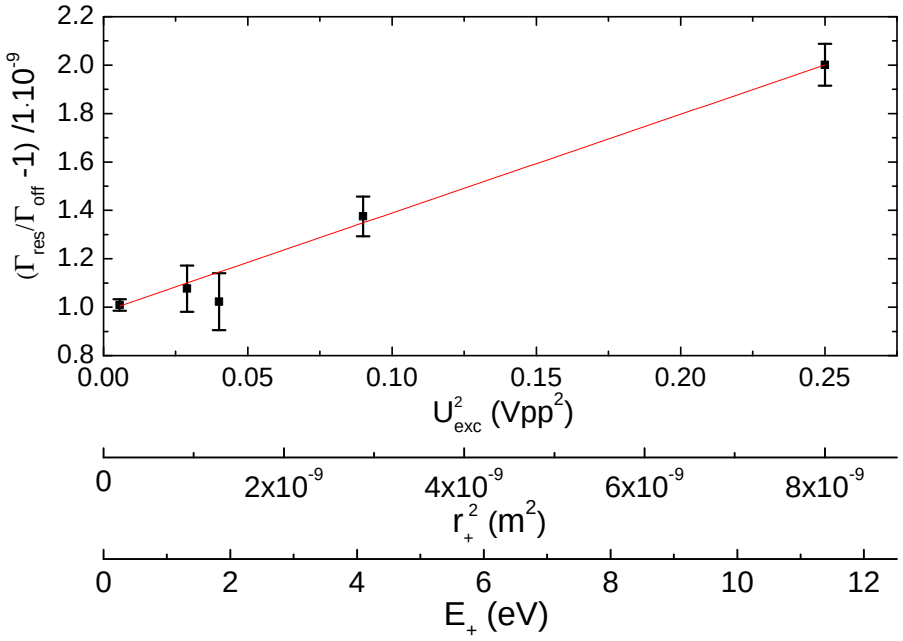

Figure 5.2: Central values from the Gaussian maximum-likelihood fits of the Γ-resonances at different E_+. Only data sets with at least 30 detected spin-flips in the PT are included. The linear dependence is mainly given by the relativistic mass increase, see section 3.5.2. The linear extrapolation to zero modified cyclotron energy is shown in red. The resonance with the smallest modified cyclotron energy has the largest data set and thus the smallest statistical uncertainty. In that way, we reduce the impact of the extrapolation. With $\Gamma_{\text{off}} = 4376.210\,497\,791$ we apply the same scaling constant as in fig. 4.20[b] [131].

b Scaling factor of the x-axis: $r_+ \approx \sqrt{2m\frac{\delta\Gamma}{\Gamma}c^2/\omega_+^2}U_{\text{exc}} = 1.7889 \cdot 10^{-4}\,\text{m/Vpp} \cdot U_{\text{exc}}$, see eq. (5.1) and eq. (5.22).

$$\Gamma_{\mathrm{stat}} = 4376.210\,502\,112(102). \tag{5.2}$$

So far, no systematic corrections have been applied.

Alternative Evaluation of the Γ-Resonances

Instead of the elaborated maximum-likelihood analysis, which is described in section 4.5.2 and is used throughout this thesis, here I study an alternative data analysis to extract the central value of the Γ-resonances. This simplified approach is only based on average values and standard deviations, which do no require any elaborated fitting routine.

As illustrated in fig. 4.18(b), the magnetic field fluctuations determined by subsequent PnA-cycles are normal distributed. Since the probed Larmor frequency ν_{MW} is determined from the first 5 s PnA-cycle and from the theoretically predicted g-factor value[3], all measured Γ^* are Gaussian distributed, with the probability density $\rho^*_{\mathrm{all}}(\mu^*_{\mathrm{all}},\sigma^*_{\mathrm{all}})$. Under these conditions, we can also assume, that the measured Γ-ratios, where spin-flips are induced, are Gaussian distributed, $\rho^*_{\mathrm{sf}}(\mu^*_{\mathrm{sf}},\sigma^*_{\mathrm{sf}})$. The desired probability density of all spin-flip-Γ's, $\rho_{\mathrm{sf}}(\mu_{\mathrm{sf}},\sigma_{\mathrm{sf}})$, is also Gaussian distributed due to the magnetic field fluctuations during the phase evolution time of 5 s. Furthermore, the probability density of all measured spin-flip-Γ's, ρ^*_{sf}, can be written as the product of ρ^*_{all} and ρ_{sf}, see also fig. 5.3:

$$\rho^*_{\mathrm{sf}} = \frac{1}{\sigma^*_{\mathrm{sf}}\sqrt{2\pi}} e^{-\frac{1}{2}\left(\frac{\Gamma^*_{\mathrm{sf}}-\mu^*_{\mathrm{sf}}}{\sigma^*_{\mathrm{sf}}}\right)^2} \stackrel{!}{=} \mathrm{const}\cdot\rho^*_{\mathrm{all}}\cdot\rho_{\mathrm{sf}}. \tag{5.3}$$

The corresponding average value and standard deviation can be formulated as follows:

$$\sigma^*_{\mathrm{sf}} = \frac{\sigma^*_{\mathrm{all}}\sigma_{\mathrm{sf}}}{\sqrt{(\sigma^*_{\mathrm{all}})^2+(\sigma_{\mathrm{sf}})^2}} \quad \text{and} \tag{5.4}$$

$$\mu^*_{\mathrm{sf}} = \frac{\mu_{\mathrm{sf}}(\sigma^*_{\mathrm{all}})^2+\mu^*_{\mathrm{all}}(\sigma_{\mathrm{sf}})^2}{(\sigma^*_{\mathrm{all}})^2+(\sigma_{\mathrm{sf}})^2}. \tag{5.5}$$

1 Only in the classical picture the motional energy can vanish. In the quantum picture the ground state would have an energy of 49 neV which can be safely neglected in the extrapolation, see fig. 5.2.

2 The data analysis has been performed independently by Sven Sturm and me. The determined Γ values: $\Gamma^I_{\mathrm{stat}} = 4376.210\,502\,088(102)$ from fig. 5.2 and $\Gamma^{II}_{\mathrm{stat}} = 4376.210\,502\,136(102)$ from Sven Sturm slightly differ due to (1) different quality cuts, mainly applied after the filling of the cooling reservoirs, and (2) slightly different axial resonator parameters, which are relevant for the determination of the axial frequency. Here and in [77, 131] the average value of these two independent data evaluations is used.

3 Here, we neglect all measurement runs, where an uniformly distributed jitter is artificially added to the probed Larmor frequency.

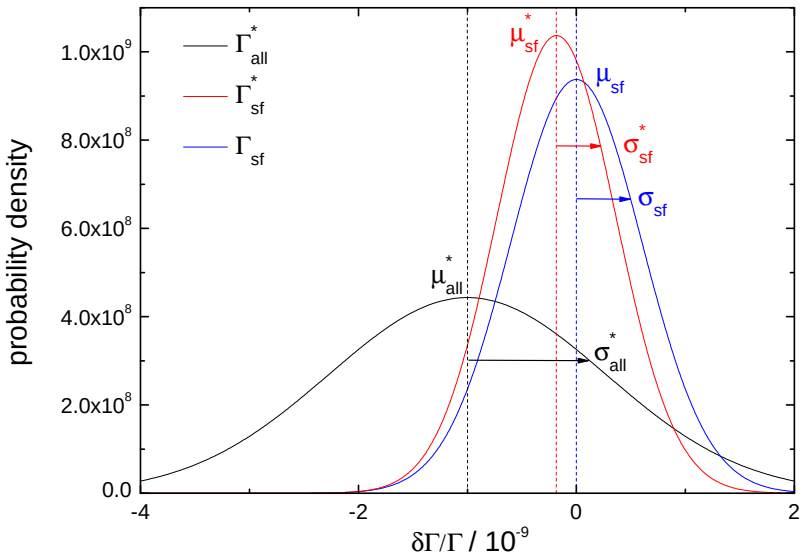

Figure 5.3: Illustration of an alternative evaluation of the Γ-resonances. The Gaussian distribution of all measured Γ^* is indicated in black. The measured Γ^* distribution, where the electron spin has flipped in the PT, is shown in red. The desired distribution of the spin-flip-Γ's is shown in blue. The bias of the mean value of all measured Γ^* : μ^*_{all}, which has been chosen with some previous knowledge, is eliminated by the described unfolding procedure. For details see text.

From these equations we can finally calculate the average value and standard deviation of the desired spin-flip Γ-resonance:

$$\sigma_{\mathrm{sf}} = \frac{\sigma^*_{\mathrm{all}}\sigma^*_{\mathrm{sf}}}{\sqrt{(\sigma^*_{\mathrm{all}})^2 - (\sigma^*_{\mathrm{sf}})^2}} \quad \text{and} \tag{5.6}$$

$$\mu_{\mathrm{sf}} = \frac{\mu^*_{\mathrm{sf}}((\sigma_{\mathrm{sf}})^2 + (\sigma^*_{\mathrm{all}})^2) - \mu^*_{\mathrm{all}}(\sigma_{\mathrm{sf}})^2}{(\sigma^*_{\mathrm{all}})^2}. \tag{5.7}$$

The average values $\mu_{\mathrm{sf}} = \Gamma_{\mathrm{mean}}$ and the corresponding uncertainties of all resonances are plotted in fig. 5.4.
It is remarkable, that the uncertainty of the extrapolated value at zero modified cyclotron energy $\delta\Gamma/\Gamma = 2.0 \cdot 10^{-11}$ is of the same order of magnitude as the uncertainty via the elaborated maximum-likelihood analysis $\delta\Gamma/\Gamma = 2.3 \cdot 10^{-11}$, compare with fig. 5.2. The discrepancy between the results of both analysis techniques is only 0.03 σ, which confirms the measured Γ value presented in eq. (5.2).

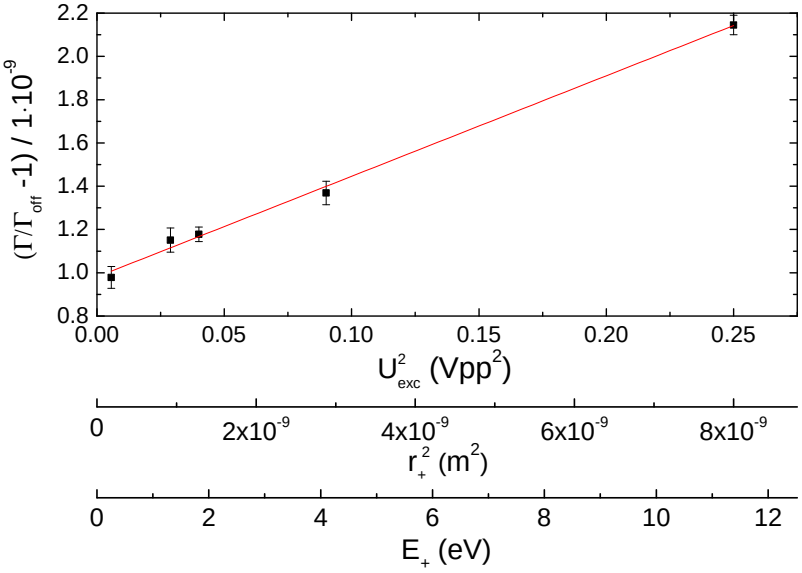

Figure 5.4: Γ-resonances of $^{12}C^{5+}$ evaluated only by average values and standard deviations as a function of the modified cyclotron energy. For details see text. ($\Gamma_{\text{off}} = 4376.210\,497\,791$)

5.2 Systematic Shifts and Uncertainties

The basics of most systematic corrections have been introduced in chapter 3 and chapter 4. In this section I will quantify the specific corrections, which occur during the electron mass measurement. A special focus is set on a systematic correction caused by the residual dipole contribution of the second PnA pulse. All listed corrections are ordered by the size of their uncertainties, starting with the dominant one.

The Image Charge Shift

By far the largest systematic shift of Γ is given by the image charge shift, which has been introduced in section 3.2.4. In case of a single $^{12}C^{5+}$ ion it amounts to:

$$\left(\frac{\Gamma_{\text{stat}} - \Gamma_{\text{final}}}{\Gamma_{\text{stat}}}\right)_{\text{image charge}} = 2.824(141) \cdot 10^{-10}. \tag{5.8}$$

This effect also dominates the systematic uncertainty budget.

The Line-Shape Model of the Axial Dip Signal

With a conservative estimation of the total error for the dip-signal line-shape model of 4.5 mHz, see table 4.9 in section 4.3.2, the relative uncertainty of the cyclotron frequency and thus the Γ ratio is:

$$\left(\frac{\delta\Gamma}{\Gamma}\right)_{\nu_{z,\text{sys}}} = \frac{\delta\nu_c}{\nu_c} = \frac{\nu_z\ \delta\nu_{z,\text{sys}}}{\nu_c^2} = 5.2 \cdot 10^{-12}. \tag{5.9}$$

Measurements of the Magnetron Frequency

During the 4.5 months of data taking the magnetron frequency has been measured via the double-dip method only three times. The largest measured shift of $\Delta\nu_- = 0.2\,\mathrm{Hz}$, see also table 4.6, corresponds to the following uncertainty of Γ :

$$\left(\frac{\delta\Gamma}{\Gamma}\right)_{\delta\nu_-} = 3.22 \cdot 10^{-12}. \tag{5.10}$$

The Dipole Contribution of the Second PnA Pulse

The detection of the modified cyclotron frequency has been already discussed at length in section 3.4.2. The uncertainties caused by magnetic field fluctuations and the other modified cyclotron phase jitters broaden the Γ-resonances and in that way are included in the uncertainty of Γ_{stat}, see eq. (5.2). Here, a more subtle effect is studied, which arises during the second PnA pulse.
The quadrupole excitation line, which is connected to one half of the split correction electrode, features small dipole components in radial and axial directions, see also section 3.3.2. These components have been numerically calculated based on a finite element simulation using COMSOL [132]:

$$\vec{F}_{\text{quad. real}} = q_{\mathrm{ion}} \begin{pmatrix} 64.7 + 38410.1\ \mathrm{m}^{-1} \cdot z \\ 0 \\ 75.7 + 38410.1\ \mathrm{m}^{-1} \cdot x \end{pmatrix} A_{\mathrm{quad}} \sin(\omega' t + \varphi_0). \tag{5.11}$$

During the second PnA pulse the resonant quadrupole excitation at the sideband frequency $\nu_{\text{2nd pulse}} \approx \nu_+ + \nu_z$ competes with an off-resonant dipole excitation at ν_+. As a result, the read-out phase has a systematic shift depending on the phase relation between the modified cyclotron phase of the ion and the starting phase of the second PnA pulse. In the worst-case scenario of an in-phase excitation, starting amplitudes of $z = r_+ = 15$ µm and a final axial amplitude of $z = 100$ µm, the numerically calculated shift of the modified cyclotron frequency is smaller than 0.05 mHz at a 10 ms pulse length and a phase evolution time of 5 s. The corresponding relative shift of the frequency ratio is smaller than

$$\left(\frac{\delta\Gamma}{\Gamma}\right)_{\text{dipole contr. 2nd PnA pulse}} < 3 \cdot 10^{-12}. \tag{5.12}$$

So far, a significant measurement of this effect has not been possible, see fig. 5.5(a). Here, subsequent PnA-cycles have been performed with a single $^{48}Ca^{17+}$ ion and the following configurations: The first PnA pulse is set to 0.025 Vpp @ 10 ms, $T_{\mathrm{evol}} = 1$ ms and the second PnA pulse to 4.5 Vpp @ 35 ms. For more than six hours these PnA-cycles have been performed at seven different starting phases of the first PnA pulse. To increase the dipole contribution of the second PnA pulse the axial frequency of the ion has been tuned on a local maximum of the sinc-like frequency spectrum of the second PnA pulse. More precisely, the axial frequency is a multiple of the inverse pulse length plus one half of the inverse pulse length, here: $\nu_z/\tau_{\text{2nd pulse}} = 670328.6\,\mathrm{Hz}/(0.035\,\mathrm{s}) = 23461.5$. The plotted data has

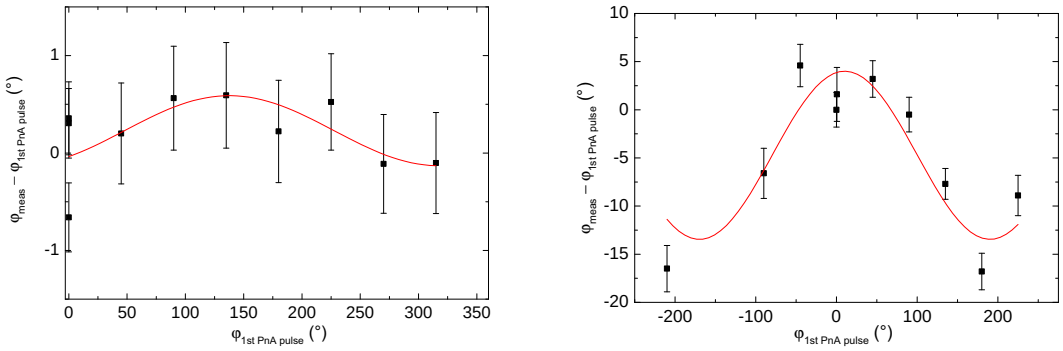

(a) **(b)**

Figure 5.5: Study of the dipole phase contributions generated by the second PnA pulse. In (a) the normal (ν_+) PnA method is analyzed. Here the difference between the measured phase and the starting phase of the first PnA pulse is plotted as a function of the starting phase. No significant systematic phase shift is detected. In (b) the same measurement is repeated for a PnA method, which detects the magnetron frequency. Here a maximal systematic phase shift of $\varphi_0 = 8.7(9)^\circ$ is detected, although the dipole contribution of the second PnA pulse has been minimized by an active dipole compensation pulse. For details see text.

been fitted by the following line-shape: $\Delta\varphi = \varphi_{\text{off}} + \varphi_0 \sin(\pi/180^\circ(\varphi_{\text{start}} - \varphi^{\text{off}}_{\text{start}}))$. In the end, a non-significant maximal systematic phase shift of $\varphi_0 = 0.3(3)^\circ$ has been determined. In fig. 5.5(b) similar PnA measurements have been performed detecting the magnetron phase instead of the modified cyclotron phase. Since in this case the axial frequency is much closer to the frequency of the second excitation pulse ($\nu_{2\text{nd pulse}} \approx \nu_z - \nu_-$) than the modified cyclotron frequency to the frequency of the second excitation pulse in the normal (ν_+) PnA method ($\nu_{2\text{nd pulse}} \approx \nu_+ - \nu_z$), the analyzed dipole contribution is significantly enhanced. Although we minimized this dipole contribution by a simultaneous active compensation via the amplitude- and phase-tuned dipole excitation line, the systematic phase shift is clearly visible in fig. 5.5(b). It causes a maximal systematic phase shift of $\varphi_0 = 8.7(9)^\circ$ [4].

To eliminate such a systematic dipole phase shift, a random starting-phase is implemented for the first PnA pulse, which causes an enhanced jitter of the measured phase, but no

4 Detailed information concerning the PnA measurement of the magnetron frequency: A single $^{16}O^{8+}$ ion is used with an axial frequency of 631539 Hz and a magnetron frequency of 6896.6 Hz. The first PnA pulse is applied via an Agilent 33250A function generator at ν_- (0.008 Vpp @ 18 ms). The phase evolution time amounts to $T_{\text{evol}} = 100$ ms. The second PnA pulse at $\nu_{2\text{nd pulse}} \approx \nu_z - \nu_-$ (0.111 Vpp @ 7 ms) is generated by one of the channels of the two-channel frequency generator Agilent 33522A. The other channel is connected to the dipole excitation line. During the second PnA pulse the undesired axial phase imprint is minimized by an active compensation. Here, the same frequency ($\nu_z - \nu_-$) is applied simultaneously to the dipole excitation line at a proper amplitude and phase-shift. Nevertheless, a residual axial phase imprint is clearly visible in fig. 5.5(b), which causes a maximal systematic phase shift of $\varphi_0 = 8.7(9)^\circ$.

systematic phase shift. In future experimental setups this effect could be diminished by reducing the dipole contributions of the quadrupole excitation, e.g. applying the quadrupole excitation to more than just one split electrode.

The Drift of the Axial Frequency

Since the axial frequency is measured before and after the simultaneous PnA measurement of the modified cyclotron frequency and the probing of the Larmor frequency, see fig. 4.15, the frequency drift between these two measurements has to be considered. The mean value of the frequency differences of the two dip measurements is $|\mathrm{d}\bar{\nu}_z| < 2.5\,\mathrm{mHz}$. Considering that only the last of the ten subsequent PnA-cycles determines the measured frequency ratio Γ^*, the second axial dip measurement is temporally closer to the relevant PnA-cycle, so that due to the axial drift we assume a relative uncertainty of Γ of $\ll 1.2 \cdot 10^{-12}$.

The Image Current Shift of the Cyclotron Resonator

In contrast to the image current shift of the axial resonator which is already incorporated by the line-shape model of the axial-dip, the image current shift of the modified cyclotron resonator has to be considered and corrected for. In analogy to the axial image current shift, introduced in eq. (3.41), the modified cyclotron image current shift can be calculated as follows:

$$\frac{\Delta\omega_+}{\omega_+} \approx -\frac{\mathrm{Im}(\gamma)}{\omega_+} = -\frac{q_{\mathrm{ion}}\mathrm{Im}(Z_{\mathrm{LC}}(\omega_+))}{2m_{\mathrm{ion}}D_{\mathrm{rad}}^2}. \tag{5.13}$$

Based on the measured resonator parameters specified in table 4.4, fig. 5.6 illustrates the image current shift as a function of the modified cyclotron frequency. With the varactor diode the modified cyclotron resonator has been tuned off-resonantly. The corresponding systematic shift of Γ is:

$$\left(\frac{\Gamma_{\mathrm{stat}} - \Gamma_{\mathrm{final}}}{\Gamma_{\mathrm{stat}}}\right)_{\text{image current}} = 2.20(55) \cdot 10^{-12}. \tag{5.14}$$

Electric Field Imperfections

Considering the uncertainty of the dominant electric field imperfection C_4: $\delta C_4 = 1.1 \cdot 10^{-5}$, see eq. (4.8), the eigenfrequency shifts described by the C_4-matrix, see eq. (3.19), cause a relative uncertainty of the free cyclotron frequency and thus also of the frequency ratio:

$$\left(\frac{\delta\Gamma}{\Gamma}\right)_{\delta C_4} = 5.0 \cdot 10^{-13}. \tag{5.15}$$

Furthermore, assuming a conservative C_6 uncertainty of 100%, where $C_6 = -0.016$, see eq. (4.9), the corresponding relative uncertainty of Γ is:

$$\left(\frac{\delta\Gamma}{\Gamma}\right)_{\delta C_6} = 5.9 \cdot 10^{-14}, \tag{5.16}$$

which is calculated by the formulas given in [120].

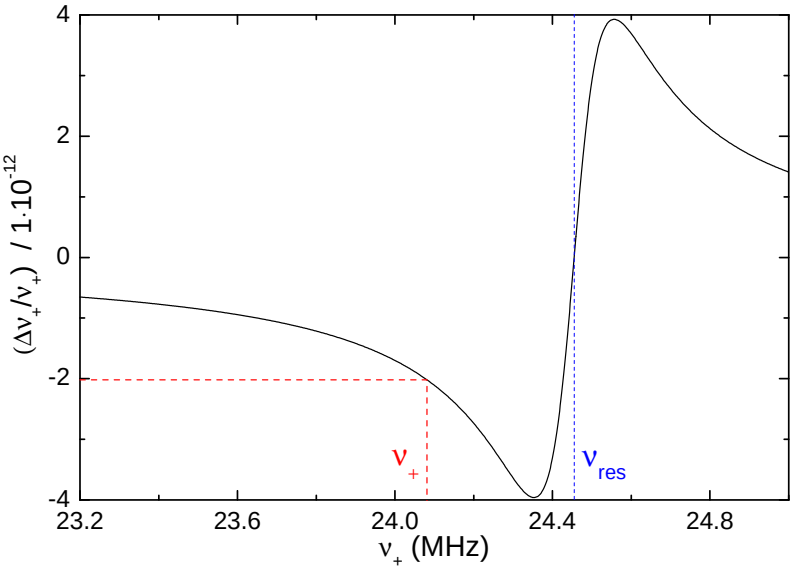

Figure 5.6: Image current shift of the $^{12}C^{5+}$ ion caused by the cyclotron resonator. The resonator parameters are listed in table 4.4.

Line-Shape Model of the Γ-Resonance

The asymmetric line-shape contribution of the Γ-resonance, see eq. (4.19), which is caused by the Boltzmann distributed axial energy and the B_2 shift of the eigenfrequencies, generates a discrepancy between the mean and the maximum of the line-shape, which amounts to

$$\left(\frac{\delta\Gamma}{\Gamma}\right)_{\text{asym}} = 3\cdot10^{-13}, \tag{5.17}$$

see also eq. (4.20). Furthermore, the deviation between the centroid of the Γ-resonance and the central value of the applied Gaussian maximum-likelihood fit is:

$$\left(\frac{\delta\Gamma}{\Gamma}\right)_{\text{fit}} = 1\cdot10^{-13}, \tag{5.18}$$

see section 4.5.2.

Magnetic Field Imperfections

The large magnetic bottle in the AT generates a residual magnetic inhomogeneity in the PT, see section 4.1.5. The linear gradient of the magnetic field, $B_1 = -13.41(23)\cdot10^{-3}\,\text{T/m}$ [13], shifts the center of the ion motion in axial direction due to the force acting on the magnetic moment generated by the cyclotron motion. At the maximally applied modified cyclotron radius of $r_+ = 90\,\mu\text{m}$ the center of the motion shifts $\Delta z = -21\,\text{nm}$, causing the same

relative shifts of the free cyclotron frequency and the Larmor frequency of $-7.4 \cdot 10^{-11}$, which completely cancel in the frequency ratio Γ.
The residual second-order magnetic field inhomogeneity in the PT, $B_2 = 1.01(0.20)\,\mathrm{T/m^2}$, evokes energy dependent shifts of both the eigenfrequencies and the Larmor frequency, see eq. (3.23) and eq. (3.78). Since the Larmor frequency and the modified cyclotron frequency shift by the same amount, the magnetic shift cancels to a large extent in the frequency ratio Γ:

$$\left(\frac{\Gamma_{\mathrm{stat}} - \Gamma_{\mathrm{final}}}{\Gamma_{\mathrm{stat}}}\right)_{\text{magn. imperfections}} = -1.36(26) \cdot 10^{-12}. \tag{5.19}$$

The error is dominated by the uncertainty of the measured B_2.

Residual Special Relativity

The relativistic increase of the ion mass accounts for a relative shift of the cyclotron frequency:

$$\frac{\Delta\nu_c}{\nu_c} = \frac{1}{\gamma} - 1, \tag{5.20}$$

where $\gamma \equiv (1 - v^2/c^2)^{-1/2}$ is the relativistic Lorentz factor and v is the velocity of the ion. After the extrapolation to zero modified cyclotron energy, the velocity of the ion is mainly given by the axial mode, $\bar{v}_z = 87(2)\,\mathrm{m/s}$ at an axial temperature $T_z = 5.44(22)\,\mathrm{K}$, resulting in a residual relativistic shift of Γ :

$$\left(\frac{\Gamma_{\mathrm{stat}} - \Gamma_{\mathrm{final}}}{\Gamma_{\mathrm{stat}}}\right)_{\text{relativistic}} = 4.20(17) \cdot 10^{-14}. \tag{5.21}$$

A further relativistic shift of the Larmor frequency is generated by the additional motional magnetic field: $\Delta B = \gamma/c^2\ (\vec{v} \times \vec{E})$. Even for the Γ-resonance with the largest modified cyclotron energy ($r_+ = 90\,\mu\mathrm{m}$) and the corresponding radial electric field $E_r = 19\,\mathrm{V/m}$ the relative magnetic field shift is only: $\Delta B/B = 8 \cdot 10^{-13}$.

All considered relative systematic shifts and corresponding uncertainties are summarized in table 5.2, sorted by the size of their respective relative uncertainties.

Table 5.2: Summary of the relative systematic shifts and uncertainties of Γ ordered by the size of the relative uncertainties.

effect	rel. shift / 10^{-12}	rel. uncertainty / 10^{-12}
image charge shift	-282.4	14.1
line-shape model of the dip	0	5.2
magnetron frequency	0	3.2
dipole contribution of 2^{nd} PnA pulse	0	< 3
drift of the axial frequency	0	$\ll 1.2$
motional magnetic field	0	$\ll 0.8$
image current shift	-2.20	0.55
electric field imperfections (C_4)	0	0.50
asymmetry of the Γ-resonance	0	0.3
magnetic field imperfections (B_2)	1.36	0.27
fitting the Γ-resonance by a Gaussian	0	0.1
electric field imperfections (C_6)	0	0.059
residual special relativity	-0.042	0.002
total relative shift	-283.3	15.4

5.3 Consistency Checks

At different energies of the modified cyclotron mode, which are proportional to the squared motional radius and thus to the squared amplitude of the first PnA excitation pulse (U_{exc}), all three eigenfrequencies shift mainly due to the relativistic mass increase and the magnetic inhomogeneity in the PT. From the combination of the following four measured eigenfrequency shifts the magnetic inhomogeneity B_2 can be calculated in different, independent ways, providing consistency checks of the energy dependent systematic shifts:

1. The slope $m_{\frac{\delta\Gamma}{\Gamma}} = 4.07(35) \cdot 10^{-9}\,\text{Vpp}^{-2}$ of the different Γ-resonances with respect to the different modified cyclotron energies, see fig. 5.2, is mainly given by the relativistic shift:

$$m_{\frac{\delta\Gamma}{\Gamma}} \cdot U_{\text{exc}}^2 \approx \frac{\delta\nu_+}{\nu_+} \approx \frac{E_+}{mc^2}. \tag{5.22}$$

2. The differences of the modified cyclotron frequencies, determined in each measurement cycle, firstly by the double-dip method and secondly by the PnA method, are shown in fig. 5.7(a) with respect to the different modified cyclotron energies. Here and in the following plots, these energies are represented by the proportional squared excitation amplitude U_{exc}^2 of the first PnA pulse. These two different measurement techniques are in remarkable agreement at zero modified cyclotron energy: $< \nu_+^{\text{PnA}} - \nu_+^{\text{DD}} > /\nu_+ = 7(10) \cdot 10^{-11}$ [5]. The slope $m_{\nu_+^{\text{PnA}} - \nu_+^{\text{DD}}} = -0.201(10)\,\text{Hz}\,\text{Vpp}^{-2}$ is given by the

5 The specified uncertainty includes the uncertainty of the dip line-shape model. The difference without this uncertainty amounts to: $< \nu_+^{\text{PnA}} - \nu_+^{\text{DD}} > /\nu_+ = 7(4) \cdot 10^{-11}$.

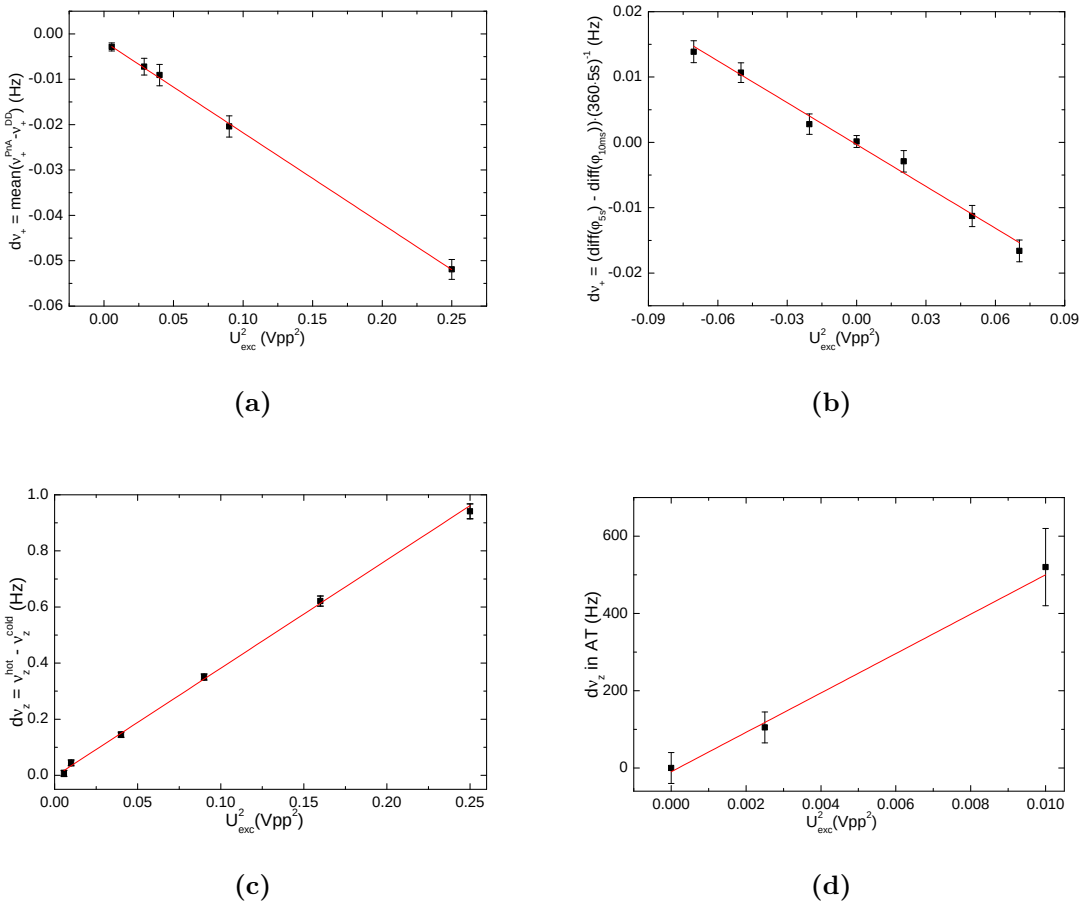

Figure 5.7: Consistency checks. Illustrations of various eigenfrequency shifts as a function of the squared amplitude of the first PnA pulse, which is proportional to the modified cyclotron energy. Detailed descriptions are given in the text.

relativistic- and the B_2-shift:

$$m_{\nu_+^{\mathrm{PnA}}-\nu_+^{\mathrm{DD}}} \cdot U_{\mathrm{exc}}^2 \approx -\frac{E_+ \cdot \nu_+}{m \cdot c^2} - \frac{B_2 \cdot E_+}{B_0 \cdot m \cdot (2\pi)^2 \cdot \nu_+}. \tag{5.23}$$

The same frequency shift has been measured in subsequent PnA-cycles at randomly chosen modified cyclotron energies ($U_{\mathrm{exc}} = 0.14,\ 0.2,\ 0.3$ Vpp). In fig. 5.7(b) the phase differences are plotted against the energy differences. The linear fit has the following slope: $m_{\nu_+ \text{by PnA}} = -0.213(13)\ \mathrm{Hz} \cdot \mathrm{Vpp}^{-2}$.

3. Also the axial frequency shift, caused by the different modified cyclotron energies and the axial B_2-shift has been detected, see fig. 5.7(c). The slope $m_{\nu_z} = 3.863(84)\ \mathrm{Hz} \cdot$

Vpp^{-2} depends quasi exclusively on the B_2-shift at different cyclotron energies:

$$m_{\nu_z} \cdot U_{\mathrm{exc}}^2 \approx \frac{B_2 \cdot E_+}{B_0 \cdot m \cdot (2\pi)^2 \cdot \nu_z}. \tag{5.24}$$

4. The axial frequency shift in the AT with the slope $m_{\nu_z}^{\mathrm{AT}} = 50.9(1.1) \cdot 10^3\,\mathrm{Hz} \cdot \mathrm{Vpp}^{-2}$, see fig. 5.7(d), depends on the magnetic bottle in the AT:

$$m_{\nu_z^{\mathrm{AT}}} \cdot U_{\mathrm{exc}}^2 \approx \frac{B_2^{\mathrm{AT}} \cdot E_+}{B_0^{\mathrm{AT}} \cdot m \cdot (2\pi)^2 \cdot \nu_z^{\mathrm{AT}}}. \tag{5.25}$$

In table 5.3 the different values for the B_2 in the PT are summarized. They all agree within their error bars and thus do not give any hint at further unknown energy-dependent shifts, validating the model of systematics discussed above.

Table 5.3: Consistency checks. Four independent measurement approaches have been applied to determine B_2 in the PT.

combination	combination of equations	B_2 (T/m^2)
$m_{\frac{\delta\Gamma}{\Gamma}} \leftrightarrow m_{\nu_+^{\mathrm{PnA}} - \nu_+^{\mathrm{DD}}}$	(5.22) and (5.23)	1.01(20)
$m_{\frac{\delta\Gamma}{\Gamma}} \leftrightarrow m_{\nu_+ \text{by PnA}}$	(5.22) and (5.23)	1.12(22)
$m_{\frac{\delta\Gamma}{\Gamma}} \leftrightarrow m_{\nu_z}$	(5.22) and (5.24)	1.053(93)
$m_{\nu_+^{\mathrm{PnA}} - \nu_+^{\mathrm{DD}}} \leftrightarrow m_{\nu_z^{\mathrm{AT}}}$	(5.23) and (5.25)	1.40(50)

5.4 Final Results

The statistical value specified in eq. (5.2) has to be corrected by the systematic shift listed in table 5.2 to derive the final Γ value:

$$\begin{aligned} \Gamma_{\mathrm{final}} &= \Gamma_{\mathrm{stat}} + \Delta\Gamma_{\mathrm{sys}} \\ &= 4376.210\,502\,112(102) - 1.240(69) \cdot 10^{-6} \\ &= 4376.210\,500\,872(102)(69) \qquad (28\ \mathrm{ppt}). \end{aligned} \tag{5.26}$$

In combination with the predicted g-factor, see eq. (2.18), and the calculated ion mass of $^{12}\mathrm{C}^{5+}$, see eq. (2.17), we determine the following value of the atomic mass of the electron using eq. (2.16)[6]:

$$m_e = 0.000\,548\,579\,909\,069\,4\,(128)(86)(13)\ \mathrm{u} \qquad (28\ \mathrm{ppt}). \tag{5.27}$$

The numbers in the brackets represent (1) the statistical and (2) systematic uncertainty of the determination of the Γ-ratio as well as (3) the uncertainty of the theoretical g-factor, which also includes the uncertainty of the ion mass.
With a relative uncertainty of $\delta m_e/m_e = 2.8 \cdot 10^{-11}$ the atomic mass of the electron has

6 The value differs slightly (0.15σ) from the value in [77] due to a sign error in the image current shift.

been determined with so far unrivaled precision. In fig. 5.8 the previous electron mass measurements and the corresponding averaged literature values published by the CODATA group are presented and normalized to our measured value. The current averaged CODATA

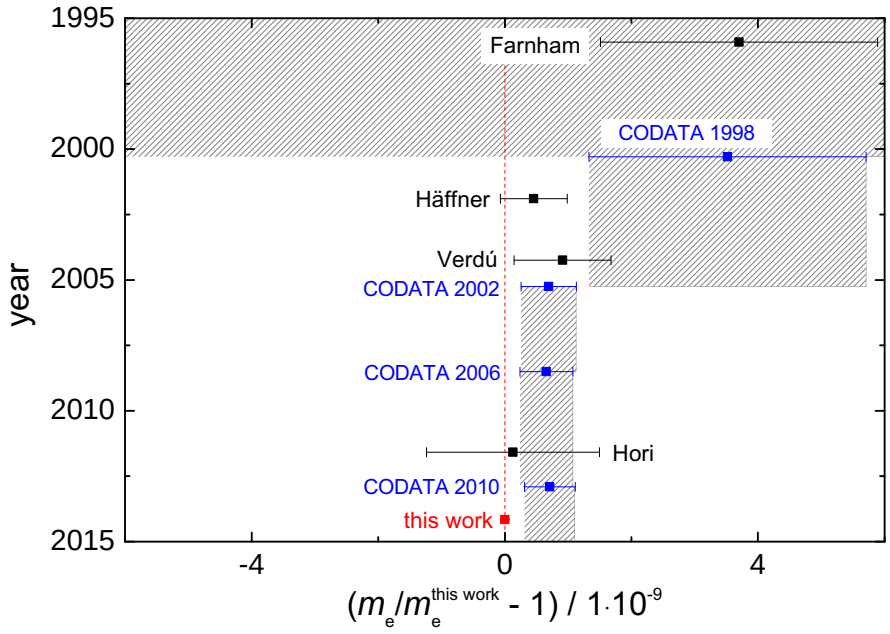

Figure 5.8: Atomic electron mass values measured in the last twenty years and normalized to our value. The error bars of our value are covered by the red marker. For details see text.

2010 value [65] relies on three different measurement approaches: (1) two bound-electron g-factor measurements from the group of Günter Werth performed by Hartmut Häffner [128] and José Verdú [118], (2) a direct measurement by D.L. Farnham and colleagues [73] and (3) an indirect spectroscopic measurement on antiprotonic helium by Masaki Hori and colleagues [76]. All these measurements have been introduced in section 2.6.2. In particular, the phase-sensitive measurement technique, PnA [58], enabled a 19-fold improvement with respect to our previous most precise value of the electron's mass [148]. Moreover, our value surpasses the relative uncertainty of the CODATA 2010 value by a factor of 13 and deviates 1.8σ from it. However, probably two additional small systematic corrections have

to be applied to the Larmor-to-cyclotron frequency ratio for $^{16}O^{7+}$ [118][7]. Considering these effects, our value deviates only 1.1 σ from the averaged value of the older electron mass measurements.

In combination with the atomic mass of the proton $m_p = 1.007\ 276\ 466\ 812(90)$ u [65], the value of the proton-to-electron mass ratio has been improved by a factor of four:

$$m_p/m_e = 1836.152\ 673\ 77(17) \qquad (89\ \text{ppt}). \tag{5.28}$$

This mass ratio is an essential input parameter in atomic physics. Due to our new electron mass value, at present this ratio is limited by the uncertainty of the proton mass of $\delta m_p/m_p = 8.9 \cdot 10^{-11}$.

With the older electron mass values from D.L. Farnham [73] and M. Hori [76], which have not been determined by the bound-electron g-factor, an averaged electron mass of $m_e = 0.000\ 548\ 579\ 909\ 69(64)$ u (1.2 ppb) can be derived. In combination with the ion mass $m(^{12}C^{5+})$, see eq. (2.17), and our final Γ-ratio, see eq. (5.26), we can also derive the bound-electron g-factor of hydrogenlike carbon, by using eq. (2.13):

$$g_{\text{meas}}(^{12}C^{5+}) = 2.001\ 041\ 592\ 44\ (232)(5)(3) \qquad (1.2\ \text{ppb}). \tag{5.29}$$

The numbers in the brackets represent the uncertainties caused by (1) the uncertainty of the electron mass (99.97% of the total uncertainty), (2) the statistical uncertainty of the measured Γ-ratio (2.0% of the total uncertainty) and (3) the systematic uncertainty of the measured Γ-ratio (1.4% of the total uncertainty). The uncertainty of the ion mass only amounts to 0.013% of the total uncertainty. This measured g-factor deviates only 0.9 σ from the predicted one, see eq. (2.18).

In the future two experimental improvements could even further reduce the uncertainty of the atomic electron mass:

- The dominant systematic uncertainty, given by the image charge effect, could be decreased by increasing the trap size, due to its inverse scaling with the cubic trap radius ($\propto 1/r^3$). At the same time the impact of patch potentials on the electrode surfaces would reduce which decreases the uncertainty of the radial shift of the ion

7 More specifically, the image charge shift has not been considered in that measurement and an energy dependent B_2-shift of the Γ resonance has been mistakenly applied. The image charge effect of a single $^{16}O^{7+}$ ion located in a cylindrical trap with a radius of $r = 3.5$ mm increases the frequency ratio of about $\Gamma = 4164$ by 0.37 ppb. In combination with the presumably mistakenly subtracted energy dependent B_2-shift of -1.9 ppb denoted as "Extrapolation T_z/L_{MW} in table 5.2 [118, p. 121], the corresponding electron mass should be 1.5 ppb smaller than considered in the CODATA 2010 evaluation. Since the measurement has been performed more than a decade ago, the verification of these additional shifts is not absolutely clear. Due to that reason we would propose to shift that electron mass value by -0.75 ppb and extend the uncertainty from 0.77 ppb of the measurement to 0.86 ppb ($= \sqrt{\sigma_{\text{stat}}^2 + \sigma_{\text{sys}}^2 + (\sigma_{\text{new}}/\sqrt{12})^2} = \sqrt{0.72^2 + 0.17^2 + (1.5/\sqrt{12})^2}$ ppb).

motional center.

- At the moment the statistical uncertainty of the measured Γ ratio is dominated by magnetic field fluctuations. Most likely, this effect could be reduced by the implementation of radial compensation coils, see section 4.2.1. In the presumable case that the magnetic field fluctuations are generated by vibrations of the foundation, also a damped platform for the experimental setup might reduce these fluctuations. However, this modification would require a laborious and risky movement of the complete magnet.

CHAPTER 6

Probing the Isotope Shift: $\Delta g = g(^{40}\mathrm{Ca}^{17+}) - g(^{48}\mathrm{Ca}^{17+})$

In the present chapter, I will report on the first isotope shift measurement of bound electron g-factors of highly charged ions. Despite a 20% mass difference between the two calcium isotopes ^{40}Ca and ^{48}Ca, they have an almost identical nuclear charge radius thus providing a unique system across the entire nuclear chart to test the pure relativistic nuclear recoil effect by measuring the g-factor difference $\Delta g = g(^{40}\mathrm{Ca}^{17+}) - g(^{48}\mathrm{Ca}^{17+})$. The corresponding theoretical prediction requires bound-state quantum electrodynamics beyond the Furry picture, which has been introduced in section 2.3 and in section 2.7.3.
In the beginning of this chapter, in section 6.1, a special focus will be set on the challenging spin state detection of the calcium ions, due to the heaviness of these isotopes. In section 6.2 and section 6.3 the measured Γ values and the systematic shifts are briefly discussed. In section 6.5, the final results of the Γ measurements on the calcium isotopes $^{40}\mathrm{Ca}^{17+}$ and $^{48}\mathrm{Ca}^{17+}$ are presented, which moreover represent the to date most precise g-factor measurements on lithiumlike ions.
The Γ measurements on $^{40}\mathrm{Ca}^{17+}$ and $^{48}\mathrm{Ca}^{17+}$, the mass measurement of ^{48}Ca as well as the corresponding theoretical calculation of the isotope shift have been submitted for publication [95].

6.1 Spin-Flip Detection with Calcium Isotopes - The Cycle-Weight

In the magnetic bottle of the AT the axial frequency jump caused by an induced spin-flip scales with the inverse of the ion's mass, see eq. (3.77). In contrast to the previous measurements, where the axial frequency shifts have been $\Delta\nu_z^{\mathrm{sf}} = \pm 586\,\mathrm{mHz}$ for $^{12}\mathrm{C}^{5+}$ and $\Delta\nu_z^{\mathrm{sf}} = \pm 240\,\mathrm{mHz}$ for $^{28}\mathrm{Si}^{13+}$ [13] and $^{28}\mathrm{Si}^{11+}$ [14], it is a particular challenge to resolve the spin-states for the calcium isotopes, where $\Delta\nu_z^{\mathrm{sf}} = \pm 170\,\mathrm{mHz}$ for $^{40}\mathrm{Ca}^{17+}$ and only $\Delta\nu_z^{\mathrm{sf}} = \pm 140\,\mathrm{mHz}$ for $^{48}\mathrm{Ca}^{17+}$.
Applying a coherent detection technique, introduced in section 3.4.2, we measure phase differences of the axial motion to detect the spin state of the single calcium ion. At a phase evolution time of 1 s and a readout time of 552 ms the generated axial frequency shift corresponds to an axial phase shift of $\Delta\varphi_z^{\mathrm{sf}} = 360^\circ \cdot T_{\mathrm{tot}} \cdot \Delta\nu_z^{\mathrm{sf}} = \pm 78^\circ$ for $^{40}\mathrm{Ca}^{17+}$ and $\Delta\varphi_z = \pm 65^\circ$ for $^{48}\mathrm{Ca}^{17+}$. In the final measurement cycle, presented in fig. 4.15, we determine the axial frequency differences in the AT by averaging over four successive axial phase measurements. Between these measurement sequences we try to induce spin-flips for

30 s at maximum MW-power and at a fixed MW-frequency.
In fig. 6.1(b) 1790 subsequently measured axial frequency differences are histogrammed. Here, a single $^{48}\mathrm{Ca}^{17+}$ ion is studied in the AT. The plotted probability density ρ_{AT} is modeled by a superposition of three Gaussian distributions:

$$\begin{aligned}\rho_{\mathrm{AT}}(\Delta\nu_z) = {} & \mathcal{G}_{\text{no sf}}(\Delta\nu_z|1-A,0,\sigma_{\Delta\nu_z}) \\ & + \mathcal{G}_{\text{sf up}}(\Delta\nu_z|A/2,+\Delta\nu_z^{\mathrm{sf}},\sigma_{\Delta\nu_z}) + \mathcal{G}_{\text{sf down}}(\Delta\nu_z|A/2,-\Delta\nu_z^{\mathrm{sf}},\sigma_{\Delta\nu_z}),\end{aligned} \tag{6.1}$$

where $\mathcal{G}_{\text{no sf}}$ is the Gaussian distribution of the axial frequency differences without any spin-flips, featuring an amplitude $(1-A)$, a mean value of zero and a standard deviation $\sigma_{\Delta\nu_z}$. $\mathcal{G}_{\text{sf up}}$ and $\mathcal{G}_{\text{sf down}}$ denote the Gaussian distributions, where a spin-flip up (mean value: $+\Delta\nu_z^{\mathrm{sf}}$) or spin-flip down (mean value: $-\Delta\nu_z^{\mathrm{sf}}$) occur. From a maximum-likelihood (ML) fit, we obtain the following three parameters, see fig. 6.1(b): (1) the spin-flip rate: 26.5%, (2) the frequency jitter: $\sigma_{\Delta\nu_z} = 25\,\mathrm{mHz}$ [1] and (3) the axial frequency jump generated by a spin-flip: $\Delta\nu_z^{\mathrm{sf}} = \pm 140$ mHz. One way to decrease the probability of wrong spin state detection is given by the introduction of simple quality cuts, e.g. by ignoring all measurement cycles, where 60 mHz $< |\Delta\nu_z| <$ 95 mHz. To circumvent the emerging loss of statistics, we introduce the following AT-weight w_{AT} for each measured axial frequency difference, in a way that $w_{\mathrm{AT}} = 0$, if the ion is in spin down, $w_{\mathrm{AT}} = 1$, if the ion is in spin-up and $w_{\mathrm{AT}} = 0.5$, if the spin state is not known. More precisely, the AT-weight is defined as:

$$w_{\mathrm{AT}}(\Delta\nu_z) \equiv \begin{cases} \frac{\mathcal{G}(\Delta\nu_z|A,\Delta\nu_z^{\mathrm{sf}},\sigma_{\Delta\nu_z})}{2\cdot\rho_{\mathrm{AT}}(\Delta\nu_z)} + 0.5 \text{ if: } \Delta\nu_z > \text{spin-flip cut}, \\ -\frac{\mathcal{G}(\Delta\nu_z|A,-\Delta\nu_z^{\mathrm{sf}},\sigma_{\Delta\nu_z})}{2\cdot\rho_{\mathrm{AT}}(\Delta\nu_z)} + 0.5 \text{ if: } \Delta\nu_z < \text{spin-flip cut}, \end{cases} \tag{6.2}$$

where the spin-flip cut is 70 mHz for $^{48}\mathrm{Ca}^{17+}$, see fig. 6.2.
In a usual measurement cycle we try to induce a spin-flip at least three times in the AT and then proceed with the measurement process, until the cut-criterion $|\Delta\nu_z| >$ spin-flip cut is fulfilled for the first time. For the first and the last frequency jump, which fulfills this cut-criterion, the AT-weight is calculated. The spin-flip probability in the PT (w_{PT}) is calculated from the two AT-weights (1) before entering the PT ($w_{\mathrm{AT}}^{\mathrm{before}}$) and (2) directly after leaving the PT ($w_{\mathrm{AT}}^{\mathrm{after}}$):

$$w_{\mathrm{PT}} = w_{\mathrm{AT}}^{\mathrm{before}} \cdot (1 - w_{\mathrm{AT}}^{\mathrm{after}}) + w_{\mathrm{AT}}^{\mathrm{after}} \cdot (1 - w_{\mathrm{AT}}^{\mathrm{before}}). \tag{6.3}$$

1 It is remarkable, that the measured axial frequency of $^{48}\mathrm{Ca}^{17+}$ ($\sigma_{\Delta\nu_z} = 25$ mHz), see fig. 6.1(b), can be predicted by the measured axial frequency of $^{12}\mathrm{C}^{5+}$ ($\sigma_{\Delta\nu_z} = 73$ mHz), see fig. 6.1(a), only considering the fluctuations of the high-precision voltage source (UM1-14) of $6\cdot10^{-8}$ and fluctuations of the modified cyclotron energy. In detail, the axial frequency fluctuations caused by voltage fluctuations amount to 412 kHz/$2\cdot6\cdot10^{-8} \approx 13$ mHz. Moreover, axial frequency fluctuations are generated by modified cyclotron energy fluctuations via B_2-coupling, see eq. (3.23). These fluctuations scale with $q_{\mathrm{ion}}/m_{\mathrm{ion}}^2$. In combination, $\sigma_{\Delta\nu_z}(^{48}\mathrm{Ca}^{17+}) = 24$ mHz is predicted from the measured $\sigma_{\Delta\nu_z}(^{12}\mathrm{C}^{5+}) = 73$ mHz, which is in very good agreement with the measured value.

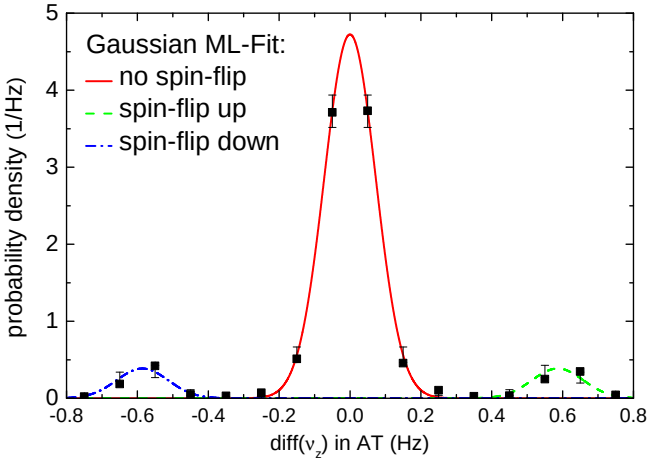

(a)

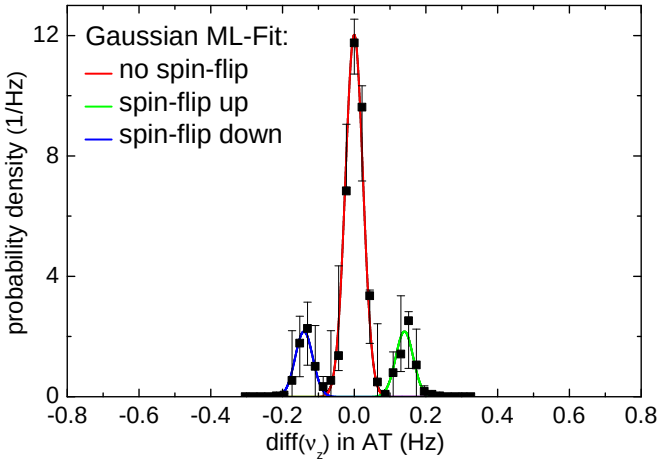

(b)

Figure 6.1: Probability densities of subsequently measured axial frequency differences ($\Delta\nu_z \equiv \mathrm{diff}(\nu_z)$) in the AT for a single $^{12}C^{5+}$ ion in (a) and $^{48}Ca^{17+}$ in (b). Between these axial frequency measurements 30 s spin-flip drives are applied. The probability densities consist of a superposition of three Gaussian distributions, where (1) no spin-flip (red curve), (2) a spin-flip up (green curve) and (3) a spin-flip down (blue curve) is induced. In (a) the axial frequency differences of a single $^{12}C^{5+}$ ion have been measured by a simple axial peak signal plus zero padding, see section 3.4.1. In total the studied data set contains 4682 spin-flip drives. The spin-flip rate amounts to 14.1% and an induced spin-flip generates an axial frequency jump of ±586 mHz. With an axial frequency jitter of $\sigma_{\Delta\nu_z} = 73$ mHz, in 99.995% ($\Delta\nu_z^{\mathrm{sf}}/2 = 4.0 \cdot \sigma_{\Delta\nu_z}$) of the measurement cycles the spin-flip is correctly detected. In (b) the axial frequency differences of a single $^{48}Ca^{17+}$ ion have been measured, using a phase-sensitive detection method, described in section 3.4.2. The data set contains 1790 spin-flip drives. The spin-flip rate amounts to 26.5%. An induced spin-flip generates an axial frequency jump of ±140 mHz. With an axial frequency jitter of $\sigma_{\Delta\nu_z} = 25$ mHz, in 99.5% ($\Delta\nu_z^{\mathrm{sf}}/2 = 2.8 \cdot \sigma_{\Delta\nu_z}$) of the measurement cycles the spin-flip is correctly detected. All the denoted parameters are specified via the maximum-likelihood fits, see the red, green and blue curves. The black data is just plotted for visualization. The shown binomial error bars are determined from the number of measurement cycles per histogram-bin and the probability density at the bin center given by the ML fits.

Here, $w_{\mathrm{PT}} = 1$ corresponds to a spin-flip in the PT, $w_{\mathrm{PT}} = 0$ corresponds to no spin-flip in the PT and $w_{\mathrm{PT}} = 0.5$ corresponds to no spin-flip information in the PT. Finally, the

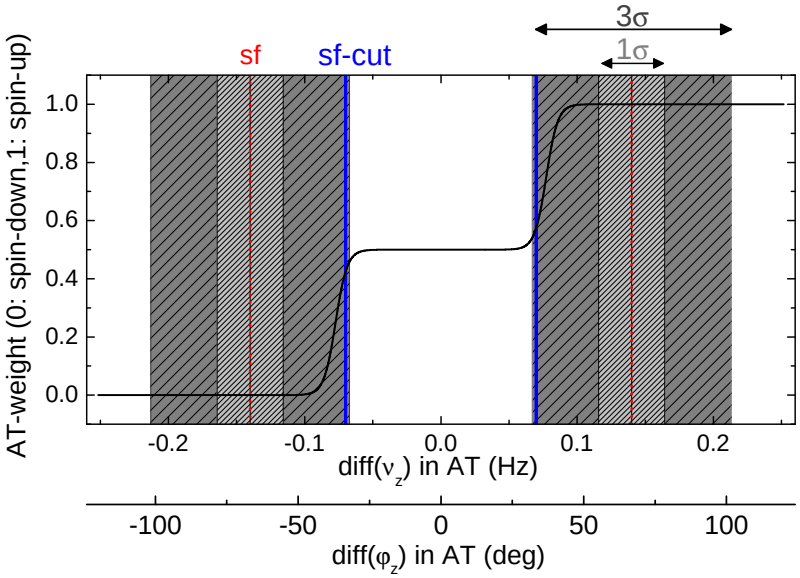

Figure 6.2: Look-up table of the AT-weight. Here, the AT-weight (curved black line) is plotted as a function of the measured axial frequency difference. The red lines denote the axial frequency jump in case of a spin-flip at $\pm\Delta\nu_z^{\mathrm{sf}}$. The blue lines symbolize the spin-flip cut criteria at $\pm\Delta\nu_z^{\mathrm{sf}}/2$. The bright gray shaded area illustrates the $1\sigma_{\Delta\nu_z}$-interval and the dark gray shaded area the $3\sigma_{\Delta\nu_z}$-interval.

Gaussian line-shape of the Γ-resonance, see eq. (4.22), gets modified by adding a fourth fit-parameter (off_Γ), which describes the wrong spin-flip detection rate in the PT:

$$\mathcal{G}_{\mathrm{PT}}^{\mathrm{mod}}(\Gamma^*|\mathrm{sf}_0,\Gamma_{\mathrm{res}},\sigma_\Gamma,\mathrm{off}_\Gamma) \equiv \mathrm{off}_\Gamma + \frac{\mathrm{sf}_0}{2\pi\sigma_\Gamma^2} e^{-\frac{(\Gamma^*-\Gamma_{\mathrm{res}})^2}{2\sigma_\Gamma^2}}. \tag{6.4}$$

The PT-weight finally has to be included in the maximum likelihood function, compare with eq. (4.23):

$$\begin{aligned}\mathcal{L}(\mathrm{sf}_0,\Gamma_{\mathrm{res}},\sigma_\Gamma,\mathrm{off}_\Gamma) = \prod_{i=1}^{N} & w_{\mathrm{PT}}(i) \cdot \mathcal{G}_{\mathrm{PT}}^{\mathrm{mod}}(\Gamma^*(i)|\mathrm{sf}_0,\Gamma_{\mathrm{res}},\sigma_\Gamma,\mathrm{off}_\Gamma) \\ & + (1 - w_{\mathrm{PT}}(i)) \cdot (1 - \mathcal{G}_{\mathrm{PT}}^{\mathrm{mod}}(\Gamma^*(i)|\mathrm{sf}_0,\Gamma_{\mathrm{res}},\sigma_\Gamma,\mathrm{off}_\Gamma)),\end{aligned} \tag{6.5}$$

where N is the number of measurement cycles. A more rigorous explanation for this weighted maximum likelihood function will be given in the doctoral thesis of Kurt Franke. In comparison to the common cut analysis, we improve the relative uncertainty of the final Γ_{res} by 20 ppt by using the weighting method, where all measurement cycles are

considered[1].

6.2 Statistical Γ-Values

After several weeks of learning how to produce ionized calcium ions in the mEBIT, see section 4.3.1 for details, we managed to reliably produce single lithiumlike calcium ions ($^{40}Ca^{17+}$) within two days. The final data acquisition of $^{40}Ca^{17+}$ has been performed within two months starting in the beginning of March 2014. Here, three Γ-resonances have been measured at three different modified cyclotron energies, see fig. 6.3(a).
Directly after the removal of $^{40}Ca^{17+}$ we managed to prepare a single $^{48}Ca^{17+}$ ion within a week. The data taking has only lasted 1.5 months starting in the beginning of June 2014. Five Γ-resonances have been recorded at three different modified cyclotron energies, see fig. 6.3(b).
During the $^{48}Ca^{17+}$ measurements at large modified cyclotron energies ($U_{\mathrm{exc}} \geq 2$ Vpp) accidentally a wrong tuning ratio has been applied: $\Delta TR = TR_{\mathrm{wrong}} - TR_{\mathrm{opt}} = -1 \cdot 10^{-4}$.
In the extrapolation of the fitted Γ_{mean} values to zero modified cyclotron energies, see fig. 6.3(b), a conservative estimation for higher-order electric field anharmonicities has already been included.
After the linear extrapolation to zero modified cyclotron energies, we determine the following statistical Γ values:

$$\Gamma_{\mathrm{stat}}(^{40}Ca^{17+}) = 4282.429\,539\,43\,(21) \qquad (49\ \mathrm{ppt}) \quad \text{and} \tag{6.6}$$

$$\Gamma_{\mathrm{stat}}(^{48}Ca^{17+}) = 5138.837\,961\,92\,(30) \qquad (58\ \mathrm{ppt}). \tag{6.7}$$

1 All measurement cycles are considered, except for the measurement cycles during and after the filling of the liquid gas reservoirs, see also section 5.1.

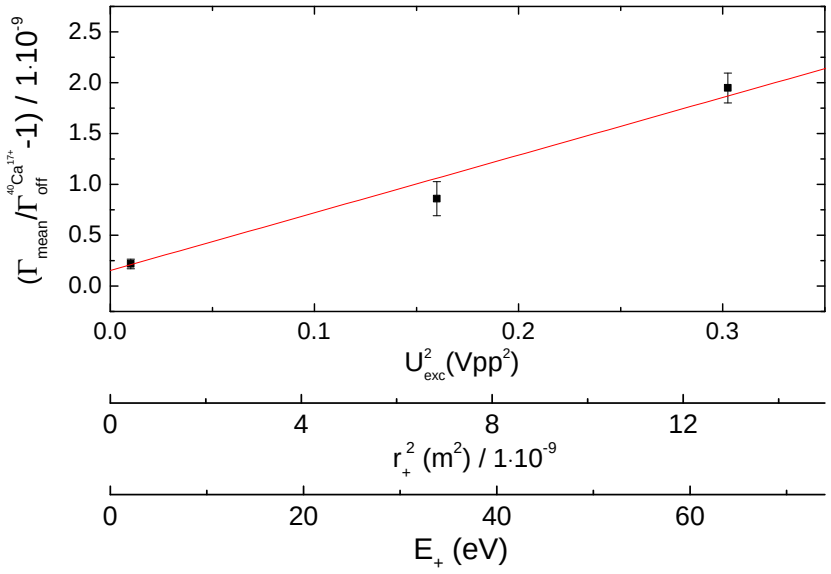

(a)

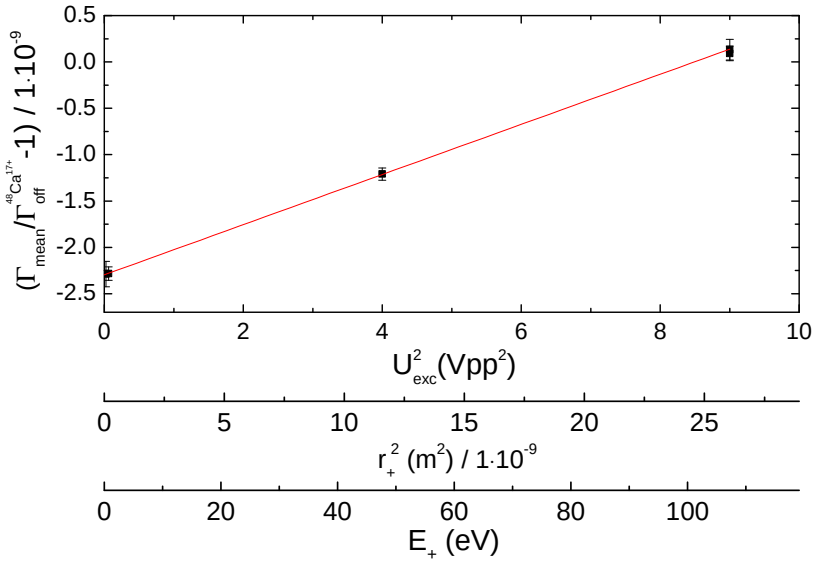

(b)

Figure 6.3: Illustration of all measured calcium Γ values as a function of the cyclotron energies. In (a) the three fitted central values of the $^{40}\mathrm{Ca}^{17+}$ Γ-resonances are shown with a normalization factor of $\Gamma_{\mathrm{off}}^{^{40}\mathrm{Ca}^{17+}} = 4282.429\ 538\ 772$. The linear fit (red line) has an offset value of $1.54(49) \cdot 10^{-10}$ and a slope of $m_{\frac{\delta\Gamma}{\Gamma}} = 5.67(49) \cdot 10^{-9}\ \mathrm{Vpp}^{-2}$. In (b) the five fitted central values of the $^{48}\mathrm{Ca}^{17+}$ Γ-resonances are shown with a normalization factor of $\Gamma_{\mathrm{off}}^{^{48}\mathrm{Ca}^{17+}} = 5138.837\ 973\ 696$. The linear fit (red line) has an offset value of $-2.29(58) \cdot 10^{-9}$ and a slope of $m_{\frac{\delta\Gamma}{\Gamma}} = 2.70(14) \cdot 10^{-10}\ \mathrm{Vpp}^{-2}$.

6.3 Systematic Shifts and Uncertainties

Systematic shifts and the corresponding uncertainties of the absolute g-factors of $^{40}Ca^{17+}$ and $^{48}Ca^{17+}$ are calculated in a very similar to the systematic shifts of $^{12}C^{5+}$ introduced in section 5.2.

One major difference is given in the image current shift caused by the interaction between the ion and the cyclotron resonator. For the detection of multiple ions, see section 4.3.1, and in particular for a potential further cooling of the modified cyclotron mode, we tuned the cyclotron resonator by adjusting its parallel capacitance, before we started the measurement campaign on $^{40}Ca^{17+}$. Adjusting the varactor diode in a way that the cyclotron resonator is in resonance with the modified cyclotron mode of the $^{40}Ca^{17+}$ ion, we achieved cooling time constants of about 10 s, measured by the time-resolved decrease of the cyclotron peak signal. However, we detected cyclotron temperatures of several hundred Kelvin instead of the expected liquid helium temperature of 4.2 K. This unfavorable high temperature might be explained by an oscillation of the cyclotron detection system, which is indicated by the raised Q value from a few 100 up to several 1000 by changing the applied voltage of the varactor diode. A further reason for this high temperature might be given by some broad band noise coupled from other electronic devices, e.g. from the lab computers. During the measurement process the resonator frequency of the detuned cyclotron resonator has been $\nu_{\mathrm{res}} = 24\,376(10)$ kHz, which is relatively close to the modified cyclotron frequency of the ion: $\nu_+(^{40}Ca^{17+}) = 24\,586\,288$ Hz.

Considering the resonator characteristics given in table 4.4, the image current shift amounts to $1 - \Gamma_{\mathrm{final}}/\Gamma_{\mathrm{stat}} = -1.1(12) \cdot 10^{-11}$ with a particularly conservative estimation of the uncertainty, since the resonator frequency and the modified cyclotron frequency are so close and small deviations of the resonator parameters do not linearly scale with the image current shift, see e.g. fig. 5.6.

During the subsequent $^{48}Ca^{17+}$ measurements we used the same configuration of the cyclotron resonator. Since the modified cyclotron frequency of $\nu_+ = 20\,485\,535$ Hz is far-off the cyclotron resonator, the image current shift is significantly smaller: $1 - \Gamma_{\mathrm{final}}/\Gamma_{\mathrm{stat}} = 6(10) \cdot 10^{-13}$.

In table 6.1 all systematic shifts and uncertainties are summarized. Considering these

Table 6.1: Systematic shifts and uncertainties of the measured Γ's of $^{40}Ca^{17+}$ and $^{48}Ca^{17+}$.

effect	$^{40}Ca^{17+}$ (ppt)	$^{48}Ca^{17+}$ (ppt)
image charge shift	−941(47)	−1130(57)
image current shift	11(12)	−0.6(10)
magnetic field imperfections	0.46(31)	0.45(37)
line-shape model of the dip-signal	0(14)	0(12)
electric field imperfections	0.00(39)	0.00(51)
ν_- measurement	0.0(30)	0.0(26)
drift of axial potential	0.0(12)	0.0(12)
residual relativistic shift	−0.010(1)	−0.010(1)
line-shape model Γ resonance	0.0(6)	0.0(6)
total systematic shift	−930(51)	−1129(58)

shifts we obtain the following final Γ values:

$$\Gamma_{\mathrm{final}}(^{40}\mathrm{Ca}^{17+}) = 4282.429\,535\,45(21)(22) \qquad (70\ \mathrm{ppt}), \tag{6.8}$$

$$\Gamma_{\mathrm{final}}(^{48}\mathrm{Ca}^{17+}) = 5138.837\,956\,12(30)(30) \qquad (81\ \mathrm{ppt}), \tag{6.9}$$

where the statistical and systematic uncertainties of the frequency ratios are listed separately.
In the g-factor difference some systematic shifts, in particular the dominant image charge shift, will cancel, see section 6.5.

6.4 Consistency Checks

Similar to the consistency checks which we performed with the single $^{12}\mathrm{C}^{5+}$ ion, see section 5.3, I also studied the energy dependence of (1) the measured Γ ratios, see fig. 6.3 (a) and (b), (2) the modified cyclotron frequency difference between the double-dip and PnA detection technique, see fig. 6.4(a) and (b), as well as (3) the axial frequency shift in the AT, see fig. 6.4(c) and (d) for $^{40}\mathrm{Ca}^{17+}$ and $^{48}\mathrm{Ca}^{17+}$. Combining these three different energy dependencies, we can extract B_2 in the PT in two independent ways, see table 5.3.

Table 6.2: Consistency checks. Two independent measurement approaches have been applied to determine B_2 in the PT using $^{40}\mathrm{Ca}^{17+}$ and $^{48}\mathrm{Ca}^{17+}$. In the fourth column the corresponding values measured with a single $^{12}\mathrm{C}^{5+}$ ion are listed, see also table 5.3.

combination	combination of equations	B_2 (T/m^2) $^{40}\mathrm{Ca}^{17+}$	$^{48}\mathrm{Ca}^{17+}$	$^{12}\mathrm{C}^{5+}$
$m_{\frac{\delta\Gamma}{\Gamma}} \leftrightarrow m_{\nu_+^{\mathrm{PnA}} - \nu_+^{\mathrm{DD}}}$	(5.22) and (5.23)	1.05(20)	0.75(24)	1.01(20)
$m_{\nu_+^{\mathrm{PnA}} - \nu_+^{\mathrm{DD}}} \leftrightarrow m_{\nu_z^{\mathrm{AT}}}$	(5.23) and (5.25)	1.14(23)	1.10(15)	1.40(50)

Here, it is remarkable, that I increased the maximal applied modified cyclotron radius step-by-step for the three Larmor-to-cyclotron frequency ratio measurements to study possible systematic shifts which might arise at large modified cyclotron radii: (1) $r_+^{\mathrm{max}} = 90\,\mu\mathrm{m}$ ($E_+ = 90\,\mathrm{eV}$) for the $^{12}\mathrm{C}^{5+}$ ion, see fig. 5.2, (2) $r_+^{\mathrm{max}} = 110\,\mu\mathrm{m}$ ($E_+ = 65\,\mathrm{eV}$) for $^{40}\mathrm{Ca}^{17+}$, see fig. 6.3(a) and (3) even $r_+^{\mathrm{max}} = 160\,\mu\mathrm{m}$ ($E_+ = 112\,\mathrm{eV}$) for $^{48}\mathrm{Ca}^{17+}$, see fig. 6.3(b). Fortunately the determined B_2 values listed in table 6.2 agree with each other which once more confirm our model of systematic shifts.

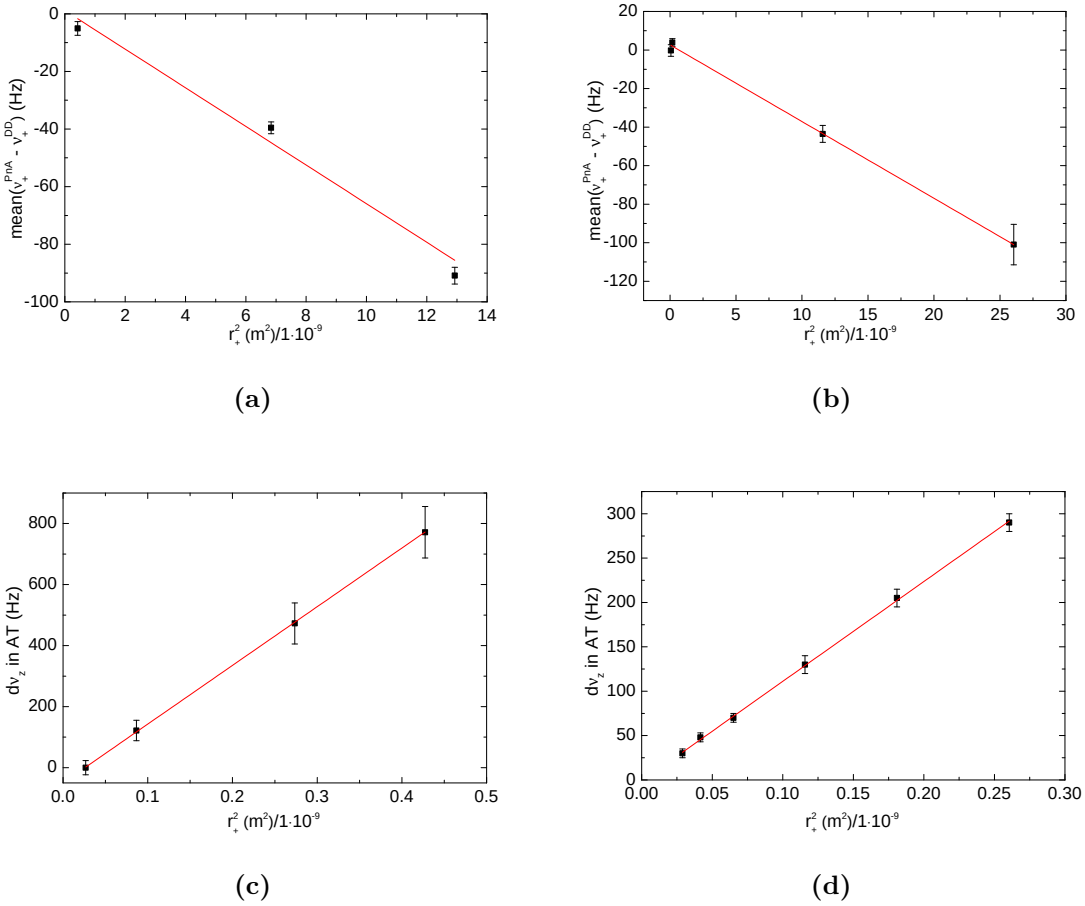

Figure 6.4: Consistency checks of the $^{40}Ca^{17+}$ and $^{48}Ca^{17+}$ measurements. Illustrations of various eigenfrequency shifts as a function of the excited squared modified cyclotron radius after the first PnA pulse. In (a) and (b) the energy dependence of $< \nu_+^{PnA} - \nu_+^{DD} >$ is shown for $^{40}Ca^{17+}$ in (a) and $^{48}Ca^{17+}$ in (b). See fig. 5.7(a) for the corresponding data measured with $^{12}C^{5+}$. In (c) and (d) the energy dependence of the axial frequency in the AT is plotted for $^{40}Ca^{17+}$ in (a) and $^{48}Ca^{17+}$ in (b). See fig. 5.7(d) for the corresponding data measured with $^{12}C^{5+}$. The fitted slopes amount to $m_{\nu_+^{\mathrm{PnA}} - \nu_+^{\mathrm{DD}}} = -0.287(13)$ Hz Vpp^{-2} in (a), $m_{\nu_+^{\mathrm{PnA}} - \nu_+^{\mathrm{DD}}} = -0.01152(8)$ Hz Vpp^{-2} in (b), $m_{\nu_z}^{\mathrm{AT}} = 82.2(78) \cdot 10^3$ Hz Vpp^{-2} in (c) and $m_{\nu_z}^{\mathrm{AT}} = 3.26(12) \cdot 10^3$ Hz Vpp^{-2} in (d).

6.5 Final Results

6.5.1 The Absolute g-Factors - Testing Many-Electron QED Calculations

Combining the measured Γ values, see eq. (6.8) and eq. (6.9), with the ion masses, see eq. (2.21) and eq. (2.20), we determine the presently most precise g-factor values of lithiumlike ions, using eq. (2.13):

$$g(^{40}\mathrm{Ca}^{17+})_{\mathrm{meas}} = 1.999\,202\,040\,55(10)(12)(110) \qquad (0.56\ \mathrm{ppb}) \qquad \text{and} \qquad (6.10)$$

$$g(^{48}\mathrm{Ca}^{17+})_{\mathrm{meas}} = 1.999\,202\,028\,85(12)(13)(80) \qquad (0.41\ \mathrm{ppb}). \qquad (6.11)$$

Here, the statistical and systematic uncertainties of the Γ ratios as well as the ion mass uncertainties are presented separately. Both g-factors are most notably limited by the uncertainty of the ion mass. Nevertheless, they are about a factor two more precise than the previously measured g-factor of lithiumlike silicon ($(\delta g/g)_{^{28}\mathrm{Si}^{11+}} = 1.1$ ppb), which has been limited by the statistical uncertainty of the measured Γ ratio [59]. In case of lithiumlike silicon, the modified cyclotron frequency has been measured by using the double-dip technique instead of using PnA.
The comparisons of the theoretically calculated g-factor values, see table 2.5:

$$g(^{40}\mathrm{Ca}^{17+})_{\mathrm{theo}} = 1.999\,202\,042(13) \qquad (65\ \mathrm{ppb}) \qquad \text{and} \qquad (6.12)$$

$$g(^{48}\mathrm{Ca}^{17+})_{\mathrm{theo}} = 1.999\,202\,032(13) \qquad (65\ \mathrm{ppb}) \qquad (6.13)$$

with the measured ones provide a stringent test of many-electron QED calculations in a magnetic field.

6.5.2 The g-Factor Difference $\Delta g = g(^{40}\mathrm{Ca}^{17+}) - g(^{48}\mathrm{Ca}^{17+})$ - Testing BS-QED beyond the Furry Picture

The g-factor difference finally yields the sought-after isotope difference

$$\Delta g_{\mathrm{meas}} = g_{\mathrm{meas}}(^{40}\mathrm{Ca}^{17+}) - g_{\mathrm{meas}}(^{48}\mathrm{Ca}^{17+}) = 11.70(16)(3)(138)\cdot 10^{-9} \quad (12\%), \qquad (6.14)$$

where the statistical and systematic uncertainties of the frequency ratios and the ion mass uncertainty are listed separately. Since the dominant systematic shifts, the image charge shifts, see table 6.1, completely[1] cancel in the g-factor difference, the denoted systematic uncertainty of the frequency ratios is smaller than the quadratically summed systematic uncertainties given in eq. (6.10) and eq. (6.11). The comparison of the measured value of the g-factor difference with the extremely precise theoretical prediction, see table 2.4:

$$\Delta g_{\mathrm{theo}} = 10.305(27)\cdot 10^{-9} \qquad (0.26\%) \qquad (6.15)$$

allows for the first time to address and stringently test the relativistic dynamic interaction of the electron spin with the motile nucleus. The 1.0σ agreement with the calculated value decisively confirms the validity of QED beyond the Furry picture even in the presence

1 Here, I assume that both ions are placed at the same position in the PT.

of strong fields and reinforces the understanding of the interaction between the bound electrons and the nucleus. The understanding of these contributions provides the opportunity to extract fundamental constants, namely the fine structure constant α, and nuclear properties via g-factor measurements in heavy atomic systems [149].

At last, I want to discuss briefly the influence of the neutron number on the root-mean-square nuclear charge radii of the two doubly magic nuclei of ^{40}Ca and ^{48}Ca. Even though the eight additional neutrons of ^{48}Ca form an additional closed $1f_{7/2}$ nuclear shell, both isotopes have a remarkably similar nuclear charge radius: $r_{\mathrm{nucl}}(^{40}\mathrm{Ca}) = 3.4776\ (19)$ fm, $r_{\mathrm{nucl}}(^{48}\mathrm{Ca}) = 3.4771\ (20)$ fm and $\Delta r = r_{\mathrm{nucl}}(^{40}\mathrm{Ca}) - r_{\mathrm{nucl}}(^{48}\mathrm{Ca}) = 0.0005\ (9)$ fm [94], see also section 2.7.2, which is still an open question in nuclear physics. In that way, the finite nuclear size contribution almost cancels in the isotope shift. For this reason, the nuclear recoil shift dominates the g-factor difference to 99.96%. However, relying on the measured g-factor difference and on the calculations of the recoil contribution, we determine the difference of the nuclear charge radii: $\Delta r = r_{\mathrm{nucl}}(^{40}\mathrm{Ca}) - r_{\mathrm{nucl}}(^{48}\mathrm{Ca}) = 0.17\ (17)$ fm, which is in reasonable agreement with the literature value[1] [150].

1 In leading-order the finite nuclear size effect scales as $\Delta g = \frac{8}{3n^3}(Z\alpha)^4 r_{\mathrm{nucl}}^2 \cdot 6.699 \cdot 10^{24}\ \mathrm{m}^{-2}$ [45], where in our case $n = 2$ (lithiumlike) and $Z = 20$.

CHAPTER 7

Outlook - A New Generation of High-Precision Penning Trap

Besides the determination of the electron mass and the g-factor difference of lithiumlike calcium isotopes, which have been presented in this thesis, further exciting bound-electron g-factor measurements have been performed in the medium-Z range in the previous years, e.g. the measurements of hydogenlike and lithiumlike silicon, see [46, 59]. Tests of QED in even stronger electric fields require heavier and higher-charged ions which are not producible at our miniature EBIS, which reaches so-far a maximally applied electron beam energy of 5.5 keV[1]. At the moment, two additional g-factor experiments are set up within the HITRAP initiative: (1) ARTEMIS [151, 152], located at HITRAP, a capturing and cooling facility for highly charged ions located at the GSI-accelerator complex, and (2) ALPHATRAP, located at the large Heidelberg-EBIS at MPIK. These experiments will be briefly summarized further below. The present g-factor experiment located in Mainz will be specialized for lighter ions, e.g. in the near future high-precision mass measurements are planned for the masses of the fundamental building blocks of atomic structure, the proton and later the neutron.
In the beginning of this last chapter, in section 7.1, I will focus on a new Penning trap design, which essentially will be used at two experiments: (1) our upgraded experimental setup and (2) in a scaled version at ALPHATRAP. In the final section, in section 7.2, I will give a brief outlook on future g-factor experiments on highly charged ions as well as on the physical agenda of our rebuilt experimental setup.

7.1 Design of a New Seven-Electrode Cylindrical Penning Trap

Aiming for relative precisions of a few 10^{-12} or even better, two major limitations illustrate the urgent need of a revised Penning trap design:

- First of all, the dominant systematic uncertainty, the *image charge shift*, can be efficiently reduced by increasing the trap radius. This effect scales with the inverse

1 The production of hydrogenlike calcium requires electron beam energies in excess of $E_{\mathrm{ion}} = 5.128\,\mathrm{keV}$. During our last creation attempts several flash-arcs limited the maximal applied high-voltage. Most of the time they occurred in the high-voltage box connected to the hat flange, see section 4.1.2. Moreover, the FEP has been destroyed once during a creation cycle and had to be replaced in a time-consuming repairing.

cubic trap radius, see eq. (3.55):

$$\Delta\omega_+ \propto \frac{1}{r^3}. \tag{7.1}$$

Furthermore, an increase of the trap radius also reduces the impact of possible patch potentials on the electrode surfaces, which again decreases potential radial shifts of the ion's center position. In that way, the relative size of the uncertainty of the image charge shift is diminished as well, which at present is conservatively estimated to 5% of the complete shift, see section 3.2.4.

- In addition, we aim for a higher harmonicity of the electric trapping potential by a further subdivision of the electrodes in axial direction, using seven cylindrical electrodes instead of five. Such a finer segmentation and the accompanying better compensation of higher electric field components enable larger excitations of the ion's motion, for example at the second PnA pulse. During the subsequent signal detection the increased signal-to-noise ratio reduces the technical jitter of the readout phase, see section 4.5.1.
  Due to a flaw in the primary calculations of the currently implemented trap, see section 4.3.2, even a compensated five-electrode trap design would improve the harmonicity of our setup.

7.1.1 Analytical Calculations of a New Trap Design

Since there is no analytical solution for the electric potential of a cylindrical Penning trap with broken rotational symmetry, the recent calculations have been split into two parts. In the first part, the potential of the cylindrical trap (excluding the vertical slits) is calculated analytically. In the subsequent second part the analytical solution is additionally studied numerically including the vertical slits, which break rotational symmetry. In the following section, these analytical calculations are summarized.

The analytical formulas to calculate the trapping potential of stacked cylindrical electrodes have been described in several papers, see e.g. [122]. Small horizontal slits separate these electrodes in axial direction, so that a linear interpolation of the potential between the electrodes is appropriate. Here, I use the calculus based on [153, 154] and [145], which I implemented in *Matlab*. More specifically, the following boundary value problem had to be solved, see also fig. 7.6:

> All electrodes have a cylindrical shape with the same inner radius r_0. They are stacked on top of each other with tiny distances dd in between them. These distances are much smaller than the axial lengths of the electrodes. Due to rotational symmetry the problem can be solved in two dimensions using cylindrical coordinates (r,z). The electric potential on adjacent cylindrical electrodes beyond the upper and lower endcap electrodes of the Penning trap, which have the same radius r_0 and basically infinite length, is zero.

The electrostatic potential $\Phi(r,z)$ of the empty Penning trap has to fulfill the Laplace

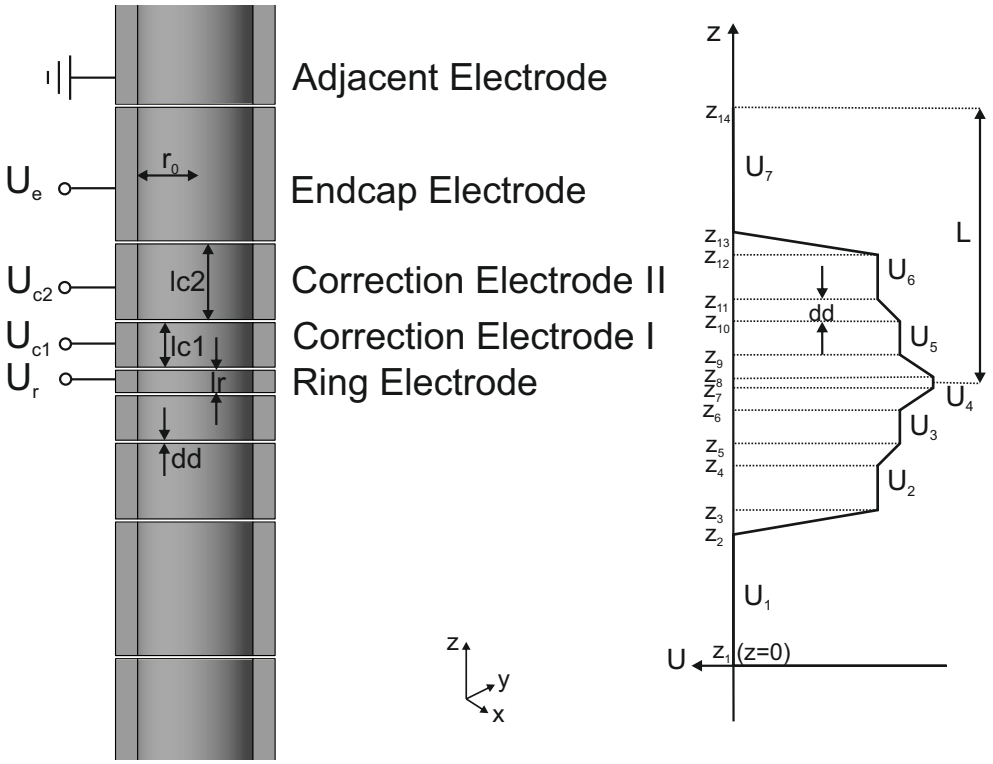

Figure 7.1: Schematic of the new seven-electrode trap with nomenclature. On the right side the potential distribution along the electrode surfaces is shown. Here, the electrode distances *dd* are depicted in an exaggerated way, to illustrate the linear interpolation between the electrode surfaces. It should be noted, that the point of coordinates is placed on the bottom of the trap, so that all z_i are positive numbers.

equation $\Delta\Phi(r,z) = \nabla^2\Phi(r,z) = 0$. In cylindrical coordinates with rotational symmetry around the z-axis the Laplace equation has the following structure:

$$\triangle\Phi(r,z) = \frac{\partial^2\Phi(r,z)}{\partial r^2} + \frac{1}{r}\frac{\partial\Phi(r,z)}{\partial r} + \frac{\partial^2\Phi(r,z)}{\partial z^2} = 0. \tag{7.2}$$

Assuming a product structure of the potential, its solution can be formulated as follows:

$$\Phi(r,z) = R(r)\cdot Z(z). \tag{7.3}$$

We can separate the partial differential equation into two ordinary differential equations:

$$\frac{\partial^2 Z(z)}{\partial z^2} + k^2 Z(z) = 0 \qquad \text{and} \tag{7.4}$$

$$\frac{\partial^2 R(r)}{\partial r^2} + \frac{1}{r}\frac{\partial R(r)}{\partial r} - k^2 R(r) = 0, \tag{7.5}$$

where k is a separation constant. Equation 7.4 describes an ordinary harmonic oscillator with the elementary solution: $Z(z) = B(k) \cdot \sin(kz)$. Equation 7.5 is a modified Bessel's equation of zeroth order and can be solved by using the Bessel function of the first kind and zeroth order: $R(r) = C(k) \cdot I_0(kr)$. The general solution of the potential is given by:

$$\Phi(r,z) = \int_{-\infty}^{+\infty} E(k) I_0(kr) \sin(kz)\ dk, \tag{7.6}$$

where $E(k) \equiv B(k) \cdot C(k)$. The integral can be written as a sum if the potential vanishes at both ends of the trap [153]:

$$\begin{aligned}\Phi(r,z) &= \sum_{n=-\infty}^{+\infty} E(k_n) I_0(k_n r) \sin(k_n z) \\ &= \sum_{n=1}^{+\infty} [E(k_n) - E(k_{-n})] I_0(k_n r) \sin(k_n z) \\ &\equiv \sum_{n=1}^{+\infty} A(k_n) I_0(k_n r) \sin(k_n z),\end{aligned} \tag{7.7}$$

where $k_n \equiv \frac{n\pi}{2L}$ and $2L$ is the complete length of the trap. With the following orthogonality criterion $\frac{1}{2L}\int_{-L}^{L} \sin(k_n z)\sin(k_m z)dz = \delta_{mn}$, we obtain:

$$A_n \equiv A(k_n) = \frac{1}{L I_0(k_n r)} \int_{-L}^{L} \sin(k_n z)\Phi(r,z)dz. \tag{7.8}$$

The radial dependences of $\Phi(r,z)$ and $I_0(k_n r)$ cancel each other so that the A_n coefficients do not feature any radial dependence. The applied voltages at the electrode surfaces ($r = r_0$) provide Dirichlet boundary conditions to calculate the A_n via 7.8. For a trap with seven cylindrical electrodes we get:

$$\begin{aligned}A_n = \frac{1}{L I_0(k_n r_0)} \Bigg[&\left(\frac{U_1 \cos(k_n z_1) - U_7 \cos(k_n z_{14})}{k_n} \right) \\ &+ \sum_{j=2}^{7} \frac{U_j - U_{j-1}}{k_n^2 dd} \left(\sin(k_n z_{2j-1}) - \sin(k_n z_{2j-2}) \right) \Bigg],\end{aligned} \tag{7.9}$$

where dd is the distance between the electrodes. For the definitions of the electrode voltages U_i and the positions in axial direction z_i see fig. 7.1. Inserting eq. (7.9) into eq. (7.7) the potential of the trap can be calculated analytically, which even holds for potentials asymmetrically applied with respect to the $z = 0$ plane. The expansion coefficients of the electric potential along the z-axis (see 3.18) can be calculated analytically:

$$C_j = 2\frac{(d_{\text{char}})^j}{U_r L j!} \sum_{n=1}^{\infty} \frac{k_n^j A_n}{I_0(k_n r_0)} \sin(\pi/2(n+j)). \tag{7.10}$$

Here, I define the characteristic trap parameter as $d_{\mathrm{char}} \equiv \sqrt{\frac{1}{2}(Z_0^2 + \frac{r^2}{2})}$ and $Z_0 \equiv \frac{l_r}{2} + dd + l_{c1} + dd + l_{c2} + dd$.

Simplified Formulas Considering an Axially Symmetric Potential

In the special case of an axially symmetric potential with grounded endcaps, which has been the scenario during the optimization process, the following simplification can be made:

$$\Phi(r,z) = \sum_{\substack{n=1 \\ \text{n odd}}}^{+\infty} \widetilde{A}(k_n) I_0(k_n r) \cos(k_n z), \tag{7.11}$$

where

$$\widetilde{A}(k_n) = \frac{2}{L I_0(k_n r_0)} \sum_{i=5}^{7} \frac{U_i - U_{i-1}}{k_n^2 dd} \left(\cos(k_n(z_{2i-1} - L)) - \cos(k_n(z_{2i-2} - L))\right) \tag{7.12}$$

and even terms in n cancel. The expansion coefficients of the potential are given by:

$$\widetilde{C_j} = 2\frac{(d_{\mathrm{char}})^j (-1)^{j/2}}{U_r j!} \sum_{\substack{n=1 \\ \text{n odd}}}^{\infty} k_n^j \widetilde{A}(k_n). \tag{7.13}$$

Optimization Process

Some of the trap parameters r_0, dd and U_r have been fixed in advance considering the following aspects:

- dd: The distances between the electrodes dd are limited on the one hand by the undesired trap capacitances, which enlarge the capacitances of the detection systems / resonators by decreasing the electrode distances. Aiming for large parallel resistances $R_p = Q\sqrt{L/C}$, see eq. (3.34), the capacitances should be as small as possible. On the other hand undefined electric field imperfections increasing with the size of these slits should be minimized. As a trade-off, we adopt the electrode distances of the present design: $dd = 140\,\mu\mathrm{m}$.
- r_0 : The trap radius is increased from $r_0 = 3.5\,\mathrm{mm}$ (existing setup) to $r_0 = 5\,\mathrm{mm}$ for the rebuilt setup, consequently reducing the image charge shift by a factor of ≈ 3. Working with very heavy, highly charged ions at ALPHATRAP the trap radius will be even larger, $r_0 = 9\,\mathrm{mm}$, reducing the image current shift by a factor of 17. In that way, the relative image charge shift of the free cyclotron frequency of $^{208}\mathrm{Pb}^{81+}$ will be $2.9 \cdot 10^{-10}$, which is of the same size as for $^{12}\mathrm{C}^{5+}$ in the present setup, see eq. (5.8).
- U_r : Working in the axial frequency range of several 100 kHz, see eq. (3.4), and using the ultra-stable voltage supply, UM1-14, with a voltage range between 0 and $-14\,\mathrm{V}$, the ring voltage (for the proton) is fixed to $U_r = -7\,\mathrm{V}$ during the trap optimization.

In a cylindrical seven-electrode trap, five parameters: l_r, l_{c1}, l_{c2}, U_{c1} and U_{c2} can be optimized to reach a highly compensated trap. In a naive approach one might require triple compensation and orthogonality for each correction electrode, see eq. (3.18) and section 3.1.3: $C_4 = C_6 = C_8 = D_{21} = D_{22} = 0$, where:

$$C_2 = D_{21}\frac{U_{c1}}{U_r} + D_{22}\frac{U_{c2}}{U_r} + E_2. \tag{7.14}$$

However, since double orthogonality $D_{21} = D_{22} = 0$ cannot be fulfilled, we require a slightly weaker orthogonality criterion, stated as *combined orthogonality*:

$$D_2^{\text{comb}} \equiv D_{21}\frac{U_{c1}}{U_r} + D_{22}\frac{U_{c2}}{U_r} = 0. \tag{7.15}$$

Our finally selected five optimization conditions are:

$$C_4 = C_6 = C_8 = C_{10} = D_2^{\text{comb}} = 0. \tag{7.16}$$

The trap design is numerically optimized by minimizing simultaneously $|C_4|$, $|C_6|$, $|C_8|$, $|C_{10}|$, and D_2^{comb}, using the *Matlab* routine *fminsearch.m* [155], which finds the local minimum of $\eta \equiv C_4^2 + C_6^2 + C_8^2 + w_1 \cdot C_{10}^2 + w_2 \cdot (D_2^{\text{comb}})^2$. Here, I introduced some weighting coefficient $w_1 \approx 1 \cdot 10^{-4} \ll 1$ and $w_2 \approx 1 \cdot 10^{-5} \ll 1$ to boost the significance of the leading-order electric field coefficients during the optimization process. These weighting coefficients have been varied during the optimization. The minimization has been performed in two different ways, using the Nelder-Mead simplex algorithm [156] as well as the Levenberg-Marquardt algorithm (with *lsqnonlin.m*). The five parameters, l_r^0, l_{c1}^0, l_{c2}^0, U_{c1}^0 and U_{c2}^0, which set the initial conditions of the minimization, have been scanned over broad ranges to obtain the global minimum. During the scans the smallest applied step sizes for the variation of the initial conditions amount to 5 µm for the three spatial parameters and 0.05 mV for both correction voltages.
Focusing on the optimal choice of electrode voltages, it is remarkable, that at the final chosen trap geometry minimal C_6, C_8 and C_{10} have similar U_{c1} to U_{c2} dependences, see the *valleys* in the U_{c1}-U_{c2}-maps shown in fig. 7.2(b), (c) and (d). These maps also illustrate, that C_4 can be mainly modified by U_{c1}, whereas C_6 and the other higher terms can be mainly modified by U_{c2}.
The cut criterion for the potential expansion in $k_n = \frac{n\pi}{2L}$ has been generously set to $n = 40000$. Setting this upper cut criterion to values larger than 40000 no significant deviations of the calculated trapping potential have been observed during the optimization process.

7.1.2 Final Parameters of the Proton Trap

The optimized parameters are summarized in table 7.1. In the final analytical calculation of the trapping potential, the residual leading-order coefficients of the electric potential amount to: $C_2 = -0.594787$, $C_4 = 8{\cdot}10^{-10}$, $C_6 = -8{\cdot}10^{-11}$, $C_8 = 4{\cdot}10^{-9}$, $C_{10} = -4{\cdot}10^{-10}$, and $D_2^{\text{comb}} = -2 \cdot 10^{-7}$.
With these optimized trap parameters and a ring voltage of $U_r = -12.5$ V, we obtain

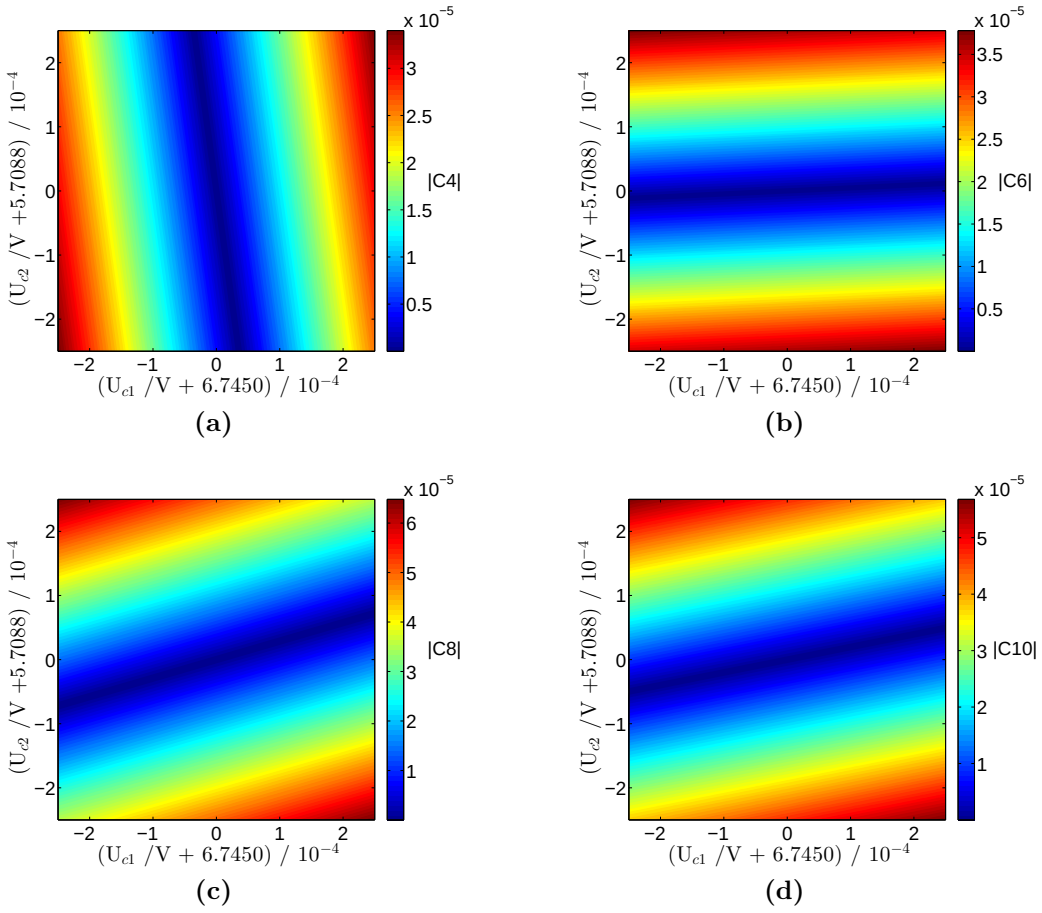

Figure 7.2: C_4-, C_6-, C_8- and C_{10}-maps, which illustrate the size of the higher-order electric field coefficients as a function of the correction voltages U_{c1} to U_{c2}, considering the optimized trap configuration presented in table 7.1.

the following axial frequencies: $\nu_z(\text{proton}) = 834.67\,\text{kHz}$, $\nu_z(^{12}\text{C}^{6+}) = 590.20\,\text{kHz}$ and $\nu_z(^{28}\text{Si}^{13+}) = 568.73\,\text{kHz}$.
For the implementation of two cyclotron resonators and the quadrupole excitation, see section 7.1.5, the ring and both inner correction electrodes are vertically split into two equal halves. To study the impact of these additional vertical slits ($dd = 140\,\mu\text{m}$) on the harmonicity of the electric potential, elaborate three dimensional numerical finite-element calculations have been performed using *Comsol*. Comparing numerical simulations with and without these vertical slits, no significant deviations in the trapping potential have been observed.

7.1.3 Performance of the New Trap - Study of the Axial Frequency Shifts

The improvement of the electric trapping potential compared to the old trap design can be illustrated by the axial frequency shifts as a function of the excited axial amplitude z_0,

Table 7.1: Fixed and optimized parameters of the proton trap. The characteristic trap parameter amounts to: $d_{\mathrm{char}} \equiv \sqrt{\frac{1}{2}(Z_0^2 + \frac{r^2}{2})} = 5.1071\,\mathrm{mm}$, where $Z_0 \equiv \frac{l_r}{2} + dd + l_{c1} + dd + l_{c2} + dd$.

trap parameters		values at 4 K
fixed	radius (r)	5 mm
	voltage of ring (U_r)	−7 V
	electrode distances (dd)	0.14 mm
optimized	length of ring (l_r)	1.0472 mm
	length of corr. el. I (l_{c1})	1.9995 mm
	length of corr. el. II (l_{c2})	3.3548 mm
	voltage of corr. el. I (U_{c1})	−6.744 96 V
	voltage of corr. el. II (U_{c2})	−5.708 86 V

see fig. 7.3. Here, the axial frequency shifts of a proton at a ring voltage of $U_r = -7\,\mathrm{V}$ ($\rightarrow\ \nu_z(\mathrm{proton}) = 625\,\mathrm{kHz}$) are calculated considering the potential coefficients $C_4, C_6, ..., C_{50}$ and using eq. (3.20) from [120] ($d\nu_z^{\mathrm{tot}} = \left|\sum_{i=4,6,...}^{50} d\nu_z(C_i)\right|$). Four different traps are studied: (1) The present five-electrode trap with a trap radius of $r_0 = 3.5\mathrm{mm}$ is indicated in turquoise, see fig. 7.3. (2) Since there has been a flaw in the trap calculation, also the optimized five-electrode trap with $C_4 = C_6 = D_2 = 0$ and $r_0 = 3.5\,\mathrm{mm}$ is shown in green. (3) As the new trap exhibits a trap radius of $r_0 = 5\,\mathrm{mm}$, the corresponding optimized five-electrode trap is shown in red. (4) Finally, the new optimized seven-electrode trap with $r_0 = 5\,\mathrm{mm}$ is illustrated in blue. The black dashed area denotes the axial shifts of the new trap in case of deviations of the electrode lengths and the inner radii of $\delta l = \pm 15\,\mu\mathrm{m}$ and $\delta r_0 = \pm 15\,\mu\mathrm{m}$. Here, both correction voltages have been optimized/adjusted like in a real trap. Adjusting the two correction voltages it is possible to cancel C_4 as well as C_6, even e.g. $\delta l \neq 0$. Compared to the present trap, the axial frequency shifts will be significantly reduced by at least four orders of magnitude, allowing much larger signal-to-noise ratios for the readout of e.g. the axial phase.

In fig. 7.4 the improvement of the signal-to noise ratio of the axial peak signal is illustrated for a single proton trapped in our present experimental setup (in turquoise) and in the future experimental setup as a function of the excited axial amplitude and the axial frequency shifts. In this calculation, also the improved axial detection system is considered: The present axial resonator exhibits a parallel resistance of $R_p = 6.8\,\mathrm{M\Omega}$ and an effective electrode distance of $D = 7.38\,\mathrm{mm}$. The future axial resonator will have a parallel resistance of at least $R_p = 50\,\mathrm{M\Omega}$ and an electrode distance of $D = 9.1\,\mathrm{mm}$. Such a toroidal resonator is presently assembled and tested within our group. So far, axial resonators at the g-factor experiment of the proton ($\nu_{\mathrm{res}} \approx 700\,\mathrm{kHz}$) have demonstrated parallel resistances of $R_p = 130\,\mathrm{M\Omega}$ ($Q = 12500$), see [157, 158].

Proton SNR's far in excess of 20 dB seem to be feasible at absolutely negligible axial frequency shifts generated by electric field imperfections.

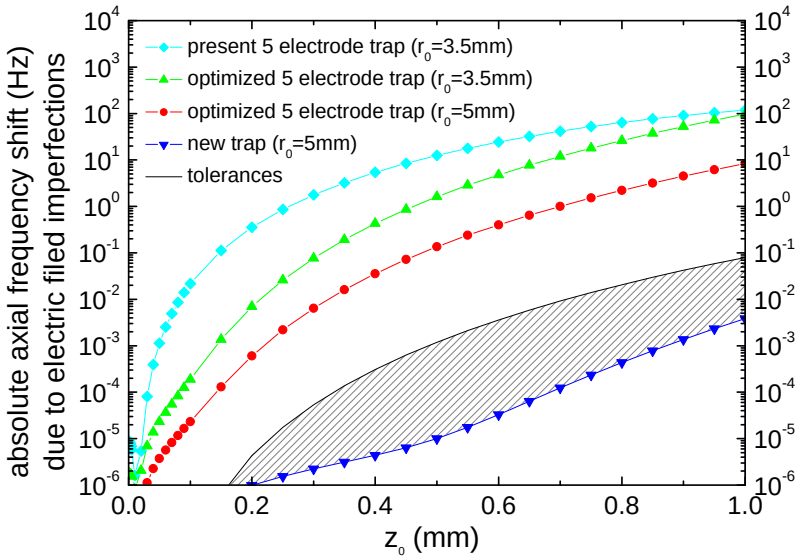

Figure 7.3: Study of the axial frequency shifts of a proton caused by electric field imperfections as a function of the excited axial amplitude ($U_r = -7\,\mathrm{V} \;\rightarrow\; \nu_z(\mathrm{proton}) = 625\,\mathrm{kHz}$). Four different scenarios are studied: (1) the present five-electrode trap with $r_0 = 3.5\,\mathrm{mm}$ (turquoise); (2) a compensated ($C_4 = C_6 = 0$) five-electrode trap with $r_0 = 3.5\,\mathrm{mm}$ (green); (3) a compensated five-electrode trap with $r_0 = 5\,\mathrm{mm}$ (red) and (4) the new optimized seven-electrode trap with $r_0 = 5\,\mathrm{mm}$ (blue). The black shaded area denotes the axial shifts of the new trap in case of deviations in the electrode lengths and the inner trap radius of $\delta l = \pm 15\,\mu\mathrm{m}$ and $\delta r_0 = \pm 15\,\mu\mathrm{m}$. For further details, see text.

7.1.4 Handling the Combined Orthogonality

For a comfortable handling of the trap a certain level of orthogonality is of great importance. In this section, the on-line optimization of the trapping potential is studied with respect to the weaker *combined orthogonality*. Due to the large single D_2's: $D_{21} = -0.798$ and $D_{22} = 0.943$, see eq. (7.14), C_2 and thus the axial frequency strongly depend on the chosen tuning ratios of the correction electrodes $TR_1 \equiv U_{c1}/U_r$ and $TR_2 \equiv U_{c2}/U_r$. However, the optimized combined $D_2^{\mathrm{comb}} = -1.9 \cdot 10^{-7}$, see eq. (7.15), enables a seven orders of magnitude smaller dependence of the axial frequency by changing both tuning ratios by the same relative size, see table 7.2. It is remarkable, that the axial frequency depends even more strongly on the change of the correction electrode voltages, see line two and three in table 7.2, than on the modification of the ring voltage (line four). In that way, it is difficult to handle $U_{c,1}$ and $U_{c,2}$ separately.

In table 7.3, I study three different trap configurations: (1) the optimized trap; (2) a trap, where the electrode lengths deviate up to 15 µm, and (3) a trap, where the electrode lengths, as well as the trap radius and the electrode distances deviate up to 15 µm. The second column specifies the size of the corresponding D_2^{comb}. In the third column the axial

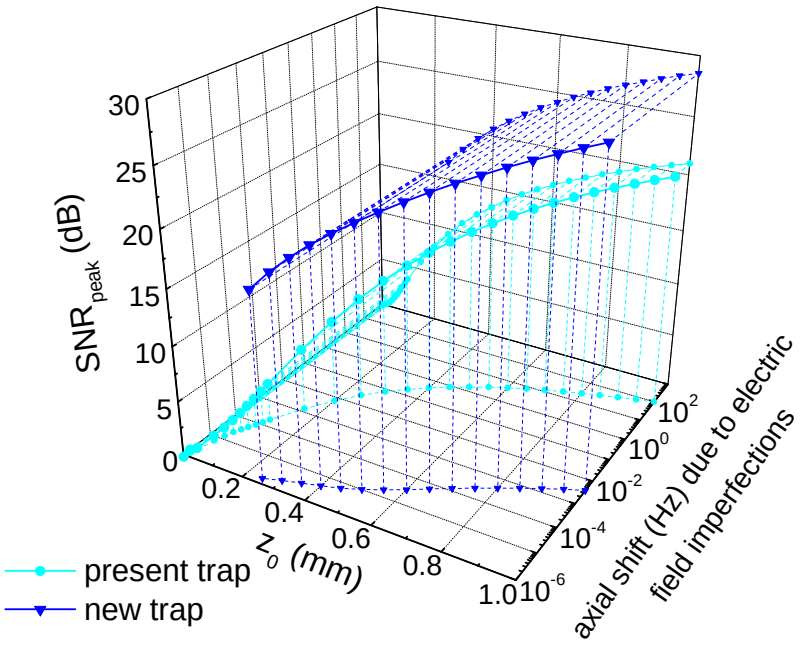

Figure 7.4: Comparison between the signal-to-noise ratio (SNR) of the axial peak signal for the present (turquoise) and future (blue) experimental setup as a function of the excited axial amplitude, also including the axial frequency shifts caused by electric field imperfections. For details see text.

frequency shift of a thermalized proton ($z_0 = 55\,\mu m$ $r_+ = r_- = 6.8\,\mu m$) is given in case of a 10% modification of D_2^{comb} by changing U_{c1} and U_{c2} by 10%. For comparison in the fourth column the axial shifts are listed, when D_2^{comb} is not modified.
In the following, I assume an imperfect seven-electrode trap with $\delta l = \pm 15\,\mu m$, $\delta dd = \pm 15\,\mu m$ and $\delta r_0 = \pm 15\,\mu m$, which corresponds to the third scenario presented in table 7.3 (third line), to study the on-line optimization of the trapping potential, performed in two steps. I start this optimization with the predicted values given in table 7.1. In the following I cancel C_4 by a modification of D_2^{comb}, which generates an axial frequency shift of only 26 Hz, see second line in table 7.4. Afterwards, I cancel C_4 and C_6 by a stepwise adjustments of TR_1 and TR_2, which generate acceptable axial frequency shifts of 54 Hz at most. In that way, the handling of the trap voltages during the on-line adjustment of the trap harmonicity seems to be manageable.

7.1.5 Final Design of the Seven-Electrode Proton Trap

The assembling and commissioning of the new experimental setup will be part of the doctoral thesis of Jiamin Hou. In the following section I will present the final design of the seven-electrode proton trap, which is presented in fig. 7.6.
At the moment, the electrodes are being manufactured by the precision mechanics workshop

Table 7.2: Study of the combined orthogonality. In four scenarios we study the sensitivity of the axial frequency of the proton ($U_r = -7\,\mathrm{V}$) as a function of voltage changes at the correction electrodes and the ring electrode. In the second column the corresponding axial frequency shifts for a proton are listed, $\nu_z(\mathrm{proton}) = 625\,\mathrm{kHz}$. Here, I assume a thermalized proton with $z_0 = 55\,\mu\mathrm{m}$, $r_+ = r_- = 6.8\,\mu\mathrm{m}$.

modification of TR's	$\lvert\Delta\nu_z(\mathrm{proton})\rvert$ (Hz)
1% in TR_1 and TR_2 (= 1% in D_2^{comb})	0.7
1% only in TR_1	4027
1% only in TR_2	4052
1% only in U_r	3114

Table 7.3: Study of axial frequency shifts caused by 10% modifications of D_2^{comb} and different trap imperfections. In the first line modifications in the optimized trap are calculated. In the the second line (imperfect trap I) only the lengths of the electrodes deviate: $\delta l = +15\,\mu\mathrm{m}$, $\delta r_0 = 0\,\mu\mathrm{m}$, $\delta dd = 0\,\mu\mathrm{m}$. In the third line (imperfect trap II) also the trap radius and the electrode distances deviate: $\delta l = +15\,\mu\mathrm{m}$, $\delta r_0 = -15\,\mu\mathrm{m}$, $\delta dd = 15\,\mu\mathrm{m}$. In the third column the ion is thermalized: $z_0 = 55\,\mu\mathrm{m}$ $r_+ = r_- = 6.8\,\mu\mathrm{m}$. In the fourth column the excited proton has the following amplitude and radii: $z_0 = 1\,\mathrm{mm}$, $r_+ = r_- = 6.8\,\mu\mathrm{m}$.

trap configurations	D_2^{comb}	ν_z shift (Hz) by 10% change of D_2^{comb}	ν_z shifts (Hz) at $z_0 = 1\,\mathrm{mm}$
optimized trap	$-1.9 \cdot 10^{-7}$	7	−0.004
imperfect trap I	0.013	693	0.031
imperfect trap II	0.031	1648[a]	0.089

a In case of an additional offset potential of +100 mV applied to one of the correction electrodes I of *imperfect trap II* a 10% change of all four correction voltages would cause a 2 kHz shift in the axial frequency.

of the faculty of physics in Mainz, see fig. 7.5. The cylindrical electrodes are made of OFHC copper and have been produced on a lathe with accuracies of the inner diameters and axial lengths below 10 µm. The reached parallelism of the upper and lower sides of the electrodes is also well below 10 µm. To optimize the equality of the inner diameter of both correction electrodes and the ring electrode and furthermore to optimize the alignment of their inner surfaces, the electrodes are at first separately produced with smaller inner diameters. Afterwards they are stacked on top of each other with proper brass rings in between and finally the inner surface of the complete electrode stack is machined to the final inner diameter.

Cooling the trap setup from room temperature $\approx 293\,\mathrm{K}$ to 4.2 K, the copper electrodes have a shrinking coefficient of $\eta_{\mathrm{Cu}} = 1.00324$ [159], so that the production lengths of the electrodes amount to: $l_r = 1.021\,\mu\mathrm{m}$, $l_{\mathrm{c1}} = 1.976\,\mu\mathrm{m}$ and $l_{\mathrm{c2}} = 3.336\,\mu\mathrm{m}$[2]. Unfortunately

2 Here, also the 15 µm gold/silver layers have been considered.

Table 7.4: Study of the on-line optimization of the trapping potential of an imperfect trap. Starting (first line) with the predicted voltages given in table 7.1, then canceling C_4 by scaling of D_2^{comb} (second line) and finally canceling C_4 and C_6 by tiny modifications of TR_1 and TR_2, the on-line operation of the trap seems to be manageable due to the relatively small axial frequency shifts listed in the fourth column. For further details see text.

	U_{c1} (V)	U_{c2} (V)	ν_z (Hz)	$\Delta\nu_z$
start with optimized voltages	−6.7450	−5.7089	621592	0
minimize C_4 by scaling D_2^{comb}	−6.7266	−5.6933	621618	26
minimize C_4 and C_6 by TR_1 and TR_2	−6.7437	−5.6897	621662	54

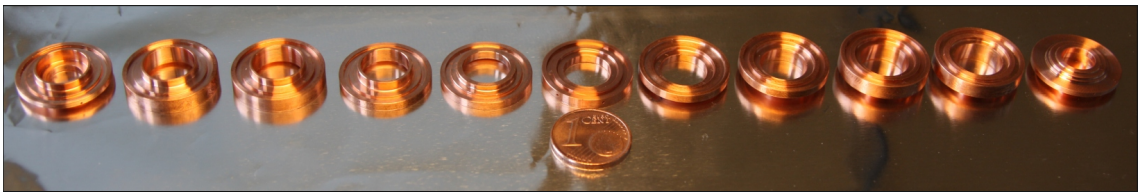

Figure 7.5: Photo of the new trap electrodes. From left to right: outer endcap, inner endcap one, inner endcap two, correction electrode two, correction electrode one, ring electrode, correction electrode one, correction electrode two, inner endcap two, inner endcap one, outer endcap. As a reference a one euro cent coin is placed below the ring electrode. All electrodes will be coated by a ≈ 3 µm silver layer and on top a ≈ 12 µm pure gold layer[a]. The inner correction electrodes as well as the ring electrode will be split in an electrical discharge machining (EDM). Each endcap electrode has been subdivided into three parts (outer endcap, inner endcap one, inner endcap two) to enable a reliable transport of the trapped ions. For further details, see text.

a At the moment, the layer thicknesses are not completely settled. The thickness of the silver layer will be $0-4$ µm and the thickness of the gold layer will be $11-15$ µm so that the absolut thickness amounts to 15 µm.

the shrinking coefficient of the insulator rings between the electrodes, made of sapphire or quartz glass ($\eta_{\mathrm{quartz}} \approx \eta_{\mathrm{sapphire}} = 1.0008045$) [159], is smaller than the shrinking coefficient of copper. When fixing the electrodes from outside by the insulator rings, like in the present Penning trap design, see fig. 3.3(a), adjacent electrodes could get radially misaligned during the cooling process. Using insulator rings with an inner diameter of 17 µm such misalignment would amount up to 20 µm. To circumvent this undesired effect, a sophisticated stacking design has been developed, where the ring and both correction electrodes embrace T-shaped quartz glass rings, see fig. 7.6. Consequently, during the cooling process the copper electrodes shrink on these quartz glass rings and in that way automatically align. Due to the more complex ring geometry, quartz glass has been chosen for the three central insulator rings instead of sapphire, which is more difficult to machine. Moreover, trap capacitances are reduced by using quartz glass ($\varepsilon_r \approx 3.75$ at 25° and $10^3 - 10^9$ Hz) instead of sapphire ($\varepsilon_r = 9.3...11.5$ at 25° and $10^3 - 10^9$ Hz). These quartz glass rings have been produced with tolerances < 5 µm by Aachener Quarz-Glas Technologie Heinrich in Aachen, Germany, and the sapphire rings (also the three pads and the rod, see

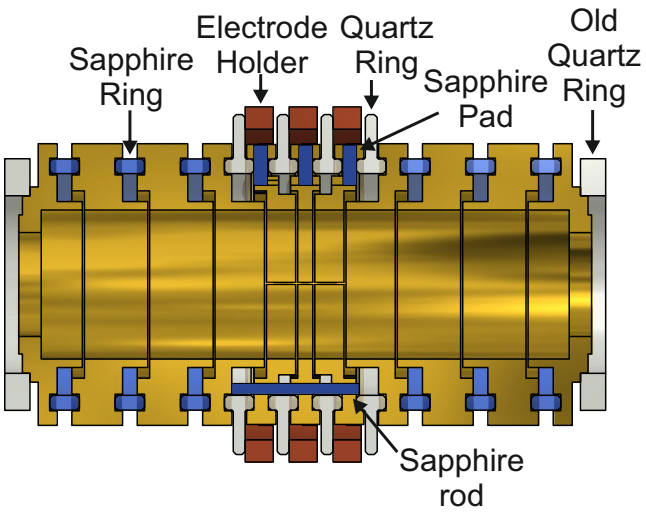

Figure 7.6: Cross section of the final design of the seven-electrode proton trap. Illustration of the sapphire and quartz glass rings fixing the electrodes. For details see text.

below) also with tolerances $< 5\,\mu m$ by the Saphirwerk AG in Brügg, Switzerland. For the cyclotron resonators, see also below, as well as for the quadrupole excitation, the ring and the inner correction electrodes are vertically split. The electrode splitting into two parts will be realized in a spark eroding process, also stated as electrical discharge machining (EDM). Such as for the existing traps, see section 4.1.5, the copper electrodes will be finally coated by a 1 µm silver layer and on top a 14 µm pure gold layer, deposited in galvanic processes. For the fixing of the split electrodes on one side three tiny sapphire pads will be placed within the vertical slits and on the other side one single rod will align all three electrodes, see also fig. 7.6. Preventing the split electrodes to fall apart additional copper rings (shown in red) fix these electrodes by two ceramic screws for each split electrode.
For an unperturbed electric field configuration the electrodes are designed in a way that from the inside of the trap only the gold plated electrode surfaces can be seen. A staged design of the neighboring electrode surfaces ensures that this requirement also holds for the slits between the electrodes, see again fig. 7.6. Furthermore, the electrode distances amount to 140 µm only for the inner part of the trap; in the outer part of the trap the electrode distances are significantly enlarged to decrease the trap capacitances.

Further Technical Characteristics of the Trap

The axial effective electrode distances D are given in table 7.5.

The Cyclotron Resonator of the Proton

Two tuned cyclotron resonators are required for the cooling of the modified cyclotron motions of the proton as well as of the reference particle $^{12}C^{6+}$. Placing these resonators outside of the trap chamber, the undesired inductance of the wire ($\approx 10\,cm$) would significantly contribute to the total inductance. Therefore, these resonators will be placed in cylindrical OFHC copper boxes into the trap chamber next to the trap tower. One

Table 7.5: Effective electrode distances D of the new trap in axial direction for different electrode combinations.

electrodes	D (mm)
correction I and II	9.1
correction I	20.4
correction II	16.3
correction II and endcap	12.3

resonator box is spatially limited to a height of 9 cm and a diameter of < 20 mm.
The cyclotron resonator of the proton requires a resonance frequency of $\nu_{\mathrm{res}} = 57.380\,\mathrm{kHz}$ ($U_r = -12.5\,\mathrm{V}$) and a quality factor of at least a few 1000 to reach cooling times constants in the order of several seconds. Assuming a trap capacitance of 12 pF and a resonator capacitance of 3 pF, an inductance of $L = 1/(C_{\mathrm{tot}}\omega_{\mathrm{res}}^2) \approx 0.52\,\mu\mathrm{H}$ is required.
Using an ultra-pure alu-wire (99.999% purity) with a wire diameter of 1 mm and a measured residual resistive ratio (RRR) of about 1245(140), a helical resonator (19 windings, inner winding diameter: 9.6 mm and distance of adjacent windings: 1 mm) has been built, which features a resonator capacitance of 3.03 pF, an inductance of 0.63 µH, free quality factors of 2300 at 4.5 K and 340 at room temperatures. Further studies of different wire materials and annealing processes are prepared.

7.2 Outlook

In this final section I will highlight the next generation of bound electron g-factor experiments currently being set up at GSI and MPIK as well as the upgrade plans of the experimental setup presented in this thesis.

7.2.1 Bound-Electron g-Factor Measurements at Heavy Highly Charged Ions

High-precision tests of quantum electrodynamics in the strongest accessible electric fields are performed on atomic energy transitions of heavy highly charged ions. Due to the $(Z\alpha)^n$ scaling of the radiative QED corrections even the Schwinger Limit can be approached at very large Z, see fig. 2.2, e.g. causing large vacuum polarization contributions.
Especially for heavy highly charged ions two different measurement approaches exist for the determination of the studied Zeeman transitions:

- On the one hand the continuous Stern-Gerlach effect can be applied, see section 3.5, which requires an additional Penning trap with a large magnetic bottle. Considering heavy ions, it is a enormous challenge to resolve the axial frequency shifts generated by the induced spin-flips, due to their inverse scaling with the ion's mass and their linear scaling with the g-factor. Regarding boronlike lead ($Z = 82$, $g(^{208}\mathrm{Pb}^{77+}) \approx 0.60$) the axial frequency shift in our present analysis trap ($B_2 \approx 10.5 \cdot 10^3\,\mathrm{T/m^2}$, $\nu_z = 412\,\mathrm{kHz}$) would amount to $\Delta\nu_z \approx 10\,\mathrm{mHz}$. As discussed in section 6.1, already the resolution of the spin-flips of lithiumlike calcium $^{48}\mathrm{Ca}^{17+}$ ($\Delta\nu_z \approx 140\,\mathrm{mHz}$) has been a challenge.
- On the other hand the energies of the ground-state hyperfine splitting (HFS) in hydrogenlike and lithiumlike ions scale with the third power in the nuclear charge. Consequently these transitions shift into the laser-accessible region for $Z > 60$,

enabling laser-microwave double-resonance spectroscopy, e.g. described in [151]. Here, probing of the Zeeman transition in the microwave range is combined with a simultaneous optical detection of the spin-state by laser spectroscopy of the fine or hyperfine structure. During such a measurement the ion is placed in a single Penning trap. No additional Penning trap including a large magnetic bottle is needed.

Due to the large ionization energies of heavy, highly charged ions an external ion production and subsequent injection into the experimental setup is required. For this purpose two prominent facilities are used: (1) HITRAP [160] located at the GSI Helmholtzzentrum für Schwerionenforschung GmbH in Darmstadt. Here, highly charged ions will be loaded from the experimental storage ring (ESR) (initial energy $\approx 400\,\mathrm{MeV/u}$) into the HITRAP facility for deceleration and cooling (final energy $\approx 0.3\,\mathrm{meV}$). (2) The other facility, the Heidelberg EBIT [161] is located at the Max-Planck-Institut für Kernphysik (MPIK) in Heidelberg. It is one of the three high-energy electron beam ion traps (EBIT), which are presently in operation worldwide. So-far, hydrogenlike barium ($Z = 56$) has been observed in the Heidelberg EBIT. Heavier systems requiring higher electron beam energies are in preparation.
These days the following two different experiments are built to measure bound-electron g-factors of heavy highly charged ions.

ARTEMIS

ARTEMIS (AsymmetRic Trap for the measurement of Electron Magnetic moments in IonS) is currently setup in the group of Wolfgang Quint at the HITRAP facility [151, 152]. In its first configuration it is based on laser-microwave double-resonance spectroscopy [151, 152]. In general, tests of BS-QED are planned. Beyond that, nuclear magnetic moments will be determined in absence of diamagnetic shielding. Combinations of measured g_F-factors allow the simultaneous determination of electronic g-factors (g_J) and nuclear g-factors (g_I) from one experiment. One of the first measurement campaigns will focus on boronlike argon $^{40}\mathrm{Ar}^{13+}$, where also higher-order contributions of the Zeeman effect can be measured for the first time in highly charged ions [53].

ALPHATRAP

ALPHATRAP will be a successor experiment of the experiment presented in this thesis, specialized in bound-electron g-factors of highly charged ions in the lead region. At the moment this experiment is developed and assembled in the group of Sven Sturm at MPIK. The detection of the Larmor frequency is based on the continuous Stern-Gerlach effect. The trap radius of the precision trap ($r = 9\,\mathrm{mm}$) is a factor of ≈ 2.6 larger than in the existing setup. In that way, the present dominant systematic uncertainty, the image charge shift, is reduced by a factor of $2.6^3 \approx 17$. Ions up to hydrogenlike lead ($E_{\mathrm{ion}} = 99.5\,\mathrm{keV}$) will be injected from the Heidelberg EBIT. Various bound-electron g-factor measurements are planned on heavy highly charged ions without nuclear spins. Based on the idea of Vladimir M. Shabaev and colleagues, nuclear size contributions which limit the BS-QED in very strong fields will be significantly reduced by measuring e.g. the g-factors of hydrogenlike and lithiumlike ions of the same isotope [51]. Moreover, measuring the g-factor difference of a boronlike and a hydrogenlike ion of the same isotope in the lead region ($Z = 82$)

will provide an alternative excess to the fine structure constant α [149]. Since the nuclear contributions cancel to a large extent, the g-factor contribution with the largest contribution to α is the Breit term, a relativistic non-QED term.

7.2.2 High-Precision Measurement of the Atomic Proton Mass

In the near future the present bound-electron experiment will be rebuilt for a direct high-precision measurement of the atomic proton mass, as already mentioned in section 7.1. Here, the cyclotron frequency-ratio of the proton and a carbon nucleus $^{12}C^{6+}$ will be measured with the relative precision of about $1 \cdot 10^{-11}$. The underlying measurement principle has been developed by Sven Sturm. In order to cancel the impact of residual magnetic field fluctuations, which represents the dominant limitation of the present measurements, the cyclotron frequencies of the carbon ion and the proton will be alternately compared to a highly charged reference ion with a phase-sensitive measurement technique in a four-trap setup. The rebuilt setup is illustrated in fig. 7.7. A two-step measurement procedure

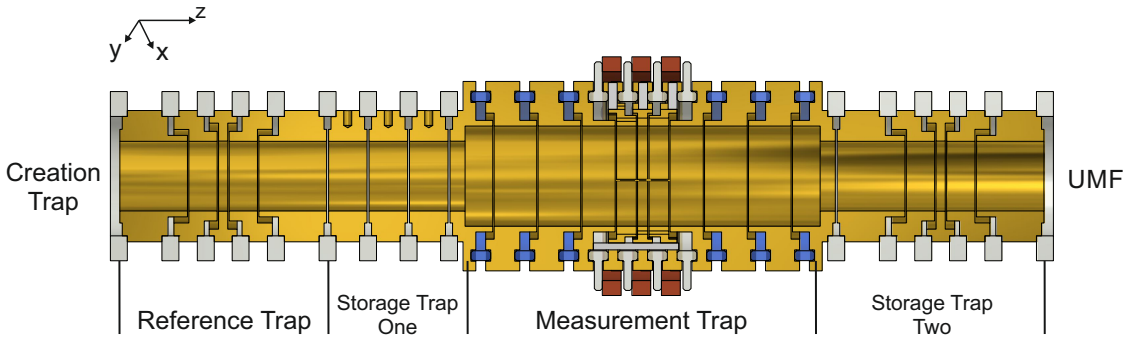

Figure 7.7: Illustration of the new Penning trap tower consisting of four Penning traps: (1) A measurement trap, based on the trap design introduced in this chapter, with an inner diameter of 10 mm. (2) A reference trap, which is the precision trap (PT) of our present setup. (3-4) Storage traps I and II. For further details see text.

will be performed, in which the proton and carbon ion are alternatively loaded into the measurement trap (MT). In the first step we measure simultaneously the modified cyclotron phase of a single proton placed in the MT against the modified cyclotron phase of a single highly charged ion, e.g. silicon, placed in the reference trap (RT). During that measurement the carbon ion is stored in the storage trap one (ST I). In the second step the proton is transported into storage trap two (ST II) while the carbon ion is transported into the measurement trap. Subsequently, the cyclotron phase of the carbon ion is simultaneously measured against the cyclotron phase of the silicon ion in the reference trap. By comparing these two cyclotron phase differences magnetic field fluctuations cancel to a large extent. To minimize systematic magnetic field shifts, the proton and the carbon ion are placed at the same position in the measurement trap, by applying exactly the same trapping voltages in both measurement steps. In that way, each ion requires its own axial resonator, which have to be exactly tuned with respect to the other axial resonator. Furthermore, two high-Q cyclotron resonators will be mounted, allowing an efficient way of cooling the modified cyclotron modes to liquid-helium temperatures.

A subsequent measurement campaign will focus on a high-precision value of the atomic mass of deuterium. In combination with a high-precision measurement of its binding energy, which is currently prepared at the Institute Laue-Langevin (ILL) in Grenoble, and the new value of the atomic mass of the proton, the atomic mass of the neutron could be significantly improved.

With these very exciting perspectives I conclude my thesis.

Bibliography

1. Higgs, P. W.: 'Broken symmetries, massless particles and gauge fields'. *Phys. Lett.* (1964), vol. 12(2): pp. 132 –133.
2. Englert, F. and R. Brout: 'Broken Symmetry and the Mass of Gauge Vector Mesons'. *Phys. Rev. Lett.* (9 1964), vol. 13: pp. 321–323.
3. Guralnik, G. S., C. R. Hagen, and T. W. B. Kibble: 'Global Conservation Laws and Massless Particles'. *Phys. Rev. Lett.* (20 1964), vol. 13: pp. 585–587.
4. Ellis, J. and T. You: 'Updated Global Analysis of Higgs Couplings'. *JHEP* (2013), vol. 1306: p. 103.
5. Peter, A. H. G.: *Dark Matter: A Brief Review*. arXiv:1201.3942. (2012).
6. Peebles, P.J.E. and B. Ratra: 'The Cosmological constant and dark energy'. *Rev. Mod. Phys.* (2003), vol. 75: pp. 559–606.
7. Fukuda, Y. et al.: 'Evidence for Oscillation of Atmospheric Neutrinos'. *Phys. Rev. Lett.* (8 1998), vol. 81: pp. 1562–1567.
8. Ahmad, Q. R. et al.: 'Measurement of the Rate of $\nu_e + d \rightarrow p + p + e^-$ Interactions Produced by ^8B Solar Neutrinos at the Sudbury Neutrino Observatory'. *Phys. Rev. Lett.* (7 2001), vol. 87: p. 071301.
9. Ellis, J. R.: *Limits of the standard model*. arXiv:hep-ph/0211168. (2002).
10. The ATLAS Collaboration: 'The ATLAS Experiment at the CERN Large Hadron Collider'. *J. Instrum.* (2008), vol. 3(08): S08003.
11. The CMS Collaboration: 'CMS Physics Technical Design Report, Volume II: Physics Performance'. *J. Phys. G* (), vol. 34(6): p. 995.
12. S.-I. Tomonaga J. Schwinger, R. P. Feynman: *Nobel Prize in Physics 1965 - Presentation Speech*. (1965).
13. Sturm, S.: *The g-factor of the electron bound in $^{28}Si^{13+}$: The most stringent test of bound-state quantum electrodynamics*. Doktorarbeit. (2012).
14. Wagner, A.: *The g-factor of the valence electron bound in lithiumlike silicon $^{28}Si^{11+}$: The most stringent test of relativistic many-electron calculations in a magnetic field*. Doktorarbeit. (2013).
15. Rutherford, E.: 'LXXIX. The scattering of α and β particles by matter and the structure of the atom'. *Philos. Mag. Series 6* (1911), vol. 21(125): pp. 669–688.

16. Bohr, N.: 'I. On the constitution of atoms and molecules'. *Philos. Mag. Series 6* (1913), vol. 26(151): pp. 1–25.

17. Aoyama, T., M. Hayakawa, T. Kinoshita, and M. Nio: 'Tenth-Order QED Contribution to the Electron $g - 2$ and an Improved Value of the Fine Structure Constant'. *Phys. Rev. Lett.* (11 2012), vol. 109: p. 111807.

18. Hanneke, D., S. Fogwell, and G. Gabrielse: 'New Measurement of the Electron Magnetic Moment and the Fine Structure Constant'. *Phys. Rev. Lett.* (12 2008), vol. 100: p. 120801.

19. Bouchendira, R., P. Cladé, S. Guellati-Khélifa, F. Nez, and F. Biraben: 'New Determination of the Fine Structure Constant and Test of the Quantum Electrodynamics'. *Phys. Rev. Lett.* (8 2011), vol. 106: p. 080801.

20. Gerlach, W. and O. Stern: 'Der experimentelle Nachweis der Richtungsquantelung im Magnetfeld'. German. *Z. Phys.* (1922), vol. 9(1): pp. 349–352.

21. Uhlenbeck, G. E. and S. Goudsmit: 'Ersetzung der Hypothese vom unmechanischen Zwang durch eine Forderung bezüglich des inneren Verhaltens jedes einzelnen Elektrons'. German. *Die Naturwissenschaften* (1925), vol. 13(47): pp. 953–954.

22. Landé, A: *Interview of Dr. A. Landé by T. S. Kuhn and J. Heilbron in Berkeley on March 6,1962, Niels Bohr Library and Archives, American Institute of Physics, College Park, MD USA*. (1962).

23. Lamb, W. E. and R. C. Retherford: 'Fine Structure of the Hydrogen Atom by a Microwave Method'. *Phys. Rev.* (3 1947), vol. 72: pp. 241–243.

24. Nafe, J. E., E. B. Nelson, and I. I. Rabi: 'The Hyperfine Structure of Atomic Hydrogen and Deuterium'. *Phys. Rev.* (12 1947), vol. 71: pp. 914–915.

25. Nagle, D. E., R. S. Julian, and J. R. Zacharias: 'The Hyperfine Structure of Atomic Hydrogen and Deuterium'. *Phys. Rev.* (10 1947), vol. 72: pp. 971–971.

26. Kusch, P. and H. M. Foley: 'Precision Measurement of the Ratio of the Atomic 'g Values' in the $^2P_{\frac{3}{2}}$ and $^2P_{\frac{1}{2}}$ States of Gallium'. *Phys. Rev.* (12 1947), vol. 72: pp. 1256–1257.

27. Foley, H. M. and P. Kusch: 'On the Intrinsic Moment of the Electron'. *Phys. Rev.* (4 1948), vol. 73: pp. 412–412.

28. Schwinger, J.: 'On Quantum-Electrodynamics and the Magnetic Moment of the Electron'. *Phys. Rev.* (4 1948), vol. 73: pp. 416–417.

29. Suslov, S. K.: 'Expectation values in relativistic Coulomb problems'. *J. Phys. B* (2009), vol. 42(18): p. 185003.

30. Yanovsky, V., V. Chvykov, G. Kalinchenko, P. Rousseau, T. Planchon, T. Matsuoka, A. Maksimchuk, J. Nees, G. Cheriaux, G. Mourou, and K. Krushelnick: 'Ultra-high intensity- 300-TW laser at 0.1 Hz repetition rate'. *Opt. Express* (2008), vol. 16(3): pp. 2109–2114.

31. Schwinger, J.: 'On Gauge Invariance and Vacuum Polarization'. *Phys. Rev.* (5 1951), vol. 82: pp. 664–679.
32. Sauter, F.: 'Über das Verhalten eines Elektrons im homogenen elektrischen Feld nach der relativistischen Theorie Diracs'. German. *Z. Phys.* (1931), vol. 69(11-12): pp. 742–764.
33. Heisenberg, W. and H. Euler: 'Folgerungen aus der Diracschen Theorie des Positrons'. German. *Z. Phys.* (1936), vol. 98(11-12): pp. 714–732.
34. Beier, T.: 'The g_j factor of a bound electron and the hyperfine structure splitting in hydrogenlike ions'. *Phys. Rep.* (2000), vol. 339(2–3): pp. 79 –213.
35. Furry, W. H.: 'On Bound States and Scattering in Positron Theory'. *Phys. Rev.* (1 1951), vol. 81: pp. 115–124.
36. Zatorski, J., Z. Harman, and C. H. Keitel. private communication. (2015).
37. Volotka, A. V. private communication. (2015).
38. Breit, G.: 'The Magnetic Moment of the Electron'. *Nature* (1928), vol. 122: p. 649.
39. Quint, W. and M. Vogel, eds.: *Fundamental Physics in Particle Traps*. Springer, 2014.
40. Blundell, S. A., K. T. Cheng, and J. Sapirstein: 'Radiative corrections in atomic physics in the presence of perturbing potentials'. *Phys. Rev. A* (3 1997), vol. 55: pp. 1857–1865.
41. Yerokhin, V. A., P. Indelicato, and V. M. Shabaev: 'Evaluation of the self-energy correction to the g factor of S states in H-like ions'. *Phys. Rev. A* (5 2004), vol. 69: p. 052503.
42. Beier, T., I. Lindgren, H. Persson, S. Salomonson, P. Sunnergren, H. Häffner, and N. Hermanspahn: 'g_j factor of an electron bound in a hydrogenlike ion'. *Phys. Rev. A* (3 2000), vol. 62: p. 032510.
43. Pachucki, K., A. Czarnecki, U. D. Jentschura, and V. A. Yerokhin: 'Complete two-loop correction to the bound-electron g factor'. *Phys. Rev. A* (2 2005), vol. 72: p. 022108.
44. Bohr, A. and V. F. Weisskopf: 'The Influence of Nuclear Structure on the Hyperfine Structure of Heavy Elements'. *Phys. Rev.* (1 1950), vol. 77: pp. 94–98.
45. Glazov, D.A. and V.M. Shabaev: 'Finite nuclear size correction to the bound-electron g factor in a hydrogenlike atom'. *Phys. Lett. A* (2002), vol. 297(5–6): pp. 408 –411.
46. Sturm, S., A. Wagner, B. Schabinger, J. Zatorski, Z. Harman, W. Quint, G. Werth, C. H. Keitel, and K. Blaum: 'g Factor of Hydrogenlike $^{28}Si^{13+}$'. *Phys. Rev. Lett.* (2 2011), vol. 107: p. 023002.
47. Zatorski, J., N. S. Oreshkina, C. H. Keitel, and Z. Harman: 'Nuclear Shape Effect on the g Factor of Hydrogenlike Ions'. *Phys. Rev. Lett.* (6 2012), vol. 108: p. 063005.

48. Shabaev, V. M.: 'QED theory of the nuclear recoil effect on the atomic g factor'. *Phys. Rev. A* (5 2001), vol. 64: p. 052104.

49. Nefiodov, A. V., G. Plunien, and G. Soff: 'Nuclear-Polarization Correction to the Bound-Electron g Factor in Heavy Hydrogenlike Ions'. *Phys. Rev. Lett.* (8 2002), vol. 89: p. 081802.

50. Volotka, A. V. and G. Plunien: 'Nuclear Polarization Study: New Frontiers for Tests of QED in Heavy Highly Charged Ions'. *Phys. Rev. Lett.* (2 2014), vol. 113: p. 023002.

51. Shabaev, V. M., D. A. Glazov, M. B. Shabaeva, V. A. Yerokhin, G. Plunien, and G. Soff: 'g factor of high-Z lithiumlike ions'. *Phys. Rev. A* (6 2002), vol. 65: p. 062104.

52. Volotka, A.V., D. A. Glazov, V. M. Shabaev, I. I. Tupitsyn, and G. Plunien: 'Many-Electron QED Corrections to the g Factor of Lithiumlike Ions'. *Phys. Rev. Lett.* (25 2014), vol. 112: p. 253004.

53. Lindenfels, D. von, M. Wiesel, D. A. Glazov, A. V. Volotka, M. M. Sokolov, V. M. Shabaev, G. Plunien, W. Quint, G. Birkl, A. Martin, and M. Vogel: 'Experimental access to higher-order Zeeman effects by precision spectroscopy of highly charged ions in a Penning trap'. *Phys. Rev. A* (2 2013), vol. 87: p. 023412.

54. Glazov, D. A. private communication. (2015).

55. Häffner, H., T. Beier, N. Hermanspahn, H.-J. Kluge, W. Quint, S. Stahl, J. Verdú, and G. Werth: 'High-Accuracy Measurement of the Magnetic Moment Anomaly of the Electron Bound in Hydrogenlike Carbon'. *Phys. Rev. Lett.* (25 2000), vol. 85: pp. 5308–5311.

56. Verdú, J., S. Djekić, S. Stahl, T. Valenzuela, M. Vogel, G. Werth, T. Beier, H.-J. Kluge, and W. Quint: 'Electronic g Factor of Hydrogenlike Oxygen $^{16}O^{7+}$'. *Phys. Rev. Lett.* (9 2004), vol. 92: p. 093002.

57. Schabinger, B., S. Sturm, A. Wagner, J. Alonso, W. Quint, G. Werth, and K. Blaum: 'Experimental g factor of hydrogenlike silicon-28'. English. *EPJ D* (2012), vol. 66(3), 71.

58. Sturm, S., A. Wagner, B. Schabinger, and K. Blaum: 'Phase-Sensitive Cyclotron Frequency Measurements at Ultralow Energies'. *Phys. Rev. Lett.* (14 2011), vol. 107: p. 143003.

59. Wagner, A., S. Sturm, F. Köhler, D. A. Glazov, A. V. Volotka, G. Plunien, W. Quint, G. Werth, V. M. Shabaev, and K. Blaum: 'g Factor of Lithiumlike Silicon $^{28}Si^{11+}$'. *Phys. Rev. Lett.* (3 2013), vol. 110: p. 033003.

60. Thomson, J. J.: 'XL. Cathode Rays'. *Philos. Mag. Series 5* (1897), vol. 44(269): pp. 293–316.

61. Thomson, J.J.: *Nobel Lecture: Carriers of Negative Electricity.* Nobelprize.org. Nobel Media AB 2014. Web. 6 Feb 2015. (1906).

62. Gabrielse, G., D. Hanneke, T. Kinoshita, M. Nio, and B. Odom: 'New Determination of the Fine Structure Constant from the Electron g Value and QED'. *Phys. Rev. Lett.* (3 2006), vol. 97: p. 030802.

63. Pospelov, M. and A. Ritz: 'Electric dipole moments as probes of new physics'. *Ann. Phys.* (2005), vol. 318(1). Special Issue: pp. 119 –169.

64. The ACME Collaboration et al.: 'Order of Magnitude Smaller Limit on the Electric Dipole Moment of the Electron'. *Science* (2014), vol. 343(6168): pp. 269–272.

65. Mohr, P. J., B. N. Taylor, and D. B. Newell: 'CODATA recommended values of the fundamental physical constants: 2010*'. *Rev. Mod. Phys.* (4 2012), vol. 84: pp. 1527–1605.

66. Mount, B. J., M. Redshaw, and E. G. Myers: 'Atomic masses of ^{6}Li, ^{23}Na, ^{39,41}K, ^{85,87}Rb and ^{133}Cs'. *Phys. Rev. A* (4 2010), vol. 82: p. 042513.

67. Bennett, G. W. et al.: 'Final report of the E821 muon anomalous magnetic moment measurement at BNL'. *Phys. Rev. D* (7 2006), vol. 73: p. 072003.

68. Davier, M., A. Hoecker, B. Malaescu, and Z. Zhang: 'Reevaluation of the hadronic contributions to the muon $g-2$ and to $\alpha(M_Z^2)$'. *Eur. Phys. J. C* (2011), vol. 71(1): p. 1515.

69. Gärtner, G. and E. Klempt: 'A direct determination of the proton-electron mass ratio'. English. *Z. Phys. A* (1978), vol. 287(1): pp. 1–6.

70. Gräff, G., H. Kalinowsky, and J. Traut: 'A direct determination of the proton electron mass ratio'. English. *Z. Phys. A* (1980), vol. 297(1): pp. 35–39.

71. Van Dyck, R. S. and P. B. Schwinberg: 'Preliminary Proton/Electron Mass Ratio using a Compensated Quadring Penning Trap'. *Phys. Rev. Lett.* (6 1981), vol. 47: pp. 395–398.

72. Van Dyck, R. S., F. L. Moore, D. L. Farnham, and P. B. Schwinberg: 'New measurement of the proton-electron mass ratio'. *Int. J. Mass Spectrom. and Ion Proc.* (1985), vol. 66(3): pp. 327 –337.

73. Farnham, D. L., R. S. Van Dyck, and P. B. Schwinberg: 'Determination of the Electron's Atomic Mass and the Proton/Electron Mass Ratio via Penning Trap Mass Spectroscopy'. *Phys. Rev. Lett.* (20 1995), vol. 75: pp. 3598–3601.

74. Wineland, D. J., J. J. Bollinger, and W. M. Itano: 'Laser-Fluorescence Mass Spectroscopy'. *Phys. Rev. Lett.* (9 1983), vol. 50: pp. 628–631.

75. Gabrielse, G., X. Fei, L. A. Orozco, R. L. Tjoelker, J. Haas, H. Kalinowsky, T. A. Trainor, and W. Kells: 'Thousandfold improvement in the measured antiproton mass'. *Phys. Rev. Lett.* (11 1990), vol. 65: pp. 1317–1320.

76. Hori, M., A Sótér, D. Barna, A. Dax, R. Hayano, S. Friedreich, B. Juhász, T. Pask, E. Widmann, D. Horváth, L. Venturelli, and N. Zurlo: 'Two-photon laser spectroscopy of antiprotonic helium and the antiproton-to-electron mass ratio'. *Nature* (2011), vol. 474: pp. 484–488.

77. Sturm, S., F. Köhler, J. Zatorski, A. Wagner, Z. Harman, G. Werth, W. Quint, C. H. Keitel, and K. Blaum: 'High-precision measurement of the atomic mass of the electron'. *Nature* (2014), vol. 506: pp. 467 –470.

78. Cohen, E. R. and B. N. Taylor: 'The 1973 Least-Squares Adjustment of the Fundamental Constants'. *J. Phys. Chem. Ref. Data* (1973), vol. 2(4): pp. 663–734.

79. Cohen, E. R. and B. N. Taylor: 'The 1986 CODATA Recommended Values of the Fundamental Physical Constants'. *J. Phys. Chem. Ref. Data* (1988), vol. 17(4): pp. 1795–1803.

80. Mohr, P. J. and B. N. Taylor: 'CODATA recommended values of the fundamental physical constants: 1998'. *Rev. Mod. Phys.* (2 2000), vol. 72: pp. 351–495.

81. Mohr, P. J. and B. N. Taylor: 'CODATA recommended values of the fundamental physical constants: 2002*'. *Rev. Mod. Phys.* (1 2005), vol. 77: pp. 1–107.

82. Mohr, P. J., B. N. Taylor, and D. B. Newell: 'CODATA recommended values of the fundamental physical constants: 2006*'. *Rev. Mod. Phys.* (2 2008), vol. 80: pp. 633–730.

83. Beier, T., H. Häffner, N. Hermanspahn, S. G. Karshenboim, H.-J. Kluge, W. Quint, S. Stahl, J. Verdú, and G. Werth: 'New Determination of the Electron's Mass'. *Phys. Rev. Lett.* (1 2001), vol. 88: p. 011603.

84. Moore, C. E.: *Tables of Spectra of Hydrogen, Carbon, Nitrogen, and Oxygen Atoms and Ions*. (1993).

85. Biémont, E., Y. Frémat, and P. Quinet: 'Ionization potentials of atoms and ions from lithium to tin (Z=50)'. *Atomic Data and Nuclear Data Tables* (1999), vol. 71(1): pp. 117 –146.

86. Ölme, A.: 'The Spectrum of Singly Ionized Boron B II'. *Physica Scripta* (1970), vol. 1(5-6): p. 256.

87. Tunklev, M, L Engström, C Jupén, and I Kink: 'The spectrum and term system of C IV'. *Phys. Scripta* (1997), vol. 55(6): p. 707.

88. Drake, G. W. F.: 'Theoretical Energies for the n=1 and 2 States of the Helium Isoelectronic Sequence up to Z=100'. *Can. J. Phys.* (1988), vol. 66.

89. Kramida, A., Yu. Ralchenko, J. Reader, and NIST ASD Team. NIST Atomic Spectra Database (ver. 5.2), [Online]. Available: http://physics.nist.gov/asd [2015, January 26]. National Institute of Standards and Technology, Gaithersburg, MD. (2014).

90. Klopper, W., R. A. Bachorz, D. P. Tew, and C. Hättig: 'Sub-meV accuracy in first-principles computations of the ionization potentials and electron affinities of the atoms H to Ne'. *Phys. Rev. A* (2 2010), vol. 81: p. 022503.

91. Pálffy, A.: 'Nuclear effects in atomic transitions'. *Contemporary Physics* (2010), vol. 51(6): pp. 471–496.

92. Soria Orts, R., Z. Harman, J. R. Crespo López-Urrutia, A. N. Artemyev, H. Bruhns, A. J. González Martínez, U. D. Jentschura, C. H. Keitel, A. Lapierre, V. Mironov, V. M. Shabaev, H. Tawara, I. I. Tupitsyn, J. Ullrich, and A. V. Volotka: 'Exploring Relativistic Many-Body Recoil Effects in Highly Charged Ions'. *Phys. Rev. Lett.* (10 2006), vol. 97: p. 103002.

93. Hughes, William M. and H. G. Robinson: 'Determination of an Isotope Shift in the Ratio of Atomic g_J Values of Hydrogen and Deuterium'. *Phys. Rev. Lett.* (21 1969), vol. 23: pp. 1209–1212.

94. Angeli, I. and K.P. Marinova: 'Table of experimental nuclear ground state charge radii: An update'. *Atomic Data and Nuclear Data Tables* (2013), vol. 99(1): pp. 69 –95.

95. Köhler, F. et al.: *Beyond the Furry picture of bound-state quantum electrodynamics with highly charged ions*. submitted. (2015).

96. Grotch, H. and R. A. Hegstrom: 'Hydrogenic Atoms in a Magnetic Field'. *Phys. Rev. A* (1 1971), vol. 4: pp. 59–69.

97. Close, F.E. and H. Osborn: 'Relativistic extension of the electromagnetic current for composite systems'. *Phys. Lett. B* (1971), vol. 34(5): pp. 400–404.

98. Pachucki, K.: 'Nuclear mass correction to the magnetic interaction of atomic systems'. *Phys. Rev. A* (1 2008), vol. 78: p. 012504.

99. Eides, M. I. and T. J. S. Martin: 'Universal Binding and Recoil Corrections to Bound State g Factors in Hydrogenlike Ions'. *Phys. Rev. Lett.* (10 2010), vol. 105: p. 100402.

100. Y., Zong-Chao: 'Calculations of magnetic moments for lithium-like ions'. *J. Phys. B* (2002), vol. 35(8): p. 1885.

101. Block, M. et al.: 'Towards direct mass measurements of nobelium at SHIPTRAP'. English. *EPJ D* (2007), vol. 45(1): pp. 39–45.

102. Chaudhuri, A., M. Block, S. Eliseev, R. Ferrer, F. Herfurth, A. Martin, G. Marx, M. Mukherjee, C. Rauth, L. Schweikhard, and G. Vorobjev: 'Carbon-cluster mass calibration at SHIPTRAP'. English. *EPJ D* (2007), vol. 45(1): pp. 47–53.

103. Savard, G., St. Becker, G. Bollen, H.-J. Kluge, R.B. Moore, Th. Otto, L. Schweikhard, H. Stolzenberg, and U. Wiess: 'A new cooling technique for heavy ions in a Penning trap'. *Phys. Lett. A* (1991), vol. 158(5): pp. 247 –252.

104. Eliseev, S., K. Blaum, M. Block, C. Droese, M. Goncharov, E. Minaya Ramirez, D. A. Nesterenko, Yu. N. Novikov, and L. Schweikhard: 'Phase-Imaging Ion-Cyclotron-Resonance Measurements for Short-Lived Nuclides'. *Phys. Rev. Lett.* (8 2013), vol. 110: p. 082501.

105. Eliseev, S., K. Blaum, M. Block, A. Dörr, C. Droese, T. Eronen, M. Goncharov, M. Höcker, J. Ketter, E.Minaya Ramirez, D.A. Nesterenko, Yu.N. Novikov, and L. Schweikhard: 'A phase-imaging technique for cyclotron-frequency measurements'. English. *Appl. Phys. B* (2014), vol. 114(1-2): pp. 107–128.

106. Yurtsever, E. and N. Elmaci: 'Dissociation Dynamics of Small Carbon Clusters'. English. *Tr. J. of Chemistry* (1997), vol. 21: pp. 35–41.

107. Belau, L., S. E. Wheeler, B. W. Ticknor, M. Ahmed, S. R. Leone, W. D. Allen, H. F. Schaefer, and M. A. Duncan: 'Ionization Thresholds of Small Carbon Clusters: Tunable VUV Experiments and Theory'. *J. Am. Chem. Soc.* (2007), vol. 129(33): pp. 10229–10243.

108. Beyer, H.F., G. Menzel, D. Liesen, A. Gallus, F. Bosch, R. Deslattes, P. Indelicato, Th. Stöhlker, O. Klepper, R. Moshammer, F. Nolden, H. Eickhoff, B. Franzke, and M. Steck: 'Measurement of the ground-state lambshift of hydrogenlike uranium at the electron cooler of the ESR'. English. *Z. Phys. D* (1995), vol. 35(3): pp. 169–175.

109. Nagy, Sz., T. Fritioff, A. Solders, R. Schuch, M. Björkhage, and I. Bergström: 'Precision mass measurements of $^{40}Ca^{17+}$ and $^{40}Ca^{19+}$ ions in a Penning trap'. English. *EPJ D* (2006), vol. 39(1): pp. 1–4.

110. Audi, G., M. Wang, A.H. Wapstra, F.G. Kondev, M. MacCormick, X. Xu, and B. Pfeiffer: 'The Ame2012 atomic mass evaluation'. *Chin. Phys. C* (2012), vol. 36(12): p. 1603.

111. Rodrigues, G.C., P. Indelicato, J.P. Santos, P. Patté, and F. Parente: 'Systematic calculation of total atomic energies of ground state configurations'. *Atomic Data and Nuclear Data Tables* (2004), vol. 86(2): pp. 117 –233.

112. Earnshaw, S.: *On the nature of the molecular forces which regulate the constitution of the luminiferous ether.* (1842).

113. Paul, W. and H. Steinwedel: 'Ein neues Massenspektrometer ohne Magnetfeld'. *Z. Naturforsch. A* (1953), vol. 8a: pp. 448–450.

114. Paul, Wolfgang: 'Electromagnetic traps for charged and neutral particles'. *Rev. Mod. Phys.* (3 1990), vol. 62: pp. 531–540.

115. Dehmelt, H. G.: *The Nobel Prize in Physics 1989.* (1989).

116. Penning, F. M.: 'Die Glimmentladung bei niedrigem Druck zwischen koaxialen Zylindern in einem axialen Magnetfeld'. *Physica III* (1936), vol. 9: p. 873.

117. Pierce, J. R.: 'Theory and Design of Electron Beams'. Ed. by Nostrand, Van. New York, 1949.

118. Verdú, J. L.: *Ultrapräzise Messung des elektronischen g-faktors in wasserstoffähnlichem Sauerstoff.* Doktorarbeit. (2003).

119. Brown, L. S. and G. Gabrielse: 'Geonium theory: Physics of a single electron or ion in a Penning trap'. *Rev. Mod. Phys.* (1 1986), vol. 58: pp. 233–311.

120. Ketter, J., T. Eronen, M. Höcker, S. Streubel, and K. Blaum: 'First-order perturbative calculation of the frequency-shifts caused by static cylindrically-symmetric electric and magnetic imperfections of a Penning trap'. *Int. J. Mass* (2014), vol. 358(0): pp. 1 –16.

121. Brown, Lowell S. and Gerald Gabrielse: 'Precision spectroscopy of a charged particle in an imperfect Penning trap'. *Phys. Rev. A* (4 1982), vol. 25: pp. 2423–2425.

122. Gabrielse, G., L. Haarsma, and S. L. Rolston: 'Open-Endcap Penning Traps for High Precision Experiments'. *Int. J. Mass Spectrom. and Ion Proc.* (1989), vol. 88: pp. 319–332.

123. Ramo, S.: 'Currents Induced by Electron Motion'. *Proc. IEEE* (1939), vol. 27(9): pp. 584–585.

124. Stahl, S. K.-H.: *Aufbau eines Experimentes zur Bestimmung elektronischer g-Faktoren einzelner wasserstoffähnlicher Ionen*. Doktorarbeit. (1998).

125. Johnson, J. B.: 'Thermal Agitation of Electricity in Conductors'. *Phys. Rev.* (1 1928), vol. 32: pp. 97–109.

126. Nyquist, H.: 'Thermal Agitation of Electric Charge in Conductors'. *Phys. Rev.* (1 1928), vol. 32: pp. 110–113.

127. Wineland, D. J. and H. G. Dehmelt: 'Principles of the stored ion calorimeter'. *J. Appl. Phys.* (1975), vol. 46(2): pp. 919–930.

128. Häffner, H.: *Präzisionsmessung des magnetischen Moments des Elektrons in wasserstoffähnlichem Kohlenstoff*. Doktorarbeit. (2000).

129. Van Dyck, R. S., F. L. Moore, D. L. Farnham, and P. B. Schwinberg: 'Number dependency in the compensated Penning trap'. *Phys. Rev. A* (11 1989), vol. 40: pp. 6308–6313.

130. Sturm, S., A. Wagner, M. M. Kretzschmar, W. Quint, G. Werth, and K. Blaum: 'g-factor measurement of hydrogenlike $^{28}Si^{13+}$ as a challenge to QED calculations'. *Phys. Rev. A* (3 2013), vol. 87: p. 030501.

131. Köhler, F., S. Sturm, A. Kracke, G. Werth, W. Quint, and K. Blaum: *The electron mass from g-factor measurements on hydrogen-like carbon* $^{12}C^{5+}$. accepted by the Journal of Physics B: Atomic, Molecular and Optical Physics, as a Special Issue Article. (2015).

132. Multiphysics, COMSOL: *version 4.2 a*. COMSOL, Inc.

133. Cornell, E. A., R. M. Weisskoff, K. R. Boyce, and D. E. Pritchard: 'Mode coupling in a Penning trap: π pulses and a classical avoided crossing'. *Phys. Rev. A* (1 1990), vol. 41: pp. 312–315.

134. Kretzschmar, M.: 'A quantum mechanical model of Rabi oscillations between two interacting harmonic oscillator modes and the interconversion of modes in a Penning trap'. *AIP Conf. Proc.* (1999), vol. 457(1).

135. Ketter, J., T. Eronen, M. Höcker, M. Schuh, S. Streubel, and K. Blaum: 'Classical calculation of relativistic frequency-shifts in an ideal Penning trap'. *Int. J. Mass* (2014), vol. 361(0): pp. 34 –40.

136. Castiglioni, P.: *Zero Padding*. (2014).

137. Dehmelt, H.: 'Continuous Stern-Gerlach effect: Principle and idealized apparatus'. (1986), vol. 83(8): pp. 2291–2294.

138. Schabinger, B.: *Ein Experiment zur Bestimmung des g-Faktors des gebundenen Elektrons in wasserstoff- und lithiumähnlichen mittelschweren Ionen*. Doktorarbeit. (2011).

139. Hermanspahn, N. H.: *Das magnetische Moment des gebundenen Elektrons in wasserstoffartigem Kohlenstoff (C^{5+})*. Doktorarbeit. (1999).

140. Otamendi, J. A.: *Development of an Experiment for Ultrahigh-Precision g-Factor Measurements in a Penning-Trap Setup*. Doktorarbeit. (2007).

141. Alonso, J., K. Blaum, S. Djekic, H.-J. Kluge, W. Quint, B. Schabinger, S. Stahl, J. Verdú, M. Vogel, and G. Werth: 'A miniature electron-beam ion source for in-trap creation of highly charged ions'. *Rev. Sci. Instrum.* (2006), vol. 77(3).

142. Tönges, M.: *Aufbau einer Mikrowellen-Anlage zur Spektroskopie an wasserstoffähnlichen Ionen in einem Penningkäfig*. Dipolmarbeit. (1996).

143. Gabrielse, G. and J. Tan: 'Self-shielding superconducting solenoid systems'. *J. Appl. Phys.* (1988), vol. 63(10): pp. 5143–5148.

144. Gabrielse, G, J Tan, P Clateman, L.A Orozco, S.L Rolston, C.H Tseng, and R.L Tjoelker: 'A superconducting solenoid system which cancels fluctuations in the ambient magnetic field'. *Journal of Magnetic Resonance (1969)* (1991), vol. 91(3): pp. 564 –572.

145. Ulmer, S.: *First Observation of Spin Flips with a Single Proton Stored in a Cryogenic Penning Trap*. Doktorarbeit. (2011).

146. Blaum, K. and S. Sturm: *Lecture: "Stored charged particles"*. (2014).

147. Royston, P.: 'Remark AS R94'. *Applied Statistics*. Vol. 44. 1995: pp. 547–551.

148. Beier, T., S. Djekic, H. Häffner, P. Indelicato, H.-J. Kluge, W. Quint, V. M. Shabaev, J. Verdú, T. Valenzuela, G. Werth, and V. A. Yerokhin: 'Determination of the electron's mass from g-factor experiments on $^{12}C^{5+}$ and $^{16}O^{7+}$'. *Nucl. Instrum. Methods Phys. Res. B* (2003), vol. 205(0): pp. 15 –19.

149. Shabaev, V. M., D. A. Glazov, N. S. Oreshkina, A. V. Volotka, G. Plunien, H.-J. Kluge, and W. Quint: 'g-Factor of Heavy Ions: A New Access to the Fine Structure Constant'. *Phys. Rev. Lett.* (25 2006), vol. 96: p. 253002.

150. Volotka, A. V. private communication. (May 2015).

151. Quint, W., D. L. Moskovkhin, V. M. Shabaev, and M. Vogel: 'Laser-microwave double-resonance technique for g-factor measurements in highly charged ions'. *Phys. Rev. A* (3 2008), vol. 78: p. 032517.

152. Lindenfels, D. von, N. P. M. Brantjes, G. Birkl, W. Quint, V. M. Shabaev, and M. Vogel: 'Bound electron g-factor measurement by double-resonance spectroscopy on a fine-structure transition'. *Can. J. Phys.* (2011), vol. 89(1): pp. 79–84.

153. Roux, C., C. Böhm, A. Dörr, S. Eliseev, S. George, M. Goncharov, Y.N. Novikov, J. Repp, S. Sturm, S. Ulmer, and K. Blaum: 'The trap design of PENTATRAP'. *Appl. Phys. B* (2012), vol. 107(4): pp. 997–1005.

154. Roux, C.-E.: *High-Resolution Mass Spectrometry: The Trap Design and Detection System of PENTATRAP and New Q-Values for Neutrino Studies*. Doktorarbeit. (2012).

155. MATLAB: *version 8.1.0.604 (R2013a)*. Natick, Massachusetts, USA: The MathWorks Inc., (2013).

156. Lagarias, Jeffrey C., James A. Reeds, Margaret H. Wright, and Paul E. Wright: 'Convergence Properties of the Nelder–Mead Simplex Method in Low Dimensions'. *SIAM J. on Optimization* (May 1998), vol. 9(1): pp. 112–147.

157. Mooser, A., H. Kracke, K. Blaum, S. A. Bräuninger, K. Franke, C. Leiteritz, W. Quint, C. C. Rodegheri, S. Ulmer, and J. Walz: 'Resolution of Single Spin Flips of a Single Proton'. *Phys. Rev. Lett.* (14 2013), vol. 110: p. 140405.

158. Mooser, A.: *Der g-Faktor des Protons*. Doktorarbeit. (2013).

159. Repp, J.: *The setup of the high-precision Penning-trap mass spectrometer PENTATRAP and first production studies of highly charged ions*. Doktorarbeit. (2012).

160. Kluge, H.-J. et al.: 'Chapter 7 HITRAP: A Facility at {GSI} for Highly Charged Ions'. *Current Trends in Atomic Physics*. Ed. by Salomonson, S. and E. Lindroth. Vol. 53. Advances in Quantum Chemistry. Academic Press, 2008: pp. 83 –98.

161. Crespo López-Urrutia, J R, A Dorn, R Moshammer, and J Ullrich: 'The Freiburg Electron Beam Ion Trap/Source Project FreEBIT'. *Phys. Scripta* (1999), vol. 1999(T80B): p. 502.

Danksagung

Zu guter Letzt noch ein paar Sätze über meine große Freude, nun seit fast vier Jahren an diesem spannenden Experiment und in diesem unglaublich sympathischen, hoch motivierten Team zu arbeiten. Bei euch und allen weiteren Personen, die bei der Umsetzung dieser Doktorarbeit beteiligt waren, möchte ich mich von ganzem Herzen bedanken.

Ich beginne mit meinem ersten Betreuer dieser Doktorarbeit, Wolfgang Quint. Du hattest mich vor etwa vier Jahren keine fünf Minuten nach meiner schriftlichen Anfrage angerufen und in deiner so freundlichen Art von diesem Experiment geschwärmt. Diese Begeisterung hat sofort abgefärbt und ist bei mir über die Jahre immer weiter gewachsen. Ganz besonders danke ich dir für all die freitäglichen Gespräche in Mainz. Es war für mich eine sehr große Freude in diesen Treffen von dir und deinem umfassenden und tiefen Verständnis unseres Forschungsgebiets zu lernen. Ich danke dir für deine permanente, so sympathische Unterstützung und für die großen Freiräume, die du mir bei meiner Arbeit geschaffen hast.

Herrn Selim Jochim danke ich für ihre direkte Bereitschaft meine Arbeit als zweiter Gutachter zu betreuen.

Bevor ich euch, Klaus Blaum, Jiamin Hou, Anke Kracke, Sven Sturm und Günter Werth einzeln danke, wollte ich euch als Team, natürlich inklusive Wolfgang, einen riesigen Dank aussprechen. Ich habe mich vom ersten Arbeitstag an unglaublich wohl gefühlt und habe diese sehr enge, harmonische Zusammenarbeit an diesem großartigen Projekt sehr genossen.

Lieber Klaus, auch wenn du offiziell ja gar nicht mein Betreuer warst, hast du dich enorm und mit viel zeitlichem Aufwand für mich eingesetzt. Mich beeindruckt es sehr, wie du deine Gruppe leitest, auf deine lockere, so sympathische Art. Der sehr dichte Austausch in Form von unzähligen Emails, Mats Treffen oder Mats Tagen haben mich immer sehr motiviert. Ich danke dir sehr für all deinen Einsatz und deine unglaubliche Erreichbarkeit. Für mich ist es noch immer ein faszinierendes Rätsel, wie schnell und eigentlich rund um die Uhr du meine Emails beantwortest. Des Weiteren danke ich dir für all den Einsatz bei den Papern und die vielen Anregungen zu Konferenzen und Seminaren.

Liebe Jiamin, du bist nun seit etwa einem Jahr in unserer Gruppe und hast die Position der hauptverantwortlichen Doktorandin mit viel Einsatz und Motivation übernommen. Ich

danke dir für die sehr nette Zusammenarbeit im letzten Jahr und wünsche dir viel Freude und Erfolg mit dem Experiment und dem nun anstehenden Umbau.

Liebe Anke, als ich vor fast vier Jahren zu euch, also zu der Zeit vor allem zu Sven und dir, gestoßen bin, warst du gerade mit deiner Messung an lithiumähnlichen Silizium beschäftigt. Die Art, wie ihr beide mich in eure Gruppe integriert habt, war großartig. Zunächst habt ihr mich mit viel Einsatz und unglaublicher Unterstützung eingearbeitet und später dann haben wir immer mehr sehr eng zusammengearbeitet. Ich hatte immer das Gefühl, dass wir bei all den Aufgaben sehr gut harmonieren. Ich danke dir für all deine Unterstützung, sei es direkt im Labor, bei Rechnungen oder Vorbereitungen von Talks oder Papern. Viel Erfolg und Freude auf deinem weiteren Weg und bis zum nächsten Volleyballspiel oder Treffen.

Lieber Sven, ein ganz besonders großes Glück war es für mich mit einem solch genialen, lieben Physiker wie dir zusammenzuarbeiten und dir bei deiner Ideenumsetzung zu helfen. Dein unfassbar tiefes Verständnis von Physik, deine einmalige Art mit Freude und Begeisterung Dinge Schritt für Schritt zu erklären, deine unzähligen genialen Ideen, dein schnelles Durchdringen und Lösen von Problemen, all das hat mich sehr beeindruckt. Abgesehen von all dieser Physikalität bedanke ich mich ganz herzlich bei dir für deine sehr liebe, sensible und sehr enge, tägliche Zusammenarbeit. Ein riesiges Dankeschön für all deine Hilfe und Unterstützung. Ich wünsche dir, dass du auch in Zukunft all deine großartigen Ideen umsetzen kannst. Ich freue mich sehr nach diesen etwas monotonen Schreibmonaten noch für eine Weile wieder mit dir im Labor zu arbeiten.

Als letztes Gruppenmitglied danke ich Herrn Günter Werth. Ihre Begeisterung an der Physik und der damit einhergehende Einsatz beeindrucken mich sehr. Ich danke Ihnen, für die vielen Gespräche über den Fortschritt der Messungen und der Unterstützung bei meiner Arbeit, insbesondere bei der Vorbereitung von Präsentationen und Papern. Große Freude hatte ich bei den vielen Gesprächen zum Mittagessen in der Mensa und den unzähligen Geschichten aus ihrem wissenschaftlichen Leben.

Des Weiteren danke ich meinen Kollegen vom Proton g-Faktor Experiment, besonders Holger Kracke, Andreas Mooser und Georg Schneider. Die Zeit mit euch war großartig.

Ein großer Beitrag zum Gelingen dieser Arbeit kommt aus der theoretischen Physik. Hierbei bedanke ich mich ganz herzlich bei Jacek Zatorski, Zoltán Harman und Christoph H. Keitel, die durch ihre Rechnungen die Bestimmung der Elektronenmasse ermöglicht haben. The calculations of the isotope shift and the g-factors of the lithiumlike calcium ions have been performed by Vladimir M. Shabaev, Dmitry A. Glazov und Andrey V. Volotka. The collaboration, the meetings and emails have been a great pleasure and quiet helpful to understand at least some part of your complicated calculations, thank you very much. In diesem Zusammenhang danke ich auch Sergey Eliseev und dem gesamten SHIPTRAP Team für die Messung der ^{48}Ca Masse.

Ein großes Dankeschön auch an Erwin Gries und Herbert Geibel für das wöchentliche Abfüllen des flüssigen Heliums und an die Mitarbeiter der Werkstätten des Insituts für Physik der Uni Mainz, die zur Zeit die Elektroden der neuen Protonfalle mit sehr großem Aufwand und höchster Präzision anfertigen.

Ein sehr lieber Dank gilt auch meinen Mensa-Kollegen aus der Budker-Gruppe, hier vor allem Dionysis Antypas, Nathan Leefer und Arne Wickenbrock. Eure offene und integrierende Art hat für mich die Atmosphäre in der Fakultät weiter gesteigert. Insbesondere unsere Freizeitaktivitäten während meiner Schreibphase haben mir Energie gegeben. Schade, dass ihr erst im letzten Jahr meiner Doktorarbeit eingetrudelt seit.

Als Vorletztes danke ich meinen Eltern, Gudrun und Thomas Köhler und meinen beiden Geschwistern und ihren Familien. Ohne eure permanente, grenzenlose, liebevolle Unterstützung in den letzten 30 Jahren, würde ich diese Zeilen hier nicht schreiben.

Liebe Kri (Kristin Langes ;-)), gut, dass du damals den Psychologie-Masterstudiengang in Frankfurt präferiert hast, sonst wäre ich sicherlich nicht in diesem Keller-Paradies gelandet. Aus unserer supra-CMB Liebe schöpfe ich jede Sekunde die größtmögliche Lebensfreude überhaupt. Das ist für mich das größte Lebensglück. In der letzten Zeit war ich sicherlich relativ viel auf das Fertigstellen dieser Arbeit fokussiert, das ein paar unserer gemeinsamen Abende frecherweise dominiert hat. Jetzt und vor allem nach dieser Verteidigung wird der Fokus auch wieder anders gesetzt. Das Beste in den letzten schreibwütigen Monaten war natürlich nicht diese Arbeit, sondern das heranwachsende Lebensgeschenk in deinem Bauch. Darauf freue ich mich unglaublich.